

QATAR UNIVERSITY

COLLEGE OF ENGINEERING

BIO-INSPIRED FABRICATION OF ULTRAFILTRATION MEMBRANES

INCORPORATING POLYDOPAMINE FUNCTIONALIZED GRAPHENE OXIDE

NANOPARTICLES

BY

ABEDALKADER I. ALKHOUSAAM

A Dissertation Submitted to

the College of Engineering

in Partial Fulfillment of the Requirements for the Degree of

Doctorate of Philosophy in Environmental Engineering

June 2021

© 2021 Abedalkader I. Alkhouzaam. All Rights Reserved.

COMMITTEE PAGE

The members of the Committee approve the Dissertation of
Abedalkhader I. Alkouzaam defended on 20/04/2021.

Hazim Qiblawey
Thesis/Dissertation Supervisor

Viktor Kochkodan
Committee Member

Alaa AlHawari
Committee Member

Abdelbaki Benamor
Committee Member

Approved:

Khalid Kamal Naji, Dean, College of Engineering

ABSTRACT

Alkhouzaam, Abedalkader, I, Doctorate : June : 2021, Doctorate of Philosophy in Environmental Engineering

Title: Bio-Inspired Fabrication of Ultrafiltration Membranes incorporating Polydopamine Functionalized Graphene Oxide Nanoparticles

Supervisor of Dissertation: Hazim, Qiblawey.

Graphene oxide (GO) and its based materials have gained a significant interest in the membrane functionalization sector in the recent years. Inspired by their unique and tunable properties, several GO-based nanomaterials have been investigated and utilized for various membranes in water treatment, purification and desalination sectors. In this dissertation, novel polysulfone (PSF) ultrafiltration membranes incorporating polydopamine-functionalized reduced graphene oxide nanoparticles (rGO-PDA) were fabricated and investigated. Starting from natural graphite, GO nanoparticles with high oxidation degree were synthesized using an improved Hummers' method. A GO functionalization based on the bio-inspired PDA was then conducted to produce rGO-PDA nanoparticles. The high-oxidation degree of graphite and the successful functionalization with PDA were confirmed using several analytical techniques including CHNSO elemental analysis, XPS, FTIR-UATR, Raman spectroscopy and XRD. Several bands have emerged in the FTIR spectra of rGO-PDA attributed to the amine groups of PDA confirming the successful functionalization of GO. Raman spectra and XRD patterns showed different crystalline structures and higher interlayer spacing of rGO-PDA. The change in elemental compositions was confirmed by XPS and CHNSO elemental analysis while

the change in the morphological structure was confirmed by SEM and TEM analyses.

The second part of the dissertation was on the embedding of the above-mentioned nanoparticles in a membrane matrix. Pristine PSF, PSF/GO, and PSF/rGO-PDA mixed matrix membranes (MMMs) were prepared by embedding GO and rGO-PDA at concentrations from 0 to 0.15 wt% using the phase inversion technique. All membranes were analysed using FTIR-UATR, SEM, AFM, and contact angle. The cross-section SEM images showed better distribution of rGO-PDA nanoparticles in the pores and polymer wall whereas the pristine GO nanoparticles aggregate and partially block the pores. Thus, the flux increased with the embedding of rGO-PDA without affecting the rejection properties, while it decreased with the embedding of pristine GO. The highest pure water permeability (PWP) was obtained with PSF/rGO-PDA-0.1 to be approximately twice that of the pristine PSF and PSF/GO-0.1. All membranes exhibited complete rejection of BSA and HA and showed almost similar rejection performance against different dyes. The flux recovery ratio of the pristine PSF after three fouling cycles (FRR_3) against BSA and HA were recorded to be 57.8% and 70.7% respectively. FRR_3 was enhanced by around 30% with PSF/rGO-PDA composites. The MMMs prepared in this work are expected to have great potential on ultrafiltration and provide insights on developing other types of membranes embedding rGO-PDA with different materials and for different purposes..

DEDICATION

This dissertation is lovingly dedicated to

my parents, wife, brothers and sister

my beautiful children, Omar & Joud

my advisors & professors

Without their endless love, support, prayers, and encouragement

with the grace of Allah Almighty

it would not have been made possible

I am truly thankful for having you all in my life.

ACKNOWLEDGMENTS

Starting with the Name of Allah, the Most Beneficent, the Most Merciful; and prayers and peace be upon our Prophet Muhammad, the Messenger of Allah and all his family and companions. First and foremost, praise be to Allah who provided me with health, knowledge and competence until I reached the end of this PhD journey.

I would like to acknowledge Qatar National Research Fund (QNRF, a member of Qatar Foundation) for supporting and funding this work through the Graduate Sponsorship Research Award [GSRA4-1-0504-17043] that made this work possible.

I would like to express my sincere appreciation to my advisor Prof. Hazim Qiblawey for the continuous support of my PhD study and related research, for his patience, motivation, and immense knowledge. His guidance helped me and paved the way in all the time of research and writing of this dissertation. I would like also to extend my sincere appreciation to my co-advisor, Prof. Majeda Khraisheh for her encouragement and collaborative support in this work.

I extend my appreciation to the faculty and lab technicians of the Department of Chemical Engineering for their support in this research. I would like to thank also the Central Lab Unit (CLU), Gas Processing Center (GPC), Center of Advanced Materials (CAM) at Qatar University; and Core Labs in Qatar Environmental and Energy Research Institute (QEERI) for their support in the materials characterization.

Last but not the least, I would like to express my deep thanks and gratitude to my parents, brothers and sister for their encouragements and support; and special thanks to my wife for her patience and spiritual support throughout this journey.

TABLE OF CONTENTS

DEDICATION	v
ACKNOWLEDGMENTS	vi
LIST OF TABLES	x
LIST OF FIGURES	xii
NOMENCLATURE & ABBREVIATIONS	xvii
CHAPTER 1: INTRODUCTION	1
1.1. Scope and Objectives	4
CHAPTER 2: BACKGROUND	7
2.1 Graphene Oxide (GO)	7
2.1.1 GO synthesis	8
2.1.2 Reduced GO (rGO) and Functional GO Structures (f-GO).....	11
2.2 Polydopamine (PDA)	15
2.3 Fabrication Methods of GO-based Membranes	19
2.3.1 Non-solvent induced phase separation (NIPS)	19
2.3.2 Vacuum/ evaporation/ pressure-assisted self-assembly techniques.....	21
2.3.3 Layer-by-layer self-assembly (LBL)	23
2.3.4 Interfacial polymerization (IP).....	24
2.4 Antifouling Properties of GO-based Membranes.....	28
2.5 Applications & Properties of GO-based Membranes.....	31
2.5.1 GO-based RO membranes	32

2.5.2	GO-based NF membranes.....	38
2.5.3	GO-based UF membranes.....	46
2.5.4	GO-based MF membranes.....	54
2.5.5	GO-based FO membranes.....	57
2.5.6	GO-based MD and PV membranes.....	64
CHAPTER 3: METHODOLOGY & EXPERIMENTAL WORK.....		70
3.1	Materials.....	70
3.2	Synthesis of Graphene Oxide Nanoparticles.....	70
3.3	Functionalization of Graphene Oxide with Polydopamine.....	72
3.4	Fabrication of Mixed Matrix Membranes (MMMs).....	73
3.5	Materials Characterization.....	75
3.5.1	Characterization of GO nanoparticles.....	75
3.5.2	Characterization of rGO-PDA nanoparticles.....	76
3.5.3	Characterization of the membranes.....	78
3.6	Permeability & Separation Experiments.....	79
3.7	Dynamic Fouling Experiments.....	81
CHAPTER 4: RESULTS & DISCUSSION.....		84
4.1	Characterization of GO Nanoparticles.....	84
4.1.1	Morphology and chemical compositions.....	84
4.1.2	FTIR-UATR spectral analysis.....	91
4.1.3	Raman spectral analysis.....	94

4.1.4	Thermal stability	98
4.2	Characterization of rGO-PDA Nanoparticles	100
4.2.1	Structural and morphological properties.....	100
4.2.2	Compositional properties	103
4.2.3	FTIR-UATR and Raman spectral analysis	107
4.2.4	Dispersibility & hydrophilicity properties	111
4.2.5	Thermal stability	114
4.3	Characterization of the membranes.....	115
4.3.1	Structural and morphological properties.....	115
4.3.2	Hydrophilicity, porosity and mean pore size	120
4.4	Permeability & Separation Performance	123
4.5	Antifouling Properties	128
4.6	Comparison with the Literature	133
CHAPTER 5: CONCLUSIONS & FUTURE WORK		138
LIST OF PUBLICATIONS		144
REFERENCES		145
APPENDIX A: CHARACTERIZATION OF NANOPARTICLES		188
APPENDIX B: CHARACTERIZATION OF THE MEMBRANES		194

LIST OF TABLES

Table 2-1: Experimental conditions of GO preparation reported in the literature.....	10
Table 2-2: Summary of the recently developed GO-based RO membranes.....	37
Table 2-3: Summary of the recently developed GO-based NF membranes.....	43
Table 2-4: Summary of the recently developed GO-based UF membranes	52
Table 2-5: Summary of the recently developed GO-modified MF membranes	56
Table 2-6: Summary of the developed GO-based FO membranes and their performance in AL-FS orientation.....	63
Table 2-7: Summary of the recently developed GO-based MD and PVD membranes and their performance	68
Table 3-1: GO and rGO-PDA compositions in the prepared membranes	74
Table 3-2: Chemical formulas, structures and molecular weights of chemicals used for separation and fouling measurements.....	81
Table 3-3: Summary of the measurements and characterization performed on GO, rGO-PDA nanoparticles and the prepared membranes.....	83
Table 4-1: Elemental compositions of GO samples from CHNSO analysis	87
Table 4-2: Elemental compositions of GO samples from XPS analysis	89
Table 4-3: Comparison of experimental conditions and O/C atomic ratio of GO prepared in this study with literature values	91
Table 4-4: Crystallite sizes of GO samples estimated by Tuinstra-Koenig model.....	97
Table 4-5: XPS elemental compositions of the GO and rGO-PDA.....	107
Table 4-6: CHNSO elemental compositions of the GO and rGO-PDA.	107
Table 4-7: The average values of the root-mean-square roughness (RMS) and the average roughness (Ra) of the prepared membranes.	119

Table 4-8: The average values of the membrane thickness (l), porosity (ϵ), and mean pore size (r_m) of the prepared membranes.	123
Table 4-9: Performance comparison of the MMMs prepared in this work with other GO-based UF MMMs prepared by phase inversion in literature.	136
Table A1: Bands parameters estimated from the Raman first-order spectra fits.	190
Table A2: Bands parameters estimated from the Raman second-order spectra fits. .	191
Table A3: Peaks parameters and the atomic compositions estimated from the XPS spectra fits for the pristine GO and rGO-PDA nanoparticles.	192
Table A4: D and G bands' parameters of the Raman spectra and the estimated crystallite size of the GO and rGO-PDA nanoparticles.	192
Table A5: Bands parameters estimated from the Raman first-order spectra fits for the pristine GO and rGO-PDA nanoparticles.	193
Table A6: Bands parameters estimated from the Raman second-order spectra fits for the pristine GO and rGO-PDA nanoparticles.	193
Table B1: The output of the correlation test of PWP, contact angle, mean pore size (R_m), average roughness (R_a) and flux recovery ratios (FRR).	198

LIST OF FIGURES

Figure 1-1: The basic concepts and classifications of membrane processes.	2
Figure 1-2: Number of publications related to GO-based membranes in recent years..	4
Figure 2-1: Illustration of GO synthesis via the Hummers method.....	9
Figure 2-2: Stability measurments of GO-PVDF (top) and rGO-PVDF (below) membranes in water [91]	12
Figure 2-3: Illustrations of the chemical structure of: (a) guanidyl-f-GO (GFG) [100], (b) Tannic acid-f-GO (GO-TA) [101], (c) Starch-f-GO (GO-ST) [103], (d) 3-aminopropyltriethoxysilane f-GO (GO-APTS) [109], (e) <i>p</i> -aminophenol-f-GO [32], (f) amine-functionalized ZIF-8-GO nanocomposite [110], (g) Ethylenediamine-f-GO (GO-EDA) and (h) Polyethylenimine-f-GO (GO-PEI) [111].....	14
Figure 2-4: Methods used for membranes functionalization with PDA.....	16
Figure 2-5: GO-based MMMs fabrication using NIPS technique.....	20
Figure 2-6: illustration of the GO composite membranes fabrication using (a) VAS, (b) EAS, and (c) PAS methods.	21
Figure 2-7: photographs and cross-section TEM images of GO/mPAN prepared using: (a) and (d): PAS, (b) and (e): VAS, (c) and (f): EAS techniques [145].....	22
Figure 2-8: Freestanding rGO membrane fabrication using VAS technique [146].....	23
Figure 2-9: Illustration of the LBL self-assembly technique using polycation and negatively charged GO solution.....	24
Figure 2-10: Illustration of the interfacial polymerization (IP) technique to prepare: (a) TFN membrane incorporating GO into the PA layer, (b) TFC membrane having GO on the surface of PA layer (s-TFC), (c) TFC membrane having an interlayer of GO (i-TFC), and (d) TFC membrane incorporating GO into the polymer matrix (m-	

TFC).....	25
Figure 2-11: Types of membrane fouling.	28
Figure 2-12: effect of GO flake size on the PA layer structure [267].....	59
Figure 2-13: Illustration of laminate GO membrane fabrication (a) assembly of GO-PVA thin layer via the PAS technique, (b) GO-PVA drying, (c) membrane crosslinking with GA, and (d) the final membrane (c-GO-PVA) [295]......	67
Figure 3-1: Schematic illustration of GO synthesis and the reaction conditions.....	71
Figure 3-2: Illustration of the functionalization reaction of GO with PDA.....	73
Figure 3-3: Illustration of the fabrication process of the pristine PSF, PSF/GO and PSF/rGO-PDA MMMs using the NIPS technique.	74
Figure 3-4: Illustration of the GO/rGO-PDA assembly using the PAS technique.	77
Figure 3-5: Process flow diagram of the cross-flow membrane unit.....	80
Figure 4-1: SEM images of the prepared GO samples.	85
Figure 4-2: TEM images of the prepared GO samples	86
Figure 4-3: XPS survey spectra of the prepared GO samples.	88
Figure 4-4: Deconvolution of C 1s and O 1s core-level XPS spectra of GO1-a.	89
Figure 4-5: FTIR spectra of prepared GO samples: (a) group 1 and (b) group 2.	92
Figure 4-6: FTIR spectra treatment and deconvolution for the quantitative analysis of GO1-a.....	93
Figure 4-7: ORB% obtained from FTIR quantification compared to O wt% obtained from CHNSO elemental analysis.....	94
Figure 4-8: Raman spectra of prepared GO samples: spectra have been stacked vertically for clarity.....	95
Figure 4-9: Illustration of Raman spectra deconvolution and peak fitting using GO1-a	

as an example.....	96
Figure 4-10: (a) I_D/I_G ratio of first-order Raman spectra and (b) positions of 2D and D+D' bands of second-order Raman spectra as functions of C (%).	97
Figure 4-11: TGA curves (solid lines) of GO samples and corresponding derivative curves (dotted lines).....	99
Figure 4-12: Plots of weight loss (%) in stages 2 and 3 of thermal decomposition obtained by TGA as a function of O (wt%).....	100
Figure 4-13: XRD patterns of GO and rGO-PDA nanoparticles.....	101
Figure 4-14: SEM images of GO and rGO-PDA nanoparticles.	102
Figure 4-15: TEM images of GO and rGO-PDA nanoparticles.	103
Figure 4-16: XPS survey spectra of GO and rGO-PDA nanoparticles.....	104
Figure 4-17: High-resolution and deconvolution of XPS spectra of (a) GO C 1s, (b) GO-PDA C 1s, (c) GO O 1s, (d) GO-PDA O 1s, and (e) GO-PDA N 1s core-levels.	106
Figure 4-18: FTIR spectra of the pristine GO and rGO-PDA nanoparticles.	108
Figure 4-19: (a) Raman spectra of GO and rGO-PDA nanoparticles and illustration of Raman spectra deconvolution and peaks fitting for (b) GO and (c) rGO-PDA.....	110
Figure 4-20: Photographs of GO and rGO-PDA dispersions in various solvents.	112
Figure 4-21: Optical micrographs of GO and rGO-PDA dispersions in DIW (0.02 mg/mL).	112
Figure 4-22: Contact angle measurements of the pristine PS-30, PS/GO, and PS/rGO-PDA membranes.	113
Figure 4-23: TGA curves (solid lines) of GO and rGO-PDA nanoparticles and the corresponding derivative curves (dotted lines).	115

Figure 4-24: FTIR-UATR spectra of M_0 , M_{GO4} , and M_{PDA4} membranes.....	116
Figure 4-25: Surface and cross-section SEM images of M_0 , M_{PDA1} , and M_{GO1} membranes.....	118
Figure 4-26: AFM images of the pristine PSF, PSF/GO and PSF/rGO-PDA composite membranes.....	120
Figure 4-27: Contact angle values of the pristine PSF, PSF/GO, and PSF/rGO-PDA composite membranes.....	121
Figure 4-28: The PWP (LMH/bar) of the pristine PSF, PSF/GO, and PSF/rGO-PDA composite membrane (1 bar, 23 °C, 1 h).....	124
Figure 4-29: The correlations of the PWP with (a) water contact angle (CA), (b) average roughness (Ra), and (d) the correlation of CA with Ra.....	126
Figure 4-30: Dyes rejection performance of M_0 , M_{GO3} , and M_{PDA3} (25 ppm dye concentration, 1 bar, 23 °C, 1 h).....	127
Figure 4-31: Photographs of the feed and permeate sample from the filtration experiments of (a) DR80 and (b) MB dyes.....	127
Figure 4-32: The flux recovery ratio (FRR%) of the tested membranes against (a) BSA and (b) HA.....	129
Figure 4-33: The fouling resistance parameters (cycle 1) of the tested membranes against (a) BSA and (b) HA.....	131
Figure 4-34: The correlations of the (a) BSA FRR_3 and (b) HA FRR_3 with the contact angle.....	132
Figure 4-35: Photographs of M_0 , M_{GO4} , and M_{PDA4} after the third cycle of HA fouling.....	133

Figure A1: Illustration of FTIR spectra treatment and deconvolution for the quantitative analysis.....	188
Figure A2: Illustration of Raman spectra deconvolution and peak fittings	189
Figure B1: determination of the average membranes thickness by the cross-section SEM images.....	194
Figure B2: FTIR-UATR spectra of the prepared membranes.	195
Figure B3: SEM images of pristine PSF and PSF/GO MMMs.	196
Figure B4: SEM images of pristine PSF and PSF/rGO-PDA MMMs	197
Figure B5: Viscosity measurements of the casting solutions of M ₀ , M _{GO3} and M _{PDA3}	198

NOMENCLATURE & ABBREVIATIONS

J_w	Pure water flux ($L.m^{-2}.h^{-1}$, LMH)
J_{w0}	Initial pure water flux (LMH)
J_{wf}	Foulant water flux (LMH)
J_{wl}	Pure water flux after cleaning
R_t	Total fouling ratio
R_r	Reversible fouling ratio
R_{ir}	irreversible fouling ratio
V	Permeate volume (L)
A	Effective membrane area (m^2)
t	Filtration time (h)
Q	Volumetric flowrate ($L h^{-1}$)
C_p	Solute concentration in the permeate
C_f	Solute concentration in the feed
R	Solute rejection (%)
ΔP	Trans-membrane pressure difference (bar)
ε	Membrane porosity (%)
w_w	The weight of the wet membrane sample (g)
w_d	The weight of the dry membrane sample (g)
l	Membrane thickness (cm)
L_a	Crystallite size (nm)
ρ_w	Water density ($0.998 g cm^{-3}$)
r_m	Mean pore size (nm)
η	Water viscosity ($9.3 \times 10^{-4} Pa s$)
C/O	Carbon/oxygen atomic ratio
CA	Contact angle ($^\circ$)
FRR _x	Flux recovery ratio for cycle x (%)
PWP	Pure water permeability ($L.m^{-2}.h^{-1}.bar^{-1}$, LMH/bar)
RSF	Reverse solute flux ($g.m^{-2}.h^{-1}$, GMH)
SRSF	Specific reverse solute flux ($g.m^{-2}.h^{-1}$, GMH)
ACS-GO	6-aminoethylamino-6-deoxychitosan/graphene oxide composite
AFM	Atomic force microscopy
AGMD	Air gap membrane distillation
AGO	Amine-functionalized graphene oxide
AL-DS	Active layer oriented towards draw solution
AL-FS	Active layer oriented towards feed solution
AO	Acridine Orange dye
AP	silver phosphate
APTS	3-aminopropyltriethoxysilane
AR	Acid Red dye
a-ZnO	amino-functionalized zinc oxide (ZnO)
BC	Blue Corazol dye
BHMTM	(2,2'-bis(1-hydroxyl-1-trifluoromethyl-2,2,2-trifluoroethyl)-4,4'-methylenedianiline,
BPPO	brominated poly(2,6-dimethyl-1,4-phenylene oxide)

BSA	Bovine serum albumin
CAC	Cellulose acetate
CA	Calcium alginate
CB	Chlorazol black dye
CFP	Chlorazol fast pink dye
CGO	Crumpled graphene oxide
CHS	Chitosan
CNTs	Carbon nanotubes
COD	Chemical oxygen demand.
CPX	ciprofloxacin
CR	Congo red dye
CSGO	cysteine functionalized graphene oxide
CTA	cellulose triacetate
DA	Dopamine
DCMD	Direct contact membrane distillation
DDA	Dodcylamine
DMA	Dimethylacetamide
DMF	N,N-dimethyl formamide
DOC	Dissolved organic carbon
DOMs	Dissolved organic matters
DR	Direct red dye
DR16	Direct red 16 dye
DR23	Direct red 23 dye
DR80	Direct red 80 dye
DS	Draw solution
EDA	ethylenediamine
EDC	1-ethyl-3-(3-dimethylaminopropyl) carbodiimide hydrochloride
EDTA	Ethylene diamine tetraacetic acid
ETS10	Engelhard Titanosilicate-10
EV	Ethyl violet dye
f-GO	Functionalized/modified graphene oxide, graphene oxide-based materials
FO	Forward osmosis
FS	Feed solution
FTIR-UATR	Fourier transform infrared spectroscopy-universal attenuated total reflectance sensor
GA	Glutaraldehyde
GAHMs	graphene oxide/alginate hydrogel membranes
GFG	Guanidyl-functionalized graphene oxide
GO	Graphene Oxide
GOA	Graphene oxide aerogel
GOCA	Graphene oxide embedded calcium alginate
GO-NBA	n-butylamine functionalized graphene oxide
GO-ND	graphene oxide-nanodiamond
GONRs	Graphene oxide nanoribbons
GO-ODA	Octadecylamine-functionalized graphene oxide

GOQD	Graphene oxide quantum dots
GO-SA-A	Graphene oxide/sodium alginate aerogel
GO-SA-H	Graphene oxide/sodium alginate hydrogel
GO-ST	Starch functionalized graphene oxide
GO-TETA	Triethylenetetramine-functionalized graphene oxide
Gr	Graphite
G-PANCMi	Graphene-poly(acrylonitrile-co-maleimide)
HA	Humic acid
hGO	Holey graphene oxide
hPAN	hydrolyzed Polyacrylonitrile
HPEI	hyperbranched polyethylenimine
IP	Interfacial polymerization
i-TFC	Thin film composite membrane having interlayer of nanomaterial
KCuHCF	potassium copper hexacyanoferrate
LB3R	Lanasol blue 3R dye
LBL	Layer by layer self-assembly
LGO-OFs	blue lemon@quaternary graphene oxide open frameworks
LIG	Laser-induced graphene
MB	Methylene blue dye
MBA	N,N'-methylenebisacrylamide
MCE	Mixed cellulose ester
MD	Membrane distillation
MF	Microfiltration
MG	Malachite green dye
MMGO	metformin/GO/Fe ₃ O ₄ hybrid composite
MMMs	Mixed matrix membranes
MO	Methyl orange dye
MOFs	Metal organic frame works
MPD	m-Phenylenediamine
m-TFC	Thin film composite membrane having nanomaterial in the substrate matrix
MWCNTs	Multiwall carbon nanotubes
MWCO	Molecular weight cut-off
MXDA	m-xylylenediamine
NF	Nanofiltration
N-GOQD	Nitrogen-doped graphene oxide quantum dots
NHS	N-hydroxysuccinimide
NIPAM	N-isopropylacrylamide
NMP	1-methyl-2-pyrrolidone
NOMs	Natural organic matters
OCCM	O-(Carboxymethyl)-Chitosan
OCNTs	oxidized carbon nanotubes
OMWCNTs	Oxidized multiwall carbon nanotubes
ORII	Orange II sodium salt
PA	Polyamide
PAA	Polyallylamine

PAAc	poly(acrylic acid)
PAMAM	polyamidoamine
PAN	Polyacrylonitrile
PANI	polyaniline
PAS	Pressure-assisted self-assembly
PBI	Polybenzimidazole
PCA	Polycarbonate
PDA	polydopamine
PDDA	Poly dimethyl diallyl ammonium chloride
PDMDAAC	dimethyl diallyl ammonium chloride
PE	Polyethylene
PEI	Polyethylenimine
PES	Polyethersulfone
PES-g-NH ₂	Aminated PES substrate
PFSA-g-GO	perfluorosulfonic acid (PFSA) functionalized graphene oxide
p-GO	Pristine graphene oxide
PGS	Palygorskite nanorods
PI	polyimide
PIP	Piperazine
PMGO	PDMDAAC- modified magnetic graphene oxide
PMIA	Poly(m-phenylene isophthalamide)
POSS-GO	glycidyl polyhedral oligosilsesquioxane-functionalized graphene oxide
PP	polypropylene
PrGO	partially reduced graphene oxide
PRL	Primary rejection layer membrane
PSBMA	poly(sulfobetaine methacrylate)
PSF	Polysulfone
PV	Pervaporation
PVA	Polyvinyl Alcohol
PVC	Polyvinyl chloride
PVD	Pervaporation desalination
PVDF	Polyvinylidene fluoride
PVP	Polyvinylpyrrodione
QGO	Quaternized graphene oxide
RB5	Reactive black 5 dye
rGO-PDA	Polydopamine-functionalized graphene oxide
RO	Reverse osmosis
RR49	Reactive red 49 dye
RY	Reactive Yellow
SA	Sodium Alginate
SEM	Scanning electron microscope
Sep-GO	sepiolite/graphene oxide
SGMD	Sweep gas membrane distillation
SGO	Sulfonated graphene oxide
SO	Safranin O

SPSF	Sulfonated polysulfone
SSA	Specific surface area
ST	Starch
s-TFC	Surface coated thin film composite membrane
SY	Sunset yellow dye
TA	Tannic acid
TFC	Thin film composite
TFN	Thin film nanocomposite
TMC	Trimesoyl chloride
TMS	Tetramethylenesulfone
Tris	tris-(hydroxymethyl)aminomethane
TSC	Trisodium citrate
TY	Titan yellow dye
VAS	Vacuum-assisted self-assembly
VMD	Vacuum membrane distillation
XPS	X-ray photoelectron spectrometer
XRD	X-ray diffraction analysis
ZIF-8-GO	zeolitic imidazole framework-8 decorated with graphene oxide

CHAPTER 1: INTRODUCTION

The limitation of water resources with the huge increase in population generate a critical problem to water security globally [1]; and suitable solutions must be developed to align consumption and supply over time while protecting water quality. Several technologies have been developed over the years to provide alternative water supplies by wastewater treatment, recycle and seawater desalination [2, 3]. These technologies include distillation, membrane filtration, ion exchange, and aqueous adsorption [4, 5]. Selection and use of these technologies throughout the world depend on the power requirements, availability of resources, contamination level, and economic factors [6]. Therefore, cost and power efficient technologies need to be developed for desalination and wastewater treatment. Among the various methods developed for water treatment, membrane filtration have gained wide acceptance due to their low cost, high efficiency, and ease of operation [7, 8].

Membrane separation is a well-developed technology and is considered one of the most economical and efficient methods that can afford clean water [9, 10]. The membrane water treatment can be described by the separation of two phases through a semi-permeable barrier which allows passing of certain molecules (e.g. water) while rejecting others (e.g. bacteria, proteins, ions, etc.). Figure 1-1 classifies the major membrane processes and describes the basic concepts and properties of each process.

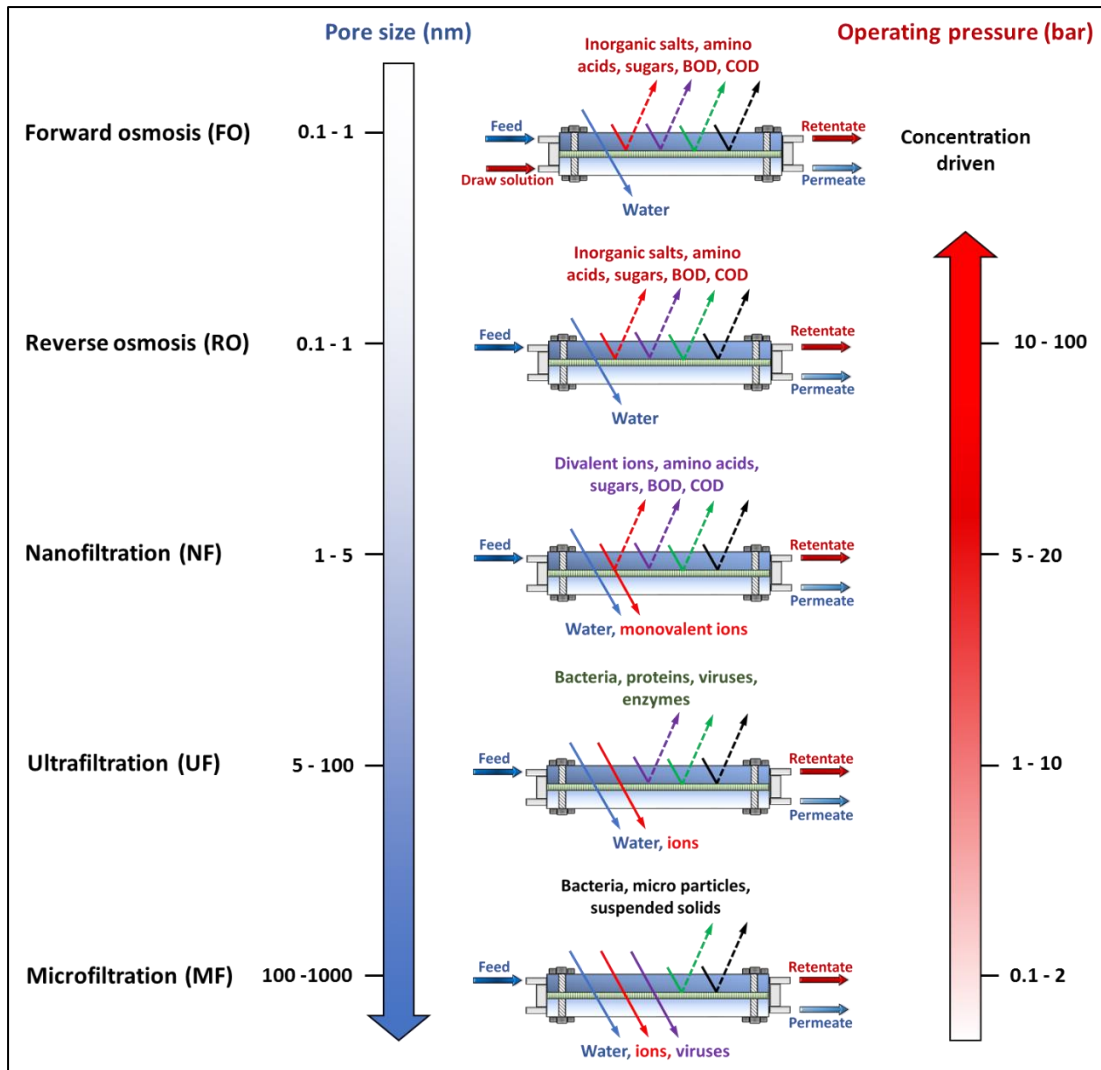


Figure 1-1: The basic concepts and classifications of membrane processes.

Developing and investigating new membrane materials gained huge interest in both academia and industry to explore new materials that can enhance the membrane performance and/ or increase the membrane resistance against various foulants. [11, 12]. Therefore, developing antifouling membranes for desalination and water treatment purposes has become an important research objective [13-17]. Different methods, materials and modifications have been investigated over the years to produce antifouling membranes with enhanced flux and rejection properties. The use

of nanotechnology is one of the well investigated methods being developed in membrane sector [18]. The addition of nanomaterial (nanofiller) to conventional membranes was reported to enhances their performance with respect to flux, rejection and fouling resistance [19]. Several nanomaterials have been used as membrane fillers and showed excellent performance such as graphene based materials, metal organic frame works (MOFs), zeolites, carbon nanotubes (CNTs), nano-silica (SiO_2), titanium dioxides (TiO_2), etc. [20].

One of the lately explored nanomaterials in membrane technology is graphene oxide (GO) and GO-based materials due to their unique properties [21]. Among the various membrane nanofillers, GO and its derivatives proved their efficiency as nanofillers that can enhance the membranes performance with respect to water flux and rejection as well as their fouling resistance [19, 22]. Due to their easy accessibility, chemical stability and tunable properties, several GO-based materials were developed over the years for different purposes and applications including membranes [23, 24], adsorption [25, 26], catalysis [27, 28], supercapacitors and sensing applications [29, 30]. Such unique properties resulted in significant research interest in the last years to develop different membranes incorporating pristine GO (p-GO) and GO-based (f-GO) nanoparticles. Figure 1-2 depicts the increasing number of publications related to GO-based membranes over the period of 2012 to 2020 that are indexed within Scopus. Over this period, nanofiltration (NF) gained the highest research interest (39%), in terms of publications, among other GO-based membranes followed by ultrafiltration (UF) (24%), forward osmosis (FO) (15%), reverse osmosis (RO) (10%), membrane distillation (MD) (5%), microfiltration (MF) (4%) and pervaporation desalination (PVD, 3%). Prior to 2012, no obvious research input on GO embedding in membranes for water treatment was reported. GO was mainly used

with UF and NF membranes in the beginning, while after 2015, other GO-based membranes started to evolve. The total number of publications in 2020 has been doubled to year 2016 suggesting an increasing interest in GO-based membranes especially for NF, UF, FO and MD applications.

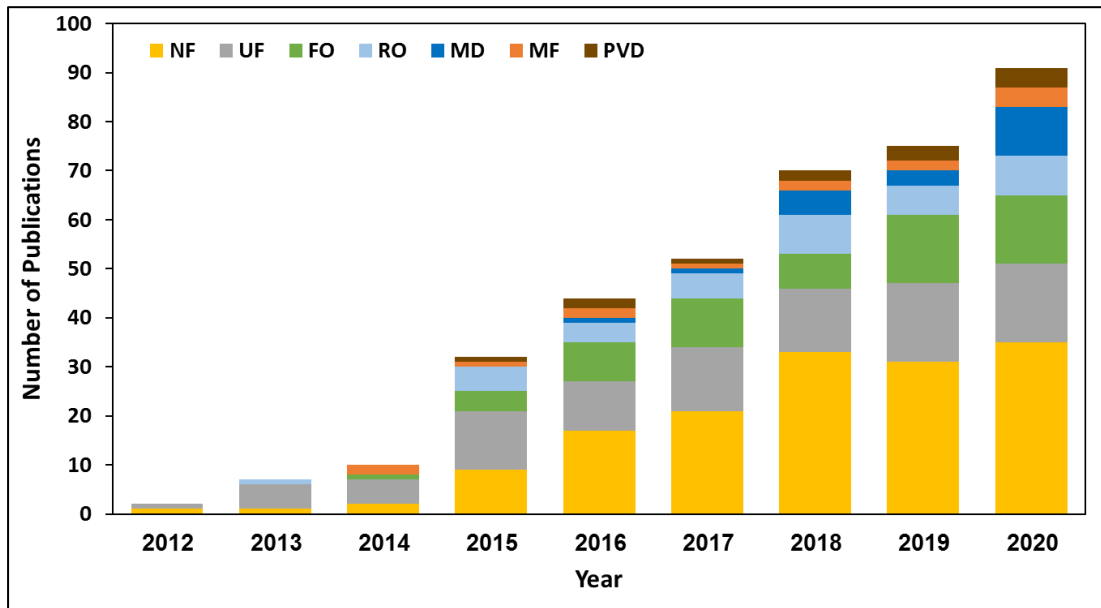


Figure 1-2: Number of publications related to GO-based membranes in recent years. Data were obtained from Scopus by searching for articles having "graphene oxide" and "the name of membrane process" in the author's keywords or in the title. For example, the query strings of nanofiltration was the following: AUTHKEY ("graphene oxide" AND nanofiltration) OR TITLE ("graphene oxide" AND nanofiltration) AND DOCTYPE (ar). Data were obtained on October 5, 2020.

1.1. Scope and Objectives

This dissertation aims to develop novel nano-functionalized mixed matrix membranes (MMMs) to be applied to the wastewater treatment sector. Graphene oxide-functionalized membranes have been chosen as the overall research theme for several reasons. Over the past few years, there has been a significant increase in research relating to GO and GO-based nanomaterials as promising and efficient

nanofillers that can improve the membranes performance and fouling resistance against various foulants [19]. The ease of tuning GO properties and its capability to be modified and functionalized with various functional groups paved the way to develop various membranes and for different applications.

A successful functionalization of GO nanoparticles can significantly enhance the membrane properties. One of the efficient functionalization methods being done in this aspect is the amine functionalization of GO nanoparticles. The amination of GO was investigated in several studies using different amines and was found to enhance the GO properties such as the hydrophilicity, dispersibility, conductivity, antibacterial properties, surface area, adsorption capacity, mechanical and thermal stability, and the antifouling properties of the materials in contact with water like membranes [31]. Amine-functionalized GO (AGO) nanoparticles were considered as promising nanofillers in various membrane processes. Some examples of the AGO nanofillers include GO-p-aminophenol for RO [32], m-xylylenediamine-f-GO (GO-MXDA) for FO [33], octadecylamine-f-GO (GO-ODA) and triethanolamine-f-GO (GO-TEOA) for NF [34, 35], 3-aminopropyltriethoxysilane-f-GO (GO-APTS) for UF [36], and N-butylamine-f-GO (GO-ButA) for MD [37].

Owing to its unique properties over other amines and the abundant functional groups on its surface, polydopamine (PDA) has been widely utilized for the functionalization of several nanomaterials. The amination of GO nanoparticles using PDA was reported in some studies for different purposes including anticorrosion coatings [38], electrocatalysis applications [39], and sensing applications [40]. However, no clear input has been done on the utilization of polydopamine-functionalized graphene oxide (GO-PDA) nanoparticles in membranes as revealed by the literature review conducted in Chapter 2. Additionally, to the author's knowledge

the use of GO-PDA nanoparticles as nanofiller in ultrafiltration (UF) mixed matrix membranes (MMMs) has not been investigated in literature yet.

Therefore, by identifying the the gap of knowledge and the challenges in this area, the main research objectives of this dissertation were defined as follow:

1. Synthesis of graphene oxide (GO) nanoparticles with high oxidation degree based on different improvements on the conventional Hummers' method.
2. Characterization of the obtained GO nanoparticles using different analytical techniques to explore the effect of the improved reaction conditions on the oxidation degree as well as the structural and morphological properties of GO.
3. Functionalization of GO nanoparticles of highest oxidation degree with polydopamine to produce GO-PDA.
4. Characterization of the pristine GO and GO-PDA nanoparticles using different analytical techniques to investigate the effect of PDA functionalization on the structural, spectral, hydrophilic, and dispersion properties of GO particles.
5. Fabrication of two sets of polysulfone (PSF) UF MMMs incorporating pristine GO and GO-PDA nanoparticles via the non-solvent induced phase separation (NIPS) technique.
6. Characterization of the pristine PSF, PSF/GO and PSF/GO-PDA MMMs to investigate the effect of GO and GO-PDA embedding on the PSF properties.
7. Testing the performance of the prepared membranes with respect to their permeability and separation properties to investigate and compare the effect of both nanomaterials on the PSF performance.
8. Testing the antifouling properties of the prepared membranes against protein and organic foulants to investigate and compare the effect of both nanomaterials on the PSF fouling resistance.

CHAPTER 2: BACKGROUND

This chapter reviews and highlights the recent studies on the utilization of pristine GO (p-GO) and other GO-based (f-GO) nanoparticles in water treatment, purification and desalination using pressure, concentration and thermal-driven membrane processes. General overview about GO nanoparticles, synthesis methods, and functional GO nanoparticles is provided and discussed in Section 2.1. Section 2.2 provides an overview about the polydopamine (PDA) and its applications in the membrane processes. Section 2.3 summarizes and describes the fabrication methods of GO-based membranes. Section 2.4 discusses the antifouling properties of GO-based membranes. Finally, Section 2.5 summarizes and discusses the advancements of the utilization of p-GO and f-GO nanoparticles in enhancing membranes performance for different applications.

2.1 Graphene Oxide (GO)

Graphene is a 2D material which can be produced from natural graphite (Gr). It is made of sp^2 hybridized carbon atoms organized in a honeycomb structure [41, 42]. Graphene-based materials have been widely investigated in the past years for various applications due to their attractive properties. These applications include membrane separation processes [43-45], heavy metals adsorption [26, 46], dyes adsorption [47], microwave absorption [48, 49], photocatalysis [28, 50] and sensing applications [51, 52]. Graphene possesses high tensile strength which is estimated to be 300 times stronger than A36 structural steel and 40 times stronger than diamond [42].

One of the widely explored graphene-based materials is GO that can be

produced by the oxidation of graphite. GO exhibits attractive chemical, electrical, and optical properties caused by the graphene skeleton and its oxygen content. The oxygenated functional groups located on the edges of GO sheets causes its hydrophilic properties and make the surface modifications easier to produce other graphene-based materials [53, 54].

2.1.1 GO synthesis

GO can be synthesized using several approaches. Brodie's method developed in 1859 was the first one using HNO_3 and KClO_3 as the oxidant and intercalant [55]. However, several drawbacks associated with this approach have been reported. The reaction needs about 4 days with 4 oxidation cycles, washing, and drying to complete. Additionally, the highly explosive ClO_2 gas is produced during the reaction caused by mixing of acids with chlorate [56]. The most commonly used approach for GO production nowadays is Hummers method that was reported in 1958 [57]. Sulfuric acid (H_2SO_4), sodium nitrate (NaNO_3) and potassium permanganate (KMnO_4) are used for graphite oxidation (Figure 2-1). Hummers method eliminated the flaws of Brodie's method where the use of KMnO_4 as oxidant completes the reaction within shorter time. Also, it eliminates the risk of ClO_2 gas formation as chlorate is not being used in the GO synthesis. However, there are few flaws associated with Hummers method as well including the formation of Gr-GO mixture due to the incomplete oxidation of graphite, and the formation of toxic gases (e.g. NO_2 and N_2O_2) due to the use of NaNO_3 [58]. Several improvements have been developed on the conventional Hummers method to enhance the GO properties, improve the yield, and/ or to reduce the flaws of the conventional method. Most of these studies excluded the use of NaNO_3 to avoid the formation and release of the toxic gases (e.g. NO_x) [59].

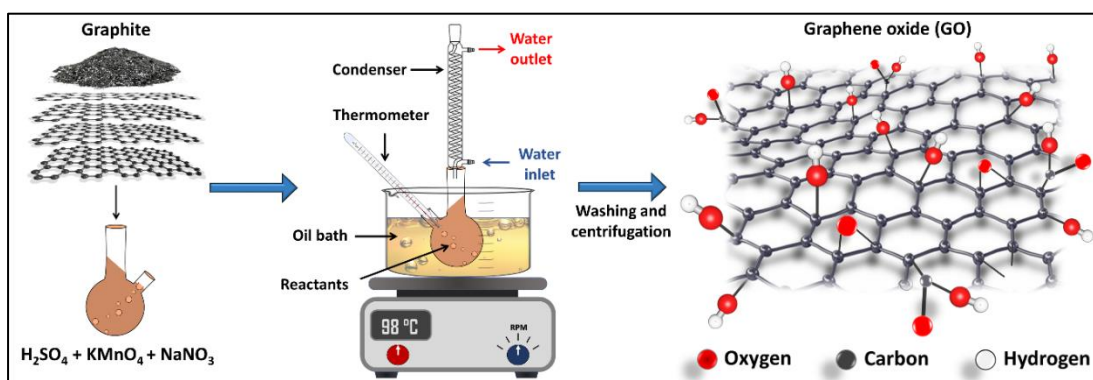


Figure 2-1: Illustration of GO synthesis via the Hummers method.

The variation of oxidation conditions and reactant ratios results in GO particles with different physico-chemical properties making them applicable for wide range of applications [60]. The tuning of these properties of GO particles is much easier than other nanomaterials [61]. It is well established that the oxygen-containing groups on GO edges have significant effect on membrane's permeability [62, 63]. However, there is no intensive investigations on the effect on GO preparation methods on membrane performance. In a recent study, Zambare et al. [64] investigated the effect of oxidation degree on the performance and microstructure of polysulfone-GO composite membranes (PSF/GO) prepared by the non-solvent induced phase separation (NIPS) technique. The oxidation degree was controlled by varying the loadings of oxidant ($KMnO_4$). It was reported that GO particles of high oxidation degree have more negative zeta potential and high dispersibility in the solvent leading to a uniform distribution of the particles within the polymer matrix [41]. Consequently, the rate of phase separation was enhanced and resulted in well-defined finger-like pore structure and interconnected transport channels that accelerate the permeation of water across the membrane matrix. In contrast, GO

nanoparticles of lower oxidation degree were found to have high tendency to aggregate resulting in poor dispersion within the polymer matrix [64]. The effect of physico-chemical structure of GO particles on the membrane performance was also investigated by varying the reaction temperature to produce GO particles with different properties [65]. The results showed high temperature dependence of GO flake size and oxygen content. The produced GO particles were assembled onto a mixed cellulose ester (MCE) via the vacuum assisted self-assembly technique (VAS). It was found that the GO flake size has higher impact on the membrane permeability compared to its oxygen content; where the highest permeability was obtained with GO of smallest flakes size although it has the lowest oxygen content. Table 2-1 summarizes the reactants ratios and oxidation conditions of some modified Hummers methods in literature and the corresponding oxygen/carbon (O/C) ratios of GO particles.

Table 2-1: Experimental conditions of GO preparation reported in the literature.

Reactants	T (°C)	t (h)	O/C	Ref.
Gr (100 g); KMnO ₄ (100 g); NaNO ₃ (50 g); H ₂ SO ₄ (2.3 L)	98	0.75	0.44	[57]
Gr (1 g); KMnO ₄ (3 g); H ₂ SO ₄ (20 mL); HNO ₃ (15 ml)	25	24	0.69	[66]
Gr (1 g); KMnO ₄ (3 g); NaNO ₃ (3 g); H ₂ SO ₄ (30 mL)	25	2	0.74	
Gr (3 g); KMnO ₄ (9 g); NaNO ₃ (1.5 g); H ₂ SO ₄ (98 mL)	98	1	0.59	[67]
Gr (1 g); KMnO ₄ (3 g); H ₂ SO ₄ (23 mL)	95	0.75	0.50	[56]
Gr (7.5 g); KMnO ₄ (45g); NaNO ₃ (7.5g); H ₂ SO ₄ (360 mL)	35	3	0.56	[68]
Gr (1 g); KMnO ₄ (3 g); NaNO ₃ (0.75 g); H ₂ SO ₄ (23 mL)	98	3	0.20	[41]
Gr (1 g); KMnO ₄ (6 g); H ₂ SO ₄ (46 mL)	95	6.5	0.37	[69]
Gr (1 g); KMnO ₄ (6 g); NaNO ₃ (2 g); H ₂ SO ₄ (46 mL)	95	6.5	0.33	
Gr (1 g); KMnO ₄ (6 g); H ₂ SO ₄ (70 mL); H ₃ PO ₄ (20 ml); HNO ₃ (10 ml)	85	3	0.7	[70]
Gr (1 g); KMnO ₄ (6 g); H ₂ SO ₄ (120 mL); H ₃ PO ₄ (15 ml)	50	12	0.7	[60]
Gr (1 g); KMnO ₄ (7 g); NaNO ₃ (0.5 g); H ₂ SO ₄ (23 mL)	90	2.5	0.53	[64]

2.1.2 Reduced GO (rGO) and Functional GO Structures (f-GO)

The incorporation of p-GO nanoparticles was reported to improve the performance of different membrane materials and with different applications including RO [71, 72], NF [73, 74], UF [75, 76], MF [77, 78], FO, MD [79] and PVD [80, 81]. Nevertheless, in many studies, the embedding of p-GO particles resulted in a limited membrane performance in terms of antifouling [64, 82, 83], flux [84-87], or rejection [88, 89]. The limited performance of p-GO-based membranes is usually linked to the aggregation of GO particles owing to their poor dispersibility in some solvents [90]. Additionally, p-GO-coated membranes are unstable in water due to the possibility of GO layer detachment from the membrane surface [91]. Therefore, the performance of p-GO membranes is usually inconsistent and varies significantly in literature which is attributed to the fact that GO properties are very sensitive to the oxidation conditions. Hence, a successful reduction of GO nanoparticles (rGO), functionalization (f-GO), or combination with other materials can improve their stability and dispersion properties allowing them to attain their highest potential for improving the overall membrane performance [92]. Several ways of GO reduction have been reported in literature including hydrothermal reduction [91, 93], photoreduction [94, 95], electrochemical reduction [96], and chemical reduction [97, 98]. Fan et al. [91] investigated the GO reduction degree on the performance of rGO-coated Polyvinylidene fluoride (PVDF) membranes. GO nanoparticles were hydrothermally reduced at different times and then coated on PVDF membranes via the VAS technique. The authors reported a high increase in the water flux of rGO-PVDF membranes compared to GO-PVDF accompanied with excellent dyes rejection (> 98%). However, when the reduction time exceeds 9 h, the dyes rejection significantly decreased. Additionally, rGO-PVDF membranes exhibited higher

stability in water while GO-PVDF membranes were unstable due to the detachment of GO layer from the surface in short time as illustrated in Figure 2-2.

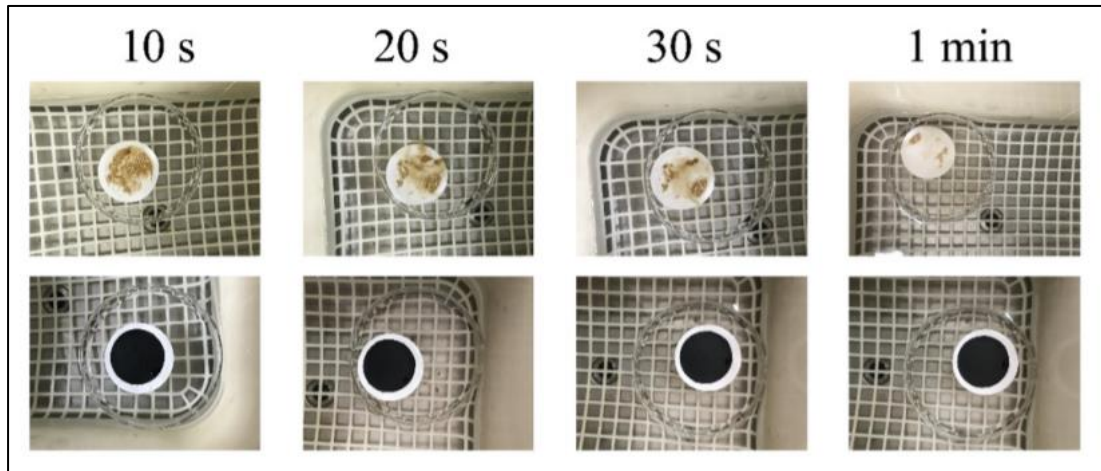


Figure 2-2: Stability measurements of GO-PVDF (top) and rGO-PVDF (below) membranes in water [91]

The chemical reduction of GO is the most used method in the membranes sector due to the ease of process and the wide variety of reducing agents. Commonly, hydrazine hydrate ($\text{N}_2\text{H}_2\cdot\text{H}_2\text{O}$) is used as a GO reductant which was firstly proposed by Stankovich et al. [97]. In this context, the functionalization of GO with various functional groups can be also considered a reduction method in the same time. These functional groups can act as reducing agents as well as capping agent to stabilize GO nanoparticles and to decorate them [99]. Some functional GO materials were reported to improve the membrane flux, rejection and antifouling properties. For example, PSF UF membranes incorporating guanidyl-f-GO particles (GFG) showed around 60% flux enhancement, compared to membranes incorporating p-GO particles, with 95.2% rejection of Bovine serum albumin (BSA) [100]. The authors related this improvement to the higher hydrophilicity of GFG nanoparticles compared to p-GO

particles, which enhanced the membrane's pore structure. Kim et al. [101] functionalized the GO particles using the self-polymerization of tannic acid (TA) and then embedded them into a polyamide (PA) RO membranes using the interfacial polymerization technique (IP). The f-GO particles (GO-TA) showed improved hydrophilicity and better compatibility with the polymer matrix leading to a significant enhancement in the membrane performance in terms of permeability, antibacterial properties and chlorine resistance compared to membranes incorporating p-GO particles. In a similar study, GO-TA nanoparticles were incorporated and showed promising performance with NF membranes [102]. Amber and co-workers [103] reported that the starch (ST) functionalization of GO particles could significantly enhance the hydrophilicity and the compatibility of GO particles with the PA thin layer of NF membranes. The results showed enhanced flux and stability of membranes embedding GO-ST particles compared to those embedding p-GO particles without affecting the salt rejection.

Some functional GO materials result in a trade-off between the rejection, flux and the fouling resistance, when embedded into membranes. For instance, 3-aminopropyltriethoxysilane f-GO particles (GO-APTS) showed significant enhancement to the flux and fouling resistance of PVDF UF membranes, while the rejection of BSA was about 57%, which is considered lower than this of other UF membranes [104]. Similar observation were reported with some UF membranes embedding GO-TiO₂ [105] and GO-GA [106]; NF membranes embedding POSS-GO [44], GO-TETA [107], and GO-PSBMA [108]. Therefore, exploring new ways of GO functionalization to produce f-GO particles with enhanced properties will pave the way for the development of new membranes with high performance and for different applications. Figure 2-3 depicts some f-GO structures used as membrane nanofillers.

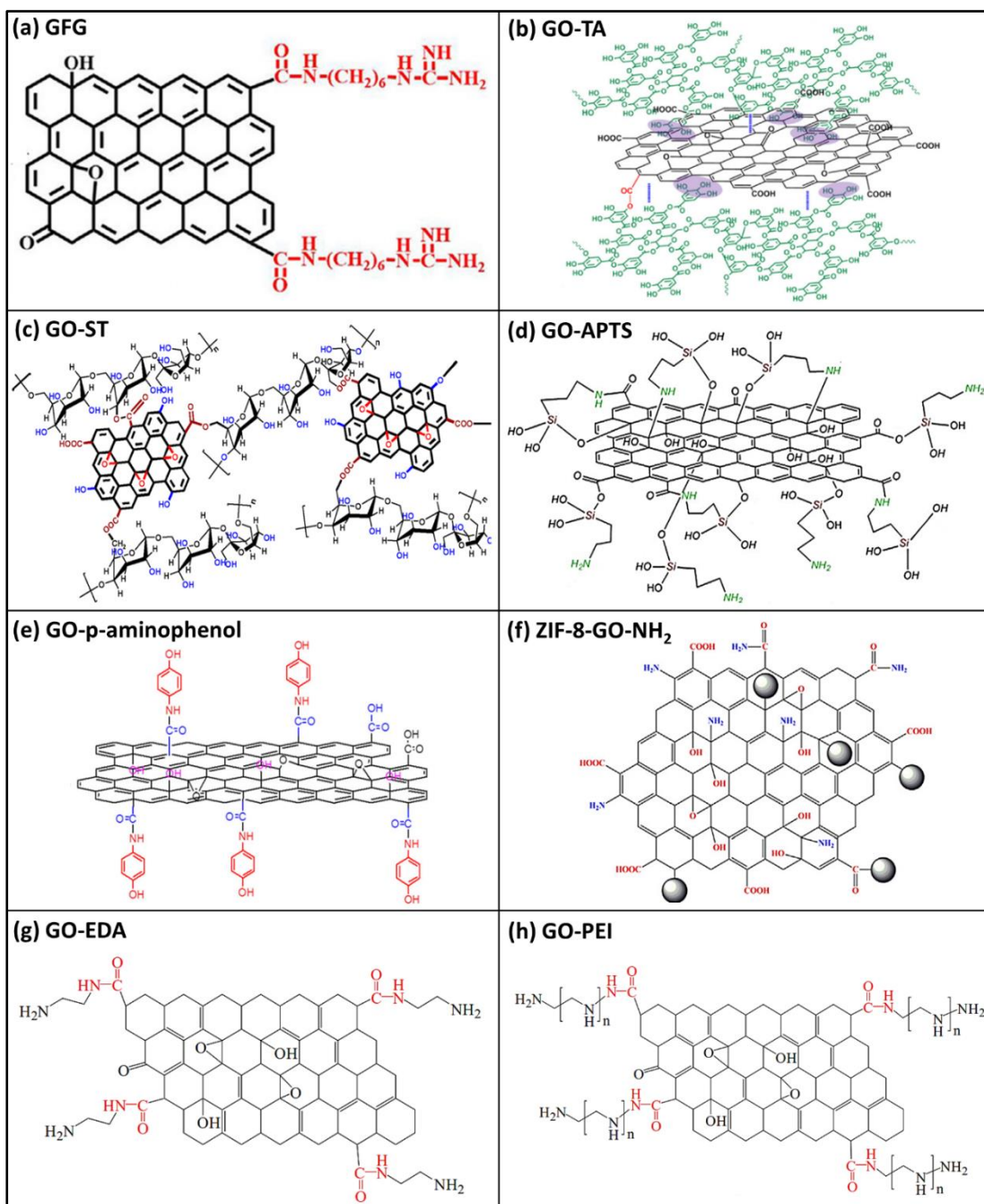


Figure 2-3: Illustrations of the chemical structure of: (a) guanidyl-f-GO (GFG) [100], (b) Tannic acid-f-GO (GO-TA) [101], (c) Starch-f-GO (GO-ST) [103], (d) 3-aminopropyltriethoxysilane f-GO (GO-APTS) [109], (e) *p*-aminophenol-f-GO [32], (f) amine-functionalized ZIF-8-GO nanocomposite [110], (g) Ethylenediamine-f-GO (GO-EDA) and (h) Polyethylenimine-f-GO (GO-PEI) [111].

2.2 Polydopamine (PDA)

In 2007, dopamine (DA), a unique mussel-inspired biomolecule, was found to undergo self-polymerization in aerobic and mild alkaline media producing thin film (polydopamine) that can be easily adhered on different materials [112]. Since then, mussel-inspired chemistry attracted good attention as an evolving technique for surface modification and functionalization of different materials [113]. Because of the abundant functional groups like amine, catechol, and imine [40] on its surface, polydopamine (PDA) is considered a versatile platform for additional modification with the various functional groups [114]. Although the exact adhesion mechanism of PDA is still unclear, it has been extensively utilized for different coating applications like membranes [115, 116], anticorrosion coatings [117] sensors and semiconductors [118, 119].

The deposition of PDA is controllable and simple and provided insights on the membrane surface functionalization. PDA can be either co-deposited with other functional materials on the membrane's surface [23, 115], used as an interlayer for post functionalization [114, 120, 121], or used as the main active layer via the self-polymerization of dopamine of the membrane surface [122]. Figure 2-4 illustrates the common methods used for membranes functionalization with PDA. Wang et al. [115] fabricated a high flux NF membranes via the co-deposition of PDA and poly(vinyl alcohol) (PVA) on a PSF substrate followed by crosslinking with trimesoyl chloride (TMC). The prepared membranes were found to have higher flux with almost similar rejection of sodium sulfate (Na_2SO_4) when compared to the conventional thin-film composite (TFC) NF membranes. The modified membranes were also found to have high antifouling properties against protein fouling as well as long-term stability. Wai et al. [121] immobilized Ag nanoparticles on a PDA-coated polyethersulfone (PES)

substrate where the PDA interlayer acted as a reductant and polymer linker that facilitated the Ag coating on the substrate. The PES/PDA/Ag composite membrane achieved higher rejection of humic acid (HA) than the pristine PES with excellent antibacterial activity against *E. coli*. In a recent study, Teng et al. [122] prepared a PDA-coated TFC membranes via the self-polymerization of dopamine on the PA layer surface. The PDA-coated membranes were found to have higher stability and selectivity than the pristine TFC membranes due to their higher hydrophilicity than the pristine TFC membranes.

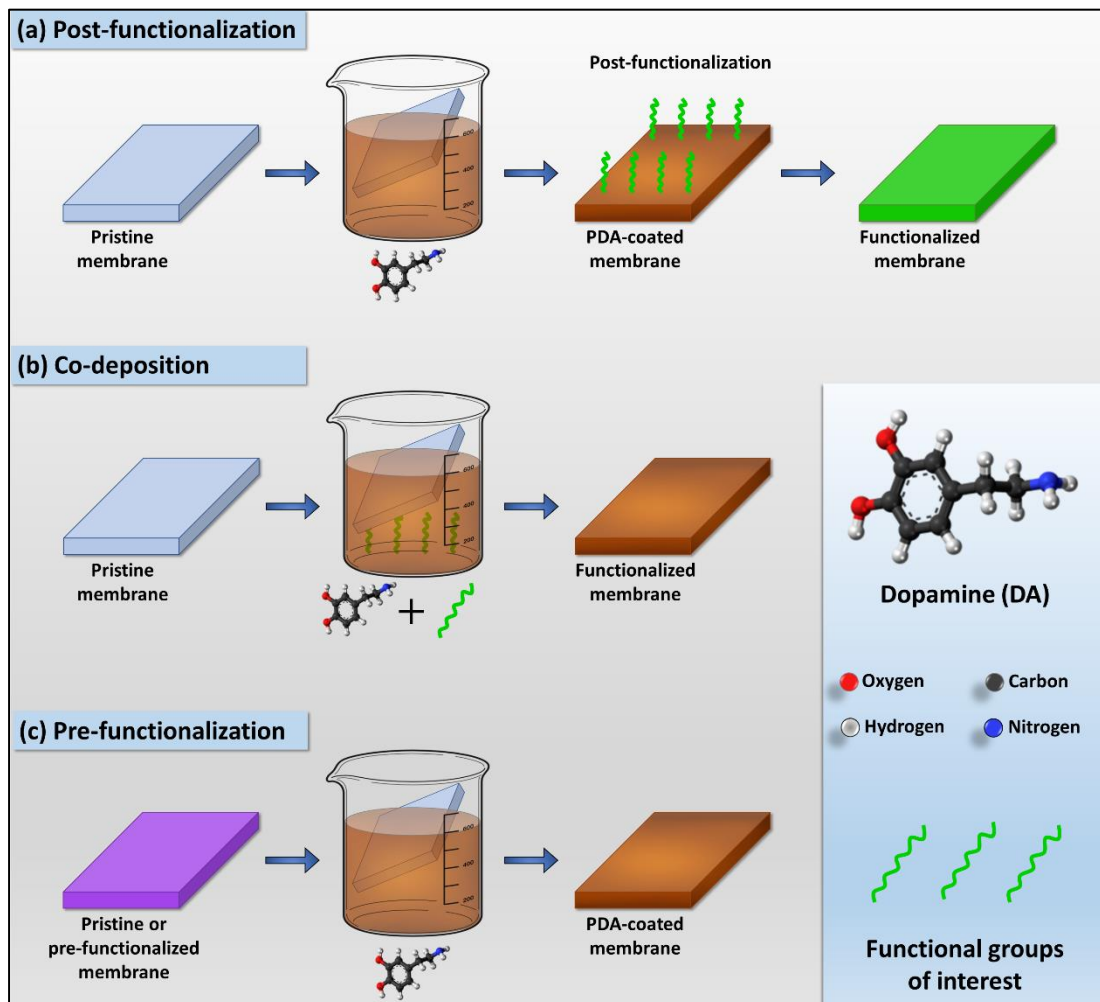


Figure 2-4: Methods used for membranes functionalization with PDA.

Because of its versatility and unique properties, bio-inspired functionalization based on PDA has been widely utilized for the functionalization of several nanomaterials like multi-walled carbon nanotubes (MWCNTs) [123], silver nanoparticles [124], hydroxyapatite nanotubes (HANTs) [125], zeolites [126], SiO₂ and TiO₂ nanoparticles [127, 128]. It has been reported that the functionalization of nanoparticles with PDA improves their hydrophilic, dispersion, antibacterial and adhesion properties which increase their potential use for several purposes [129]. The amination of GO nanoparticles using PDA was previously reported in some studies for anticorrosion coatings purposes [38], electrocatalysis applications [39], and sensing applications [40].

GO and PDA have been simultaneously used in the synthesis and functionalization of different membranes in several studies [23, 130]. However, all these studies used the methods illustrated in Figure 2-4 where the PDA layer was either co-deposited with GO nanoparticles or deposited before or after the GO nanoparticles on the membrane surface. Additionally, all these membranes were fabricated by the physical assembly approaches leading to poor mechanical stability of the membrane because of the weak interface between the adjacent layers [19]. Although the stability of the assembled GO membranes can be improved using various cross-linkers [1], these crosslinkers usually lead to a reduction in the membrane flux [121]. As an example of the post-functionalization method illustrated in Figure 2-4a, Liu et al. [131] deposited a PDA interlayer onto a mixed cellulose ester membrane (MCE) to act as a covalent linker followed by the assembly of GO layer via the vacuum-assisted self-assembly technique (VAS). The PDA/GO-coated membranes showed higher oil separation efficiency than membranes coated with PDA layer. However, a decline in the flux was observed with the GO coating layers.

Benefiting from the self-polymerization and high adhesive properties of PDA, the co-deposition of PDA and GO illustrated in Figure 2-4b was also reported in several studies to fabricate different PDA/GO-based membranes. Choi et al. [132] co-deposited a GO-PDA interlayer on PSF substrate followed by the formation of the PA layer using the interfacial polymerization technique to produce TFC-FO membranes. The authors reported a significant reduction in the flux with long-time coating due to the pores blockage by GO and PDA. Using the same technique, Liu and coworkers [133] deposited a GO and Uio-66 nanoparticles with PDA on the surface of cellulose acetate (CAc) substrate by the VAS technique. The authors reported a poor performance of membranes coated with PDA/GO layer, while the separation efficiency was significantly enhanced with membranes coated with PDA/GO/Uio-66. The PDA layer can be also coated on a pre-functionalized membrane to act as the main active layer and to provide stability of the GO layer as illustrated in Figure 2-4c. Peng et al. [130] assembled rGO@SiO₂ nanohybrid on a PVDF substrate followed by PDA coating via the self-polymerization of dopamine. The PDA coating provided active sites to the membrane surface and enhanced its hydrophilicity which resulted in good flux accompanied with high rejection of oil and dyes. In a similar study by Yang et al. [134], GO nanoparticles were vacuum-assembled on a MCE substrate, reduced with hydriodic acid vapor (HI) and then coated with PDA by dipping into dopamine solution. It has been found that the rGO layer with PDA-coated membrane have higher stability than the uncoated membranes and could achieve higher flux and lower reverse solute flux (RSF) with FO measurements.

2.3 Fabrication Methods of GO-based Membranes

Several techniques have been evolved for the synthesis of GO-based membranes to produce different types of membranes with different characteristics. The selection of the fabrication method and the type of GO-based membranes is mainly governed by the application. These methods include non-solvent induced phase separation (NIPS), vacuum/evaporation/pressure-assisted self-assembly methods (VAS, EAS, and PAS), layer-by-layer assembly (LBL), interfacial polymerization (IP), blending, and coating [63]. The subsections below provide a summary on the fabrication methods and types of the recently investigated GO-based membranes.

2.3.1 Non-solvent induced phase separation (NIPS)

Non-solvent induced phase separation (NIPS) is one of the most used techniques in the preparation of polymeric membranes [135]. Three components are involved in the NIPS technique (polymer, solvent and non-solvent) where the membrane is formed through the exchange of the solvent from the polymer solution through the non-solvent from a coagulant bath [136]. A wide range of polymer materials were utilized for membrane fabrication via NIPS method like PSF, PES, PVDF, and CAC. In addition to the fabrication of pristine polymer substrates, NIPS can be used to fabricate GO-based mixed matrix membranes (GO-MMMs) by incorporating the GO-based material into the polymer matrix. This can improve the pore structure and enhance the flux, rejection and antifouling properties of the membrane [137, 138]. The fabrication of MMMs membranes using NIPS technique goes through the following stages [139, 140]:

1. Preparation of the casting solution: The casting solution is usually prepared by direct mixing of polymer and the functional materials in appropriate solvent

until a clear and homogenous solution is obtained [141]. GO is usually sonicated for some time to ensure well-dispersion through the solvent. Common solvents used for GO-based MMMs fabrication are N,N-dimethyl formamide (DMF), Dimethylacetamide (DMA), N-Methyl-2-pyrrolidone (NMP). In addition to the GO, other additives like polyvinylpyrrolidone (PVP) and polyethylene glycol (PEG) are usually added to the polymer solution to act as pore forming agents [142].

2. Casting the solution, usually on a glass plate, using a doctor blade to adjust the desired thickness of the membrane.
3. The casted membrane is then dipped into a coagulant bath, usually deionized water (DIW), to precipitate the polymer and form the asymmetric membrane.

Figure 2-5 illustrates the NIPS technique for GO-based MMMs fabrication.

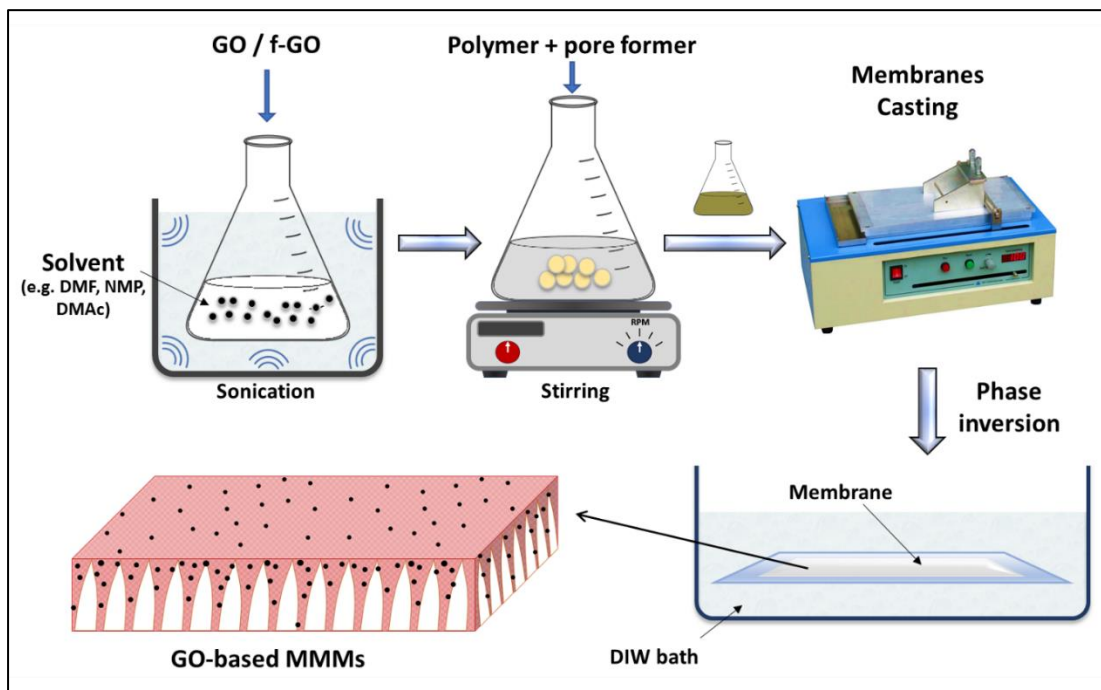


Figure 2-5: GO-based MMMs fabrication using NIPS technique.

GO-MMMs can be also fabricated by simple casting and drying (without phase inversion). This method is commonly used for the fabrication of hydrophilic dense (nonporous) membranes for pervaporation applications (PV) [81, 143].

2.3.2 Vacuum/ evaporation/ pressure-assisted self-assembly techniques

Pressure-assisted self-assembly (PAS), vacuum-assisted self-assembly (VAS) and evaporation-assisted self-assembly (EAS) techniques were used widely for the fabrication of GO-based primary rejection layer (PRL) membranes [1], and free-standing GO membranes [144]. PAS, VAS and EAS rely on the same concept where a GO suspension is deposited and filtered through a porous substrate, usually UF or MF substrate, to form a thin film of GO sheets on the surface. Figure 2-6 illustrates the setup of GO-based membrane fabrication using VAS, PAS and EAS techniques.

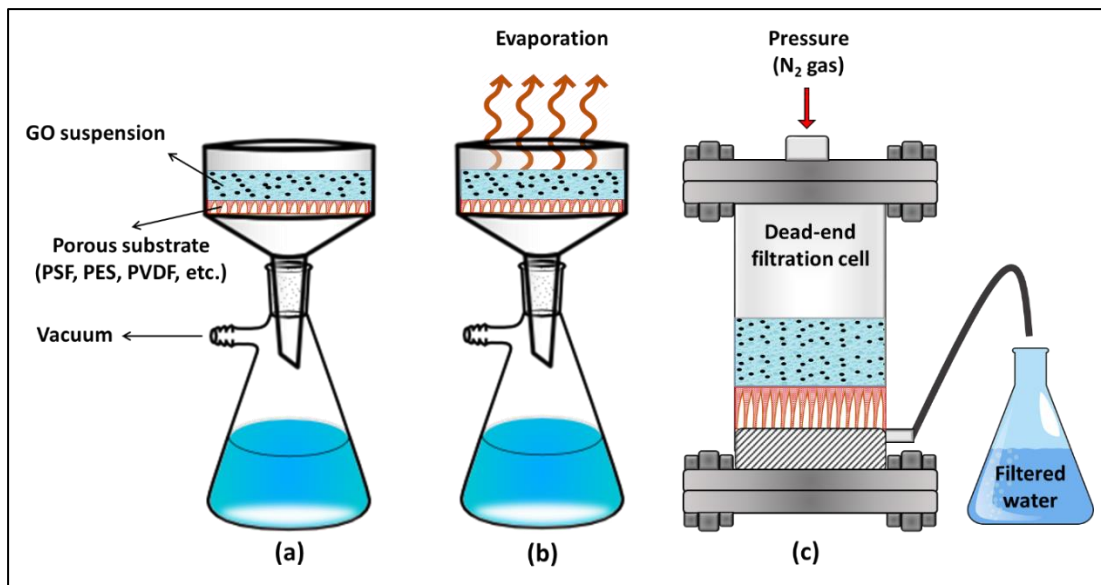


Figure 2-6: illustration of the GO composite membranes fabrication using (a) VAS, (b) EAS, and (c) PAS methods.

Tsou et al. [145] compared the performance of GO/mPAN composites prepared by PAS, VAS, and EAS. It was found that composites prepared via PAS technique exhibited high performance in pervaporation separation. This was related to the denser and higher ordered laminate structure of GO membranes prepared by PAS compared to those prepared by VAS and EAS methods (Figure 2-7a-f).

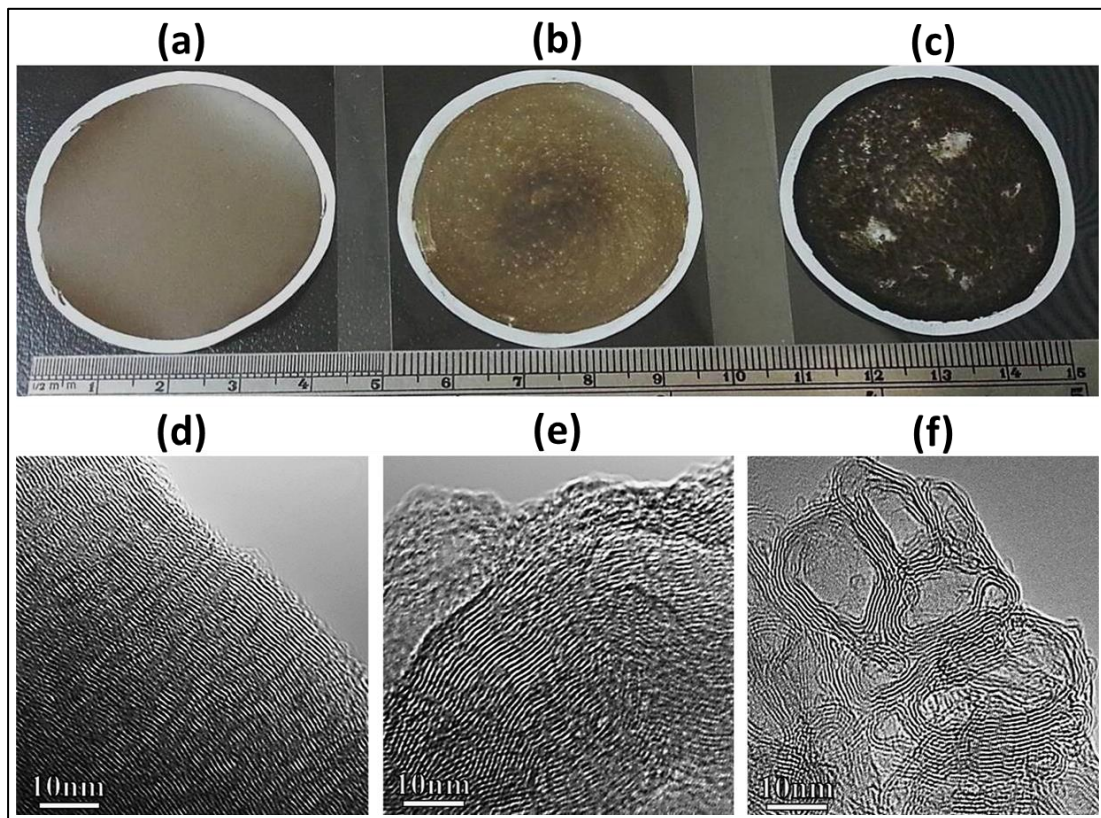


Figure 2-7: photographs and cross-section TEM images of GO/mPAN prepared using: (a) and (d): PAS, (b) and (e): VAS, (c) and (f): EAS techniques [145].

Free-standing GO membranes can be also fabricated using the same techniques while the extraction of the GO-film from the support differs from a study to another. Liu et al. [146] prepared a freestanding forward osmosis GO membrane using VAS technique by filtering a GO suspension through a mixed cellulose ester substrate (MCE). The GO film was then exposed to hydriodic acid (HI) vapor to be

reduced to rGO. The rGO film was then extracted from the MCE substrate by dipping the rGO film into water where the free-standing rGO film floated on the water surface (Figure 2-8). Similarly, Chen and co-workers [144] fabricated freestanding GO membrane using VAS method by filtering the GO suspension on a porous nitrocellulose substrate. However, the freestanding film was extracted by dipping it in NMP and ethyl ether sequentially. Zhao et al. [147] filtered a GO and GO-Palygorskite (GO-PGS) composite through cellulose acetate (CAc) membrane using the VAS method. The CA membrane was then dissolved in acetone to obtain a freestanding MF GO membrane. Freestanding GO membranes usually exhibit good separation performance, however, their poor stability compared to other types of membranes limits their usage under high pressure (e.g. NF and RO) [148].

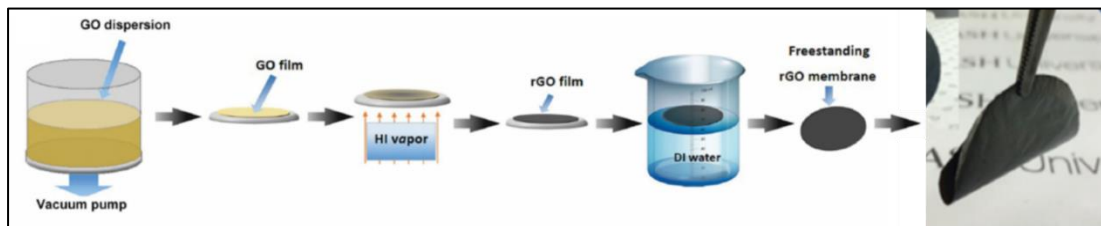


Figure 2-8: Freestanding rGO membrane fabrication using VAS technique [146].

2.3.3 Layer-by-layer self-assembly (LBL)

The LBL self-assembly is a commonly used technique used to produce GO thin films charged at the molecular level by sequential depositions of oppositely charged GO suspensions or polycations/polyanions solutions [148]. The LBL assembly depends mainly on either the electrostatic interactions or the hydrogen bonding between the oppositely charged layers [149]. Before the assembly process, the substrate should be treated to have charged surface [150]. In a recent study,

Halakoo and Feng [80] prepared GO-based membranes via LBL assembly method using PEI/GO for desalination by pervaporation (PVD). Nan et al. [151] fabricated positively charged NF membranes using LBL assembly technique on a hydrolysed PAN substrate (hPAN) using PEI/GO solutions. Choi and co-workers [152] prepared a multilayer GO-based membrane by LBL assembly of oppositely charged GO and aminated-GO (AGO) particles on a polyamide TFC membrane. The LBL assembly of GO/AGO was repeated several times to obtain a GO multilayer-based membrane. Kang et al. [153] prepared novel FO membranes based on LBL assembly technique using GO and oxidized carbon nanotubes (OCNTs) solutions and reported improved performance compared to GO-based membranes. Figure 2-9 illustrates an example of the LBL assembly method using polycation/GO solutions.

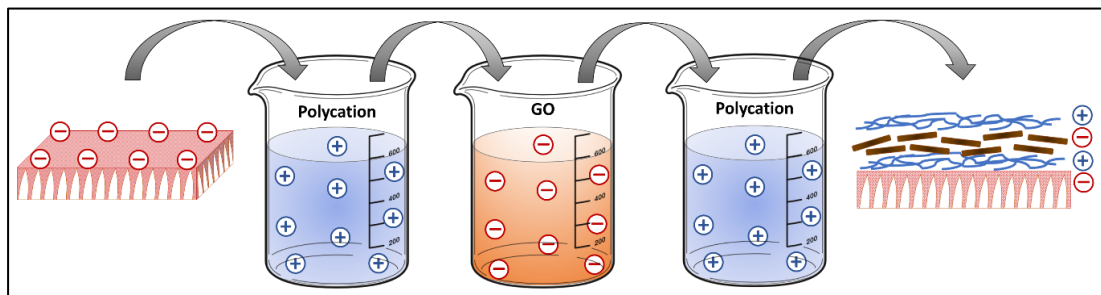


Figure 2-9: Illustration of the LBL self-assembly technique using polycation and negatively charged GO solution.

2.3.4 Interfacial polymerization (IP)

Interfacial polymerization (IP) is one of the well-established techniques used to fabricate thin-film composite membranes (TFC). This technique relies on the polymeric reaction of two monomers dissolved in two immiscible solvents (aqueous/organic) [154, 155]. TFC membranes are usually fabricated by soaking a UF or MF substrate (e.g. PES, PSF, PVDF, etc.) in an aqueous solution, drying the

substrate, and finally soaking the substrate in the organic solution [156]. The two monomers react then at the aqueous/organic interface to form a polyamide barrier (PA). Figure 2-10 illustrates the PA-TFC layer formation using the IP reaction.

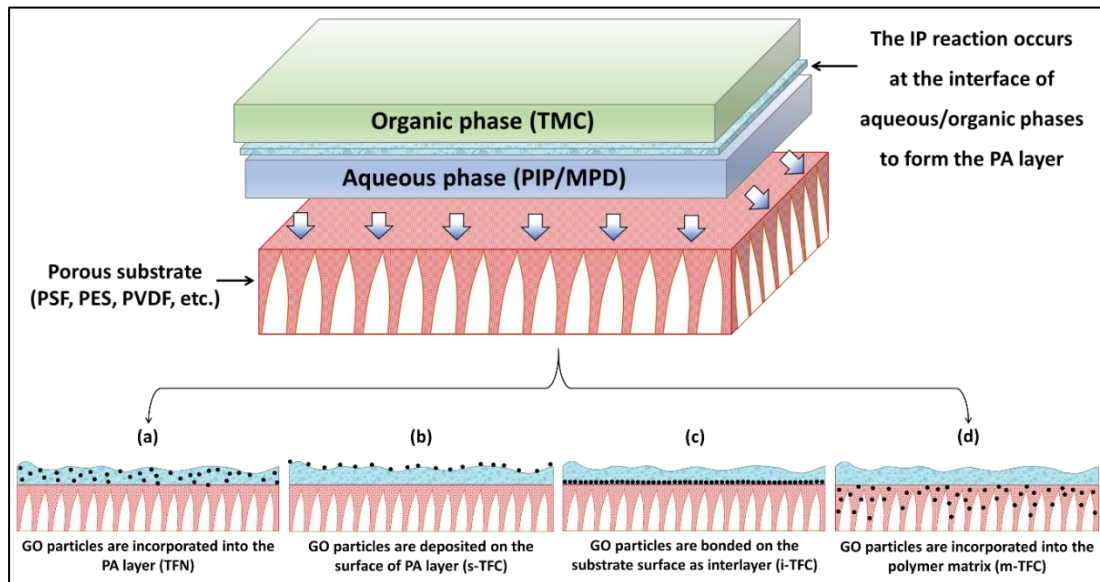


Figure 2-10: Illustration of the interfacial polymerization (IP) technique to prepare: (a) TFN membrane incorporating GO into the PA layer, (b) TFC membrane having GO on the surface of PA layer (s-TFC), (c) TFC membrane having an interlayer of GO (i-TFC), and (d) TFC membrane incorporating GO into the polymer matrix (m-TFC).

Most of the NF TFC membranes are produced by the reaction of piperazine (PIP) in the aqueous medium and trimesoyl chloride (TMC) in the organic medium [73, 85, 157]; while with RO and FO TFC membranes, m-phenylenediamine (MPD) in the aqueous medium and TMC in the organic medium are commonly used [158-160]. The nanofillers like GO and its derivatives are usually loaded into the PA layer during the IP reaction (Figure 2-10a) to form a thin film nanocomposite layer (TFN) at which the most of the salt rejection occurs [160]. p-GO nanoparticles exhibit poor dispersibility in some organic solvents (e.g. hexane and dodecane) [161]. Therefore,

most of GO-based TFN membranes are synthesized by incorporating the GO in the aqueous layer (PIP and MPD). Li and co-workers [162] prepared a TFN RO membranes by incorporating silver phosphate loaded GO quantum dots (GOQD-AP) in the PA layer by loading GOQD-AP particles in the MPD aqueous phase. Similar technique was used by Rajakumaran et al. [163] by loading the zinc oxide and GO nanocomposite (GO-ZnO) in MPD aqueous phase to form a GO-based TFN RO membranes. Modification and functionalization of GO can enhance its dispersion properties and then can be loaded into the TMC organic phase during the IP reaction [164]. Other morphologies of GO-based TFC membranes can be fabricated by depositing the GO particles on the PA layer surface, as interlayer between the substrate and the PA layer, or by incorporating them into the substrate matrix (hereinafter referred to as s-TFC, i-TFC, and m-TFC, respectively). The preparation of GO-based s-TFC membranes is simply done by the deposition of GO particles onto the PA layer after the IP reaction using several techniques like LBL assembly [80, 152, 165, 166], chemical grafting and direct coating [23, 167] (Figure 2-10b). The chemical grafting of a GO layer onto the PA layer surface is usually facilitated by -(3-dimethylaminopropyl)-3-ethylcarbodiimide hydrochloride (EDC) and N-hydroxysuccinimide (NHS) [43, 72, 168]. In this method, the PA layer surface and GO particles are both activated by EDC/NHS, ethylenediamine (EDA) is then grafted onto the activated membrane surface followed by grafting the activated GO solution onto the surface.

GO-based i-TFC membranes can be prepared by binding the GO particles to the substrate surface prior to PA layer formation as illustrated in Figure 2-10c. Like the s-TFC membranes, the GO-based interlayer can be assembled on the substrate surface using direct coating or self-assembly based approaches. In a recent study,

Kang et al. [73] fabricated a GO-interlayer-based TFC nanofiltration membranes using VAS and IP techniques. A GO suspension was first filtered through a porous PES substrate using VAS method, and the PA layer was then formed by IP method using PIP/TMC as aqueous/organic layers. In a similar study, Zhao et al. [169] assembled a GO/MWCNT interlayer on a nylon substrate using VAS technique followed by PA layer formation using the IP reaction. The coating of a GO-based interlayer can be facilitated by the adhesion properties of some highly adhesive polymers. For example, Ng et al. [167] used the adhesion properties of polyvinyl alcohol (PVA) to coat a PVA-GO composite layer onto a PSF substrate followed by the IP reaction. Choi et al. [132] used the self-polymerization and high adhesive properties of polydopamine (PDA) to form a GO-PDA interlayer on PSF substrate. The IP reaction was then done using MPD/TMC to prepare TFN FO membranes.

Figure 2-10d illustrates the morphology of GO-based m-TFC where GO particles are embedded into the substrate matrix prior to the PA layer formation. This method improves the substrate hydrophilicity and porosity which indirectly enhance the performance of membrane [170]. Park et al. [139] embedded GO particles into the PSF matrix using the NIPS technique and then prepared the PA layer using IP technique to prepare TFC FO membranes. Similar technique was used by Lai et al. [85] and Wang et al. [171] to prepare TFC membranes incorporating GO into the polymer matrix. However, this could result in inefficient formation of the PA layer especially with high loading of GO because of the non-homogenous dispersion into the polymer matrix [139]. The difference in membrane fabrication method and GO layer location cause a variation in the performance of these membranes which will be discussed in Section 2.5.

2.4 Antifouling Properties of GO-based Membranes

Fouling is one of the main challenges facing the membrane technologies and their applications in industrial scale. Fouling is a phenomenon where the contaminants in the feed water accumulate on the membrane surface or within the pores, consequently resulting in a flux decline and reducing the permeate quality [172, 173]. Fouling can be divided into four main categories depending on the type of foulant in the feed: colloidal fouling [174, 175], biofouling [176, 177], scaling [178-180], and organic fouling [181, 182]. Figure 2-11 depicts the four types of membrane fouling.

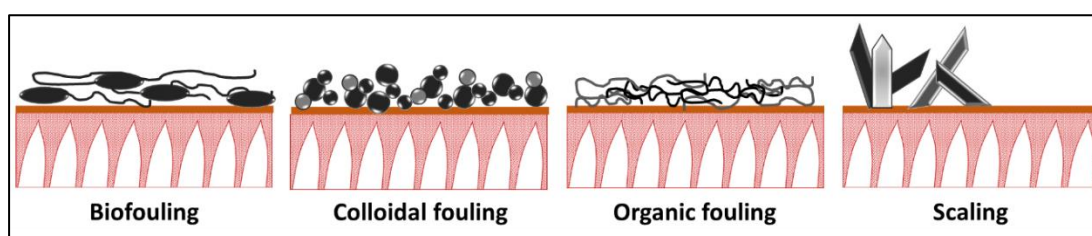


Figure 2-11: Types of membrane fouling.

Although the performance of fouled membranes can be moderately restored by various washing methods, the operation difficulties and costs are inevitably increased [183]. Among the other nanomaterials, p-GO and f-GO nanoparticles showed high antifouling properties with different membranes and for different applications. Generally, BSA and HA are used as model foulants representing protein and organic fouling, respectively. BSA is a globular protein that is extracted from bovine blood. It is usually used as model protein in different science applications due to its availability, ease of production and stability at room temperature [184]. Humic acids (HA) are natural organic matters (NOMs) extracted from soil humus [185]. NOMs exist in natural waters at varying concentrations depending on the water source (e.g. ~20 ppm in rivers) [186].

The embedding of p-GO nanoparticles was reported to significantly improve the fouling resistance [74, 187-191]. However, more studies reported a limited fouling resistance of p-GO-based membranes resulting in moderate flux recovery ratio (FRR < 80%) [82, 83, 90, 192-194]. This can be related to the fact that p-GO particles tend to aggregate because of their poor dispersion in some solvents. Therefore, membranes incorporating f-GO were found to have better fouling resistance than those incorporating p-GO particles [92]. In a recent study by Kong et al. [45], a significant enhancement on the PES antifouling properties were achieved by incorporating cysteine-f-GO (CSGO) into PES matrix due to the higher hydrophilicity and lower roughness of PES/CSGO composite surface compared to the pristine PES. Similar observations were reported by Xu et al. [104] with PVDF/GO-APTS composite membranes prepared via NIPS technique. The FRR against BSA of PVDF/GO-APTS was about 1.7 and 1.1 times higher than the FRR of pristine PVDF and PVDF/GO, respectively. This was attributed to the high hydrophilicity and dispersibility of GO-APTS in the PVDF pore channels which made the pollutants washed away by water easily. Bandehali et al. [44] compared the fouling resistance of NF-MMMs incorporating p-GO (PEI/GO) and glycidyl polyhedral oligosilsesquioxane-f-GO (PEI/POSS-GO) against salt solutions. POSS-GO composites were found to have higher hydrophilicity accompanied with lower surface roughness compared to pristine PEI and PEI/GO composites leading to a significant increase in the FRR (96%) compared to 33% and 40% FRR of pristine PEI and PEI/GO composites, respectively.

Embedding GO and its derivatives into TFN and PRL based membranes was also investigated and showed promising antifouling properties. Gu et al. [195] showed that the chemical grafting of GOQDs on the surface of an APTS-functionalized alumina MF membrane (Al_2O_3 -APTS) could enhance the fouling resistance against

BSA and HA with a FRR of > 94% due to the lower roughness and higher hydrophilicity of the membrane surface. In a similar study, Li et al. [162] showed that the embedding of GOQD-AP into the PA layer of TFC-RO membranes could enhance the fouling resistance by 18% and 34% against BSA and HA, respectively. Furthermore, the GOQD-AP-based TFNs exhibited excellent antibacterial properties with a sterilization rate of 99.9% against *E. coli* due to the synergetic effects of AP and GOQD. Sulfonated GO particles (SGO) were also reported to increase the fouling resistance against both organic and protein foulants [196]. SGO-based TFNs exhibited lower reduction in flux (17% for HA and 14% for BSA) compared to pristine TFC that showed 46% and 31% decrease in flux after HA and BSA filtration, respectively. A recent study by Ng et al. [167] showed that the morphology of GO nanocomposites and the position of GO layer in the membrane highly impact the overall fouling resistance. It has been found that the TFN-RO membranes having GO-PVA layer coated on the surface of the PA layer (s-TFN) could recover 100% of the flux after the filtration of BSA and sodium alginate (SA). However, no significant enhancement of the fouling resistance was observed with membranes having the GO-PVA layer as interlayer (i-TFN). This can be linked to the higher surface hydrophilicity of (s-TFN) than (i-TFN) membranes caused by the presence of GO-PVA layer on the top of PA layer which facilitates the formation of hydrate layer and prevent the deposition and accumulation of foulant molecules on the membrane surface.

The combination of GO particles with other nanomaterials was also investigated in several studies and showed enhanced membranes fouling resistance due to the synergetic effect of these nanocomposites [197]. A recent study by Ayyaru et al. [198] showed that the use of GO-ZnO nanocomposite as nanofiller have better impact on the fouling properties than the p-GO. PVDF/GO-ZnO composite

membranes exhibited up to 92.8% FRR against BSA while the FRR was dramatically dropped with PVDF/GO composites due to the agglomeration of GO particles. Similar conclusions were reported by Rajakumaran et al. [163] with the use of spherical GO-ZnO nanocomposite into TFN-RO membranes. The grafting of TiO₂ particles onto GO sheets was also reported to enhance the surface hydrophilicity and smoothness when embedded to TFN-NF [157] and UF-MMMs [199, 200] resulting in high fouling resistance. Zhang et al. [201] reported a remarkable fouling resistance of PVDF UF composite membranes incorporating GO-OMWCNTs nanocomposites against BSA with FRR of 98.3% compared to 34% and 90% of the pristine PVDF and composites incorporating p-GO particles. Other GO-based nanocomposites reported in literature to improve the fouling resistance include GO-SiO₂ [36, 130] and ZIF-8-GO [110] for UF; GOQD-Ag [202] for RO; and GO-Fe₃O₄ [197] for FO.

2.5 Applications & Properties of GO-based Membranes

Although the utilization of GO and its derivatives in membrane separation processes is still evolving, much work in research has been conducted to investigate their impact for various applications. Most of these studies were conducted on pressure-driven membrane processes (e.g. RO, NF, and UF) due to their wide applications in the global market [19]. Much work has been done also on the GO-based FO membranes because of their advantages over pressure-driven membrane processes [197]. This section summarizes the work done on GO-based membrane technology based on their application. The advances in thermal-driven GO-based membranes (MD and PVD) will be discussed as well.

2.5.1 GO-based RO membranes

Reverse osmosis (RO) is considered the most extensively utilized process for desalination to afford drinking water [203]. Because of its advantages over other the conventional thermal distillation in terms of energy consumption, ease of operation and low environmental impacts, most of the desalination technologies recently are based on RO membrane separation [204, 205]. Different RO membranes have been prepared in literature embedding different GO-based materials. Most of these studies focused on the incorporation of f-GO materials rather than the p-GO particles. Table 2-2 summarizes the types, fabrication methods, testing conditions and the performance of the investigated GO-based RO membranes in terms of pure water permeability (PWP, LMH/bar), rejection, and FRR.

Most of these are TFC based membranes, where GO nanomaterial is incorporated into the PA layer (TFN), coated on the surface (s-TFC), or as interlayer between the substrate and PA layer (i-TFC). In a recent study by Yi et al. [43], nitrogen-doped graphene oxide quantum dots (N-GOQDs) were prepared and chemically grafted on the surface of a commercial RO-PA membrane (s-TFC) with the help of EDC/NHS. The flux and salt rejection were not significantly improved with N-GOQD addition compared to the pristine membrane (11.1 % and 2.3%, respectively). However, the chlorine resistance increased by 32.8% when grafting 0.002 mg/ml of N-GOQD on the surface of PA layer. Similar study was previously reported by Fathizadeh et al. [159] where N-GOQD-modified TFN RO membrane were prepared. However, N-GOQD were incorporated into the PA layer during the IP reaction (in the MPD aqueous layer). The modified membranes showed 3 times-higher flux than pristine TFC while maintaining the same NaCl rejection (92.1%). It was found also that further increase in the concentration of N-GOQD in the PA layer

(0.1 wt/v% and above) reduces both flux and salt rejection. High loadings of nanoparticles in the PA layer usually cause a deformation of the PA layer due to the agglomeration of nanoparticles which consequently reduces the overall performance [206]. Zhang et al. [32] investigated the effect of p-aminophenol-modified GO addition on the performance of TFC RO membranes. The modified GO particles were added in the MPD aqueous layer and blended into the PA layer during the IP reaction. The modified TFN membranes showed a remarkable increase in water flux compared to the pristine TFC membrane (by 24.5%) accompanied with high NaCl rejection of 99.7%. Li et al. [162] reported that the embedding of GOQD-AP nanocomposites into the PA layer exhibited high salt rejection (98.4%) and 50% improvement in the membrane permeability compared to pristine TFC.

Rajakumaran et al. [163] investigated the effect of particles morphological structure on RO performance by incorporating GO-ZnO nanocomposites having different morphologies (spherical, flower, and rod) into the PA layer during the IP reaction. The results showed that GO-ZnO-S (spherical) exhibited higher performance than pristine TFC and TFN membranes with other nanocomposites (flower and rod shaped). The TFN membranes loaded with 0.02 wt% GO-ZnO-S were found to have twice the flux of the pristine TFC with 96.3% salt rejection. Using EDC/NHS facilitated chemical grafting, Cao et al. [72] grafted GO particles on a commercial TFC RO membrane (ESPA 2) to investigate its effects on desalination performance and gypsum scaling. Although the modified membranes exhibited similar flux and salt rejection, the recovered flux after scaling was much lower compared to the pristine membrane. This was related to the carboxyl groups that form strong chemical bonds with Ca^{2+} and therefore make it difficult to be removed during cleaning. In a previous study, Perreault et al. [168] used the same technique (EDC/NHS facilitated grafting)

to prepare GO-coated TFC membrane (s-TFC) by grafting GO particles on the PA layer. The flux and rejection of GO-modified TFC membranes didn't differ from the pristine TFC membranes. However, the modified membranes were found to have higher antimicrobial activity than the original TFC. Novel TFN RO membranes were prepared by Safarpour et al. [161] by incorporating reduced graphene oxide (rGO)/TiO₂ nanocomposites into the PA layer via IP technique. With very low concentration of rGO/TiO₂ (0.02 wt% in MPD), the pure water flux increased by 21% without a noticeable reduction in the salt rejection (99.45%) eliminating the trade-off relation between flux and rejection. Additionally, rGO/TiO₂ TFN membranes exhibited much higher chlorine resistance compared to the pristine TFC membranes. The salt rejection of the bare TFC declined by 30% after chlorination while it declined by only 3% with rGO/TiO₂-0.02 wt% TFN membranes. Choi et al. [152] coated the surface of PA layer using oppositely charged GO and aminated GO (AGO) solutions via the LBL assembly technique. The results showed that the membrane coating with GO and AGO layers didn't affect the performance of the pristine TFC regardless of the number of the bilayers. However, the resistance against chlorine and protein fouling were significantly improved.

The incorporation of p-GO nanoparticles without prior functionalization into the PA layer was also reported to enhance the performance of TFC RO membranes in few studies. Yin et al. [158] synthesized GO particles using modified Hummers method and incorporated them during the IP reaction in the TMC organic phase in the presence of ethanol to facilitate the dispersion. The addition of 0.015 wt% GO improved the water flux by 52% while the salt rejection decreased slightly by 2%. Chae et al. [207] demonstrated that GO embedding into the MPD aqueous phase of the PA layer enhanced the desalination performance, antibiofouling and chlorine

resistance of TFC RO membranes. The flux was elevated by around 80% while retaining the same salt rejection. Further, the modified membranes were found to have higher chlorine resistance as they maintain high salt rejection even at high chlorination levels. In a recent study, Khanzada et al. [23] prepared a GO coated TFC RO (s-TFC) membranes with the help of dopamine self-polymerization, which exhibited slightly higher salt rejection (by 4%) and lower flux (by 3.8%) than the pristine TFC membrane. Kim et al. [208] prepared novel TFN RO membranes by incorporating p-GO into a polymer matrix containing N-isopropylacrylamide (NIPAM) and N,N'-methylene-bis-acrylamide (MBA). The mixture was then assembled on a porous PES substrate using the VAS technique and then polymerized in a convection oven. The prepared PES/poly(NIPAM-MBA)/GO membranes exhibited high pure water permeability (3.56 LMH/bar) and 98.5% salt rejection. Furthermore, the poly(NIPAM-MBA)/GO layer showed higher chlorine resistance when compared to commercial PA membranes. It was found that chlorine exposure damaged the PA layer of the commercial RO and reduced salt rejection. However, the poly(NIPAM-MBA)/GO membranes retain the same performance even at high chlorine exposure. Abbaszadeh et al. [166] prepared a multi-layered GO-based TFN membranes by alternating PA and GO layers via LBL technique. The modified membranes exhibited better chlorine resistance while the flux and rejection properties remained unchanged.

The fabrication of GO-based mixed matrix RO membranes (MMMs-RO) was not extensively investigated in literature because of the lower salt rejection compared to TFN-RO membranes. Ghaseminezhad et al. [209] prepared GO embedded cellulose acetate (CAc) MMMs using the NIPS technique. The CA/GO composites exhibited higher flux and rejection than the pristine CA membranes. However, the rejection is

much lower than other TFN-RO membranes. In a similar study, Chen et al. [89] prepared GO embedded cellulose triacetate (CTA) composite using melting method. However, the modified composites exhibited low pure water permeability (0.16 LMH/bar) and low salt rejection (66%) which is also lower than other RO membranes reported in the literature.

Table 2-2: Summary of the recently developed GO-based RO membranes.

Type	Method ^a	Membrane	Testing conditions		Membrane performance			Year & Ref.
			Feed compositions (ppm)	Pressure (bar)	PWP (LMH/bar)	Rejection %	FRR %	
s-TFC	Grafting	LCLE4040/N-GOQD ^b	1000 ppm NaCl	15	2.7	96.2	-	2020 [43]
TFN	IP	PSF/PA/p-aminophenol-GO	2000 ppm NaCl	15	1.6	99.7	-	2020 [32]
s-TFC	Coating	BW4040AFR/PDA-GO ^b	2000 ppm NaCl	10	4.6	97	-	2020 [23]
s-TFC	Coating	PSF/PA/GO-PVA	2000 ppm NaCl	16	~1.4	97.85	FRR _{BSA,SA} =100	2020 [167]
TFN	IP	PSF/PI/GO	2000 ppm NaCl	20	1.59	96.2	FRR _{HA} =86.7	2020 [71]
MMM	NIPS	CAC/GO	25000 ppm NaCl	25	2.6	90	FRR _{NaCl} =77	2019 [209]
s-TFC	LBL	hPAN/PA/GO	2000 ppm NaCl	27.6	1.3	92.5	-	2019 [166]
TFN	IP	PSF/PA/N-GOQD	2000 ppm NaCl	15	1.8	92.1	-	2019 [159]
TFN	IP	PSF/PA/GOQD-AP	2000 ppm NaCl	16	2.5	98.4	FRR _{BSA} =83.2	2019 [162]
							FRR _{HA} =87	
TFN	IP	PSF/PA/GO-ZnO-S	2000 ppm NaCl	20	1.57	96.3	FRR _{HA} =86.3	2019 [163]
TFN	IP	PSF/PA/GOQD-Ag	2000 ppm NaCl	16	2.4	98.9	FRR _{BSA} =82.4	2019 [202]
MMM	Melting	CTA/TMS/PEG/GO	2000 ppm NaCl	30	0.16	66	-	2018 [89]
s-TFC	Grafting	ESPA2/GO ^b	7 mM NaCl	34.5	4.8	R _{NaCl} =97.8	-	2018 [72]
			1 mM CaCl ₂			R _{CaCl2} =98.3		
TFN	VAS	PES/poly(NIPAM-MBA)/GO	2000 ppm NaCl	10	3.56	R _{NaCl} =98.5	-	2018 [208]
PRL	LBL	PSF/PA/GO-TiO ₂	1000 ppm NaCl	15	1.57	95.5	-	2017 [210]
m-TFC	NIPS	PSF/GO/PA	2000 ppm NaCl	15.5	~2.5	~98.6	-	2017 [211]
TFN	IP	PSF/PA/GO	2000 ppm NaCl and Na ₂ SO ₄	20.5	2.9	R _{NaCl} =93.8	-	2016 [158]
						R _{Na2SO4} =97.3		
TFN	IP	PSF/PA/GO-TA	2000 ppm NaCl	15.5	~2.9	~96	-	2016 [101]
TFN	IP	PSF/PA/GO	2000 ppm NaCl	15.5	1.07	R _{NaCl} =99.5	-	2015 [207]
TFN	IP	PSF/PA/rGO-TiO ₂	2000 ppm NaCl	15	3.42	R _{NaCl} =99.45	FRR _{BSA} =75	2015 [161]
s-TFC	Grafting	PSF/PA/GO	2920 ppm NaCl	27.6	1.45	R _{NaCl} =97.8	-	2014 [168]
s-TFC	LBL	PSF/PA/ AGO-GO	2000 ppm NaCl	15.5	0.9	R _{NaCl} =96.4	-	2013 [152]

^a Method of GO incorporation

^b GO coating/grafting was done on a commercial RO membrane

2.5.2 GO-based NF membranes

The interest in the development of NF membranes has grown over the past years and found wide range of applications in water treatment, food engineering, biotechnological and pharmaceutical processes [212]. Nanofiltration is a molecular separation technology that lies between ultrafiltration (UF) and reverse osmosis (RO) and combines their advantages in terms of low-energy consumption and high separation [213]. GO-based NF membranes can be used for the separation of mono/multivalent salts [34, 44, 73, 74, 85, 88, 108, 111, 151, 157, 187, 196, 214-216], dyes [108, 188, 189, 217, 218], heavy metals [44, 84, 218], and organic solvents (OSN) [219-221]. Table 2-3 summarizes the types, fabrication methods, performance and testing conditions of the investigated GO-based NF membranes. Most of GO-NF membranes are TFN-based that are prepared using IP technique (using PIP/TMC) and PRL-based that are commonly prepared via the self-assembly techniques (e.g. PAS, VAS, and LBL).

Like GO-TFN RO membranes, most of GO-TFN NF membranes are prepared by the incorporation of GO-based material into the aqueous phase (e.g. PIP) during the IP reaction. Shao et al. [111] prepared two types of positively charged aminated GO (AGO) by functionalizing the GO with polyethylenimine (PEI) and ethylenediamine (EDA). The AGO particles were then embedded into the PA layer via the IP technique. The optimal membranes were obtained by embedding 40 ppm GO-PEI and 60 ppm GO-EDA which improved the flux of the pristine TFC by 160.9% and 154.4%, respectively, accompanied with high rejection of divalent salts. Kang and co-workers [196] embedded sulfonated GO particles (SGO) into the PA layer during IP reaction. The addition of 0.3 wt% SGO into the PIP aqueous layer elevated the flux by 87% (compared to the pristine TFC) while maintaining similar

salt rejection. Zhao et al. [214] found that the incorporation of GO particles at low concentrations of monomer promotes the formation of the PA-TFN layer with better surface hydrophilicity, roughness and charge. The optimum membranes were obtained by incorporating 0.01 wt% GO into 0.25 wt% aqueous PIP solution which resulted in 32% higher flux and almost similar salt rejection. Xue et al. [34] proposed novel strategy to fabricate TFN-NF membranes incorporating octadecylamine-modified GO (GO-ODA). The aqueous phase was prepared using mixed amines of fluorine-containing monomer (BHMTM) and PIP; while the GO-ODA particles were embedded in the organic-TMC phase during the IP reaction. The prepared GO-ODA TFNs prepared with mixed amines resulted in 2.5 times the flux of neat TFN-PIP membranes while maintaining high rejection of sodium sulphate of 98.4%. It has been also reported that the stability of GO sheets along with the existence of fluorine-containing groups in BHMTM provided excellent chlorine resistance for the GO-ODA membranes. Safarpour et al. [157] prepared rGO/TiO₂ nanocomposites and embedded them into the PA layer via IP reaction on a PSF substrate. With the optimum concentration of rGO/TiO₂ nanocomposites (0.005 wt% in PIP), the flux and Na₂SO₄ rejection were improved by 27% and 7%, respectively. The embedding of p-GO particles into the aqueous phase of the PA layer was also reported to enhance the pure water flux of TFN-NF membranes while retaining high divalent salts rejection [74, 214].

TFC-NF membranes can be also prepared by embedding GO particles into the substrate polymer matrix (m-TFC) or as interlayer between the substrate and PA layer (i-TFC) before the IP reaction. In a recent study, Valamohammadi et al. [187] prepared positively charged TFN membranes by embedding GO particles into PAN matrix (m-TFC) via the NIPS technique. Hyperbranched polyethyleneimine (HPEI)

was then assembled onto the PAN-GO composite followed by a chemical cross-linking with glutaraldehyde (GA). The incorporation of GO improved the flux by 64% compared to the unfilled TFC membranes, while incorporating CNTs enhanced the flux by 38% only. Furthermore, the salt rejection results confirmed the positively charged surface of the prepared TFN-GO and the rejection was mainly governed by Donnan exclusion. In a similar study by Lai et al. [85], m-TFC NF membranes were prepared by incorporating the GO particles into the PSF matrix via NIPS technique followed by the formation of PA layer via the IP reaction. The optimum GO concentration was found to be 0.3 wt% which exhibited 50.9% and 88.5% higher flux and NaCl rejection, respectively, compared to this of the pristine TFC membranes. Kang et al. [73] prepared GO-interlayer-based TFC NF membranes (i-TFC) on a PES substrate using VAS and IP techniques. The modified membranes exhibited high rejection of divalent salts with high pure water permeability (26.63 LMH/bar). The prepared membranes showed also high stability under ultrasound and good resistance against different organic solvents.

The use of PAS, VAS, and LBL assembly techniques have been also used to fabricate primary-rejection-layer (PRL)-based GO-NF membranes with different performance and properties. Commonly, the desalination efficiency of PRL-based NF membranes is much lower than this of TFN membranes. Hence, most of these studies were conducted for other purposes including dyes removal, heavy metal removal, organic materials removal, etc. In a recent study by Kang et al. [222], novel loos NF membranes with high permeance were prepared by the vacuum-assisted assembly of GO layer onto a PES substrate followed by dip-coating of the resulted membrane into TA/Ni solution. The resulted membranes achieved high permeability compared to other membranes in literature (71.7 LMH/bar) with high rejection of Methyl blue

(MB) and Congo Red (CR) dyes. However, the rejection of divalent and monovalent salts was less than 6%. Loose NF membranes usually have higher permeance of salts and hence they are proposed for the organic compounds removal and not for desalination purposes [222, 223]. Chen et al. [84] prepared GO-NF membranes on a PES MF substrate via VAS technique for the separation of mercury from desulfurization wastewater. The composite membranes exhibited Hg (II) rejection of 80.33% with PWP of 5.26 LMH/bar. Zhang et al. [217] assembled diamine-grafted-partially reduced GO (PrGO) onto PVDF substrate membrane via the PAS technique. The prepared PrGO-based membranes showed high Methyl orange (MO) dye rejection (96.6%) with PWP of 4.16 LMH/bar; while Na₂SO₄ rejection was lower than most of NF membranes (81.5%). Yuan et al. [215] conducted investigated the effect of GO carboxylation on the desalination performance of GO-NF membranes. GO-COOH-based membranes were synthesized via PAS assembly method on a PSF ultrafiltration membrane. It was found that GO-COOH based membranes exhibited higher flux (by 23%) and salt rejection (by 10%) compared to membranes having p-GO. Using LBL assembly method, Nan et al. [151] prepared positively charged NF membranes using PEI/GO solutions on a hydrolysed PAN substrate (hPAN). The prepared membranes exhibited good permeability as well as good performance in water softening applications. Wang et al. [88] prepared PAN/GO NF membranes via VAS technique for the separation of Congo red dyes (CR) and Na₂SO₄. The membranes exhibited complete rejection of CR dyes while Na₂SO₄ rejection was as low as 56.7%. Chen et al. [188] prepared CNT-intercalated rGO membranes assembled on anodic aluminium oxide (AAO) microporous membranes via VAS method for dyes removal. When using well-dispersed CNTs-rGO, a uniform network can be formed providing many mass-transfer channels through the nanostructure.

Therefore, the composite membranes exhibited high permeability (31.5 LMH/bar) with excellent dyes rejection (97.3% for MO and >99% for other dyes).

Less work has been done in the literature on developing GO-based mixed matrix NF membranes (MMMs) because of their poor performance in desalination applications. Therefore, these membranes are usually developed for the separation of dyes and heavy metals from wastewater. In a recent study by Bandehali et al. [44], POSS-GO nanocomposites were embedded into PEI polymer matrix via NIPS technique. When embedding 0.1 wt% POSS-GO into PEI, the flux was enhanced by 84% with 78, 80, and 76% rejection of Pb(II), Cr(II) and Na₂SO₄, respectively. Luque-Alled et al. [24] fabricated PES MMMs incorporating GO-APTS using the NIPS approach. The PES/GO-APTS composites showed high rejection of dyes (SY and AO) and BSA (>96%) while the MgSO₄ rejection was 51.6%. Abdi et al. [218] reported that the embedding of magnetic GO composites (MMGO) into PES via NIPS technique improves the flux by 180%. Furthermore, copper rejection of the composite membranes was significantly enhanced (5.7 times higher than pristine PES). Similar study was conducted by Zhu et al. [108] by incorporating poly(sulfobetaine methacrylate) (PSBMA)-f-GO into PES matrix via NIPS technique. The resulted PES-GO-PSBMA NF membranes exhibited excellent dyes rejection (97.2% Reactive red and 99.2% Reactive black). However, the rejection of salts was as low as 10% for Na₂SO₄.

In general, much work has been done in the development of GO-based NF membranes for variety of applications. Based on the comparisons provided above and in Table 2-3, it can be concluded that TFN-NF membranes are the best choice for desalination purposes, while other types like MMMs and PRL-based membranes are efficient for other applications like dyes and heavy metals removal.

Table 2-3: Summary of the recently developed GO-based NF membranes.

Type	Method ^a	Membrane	Testing conditions		Membrane performance			Year & Ref.
			Feed compositions (ppm)	Pressure (bar)	PWP (LMH/bar)	Rejection %	FRR %	
MMM	NIPS	PEI/POSS-GO	1100 ppm Na ₂ SO ₄ 500 ppm Pb(II), Cr(II), and Cu(II)	4.5	7.2	R _{Na₂SO₄} = 76 R _{Pb} = 78 R _{Cr} = 80 R _{Cu} = 55	FRR _{Na₂SO₄} =96	2020 [44]
MMM	NIPS	PES/GO-APTS	100 ppm SY and AO 1000 ppm BSA; 2000 ppm MgSO ₄	4	9.9	R _{BSA,SY,AO} > 96 R _{MgSO₄} =51.6	FRR _{BSA} =64	2020 [24]
MMM	NIPS	PVA/SA/GO	100 ppm BSA 30 ppm LB3R dye	3	38.6	R _{BSA} =97.36 R _{LB} = 86.6	FRR _{BSA} =88.7	2020 [224]
m-TFC	NIPS	PES-GO/PEI/TMC	2000 ppm MgSO ₄ and LiCl	3	11.15	R _{MgSO₄} = 95.14 R _{LiCl} = 20.93	-	2020 [225]
i-TFC	VAS	PES/GO/PA	1000 ppm NaCl, MgCl ₂ , Na ₂ SO ₄ and MgSO ₄	4	26.63	R _{Na₂SO₄} = 98.5 R _{MgSO₄} = 95.88	-	2020 [73]
m-TFC	NIPS	PAN-GO/PEI	500 ppm MgCl ₂	4.5	11.5	R _{MgCl₂} = 86	FRR _{BSA} =91.2	2020 [187]
TFN	IP	PES/PA/GO-TETA	1000 ppm NaCl and Na ₂ SO ₄	6	12.17	R _{Na₂SO₄} = 65.3 R _{NaCl} = 33	FRR _{BSA} =95.3	2020 [107]
PRL	VAS	PES/GO-TA-Ni	1000 ppm NaCl, MgCl ₂ , Na ₂ SO ₄ and MgSO ₄ ; 50 ppm dyes (CR and MB)		71.7	R _{Salts} < 6 R _{CR} =98.8 R _{MB} =92.9	FRR _{MB} =90.5	2020 [222]
TFN	IP	PES-Fe ⁺³ /GO-TA	1000 ppm NaCl, MgCl ₂ , Na ₂ SO ₄ and MgSO ₄	2	21.7	R _{Na₂SO₄} = 84 R _{MgSO₄} = 91.2 R _{MgCl₂} = 32.7 R _{NaCl} = 10.8	-	2019 [102]
TFN	IP	PES/GO-ST/PA	Na ₂ SO ₄	8	10	R _{Na₂SO₄} = 96.4	-	2019 [103]
TFN	IP	PSF/PA/GO-PEI	2000 ppm NaCl, MgCl ₂ , Na ₂ SO ₄ and MgSO ₄	5	12.4	R _{Na₂SO₄} = 98.2 R _{MgSO₄} = 97.4 R _{MgCl₂} = 92.1 R _{NaCl} = 35.9	-	2019 [111]

Type	Method ^a	Membrane	Testing conditions		Membrane performance			Year & Ref.
			Feed compositions (ppm)	Pressure (bar)	PWP (LMH/bar)	Rejection %	FRR %	
TFN	IP	PSF/PA/SGO	2500 ppm NaCl, Na ₂ SO ₄ and MgSO ₄	5	2.37	R _{NaCl} = 77.6 R _{Na2SO4} = 96.45 R _{MgSO4} = 95	-	2019 [196]
PRL	VAS	PES/GO	3 ppm Hg(II)	5	5.26	80.33	-	2019 [84]
TFN	IP	PES/PA/GO	1000 ppm Na ₂ SO ₄ and MgSO ₄	4	15.63	R _{Na2SO4} = 96.56 R _{MgSO4} = 90.5		2018 [214]
TFN	IP	PES/PA/GO-ODA	2500 ppm NaCl, Na ₂ SO ₄ and MgSO ₄ 300 ppm glucose, sucrose and raffinose.	6	8.3	R _{Na2SO4} = 98.4 R _{MgSO4} = 98 R _{NaCl} = 34 R _{glucose} = 80.4 R _{sucrose} = 93.8 R _{raffinose} = 94.5		2018 [34]
PRL	PAS	PVDF/PrGO	500 ppm NaCl, and Na ₂ SO ₄ 50 ppm MO dye	8	4.16	R _{Na2SO4} = 81.5 R _{NaCl} = 42.4 R _{MO} = 96.6		2018 [217]
MMM	NIPS	PES/MMGO	30 ppm DR16 dye 20 ppm Cu(II)	4	9	R _{DR} = 99 R _{Cu} = 92	FRR _{Milk} =90.6	2018 [218]
PRL	PAS	PSF/GO-COOH	2000 ppm NaCl, and Na ₂ SO ₄	15	4.89	R _{NaCl} =39.2 R _{Na2SO4} = 87		2017 [215]
MMM	NIPS	PMIA/GO	50 ppm dyes (CR, AR, and RY)	8	15.65	R _{CR} > 92 R _{AR} > 92 R _{RY} > 95	FRR _{BSA} =98.7	2017 [226]
PRL	LBL	hPAN/(PEI/GO/PEI)	1000 ppm NaCl and MgCl ₂	5	4.2	R _{NaCl} =38.1 R _{MgCl2} = 93.9		2016 [151]
m-TFC	NIPS	PSf/GO/PA	1000 ppm NaCl, MgCl ₂ , Na ₂ SO ₄ and MgSO ₄	8	2.43	R _{Na2SO4} = 95.2 R _{MgSO4} = 91.1 R _{NaCl} = 59.5 R _{MgCl2} =62.1		2016 [85]
MMM	NIPS	PES/GO-PSBMA	1000 ppm NaCl, MgCl ₂ , Na ₂ SO ₄ and	4	11.98	R _{Salts} ≤ 10	FRR _{BSA} =94.4	2016 [108]

Type	Method ^a	Membrane	Testing conditions		Membrane performance			Year & Ref.
			Feed compositions (ppm)	Pressure (bar)	PWP (LMH/bar)	Rejection %	FRR %	
TFN	IP	PES/PA/GO	MgSO ₄ 500 ppm dyes (RR49 and RB5) 2000 ppm NaCl, MgCl ₂ , Na ₂ SO ₄ and MgSO ₄	6	14.6	R _{RB} =99.2 R _{RR} = 97.2 R _{Na2SO4} = 98.2 R _{MgSO4} = 96.5 R _{NaCl} = 56.8 R _{MgCl2} =50.5	-	2016 [74]
PRL	VAS	AAO/rGO-CNT	50 ppm dyes (DR80, MO, TY, CFP, and CB)	3	31.5	R _{dyes} > 99 R _{MO} =97.3	-	2016 [188]
PRL	LBL	PSF/OCMC/GO	1000 ppm NaCl and Na ₂ SO ₄	15	1.8	R _{NaCl} =69.1 R _{Na2SO4} =93.74	-	2015 [216]
TFN	IP	PSF/PA/rGO-TiO ₂	2000 ppm NaCl and Na ₂ SO ₄	10	6.1	R _{Na2SO4} = 94 R _{NaCl} =37	FRR _{BSA} >90	2015 [157]
MMM	NIPS	PES/GO	30 ppm DR16 dye	4	6	R _{dyes} = 96	FRR _{BSA} =90.5	2014 [189]
PRL	LBL	hPAN/GO-PEI/PAA	NaCl and Na ₂ SO ₄	5	0.81	R _{Na2SO4} = 92.6 R _{NaCl} =43.2	-	2012 [227]

^a Method of GO incorporation

2.5.3 GO-based UF membranes

Ultrafiltration (UF) is a fast-growing technology that showed significant input in the clean water production. Because of the relatively low-cost, UF is considered economical and efficient pre-treatment process for nanofiltration (NF) and reverse osmosis (RO) and can remove wide range of pollutants from wastewater [228]. It is a promising technology to produce affordable clean water because of its cleanliness, safety, ease of operation, and high separation efficiency of organic substances, proteins, bacteria, viruses, and turbidity. In addition to water and wastewater treatment, UF membranes are utilized in several applications including dairy production, chemical recovery, food industry, paint treatment, pharmaceutical and medical applications. Most of GO-UF membranes reported in literature were fabricated for the proteins removal [24, 45, 75, 76, 83, 90, 100, 104, 106, 191, 194, 199, 201, 229-235]. Other studies were conducted on the removal of dyes [24, 82, 90, 105, 192], oil [130, 236, 237], natural organic matters (NOMs) [190, 193, 238, 239] and heavy metals [86].

Table 2-4 summarizes the types, fabrication methods, performance and testing conditions of the investigated GO-based UF membranes. Most of GO-UF membranes are mixed-matrix that are prepared by NIPS technique. GO and GO-based materials are usually embedded into UF membranes to enhance the flux, rejection, or antifouling properties against various foulants. BSA is usually used for testing the separation and fouling performance of UF membranes. Several functional GO structures have been developed in literature and showed remarkable enhancement on flux and BSA rejection. A recent study by Kong et al. [45] showed that the embedding of CSGO into PES matrix via NIPS technique could improve the pure water flux by 60% with 99.7% BSA rejection. Prince and co-workers [232]

functionalized the GO with amines and carboxyl groups to increase the wettability of GO and its based membranes. The f-GO particles were then covalently embedded into poly acrylonitrile-co-maleic anhydride (PANCMA) matrix via NIPS method. The ultra-wetting GO based membranes exhibited much higher PWP than most GO-UF membranes reported in literature (978 LMH/bar) with 85% BSA rejection. The embedding of cobalt oxide/GO (CO_3O_4 -GO) nanocomposites into PES matrix was found to highly improve the flux of PES membranes while retaining similar BSA rejection [233]. The authors related the flux enhancement to the higher hydrophilicity of PES/ CO_3O_4 -GO composites compared to that of pristine PES. A recent study by Wu et al. showed that the addition of PEG-2000 and TiO_2 -GO nanocomposites to PVDF UF membranes improves the flux and BSA rejection by >400% and 43%, respectively [199]. Khakpour et al. [229] prepared PVC MMMs by embedding GO-nanodiamond nanocomposite. The hybrid membranes exhibited higher flux than pristine PVC membranes with respect to flux, rejection and fouling resistance. The shape of GO particles was found to affect the performance of UF membranes. Jiang et al. [90] conducted a study on the effect of GO shape, flat GO and crumpled GO (CGO), on the performance of PSF UF membranes. Both GO and CGO were embedded via NIPS technique. The results showed that the difference in GO shape resulted in different performance. For example, PSF-CGO exhibited 150% lower flux than PSF-GO which was related to the difference in dispersibility and stability of these particles in the NMP solvent because of the shape effect. However, PSF/CGO showed better rejection of MO dyes (52.7%) compared to PSF/GO (41.4%), while both composites exhibited complete rejection of BSA.

Generally, the flux of the MMMs can be improved with the addition of low contents of GO and GO-based materials because of the hydrophilic nature of GO. The

incorporation of a hydrophilic filler changes the overall hydrophilicity of the casting solution [240]. This increase accelerates the exchange of solvent and non-solvent during NIPS process. However, excessive addition of the GO-based nanofillers was found to cause a reduction in the flux of the membrane [76, 100, 140, 230, 240]. This can be explained by the presence of a tipping mass percentage of nanomaterial [241, 242]. Excessive loadings of GO-based nanofillers increase the viscosity of the casting solution leading to a reduction in porosity and pore size and therefore a reduction in the membrane flux. It has been reported that a tipping mass percentage is a critical point after which the permeability decreases as a result of the increase in solution viscosity [239, 242, 243]. The tipping mass percentage varies depending on the type of nanofiller and polymer [90]. PSF/Guanidyl-f-GO (PSF/GFG) MMMs were reported by Zhang et al. [100] to have PWP of 217 LMH/bar and 95.2% BSA rejection. Hu et al. [76] prepared GO embedded PES-sulfonated PSF (PES-SPSF/GO) MMMs with superior performance at low GO content (0.012 wt%). The PWP was as high as 816.9 LMH/bar (1.6 times unfilled membrane) accompanied with 99.5% BSA rejection. High performance-MMMs were also prepared by Ayyaru and Ahn [240] by embedding sulfonated GO (SGO) into PVDF matrix using NIPS method. The prepared PVDF/SGO membranes exhibited PWP of 740 LMH/bar (147% and 61% higher than the pristine PVDF and PVDF/GO) with 98% BSA rejection. SGO particles were also reported to enhance the flux of PSF MMMs by approximately 125% with > 98% BSA rejection [230].

The application of GO-UF membranes in natural organic matters (NOMs) separation has been also investigated in the literature by embedding both p-GO and f-GO particles. Kumar et al. [36] embedded aminated GO nanohybrid (GO-SiO₂-NH₂) into the sulfonated poly(ether sulfone) (SPES) for HA removal as a model NOM. The

composite membranes embedding the aminated nanohybrid exhibited high HA rejection rate (>97%) accompanied with a remarkable flux enhancement (~2.9 times higher than the pristine SPES). Algamdi et al. [238] fabricated PES/GO MMMs via the NIPS technique for HA removal. The flux of the PES/GO membranes (5 wt% GO) was 3.1 times the flux of pristine PES with insignificant decrease in HA rejection (2% decrease). Similar study was previously conducted by Chu et al. [190] on HA removal using PES/GO UF membranes. p-GO particles were coated on a commercial PES substrate with different molecular weight cut-offs (MWCO) via VAS technique. The flux of the coated membranes was approximately 20% higher than the pristine PES and the HA rejection was significantly elevated. On the other hand, some GO-UF membranes were found to have low rejection of NOMs or exhibit a trade-off between the flux and the rejection. Liu et al. [244] functionalized the GO particles with perfluorosulfonic acid (PFSA-g-GO) and then embedded them into PVDF MMMs. The prepared composites showed high PWP (587.4 LMH/bar), while the HA rejection was 79.6%. Xia and Ni [239] investigated the effect of GO embedding on the performance of PVDF UF membranes for NOM removal from micro-polluted water. With the optimum GO concentration (0.5 wt%), the flux was improved by approximately 115%. However, all the prepared membranes exhibited poor dissolved organic carbon (DOC) removal (around 10%) and slight increase in the removal of other dissolved organic matters (DOMs) such as fulvic acids, humic acids and proteins.

Some GO-based UF showed excellent performance in oil separation applications. In a recent study, Alammar et al. [236] blended GO particles with polybenzimidazole (PBI) via NIPS technique. The authors reported approximately complete oil rejection of the modified PBI/GO (99.9%) while retaining PWP of 91.3

LMH/bar. Using the VAS approach, Peng et al. [130] fabricated PVDF/rGO@SiO₂ nanohybrid membranes for oil and cationic dyes removal. The rGO@SiO₂-coated PVDF membranes were then dip-coated with polydopamine (PDA) to increase the hydrophilicity and active sites of the membranes. The optimum membrane was obtained with mass ratio of 2 mg GO/2.67 mg SiO₂ at which excellent rejection of oil and Methylene Blue (MB) dye was obtained (99.2% and 99.8%, respectively). For the similar purpose, Li et al. [237] prepared composite UF membranes with a primary rejection layer (PRL) consisting of rGO and graphitic carbon nitride composite (rGO-g-C₃N₄). The rGO-g-C₃N₄ composite was firstly modified with PDA and then assembled on a commercial cellulose acetate (CAc) membrane using VAS approach. The composite membrane exhibited high rejection of oil and dyes (99.5% and 99.8%, respectively) with approximate PWP of 75 LMH/bar.

Several GO-based UF membranes have been investigated for the dyes removal and showed promising separation performance. Using the LBL and PAS assembly approaches, Homem and co-workers [192] modified a microfiltration PES membrane with PEI/GO solutions for reactive dyes removal. The obtained membranes showed 97.8% rejection of Blue Corazol (BC) dye with a PWP of 99.4 LMH/bar. Abdel-Karim et al. [82] reported that the use of poloxamine Tetronic (T904) as pore forming agent in PES/GO MMMs could significantly improve the pure water flux from 2 to 245 LMH/bar as well as the rejection of Acridine Orange (AO) dye (by 20%). However, the rejection of Sunset Yellow (SY) dye was 45% lower than the pristine PES membrane. Jiang et al. [105] assembled GO-TiO₂ nanocomposites on a porous PES substrate via the VAS technique and investigated its performance on MO dye removal as model organic matter. The GO-TiO₂-modified membranes showed better rejection of BSA and MO dye (82.6% and 26.4%, respectively) compared to bare PES

(<10% rejection of BSA and MO) with PWP of 246 LMH/bar. The rejection of most of these dyes is considered high for UF membranes due to their small molecular sizes. This indicates that the separation of these membranes is not only dependant on the molecular sieving and might be affected by additional interactions like the surface charge and adsorption-based mechanisms. Therefore, the reported GO-UF membranes can be used to separate various contaminants and to treat different types of wastewater.

Table 2-4: Summary of the recently developed GO-based UF membranes

Type	Method ^a	Membrane	Testing conditions		Membrane performance			Year & Ref.
			Feed compositions (ppm)	Pressure (bar)	PWP (LMH/bar)	Rejection % ^b	FRR % ^b	
MMM	NIPS	PES/CSGO	1000 ppm BSA	2	41.3	99.8	92.1	2020 [45]
MMM	NIPS	PBI/GO	1000 ppm oil	-	91.3	99.9	95.1	2020 [236]
MMM	NIPS	PVDF/GONRs	1000 ppm BSA	1	532	95	86	2020 [245]
MMM	NIPS	SPES/GO-SiO ₂ -NH ₂	100 ppm BSA, HA and SA	2	268.5	R _{BSA} =92.8±0.7 R _{HA} =97±0.4 R _{SA} =89.7±0.6	FRR _{BSA} =82 FRR _{HA} =91 FRR _{SA} =95	2020 [36]
MMM	NIPS	PVDF/GO-ZnO	500 ppm BSA	1	170.73	92	92.79	2020 [198]
MMM	NIPS	PVDF/PFSA-g-GO	500 ppm BSA and HA	1	587.4	R _{BSA} =93.9 R _{HA} =79.6	FRR _{BSA} =90.8	2020 [244]
MMM	NIPS	PVDF/QGO	1000 ppm dextran-500	1	1285	~80	FRR _{BSA} =85.6	2020 [246]
MMM	NIPS	PES/ZIF-8-GO	1000 ppm BSA	1	95.49	> 95	84.4	2020 [110]
MMM	NIPS	PSF/GO-TiO ₂	500 ppm BSA	3	165.4	96.6	75.8	2020 [247]
MMM	NIPS	PSF/GO	1000 ppm BSA	1	249.5	97.2	99	2020 [64]
MMM	NIPS	PVDF/GO-PEG	500 ppm BSA	1	93	> 94	78	2020 [248]
PRL	LBL	PES/PEI/GO	10 ppm BC dye	3	99.4	97.8	>80%	2019 [192]
MMM	NIPS	PSF/GFG	200 ppm BSA	1	217	95.2	82.4	2019 [100]
MMM	NIPS	PES/SPSF-GO	1000 ppm BSA	1	816.9	99.5	92.4	2019 [76]
MMM	NIPS	PSF/CGO	1000 ppm BSA	1	48.8±3.7	R _{BSA} = 100	FRR _{BSA} =76.3±	2019 [90]
			10 ppm MO			R _{MO} = 52.7±5	17	
PRL	VAS	PES/LIG/GO-GA	1000 ppm BSA	1	78±7	R _{BSA} =69±2	91	2019 [106]
			10 ⁻⁶ CFU/ml bacteria			R _{Bacteria} =99.9±0.1		
MMM	NIPS	PES/GO	10-100 ppm HA	1	340	94.5	~95	2019 [238]
MMM	NIPS	PVDF/TiO ₂ -GO	1000 ppm BSA	1	199.97	91.38	89.22	2019 [199]
MMM	NIPS	PVC/GO-ND	1000 ppm BSA	2	220	95.08	83.07	2019 [229]
MMM	NIPS	PSF/GOQD	500 ppm BSA	1	130.54	100	~ 85	2019 [249]
MMM	NIPS	PES/GO	1000 ppm BSA	1	245	R _{BSA} = 93.3	FRR _{BSA} = ~75	2018 [82]
			68 ppm SY dye			R _{SY} = 62.3		
			200 ppm AO dye			R _{AO} = 48.4		

Type	Method ^a	Membrane	Testing conditions		Membrane performance			Year & Ref.
			Feed compositions (ppm)	Pressure (bar)	PWP (LMH/bar)	Rejection % ^b	FRR % ^b	
MMM	NIPS	PSF/SGO	1000 ppm BSA	2	175.2	> 98		2018 [230]
PRL	VAS	p-PES/GO	100 ppm PEG (200 kDa)	0.7	70 ± 5	~ 95	FRR _{BSA} =93.9	2018 [250]
MMM	NIPS	PSF/GO	50 ppm Pb	1	50	98	-	2018 [86]
PRL	VAS	PVDF/rGO-SiO ₂ /PDA	10 ppm oil and MB dye	0.9	148	R _{MB} = 99.8 R _{oil} = 99.2	FRR _{MB} =79 FRR _{oil} =87	2018 [130]
MMM	NIPS	PVDF/SGO	500 ppm BSA		740	98	88.7	2017 [240]
PRL	VAS	CAC/rGO-PDA-g-C ₃ N ₄	10 ppm oil and 5 ppm MB dye	1	75	R _{oil} = 99.5 R _{MB} = 99.8	-	2017 [237]
PRL	VAS	PES/GO	10 ppm HA	3.5	77	85.3	89.5 ± 7.3	2017 [190]
PRL	Coating	PES-g-NH ₂ /GO	20 ppm HA	0.7	79	-	70	2016 [193]
PRL	VAS	PSF/GO	1000 ppm BSA	1.4	309.2		90.4±2.8	2016 [231]
MMM	NIPS	PVC/GO	1000 ppm BSA	1	430	91.2	70.4	2016 [83]
MMM	NIPS	G-PANCM1	10 ppm BSA	1	978 ± 27	85	-	2016 [232]
PRL	VAS	PES/GO-TiO ₂	7.5 ppm MO, 10 ppm BSA	1	246	R _{BSA} = 82.6 R _{MO} = 26.4	-	2015 [105]
MMM	NIPS	PES/GO-Ag	500 BSA ppm	3	143.3	R _{BSA} = 98	67.2	2015 [140]
MMM	NIPS	PES/Co ₃ O ₄ -GO	1000 ppm BSA	1	347.9	95	81.1	2015 [233]
MMM	NIPS	PVDF/GO	3000 ppm DOC	1	94.0	10	-	2015 [239]
MMM	NIPS	BPPO/GO-PEI	500 ppm BSA	2	532.5	91	63	2014 [194]
MMM	NIPS	PVDF/GO-APTS	1000 ppm BSA	1	401.39	57	> 95	2014 [104]
MMM	NIPS	PVDF/GO	1000 ppm BSA	1	100	85	90	2014 [75]
MMM	NIPS	PVDF/rGO-TiO ₂	500 ppm BSA	3	76	98.5±1.1	88.1	2014 [200]
MMM	NIPS	PVDF/GO-OMWCNT	1000 ppm BSA	1	410	-	98.28	2013 [201]
MMM	NIPS	PES/GO-HPEI	500 ppm (PEG 20000) and (PVA 30000-70000); 1000 ppm BSA	1	153.5	R _{PEG20,000} = 85 R _{PVA} = 90	FRR _{BSA} =92.1	2013 [234]
MMM	NIPS	PSF/GO-Isocyanate	1000 ppm BSA	1	135	95	40.27	2013 [235]
MMM	NIPS	PVDF/GO	100 ppm BSA	1	26.49	79	88.56	2013 [191]
MMM	NIPS	PSF/GO	-	1	450	99	-	2013 [251]
MMM	NIPS	PVDF/GO	1000 ppm BSA	1	382.15	91.8	95.15	2012 [252]

^a Method of GO incorporation

^b Rejection and FRR values are with respect to the feed specified in the "Feed compositions" column, unless it is specified with value itself.

2.5.4 GO-based MF membranes

Microfiltration (MF) is one of the oldest membranes processes applied commercially [253]. MF can efficiently separate wide range of micro-meter sized pollutants like proteins, large bacteria, suspended solids, pathogens, yeast and oil which make it a versatile process [254]. Several GO-based MF membranes were prepared in literature for the removal of oil, yeast, proteins, NOMs, bacteria, and turbidity. GO-MF membranes usually exhibit high removal efficiency oil removal (>99%) with varying flux depending on the synthesis method and the materials intercalated with GO. For example, a significant flux enhancement has been reported by Shao et al. [255] when assembling a mixture of sepiolite and GO (Sep-GO) as PRL on a PVDF MF membrane compared to the use of p-GO particles. The significant enhancement was related to the hierarchical nanostructure on PVDF surface and the expanded channel of mass-transfer resulted from the embedded Sep nanofibers between GO sheets. The Sep-GO-coated PVDF membranes showed good multifunctional water treatment efficiency as they exhibited high rejection of MB and CR dyes (>99%) and partial removal of Fe^{+3} and Cu^{+2} (68.7% and 65.3%, respectively). Sun et al. [256] fabricated an ultrahigh-flux membrane (>4550 LMH/bar) by the vacuum assembly of GO-SiO₂ dispersion on a MCE MF substrate. The modified membrane showed high separation efficiency (>99%) with variety of oil-water emulsion including dodecane, engine oil, gasoline and rapeseed oil. Zhao et al. [147] found that the intercalating of palygorskite nanorods (PGS) into free-standing GO membranes creates hierarchical nanostructure on the membrane surface, improves the hydration capacity and enlarges mass transfer channels. Therefore, GO-PGS composite membranes exhibited 7 times higher flux than the p-GO-based membranes with complete rejection of oil. Using p-GO particles, Hu and co-workers

[77] modified a commercial alumina MF membrane via the VAS technique. The modified membranes showed 27.7% higher PWP than the pristine membranes while retaining high oil rejection (98.7%).

Zhao et al. [257] proposed an integrated water treatment of microfiltration and visible-light-driven photocatalysis via assembling g-C₃N₄-rGO nanocomposite as a photocatalyst on a commercial CA MF membrane. The hybrid membranes were tested under the integrated conditions to treat surface water and showed better performance for the removal of COD, turbidity, TOC, and bacteria compared to their performance under MF filtration alone. GO-modified MF membranes were also found to have promising performance in the removal of radioactive materials from wastewater. Kim et al. [258] modified a commercial PES MF membrane with PEI-f-GO (PEI-rGO) and potassium copper hexacyanoferrate (KCuHCF) nanoparticles via VAS approach for cesium removal from wastewater. It was reported that PEI-rGO helped effectively to uniformly distribute KCuHCF nanoparticles in the composite and to increase the interlayer spacing of the laminar membrane structure which resulted in high PWP (>500 LMH/bar). Also, the hybrid membranes achieved a complete rejection of cesium because of the selective cesium adsorption properties of KCuHCF. Table 2-5 summarizes the types, fabrication methods, testing conditions and the performance of the recently reported GO-modified MF membranes.

Table 2-5: Summary of the recently developed GO-modified MF membranes

Type	Method ^a	Membrane	Testing conditions		Membrane performance			Year & Ref.
			Feed compositions (ppm)	Pressure (bar)	PWP (LMH/bar)	Rejection %	FRR %	
PRL	VAS	PES/Cu-PEI-rGO	1 ppm Cs ⁺	1	> 500	> 98	-	2020 [258]
PRL	Coating	APTS-Al ₂ O ₃ /GOQD	50 ppm (BSA and HA)	1	1827	-	94.6	2020 [195]
PRL	VAS	PVDF/Sep-GO	Oil-water emulsion, 10 ppm MB and 50 ppm CR dyes, 20 ppm Fe ⁺³ and 20 ppm Cu ⁺²	1	531.75	R _{Oil} = 99 R _{MB} = 99.2 R _{CR} = 99.2 R _{Fe} = 68.7 R _{Cu} = 65.3	-	2019 [255]
PRL	VAS	MCE/GO-SiO ₂	Oil-water emulsion 1:9	1	4550	99.3	-	2018 [256]
PRL	Coating	PVDF/PBSA/GO-P ⁺	1000 ppm BSA	2	791	-	95.5	2018 [259]
PRL	PAS	CA/g-C ₃ N ₄ NS/rGO	1.1 COD, 8.2 TOC, 1×10 ³ cfu.L ⁻¹ <i>Ecoli</i> , 2.6 NTU turbidity	1	957	R _{turbidity} = 84 R _{Ecoli} = 97 R _{COD} = 25 R _{TOC} = 21	81.12	2016 [257]
Free.std ^b	VAS	GO-PGS	1000 ppm oil	0.5	3734	99.9	93	2016 [147]
PRL	VAS	AL ₂ O ₃ /GO	1000 ppm oil	1	667	98.7	-	2015 [77]
MMM	NIPS	PVDF/PVP/GO	1000 ppm yeast	0.25	443	-	-	2014 [78]

^a Method of GO incorporation

^b Free.std: free-standing GO membrane.

2.5.5 GO-based FO membranes

Forward osmosis (FO) has gained an extensive attention recently because of its potential applications in the desalination sector [170]. FO is a concentration-driven membrane process that does not require hydraulic pressure making it more energy-efficient with lower fouling propensity than other membrane processes [260, 261]. Additionally, FO is capable to concentrate feed solution (FS) with a concentrated draw solution (DS) making it applicable to separate wide range of contaminants [262, 263]. In spite of its advantages, FO suffers from some drawbacks such as low permeability, concentration polymerization, and reverse solute flux (RSF) [264]. FO membranes can be operated in two orientations, active layer oriented towards feed solution (AL-FS) and active layer oriented towards draw solution (AL-DS). FO membranes exhibit higher flux in AL-DS mode [265], however, AL-FS mode is recommended to prevent the internal fouling [266]. GO and GO-based materials were applied in several studies to overcome these drawbacks and/or to improve the performance of FO membranes.

Like GO-RO and GO-NF membranes, GO-FO membranes are usually fabricated using IP, LBL, PAS or VAS techniques. A recent study by Saedi-Jurkuyeh et al. [160] was conducted on the embedding of GO into TFN-FO membranes through the IP technique for desalination and heavy metals removal. The TFN layer was formed on a PSF substrate using GO-MPD and TMC solutions. With low loadings of GO (0.008 wt%), the water flux increased by 174% compared to the TFC membrane and the specific reverse solute flux (SRSF) was slightly lowered to 0.03 g/L. The optimum membrane also showed high rejection rates (99.9, 99.7, and 98.3%) for Pb, Cd, and Cr, respectively. Akther et al. [267] investigated the effect of GO flakes size on the performance and morphology of TFC-FO membranes. The

authors reported that the embedding of small-sized GO flakes into the TFN layer resulted in thinner and more uniform PA layer, while the embedding of large GO flakes resulted in a defective PA layer as depicted in Figure 2-12. Therefore, the water flux was improved by 50% accompanied with 60% reduction in the SRSF, when reducing the GO flakes size from 1.06 to 0.01 μm^2 .

Shakeri et al. [164] synthesized polyoxometalate based open frameworks using quaternary graphene oxide (QGO) and blue lemon polyoxometalate (LGO-OFs) that were then embedded into the TMC organic phase during the IP reaction. The authors reported that the incorporation of 1000 ppm LGO-OFs improved the hydrophilicity and the morphology of PA layer and hence resulted in 188% increase in the water flux with no significant change in the SRSF. Rastgar et al. [197] proposed a new method of producing magnetically modified GO-TFN layers. GO/Fe₃O₄ nanocomposites were dispersed in the MPD aqueous phase and then deposited with TMC monomer via IP reaction under the exposure of magnetic field to form a magnetically modified PA layer. It was found that when using the optimal concentration (100 ppm) of GO/Fe₃O₄ with the magnetic field exposure, the flux was improved by 117.4% and 63.2% compared to the pristine TFC and TFN membranes prepared without magnetic field exposure, respectively. However, the magnetic-modified membranes exhibited higher RSF and SRSF. Jin et al. [33] fabricated TFN-based GO-FO membranes via the IP technique using GO-m-xylylenediamine (GO-MXDA) and TMC solutions for the separation of Na₂SO₄, MgCl₂ and trisodium citrate (TSC). It was found that the highest performance was achieved when using TSC as draw solute suggesting that the solute barrier has significant impact on the performance of FO membranes.

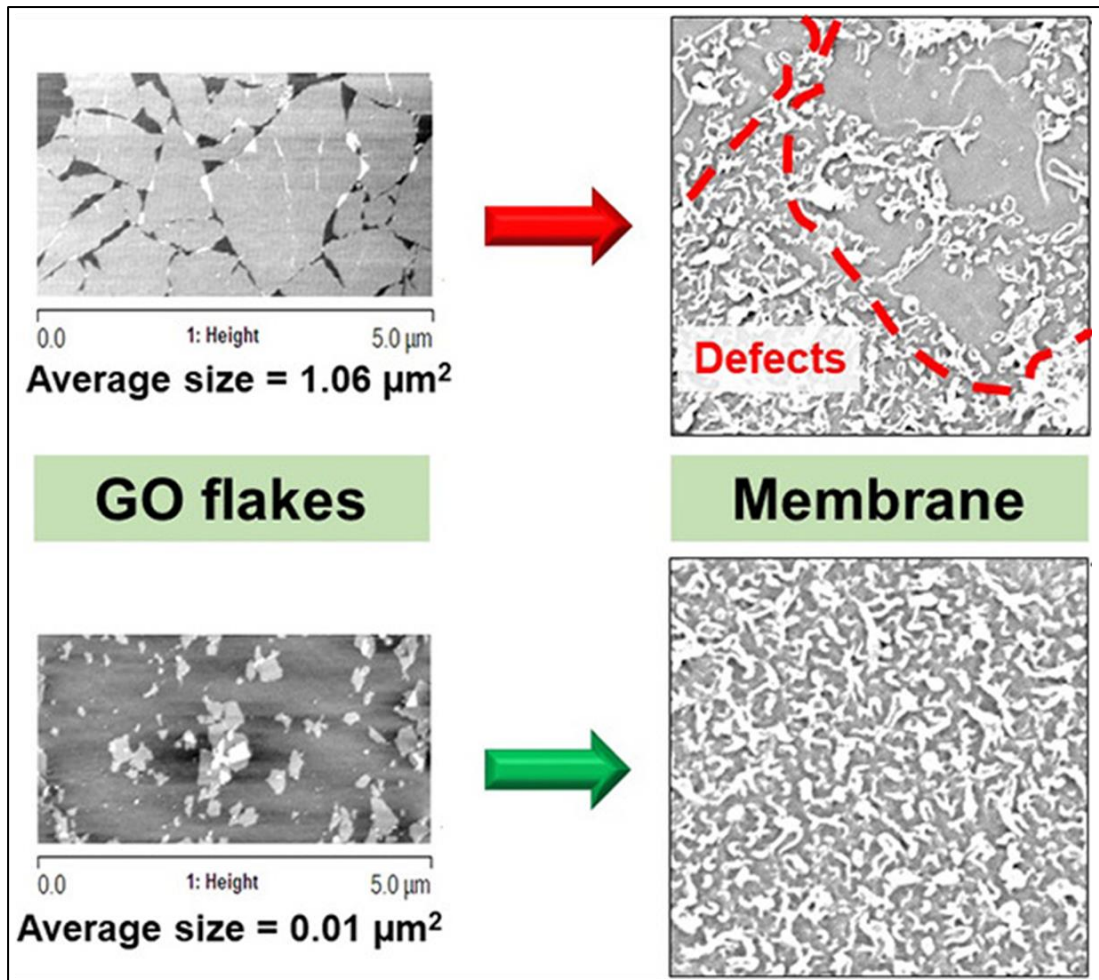


Figure 2-12: effect of GO flake size on the PA layer structure [267].

The performance of i-TFC-based GO-FO membranes was explored in several studies and showed comparable performance to the conventional TFN-FO membranes. Using the self-polymerization of dopamine, Choi and co-workers [132] deposited a GO-PDA interlayer on a PSF substrate followed by the IP reaction of MPD and TMC to produce i-TFC-based GO-FO membranes. At the optimum conditions (1 h coating time and 0.5 g/L GO concentration), the flux was improved by 57.6% with 75% reduction in the SRSF. For longer coating time, a significant reduction in the flux was observed because of pore blockage by GO and PDA. In a similar study, Zhao et al. [169] prepared i-TFC-FO membranes via the VAS assembly

of a GO-MWCNTs nanocomposite interlayer followed by the formation of PA layer via the IP technique. It was reported that the interlayer lowered the thickness of PA layer and provided ultrafast nanochannels for water transport. Therefore, the modified membranes exhibited 59% higher water flux and 45% lower SRSF compared to pristine TFC. The performance of TFC-FO membranes can be also improved by the incorporation of GO and GO-based materials into the polymer matrix prior to the formation of PA layer (m-TFC) [139, 171]. Using the NIPS approach, Park et al. [139] embedded p-GO particles into PSF matrix and the PA layer was then formed via IP technique. The authors reported a significant increase in the flux (255%) and 42% reduction in the RSF compared to pristine TFC. However, the addition of high concentrations of p-GO particles (≥ 0.5 wt%) resulted in poor structure and lower water flux which can be attributed to the presence of a tipping mass percentage of nanomaterial [240-242]. In a similar study, Wang et al. [171] embedded rGO-g-C₃N₄ into PES matrix via the NIPS technique followed by the PA layer formation. It was reported that the modified structure of PES resulted in 20% higher flux while the RSF increased by approximately 45% resulting in lower selectivity compared to the pristine TFC.

Several PRL-based GO-FO based membranes were developed in literature using PAS, VAS, and LBL approaches. Membranes having p-GO particles as PRL usually exhibit lower flux and higher SRSF than other FO membranes [268, 269]. This performance is ascribed to the presence of hydrophilic functional groups which make GO layer easily to swell and be delaminated in aqueous environment [270, 271]. Therefore, GO nanoparticles should be stabilized by crosslinking [271], chemical reduction [134, 146], mixing with other materials [153, 169, 272] or ion adjusting [273]. A recent study by Jang et al. [271] described the synthesis of FO

membranes having PRL of p-GO and EDA/PAAc-cross-linked GO assembled on a MCE substrate via the VAS approach. It was reported that membranes modified with GO/EDA/PAAc could overcome the trade-off between rejection and flux by improving the flux by 72% and reducing the RSF by 77% compared to membranes modified with p-GO. This performance was attributed to the hydrogen bonds between GO and PAAc with the anchoring of GO sheets by GO-EDA and EDA-PAAc covalent bonds. The resulted nanocomposite structure provided optimal condition for allowing the permeance of water molecules while blocking the hydrated salt ions. Kang et al. [153] found that when using PRL of GO-OCNTs nanocomposites instead of p-GO particles, the performance of PES-FO membranes can be significantly enhanced with different solutes. For example, the flux was enhanced by approximately 63% and 16%; and the SRSF was reduced by approximately 30% and 77% when using Na₂SO₄ and NaCl, respectively, as draw solutions. Using the VAS approach, Pang et al. [272] prepared two types of FO membranes using p-GO and GO-UiO-66 nanocomposite. It has been reported that the addition of UiO-66 to GO introduced uniform nanochannels that can effectively block the solute ions while allowing water molecules to pass. Therefore, FO membranes prepared with GO-UiO-66 nanocomposites achieved a higher flux (270%) and lower RSF (83.5%) than the membranes prepared with p-GO particles. Salehi et al. [274] prepared FO membranes via LBL assembly of negative p-GO nanoparticles and positive chitosan (CHS) and compared their performance with TFC membranes prepared using the same substrate (SPES-PES). The flux of CHS/GO-based membrane was 4 times higher than this of the pristine TFC membrane with lower SRSF. To stabilize the GO layer, Yang et al. [134] applied a chemical reduction of GO layer via the exposure to hydriodic acid vapor (HI) followed by dip-coating into PDA solution. It was found that the flux of

rGO membranes coated with PDA have 1.8 times higher flux and 50% lower RSF than uncoated membranes, which is attributed to the hydrophilic nature provided by PDA. Table 2-6 summarizes the types, fabrication methods, testing conditions and the performance of the recently developed GO-based FO membranes in literature.

Table 2-6: Summary of the developed GO-based FO membranes and their performance in AL-FS orientation.

Type	Method	Membrane	DS/FS	Membrane performance				Year & Ref.
				J_w (LMH)	RSF (GMH)	SRSF (g/L)	FRR %	
TFN	IP	PSF/PA/GO	2.0 M NaCl/DIW	34.3	1.1	0.03	FRR _{Heavy metals} =96	2020 [160]
TFN	IP	PSF/PA/GO	0.5 M NaCl/DIW	24.72	5.19	0.21		2020 [267]
PRL	VAS	MCE/GO-EDA-PAAc	1.0 M NaCl/DIW	34.9	7.01	0.2		2020 [271]
TFN	IP	PES/PA/LGO-OFs	1.0 M NaCl/DIW	34.7	11.9	0.34		2019 [164]
i-TFC	Coating	PSF/PDA-GO/PA	1.0 M NaCl/DIW	24.3	3.8	0.16		2019 [132]
PRL	PAS	PANI/GO	1.0 M NaCl/DIW	6.2	4.3	0.69	FRR _{SA} =98.8	2019 [268]
PRL	PAS	PES/GO	1.0 M NaCl/DIW	10.5	7.1	0.68	FRR _{SA} = 98.7	2019 [269]
PRL	LBL	PES/PDDA/GO-OCNTs	1.0 M NaCl/DIW	5.8	0.4	0.07		2019 [153]
			1.0 M Na ₂ SO ₄ /DIW	9.3	0.25	0.03		
PRL	VAS	Nylon/GO-UiO-66	2.0 M NaCl/DIW	29.16	12.86	0.44		2019 [272]
TFN	IP	PES/PA/GO-Fe ₃ O ₄	1.0 M NaCl/DIW	31.8	3.2	0.1	FRR _{SA} =95.7 FRR _{BSA} =96.4	2018 [197]
TFN	IP	PES/PA/GO	0.25 M TSC/DIW	13.2	25.8	1.96		2018 [33]
i-TFC	VAS	Nylon/GO-MWCNT/PA	1.0 M NaCl/DIW	17.24	3.73	0.22		2018 [169]
TFN	IP	PSF/PA/PVP-GO	2.0 M NaCl/10 mM NaCl	14.2	1	0.07		2017 [275]
PRL	LBL	SPES-PES/Chitosan/GO	1 M Na ₂ SO ₄ /DIW	52	4	0.08		2017 [274]
PRL	VAS	MCE/rGO/PDA	0.6 M NaCl/DIW	36.6	2.5	0.07		2017 [134]
TFN	IP	hPAN/PA/GO	0.5 M NaCl/DIW	~26	~2	0.08	FRR _{SA} >90	2016 [276]
m-TFC	IP	PSF-GO/PA	0.5 M NaCl/DIW	19.77	3.44	0.17		2015 [139]
m-TFC	IP	PES-rGO-g-C ₃ N ₄ /PA	2.0 M NaCl /DIW	41.4	9.35	0.23		2015 [171]

2.5.6 GO-based MD and PV membranes

Recently, membrane distillation (MD) and pervaporation (PV) attracted good attention as potential desalination processes. MD and PV are usually confusing because they are both thermal-driven membrane separation processes at which the membrane upstream side is in contact with hot feed liquid allowing specific components to permeate to the downstream side due to its lower vapor pressure. Also, in both processes the feed is heated to generate a vapor difference across the membrane [277]. However, there are key differences between the two processes like the role and type of the membranes used as well as the separation mechanisms occur in both processes, that were extensively discussed by Wang et al. [277].

MD separation relies on transport of vapor molecules through a porous hydrophobic membrane (0.1 to 1 μm) that is usually fabricated from PVDF, PSF, polyethylene (PE), polypropylene (PP), etc. GO-MD membranes are usually mixed matrix-based that are prepared via the NIPS technique. Commercial hydrophobic MF membranes can be also used for MD processes, however, they usually suffer from sub-optimal flux performance and pore wetting issues [278]. In a recent study, Camacho et al. [79] fabricated PSF/GO MMMs via the NIPS approach and evaluated their performance in direct contact membrane distillation (DCMD). The authors reported an improvement in the membrane porosity and pore size due to GO addition. However, at the optimum GO loading (1 wt%), the flux decreased by 22.7% with very slight enhancement in salt rejection compared to the pristine PSF. Unlike the other membrane processes, MD performs better with hydrophobic membranes due to the lower pore wettability. Therefore, GO is usually reduced or functionalized with different materials to avoid increasing the hydrophilicity and hence increasing the pore wetting of the membrane while improving the porosity and its mechanical

stability [279]. Abdel-Karim et al. [279] investigated the effect of GO reduction degree the performance of PVDF MMMs in air gap membrane distillation (AGMD) by incorporating rGO particles with different oxygen contents using the NIPS approach. It has been found that the oxygen content of the rGO have significant impact on the MD performance as well as the rGO content in PVDF. The optimum membrane (0.5 wt% rGO with 15.5% oxygen content) exhibited 170% higher flux than the pristine PVDF while maintaining high salt rejection (99.99%) and a stable performance during the long-time runs. Leaper et al. [109] compared the effect of p-GO and GO-APTS nanoparticles on the PVDF MMMs performance in AGMD. The results showed that GO-APTS exhibited 86% and 24% higher flux than the pristine PVDF and PVDF/GO, respectively, with 99.9% salt rejection which was attributed to the higher porosity of GO-APTS-based composite membranes. Zahirifar et al. [280] proposed a new method of dual-layer membrane fabrication by casting a smooth layer of PVDF-GO-ODA composite on PVDF substrate via the NIPS technique. The modified membranes showed significant increase in the surface roughness, hydrophobicity and salt rejection with 8% reduction in the flux compared to the unmodified PVDF. Additionally, the modified membranes showed lower thermal conductivity on the surface, which reduces the heat diffusion and temperature polarization across the membrane. In a similar way, a PVDF-GO mixture was immobilized on PTFE membrane surface which resulted in high performing membranes for for DCMD [281]. The PTFE/PVDF-GO composite membranes exhibited superior flux of 97 LMH and excellent stability under high salt concentrations and long-time runs. Lu et al. [37] reported a slight reduction in DCMD performance when embedding n-butylamine-f-GO (GO-NBA) into PVDF matrix. However, the PVDF/GO-NBA MMMs were found to have higher mechanical

properties than the pristine PVDF and PVDF/GO membranes due to the better crystallite structure and dispersibility of GO-NBA particles.

Regardless of its evolving in desalination sector, GO-PV membranes have been extensively used for the dehydration of organic solvents [282-289], separation of mixed organic mixtures [149, 290], and volatile organic compounds (VOC) removal from aqueous solutions [291]. As this review focuses on the GO-based membranes utilized in water treatment, only pervaporation desalination (PVD) is discussed herein. Unlike MD, PV generally requires a nonporous (dense) membranes where the permeation is mainly governed by solution-diffusion mechanism. Hence, the separation performance depends mainly on the diffusivity and solubility of feed components in the membrane and is not only dependent on molecular size like other membrane processes [292-294]. Additionally, hydrophilic membranes are preferred in PVD to increase the membrane's affinity to water molecules through hydrogen bonding, dipole-dipole interactions and ion-dipole interactions [143, 292, 295]. In a recent study, Sun et al. [296] prepared laminated GO membranes with remarkable performance in PVD and high stability under sonication destruction. p-GO sheets were first intercalated with PVA with different concentration and the composite solution was then assembled on a MCE substrate via the PAS technique followed by membrane crosslinking with GA (Figure 2-13). The microstructure and interlayer spacing of GO membranes were tailored by varying PVA content which showed clear impact on PVD performance. Using the VAS approach, Xu et al. [297] assembled p-GO and PDA-GO particles on a porous alumina membrane to study their performance and stability in PVD. The authors reported a weak stability of the membranes prepared using p-GO as it can be easily peeled off from the support during the runs. However, using PDA as a covalent linker significantly enhanced the stability of the

membrane while achieving good PVD performance (flux of 48.4 LMH and 99.7% NaCl rejection). Qian and co-workers [143] prepared CHS/GO MMMs using the simple casting/drying approach for PVD. The authors reported an improved hydrophilicity and mechanical stability caused by the GO embedding. The optimum performance was obtained with 1 wt% GO in CHS at 81 °C at which the flux was improved by 25% while maintaining high NaCl rejection (99.99%). Similar approach was conducted by Ugur Nigiz [81] to prepare SA/GO MMMs for PVD. The highest flux and rejection were 8.11 LMH and 99.41% that was obtained with 2 wt% GO at feed temperature of 60 °C. Table 2-7 compares the performance of the recently reported GO-based membranes for MD and PVD processes.

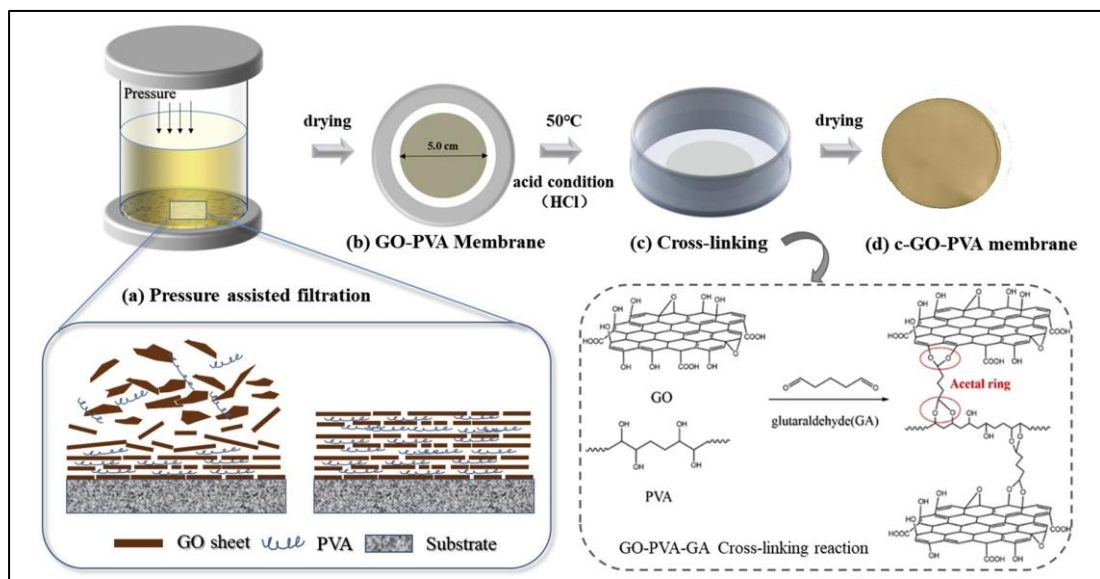


Figure 2-13: Illustration of laminate GO membrane fabrication (a) assembly of GO-PVA thin layer via the PAS technique, (b) GO-PVA drying, (c) membrane crosslinking with GA, and (d) the final membrane (c-GO-PVA) [296].

Table 2-7: Summary of the recently developed GO-based MD and PVD membranes and their performance

Type	Method	Membrane	Application	Conditions	Remarks	Year & Ref.
s-TFC	LBL	PA/PEI/GO	PVD	200,000 ppm NaCl, Na ₂ SO ₄ , MgSO ₄ and MgCl ₂ , Feed at 65 °C, flowrate =53.5 L/h	<ul style="list-style-type: none"> Flux= 8.4 LMH, R>99.9% Stable performance up to 220 h. 	2020 [80]
MMM	PAS	MCE/c-GO-PVA	PVD	10 wt% NaCl, feed at 85 °C, flowrate = 16 L/h	<ul style="list-style-type: none"> Flux= 98 LMH, R=99.99% High stability and resistance under sonication destruction 	2020 [296]
MMM	Cast/dry	SA/GO	PVD	3-7 wt% NaCl, feed at 60 °C.	<ul style="list-style-type: none"> Flux= 8.11 LMH, R=99.41% The mechanical and thermal properties were improved with GO addition. 	2020 [81]
MMM	NIPS	PSF/GO	DCMD	25,000 ppm NaCl, feed at 90 °C, permeate at 20 °C, flowrate 5.7 L/min	<ul style="list-style-type: none"> The optimum GO content in PSF is 1.0 wt% With the optimum membrane, Flux = 20.8 LMH and R=99.9% Membrane hydrophilicity decreased with GO addition. Mean pore size increased with GO addition. 	2020 [79]
MMM	NIPS	PVDF/rGO	AGMD	35,000 ppm NaCl, feed at 80 °C, permeate at 20 °C. flowrate 385 mL/min.	<ul style="list-style-type: none"> The optimum rGO content in PVDF is 0.5 wt% with 58% reduction degree. With the optimum membrane, Flux = 7 LMH and R=99.99% Stable performance up to 96 h 	2019 [279]
MMM	Cast/dry	CHS/GO	PVD	5 wt% NaCl, feed at 81 °C.	<ul style="list-style-type: none"> The optimum performance was obtained with 1 wt% GO in CHS, 81 °C and 5 wt% NaCl. At the optimum conditions, Flux = 30 LMH and R=99.99% Improved hydrophilicity with GO addition. 	2018 [143]
MMM	NIPS	PVDF/GO-APTS	AGMD	3.5 wt% NaCl solution, feed at 85 °C, permeate at 20 °C.	<ul style="list-style-type: none"> The optimum GO-APTS content in PVDF is 0.3 wt%. With the optimum membrane, Flux = 6.2 LMH and R=99.9% 	2018 [109]
MMM	NIPS	PVDF/GO-ODA	AGMD	3.5 wt% NaCl solution, feed at 60, 70, and 80 °C, permeate at 15 °C. flowrate 15 L/h	<ul style="list-style-type: none"> The optimum proportion of GO-ODA to PVDF is 5:3 With the optimum membrane, Flux = 16.7 LMH and R=98.3% Significant improvement in surface hydrophobicity and roughness and lower thermal conductivity compared to PVDF. 	2018 [280]

Type	Method	Membrane	Application	Conditions	Remarks	Year & Ref.
MMM	NIPS	PVDF/GO-NBA	DCMD	3.5 wt% NaCl solution, feed at 60 and 80 °C, permeate at 16 °C. flowrate 0.1 L/min	<ul style="list-style-type: none"> • The optimum GO-NBA content in PVDF is 0.5 wt% • With the optimum membrane, Flux = 61.9 LMH and R=99.9% 	2017 [37]
MMM	Casting	PTFE/GO-PVDF	DCMD	3500 – 34,000 ppm NaCl solution, feed at 60, 70, and 80 °C, permeate at 20 °C. flowrate 250 mL/min	<ul style="list-style-type: none"> • Flux = 97 LMH and R=99.9% • High stability under high salt concentrations and 90 days runs. 	2016 [281]
PRL	VAS	α -Al ₂ O ₃ /PDA/GO	PVD	3.5 wt% NaCl solution, feed at 90 °C	<ul style="list-style-type: none"> • Flux = 48.4 LMH and R=99.7% • High stability up to 336 h 	2016 [297]

CHAPTER 3: METHODOLOGY & EXPERIMENTAL WORK

3.1 Materials

Natural graphite flakes (-10 mesh, 99.9%) were obtained from Alfa Aesar, Germany. Sulfuric acid (H_2SO_4 , 95%), potassium permanganate (KMnO_4 , 99%), toluene ($\geq 99.5\%$) and polyvinylpyrrolidone (PVP, $\geq 95\%$) were purchased from Fisher Scientific. Phosphoric acid (H_3PO_4 , 85%), hydrogen peroxide (H_2O_2 , 30%), hydrochloric acid (HCl, 35 to 38%), Safranin O (SO, 350.88 Da), and Methyl Blue (MB, 799.81 Da) were purchased from BDH. Polysulfone (PSF, ~ 35 kDa), dopamine hydrochloride (DA), tris-(hydroxymethyl)aminomethane (Tris), humic acid (HA), bovine serum albumin (BSA, $\geq 96\%$, Mw ~ 66 kDa), Direct Red 80 (DR80, 1373.07 Da), Orange II sodium salt (ORII, 350.32 Da), ethanol ($\geq 99.8\%$), N,N-dimethylacetamide (DMA, $\geq 99\%$) and 1-methyl-2-pyrrolidinone (NMP, 99.5%) were obtained from Sigma Aldrich. Dodecane ($\geq 99\%$) and N,N-dimethylformamide (DMF, $\geq 99.8\%$) were obtained from Honeywell. Polysulfone substrate (PS-30) with 20 K molecular weight cut-off was purchased from Sepro Membranes, US. The deionized water (DIW) was produced using the ELGA PURELAB Option water purification system. All the chemicals were used as procured without further purification.

3.2 Synthesis of Graphene Oxide Nanoparticles

The laboratory synthesis of GO nanoparticles from graphite involves two steps: the oxidation of graphite to GO, followed by washing and purification of GO from impurities (acids, manganese salts, etc.). High-oxidation and NO_x -free synthesis of GO was carried out using several variations on the conventional Hummers' method [57] in the absence of NaNO_3 , and by varying the reaction temperature, time, and

reactant ratios [59]. Two groups of GO samples were synthesized by varying the reactant compositions and oxidation temperatures. The residence time within each group was also varied, as shown in Figure 3-1.

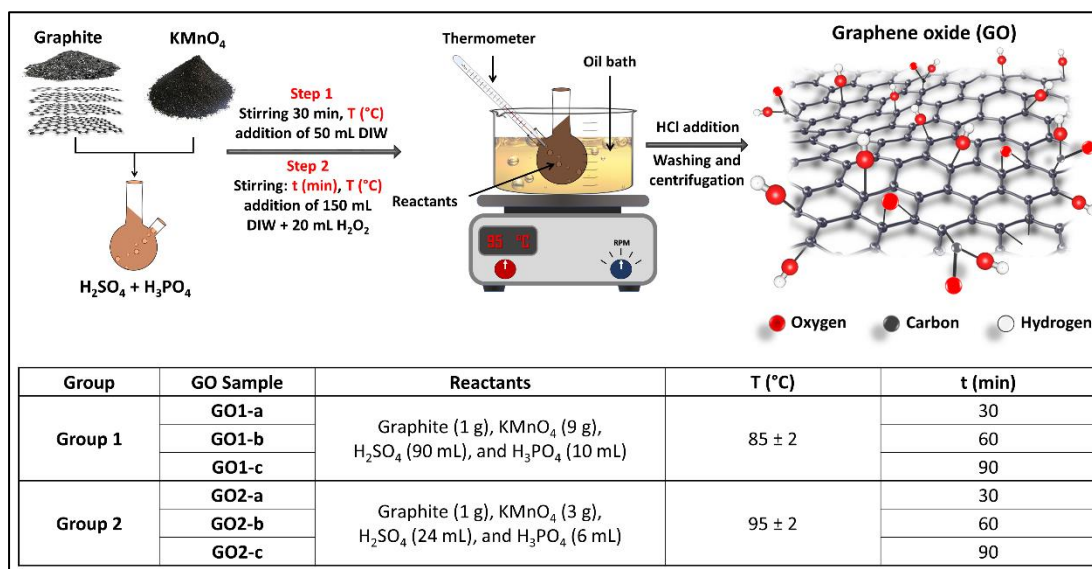


Figure 3-1: Schematic illustration of GO synthesis and the reaction conditions.

In brief, for group 1, sulfuric acid (H₂SO₄) and phosphoric acid (H₃PO₄) were mixed in a 9:1 volume ratio and stirred in an ice bath for several minutes. Graphite powder and KMnO₄ were slowly added to the mixing solution under stirring. The mixture was transferred to an oil bath at 85 ± 2 °C for 30 min. A total of 50 mL of deionized water (DIW) was added to the mixture, which was maintained under stirring at the same conditions for 30, 60, and 90 min for GO1-a, GO1-b, and GO1-c, respectively. The mixture was placed in an ice bath, and 150 mL of DIW and 20 mL of H₂O₂ were slowly added to terminate the reaction. An exothermic reaction occurred, and the solution was allowed to cool down.

Similar steps were conducted for group 2 with varying reactant compositions (Figure 3-1) and a reaction temperature of 95 ± 2 °C. The resulting solution was

diluted with 20% HCl solution and centrifuged using an Ohaus Frontier 5000 Series Multi Pro Centrifuge at 7500 rpm for 20 min. The supernatant was removed, and the residuals were washed several times with deionized water until a neutral pH was obtained. Finally, the prepared samples were dried in an oven at 80 °C for approximately 48 h.

3.3 Functionalization of Graphene Oxide with Polydopamine

The synthesized GO nanoparticles were characterized using several techniques as will be explained in Section 3.5 to investigate the properties and the oxidation degree of the obtained samples. The GO sample having the highest oxidation degree was then selected to be functionalized with polydopamine (PDA).

The amine functionalization of GO nanoparticles with PDA was performed via the temperature-assisted reflux method [67, 298]. Briefly, 100 mL of 10 mM Tris solution was prepared, and the pH was adjusted to 8.5 using HCl. 100 mg GO and 200 mg DA were dispersed in the Tris solution using a bath sonicator (SONREX DIGITEC DT 255 H, BANDELIN electronic, Germany) for 1 h. The GO-PDA suspension was stirred at 60 °C for 48 h in an oil bath under the reflux conditions. The functionalized nanoparticles were then washed and extracted by the solvent evaporation approach. The resulted product was in the form of fine powders and was dried under vacuum at 80 °C overnight. The amination of GO with PDA was reported in some studies to cause a partial reduction of GO [99, 237], therefore the functionalized GO sample was denoted as rGO-PDA. Figure 3-2 illustrates the functionalization reaction of GO and the anticipated chemical structure of rGO-PDA.

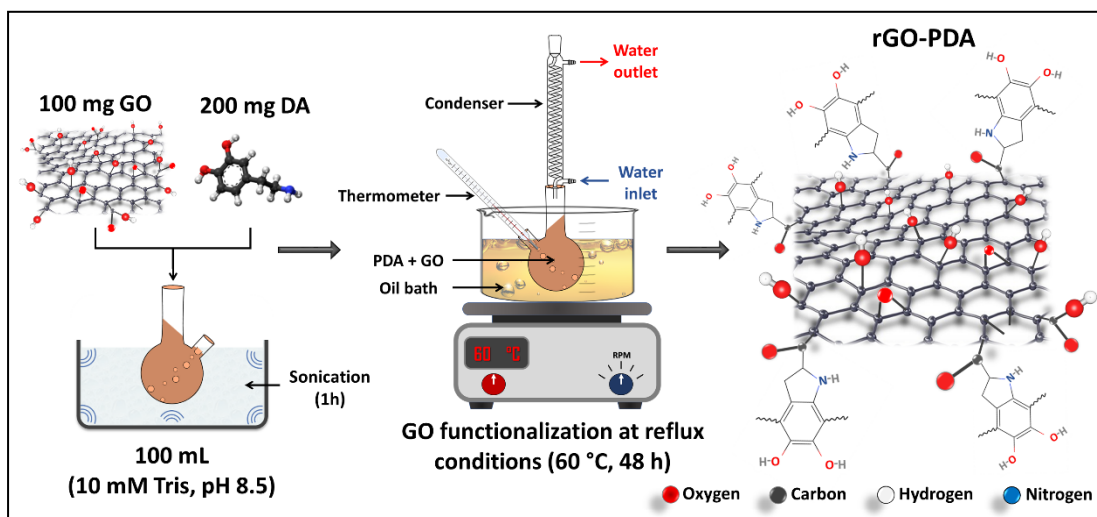


Figure 3-2: Illustration of the functionalization reaction of GO with PDA.

3.4 Fabrication of Mixed Matrix Membranes (MMMs)

The preparation of the pristine PSF, PSF/GO and PSF/rGO-PDA MMMs was conducted using the phase inversion technique described in Section 2.3.1 [90]. Briefly, a 17 wt% PSF in NMP was used as the casting solutions with PVP (3 wt% in NMP) as pores forming agent. First, two stock dispersions of GO and rGO-PDA in NMP were prepared with concentration of 0.5 mg/mL using an ultra-sonication bath for approximately 1 h to ensure well dispersion. Different concentrations of GO and rGO-PDA were then prepared (with respect to PSF) from the stock dispersions by dilution. GO-NMP and rGO-PDA-NMP suspensions were then stirred under room temperature. PVP and PSF were then loaded slowly to the solution and kept under stirring conditions overnight to allow complete dissolving of the polymer and uniform dispersion of the nanoparticles. The resulted well mixed solutions were then casted on a clean glass plate using an Elcometer 3700 doctor blade (Elcometer Ltd, UK). The casted membranes were then dipped into DIW bath after casting to allow ideal phase inversion. These membranes were then washed several times and stored in DIW until usage. Figure 3-3 illustrates the fabrication process of the pristine PSF and PSF

MMMs incorporating GO and rGO-PDA via the phase inversion technique. The notations and compositions of the prepared membranes are listed in Table 3-1.

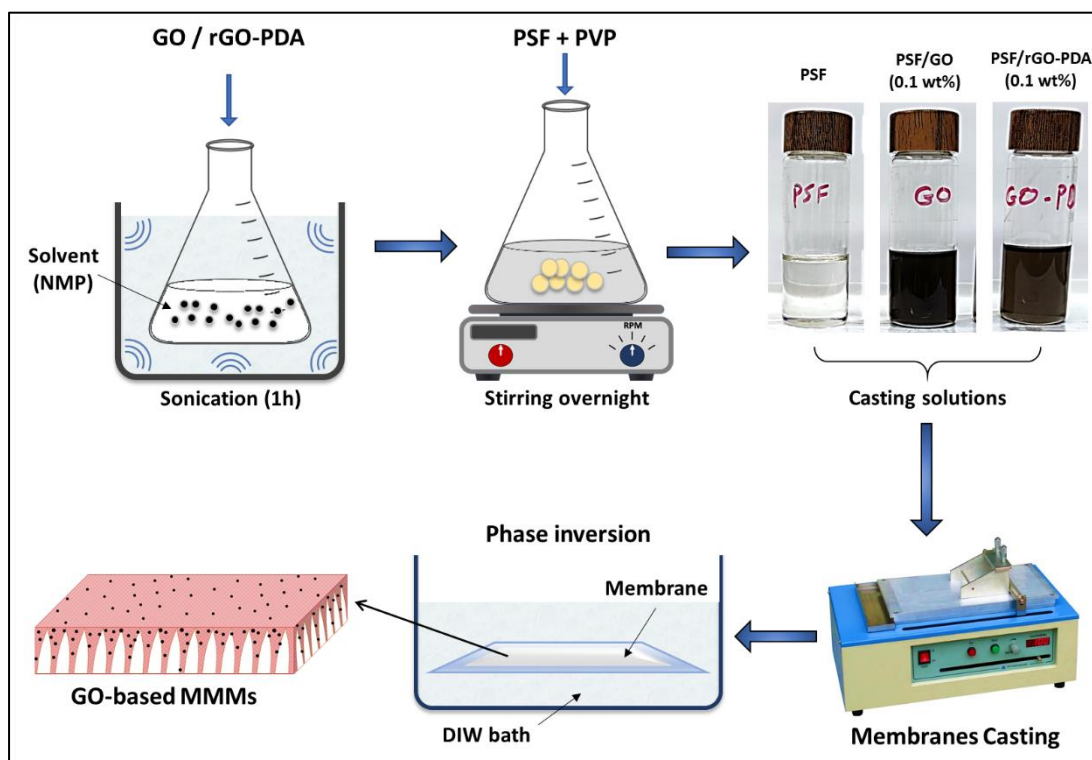


Figure 3-3: Illustration of the fabrication process of the pristine PSF, PSF/GO and PSF/rGO-PDA MMMs using the NIPS technique.

Table 3-1: GO and rGO-PDA compositions in the prepared membranes

Code	Membrane	PSF (g)	PVP (g)	NMP (mL)	Stock dispersion (mL)	GO (wt%)*	rGO-PDA (wt%)*
M ₀	PSF	5.53	0.975	25	0	-	-
M _{GO1}	PSF/GO-0.02	5.53	0.975	23	2 (GO)	0.02	-
M _{GO2}	PSF/GO-0.05	5.53	0.975	20	5 (GO)	0.05	-
M _{GO3}	PSF/GO-0.1	5.53	0.975	14	11 (GO)	0.1	-
M _{GO4}	PSF/GO-0.15	5.53	0.975	8	17 (GO)	0.15	-
M _{PDA1}	PSF/rGO-PDA-0.02	5.53	0.975	23	2 (rGO-PDA)	-	0.02
M _{PDA2}	PSF/rGO-PDA-0.05	5.53	0.975	20	5 (rGO-PDA)	-	0.05
M _{PDA3}	PSF/rGO-PDA-0.1	5.53	0.975	14	11 (rGO-PDA)	-	0.1
M _{PDA4}	PSF/rGO-PDA-0.15	5.53	0.975	8	17 (rGO-PDA)	-	0.15

* The compositions of GO and rGO-PDA are with respect to PSF weight.

3.5 Materials Characterization

3.5.1 Characterization of GO nanoparticles

The GO samples prepared in Section 3.2 were analyzed using several analytical techniques to investigate the effect of the oxidation conditions on the GO properties. An elemental analysis was conducted using a Thermo Scientific™ FLASH 2000 CHNSO elemental analyser. Fourier transform infrared spectroscopy-universal attenuated total reflectance sensor (FTIR-UATR) was performed in the range of 400–4000 cm^{-1} using a FTIR Perkin Elmer 2000. The FTIR analysis was carried out to investigate the surface functional groups of GO samples prepared under different reaction conditions. A quantitative analysis of the FTIR spectra was conducted to estimate the oxygen content and O/C ratio for comparison with the elemental analysis results [41]. The quantitative analysis was conducted as follows: the baseline spectra were subtracted from the raw spectra, and the resulting spectra were multiplied by (-1) to produce positive peaks that were then deconvoluted to Gaussian peaks for peak area estimation. The oxygen content and O/C ratio were estimated by calculating the ratio of all the oxygen related bands (ORB) to the total area of the spectra and to the area of C=C band using equations 1 and 2, respectively.

$$ORB\% = \frac{A_{ORB}}{A_{Total}} \times 100\% \quad (1)$$

$$O/C = \frac{A_{ORB}}{A_{C=C}} \quad (2)$$

The Raman spectra were recorded at room temperature using a DXR Raman spectrometer from Thermo Scientific equipped with a 532-nm laser and a 10× objective. The GO morphology was evaluated by scanning electron microscopy (SEM) with a JEOL model JSM-6390LV and transmission electron microscopy (TEM) with a FEI Talos200x. Prior to TEM analysis, the GO powder was dispersed in isopropyl alcohol and sonicated for approximately 15 minutes. A total of 20 μL of the

dispersed solution was dropped over a 300-mesh Cu grid and dried at room temperature. X-ray photoelectron spectroscopy (XPS) was performed over a 0–1200 eV range using a ThermoFisher ESCALAB 250i. Thermogravimetric analysis (TGA) was performed to evaluate the GO thermal stability using a PerkinElmer thermogravimetric analyser (Pyris 6 TGA) under nitrogen over a temperature range of 30–800 °C at a heating rate of 10 °C/min.

3.5.2 Characterization of rGO-PDA nanoparticles

The pristine GO and rGO-PDA nanoparticles were characterized using various characterization techniques to confirm the functionalization and to explore its effects on GO properties. CHNSO elemental analysis, FTIR-UATR spectra, Raman Spectra, SEM and TGA analysis were carried out using the same conditions and analysers described in Section 3.5.1. XPS measurements were conducted over a 0–1200 eV range on a Kratos AXIS Ultra DLD with Al-K α source and X-ray power of 15 Kv and 20 mA. X-ray diffraction analysis (XRD) measurements were carried out using EMPYREAN PANalytical diffractometer, Netherlands, equipped with a Cu-K α radiation source ($\lambda = 1.5406 \text{ \AA}$). TEM analysis was carried out using a FEI Tecnai F20 (200kV).

Additionally, to investigate their dispersion properties, the pristine GO and rGO-PDA were dispersed in DIW and different organic solvents including, hexane, DMA, DMF, dodecane, toluene, and NMP. The dispersion tests were performed in an ultrasonic bath for 2 h at room temperature and a concentration of 0.5 mg/mL.

To investigate the hydrophilic properties of the pristine GO and rGO-PDA, both samples were deposited on a PS-30 substrate using the pressurized assisted self-assembly (PAS) approach described in Section 2.3.2 [268]. In brief, two stock

dispersions containing 0.02 mg/mL of GO and rGO-PDA particles in DIW were first prepared using an ultrasonic bath sonicator for 2 h to ensure a good dispersion of the nanoparticles. 50 mL of the stock solution was then transferred to a dead-end membrane cell (Sterlitech, US) with effective membrane area of 14.6 cm². The cell was then pressurized with 4 bar of nitrogen gas to force the water to pass through the substrate while the nanoparticles are being assembled. The nanoparticles composition in the obtained membranes is 1 wt% with respect to the effective area of PS-30. The obtained membranes were then dried in an oven at 50 °C. Figure 3-4 illustrates the PAS technique for PS/GO and PS/rGO-PDA membranes preparation. The hydrophilicity of the pristine and the coated membranes was then explored using the OCA15 Pro contact angle analyzer (DataPhysics, Germany). The contact angle measurements were carried out at room temperature and using a DIW droplet of 2 μm at different points of each membrane sample (minimum of 10 points) and the average contact angle value was then calculated.

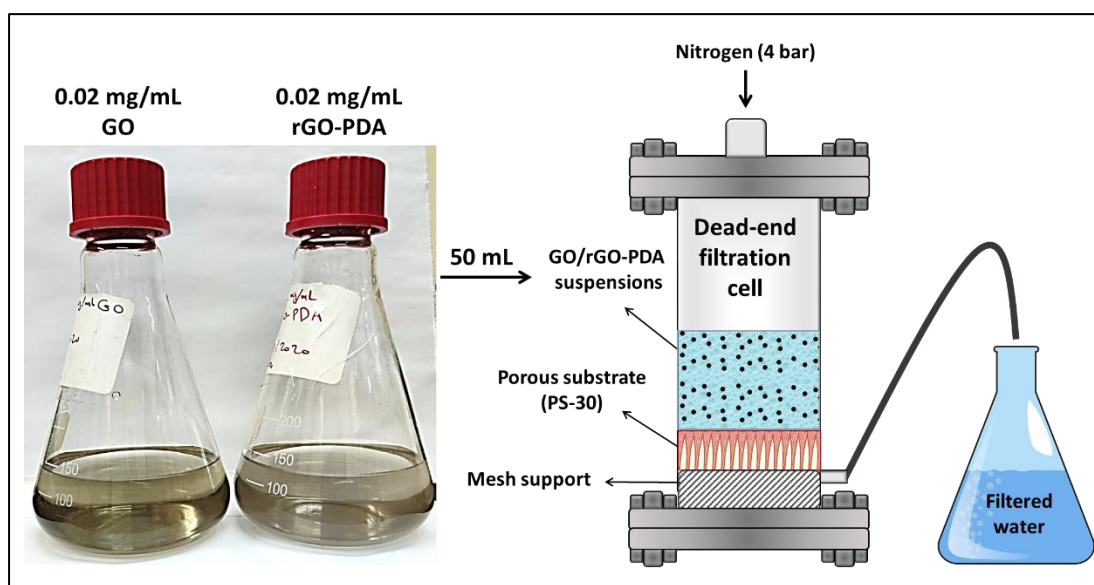


Figure 3-4: Illustration of the GO/rGO-PDA assembly using the PAS technique.

3.5.3 Characterization of the membranes

Different characterization techniques were performed on the pristine PSF and MMMs to explore the effect of GO and rGO-PDA incorporation on the structural and morphological properties of PSF. FTIR-UATR spectra were determined to investigate the change in surface chemical structure. Cross-section and surface SEM images were obtained at different magnifications. To prepare the cross-section samples, the freeze-fracturing method was used to avoid the deformation of the membrane structure by freezing the prepared membranes in liquid nitrogen and breaking them immediately [299]. Atomic force microscopy (AFM) measurements were conducted using (AFM-MFP-3D, Asylum Research) over $10 \times 10 \mu\text{m}$ scan area with a scan rate of 1 Hz. The hydrophilicity of the prepared membranes was investigated using DataPhysics contact angle analyzer (OCA15 Pro, Germany). Minimum of 15 points of each sample were tested using DIW droplet of $2 \mu\text{m}$ at room temperature and the average CA value were recorded. The viscosity of the dope solutions was measured at room temperature (Anton Paar Rheometer Model MCR 302) to investigate the effect of GO and rGO-PDA embedding on the casting solution viscosity.

The overall porosity (ε) of the prepared membranes was determined using the gravimetric method as described by Eq. 3 [90]:

$$\varepsilon = \frac{w_w - w_d}{A \times l \times \rho_w} \quad (3)$$

Where w_w is the weight of the wet membrane (g), w_d is the weight of the dry membrane (g), A is the surface area of the membrane (cm^2), l is the membrane thickness (cm) determined from the cross-section SEM (Figure B1 in Appendix B), and ρ_w is the water density at $23 \text{ }^\circ\text{C}$ (0.998 g cm^{-3}). The mean pore size (r_m) was then determined using the Guerout-Elford-Ferry equation (Eq. 4) [104, 240]:

$$r_m = \sqrt{\frac{(2.9 - 1.75\varepsilon) \times 8\eta l Q}{\varepsilon \times A \times \Delta P}} \quad (4)$$

Where η is the water viscosity at 23 °C (9.3×10^{-4} Pa.s), Q is the permeate flow rate ($\text{m}^3 \cdot \text{s}^{-1}$), and ΔP is the operational pressure (Pa).

3.6 Permeability & Separation Experiments

The separation performance and antifouling properties of the prepared membranes were studied using a commercial cross-flow membrane apparatus (Sterlitech Corp, US) equipped with a temperature control system. Flux (J_w , LMH), pure water permeability (PWP, LMH/bar) and rejection (R%) were calculated using equations 5, 6, and 7, respectively [114, 300].

$$J = \frac{V}{A \cdot t} \quad (5)$$

$$PWP = \frac{Q}{\Delta P \cdot A} \quad (6)$$

$$R(\%) = \left(1 - \frac{C_p}{C_f}\right) \times 100 \quad (7)$$

Where V is the permeate volume (L), A is the effective membrane area if the membrane (m^2), t is the operating time (h), Q is the volumetric flowrate of the permeate ($\text{L} \cdot \text{h}^{-1}$), ΔP is the trans-membrane pressure difference, C_p and C_f are the solute concentration in the permeate and feed respectively.

The rejection properties of the prepared membranes were evaluated using different dyes including Safranin O (SO), Orange II sodium salt (ORII), Methyl Blue (MB) and Direct Red 80 (DR80). Table 3-2 lists the chemical formulas and molecular weights of BSA, HA, and dyes used in separation measurements. In brief, the membrane was compacted with DIW at 4 bar for 30 min. The pressure was then reduced to 1 ± 0.1 bar with cross-flow velocity of $46.1 \pm 0.3 \text{ cm} \cdot \text{s}^{-1}$. The dyes rejection tests were then performed at gage pressure of 1 bar and the same cross-flow velocity for 1 h with 25 ppm dye concentration in the feed. The concentrations of feed and permeate, C_f and

C_p , were measured using UV-VIS spectrophotometer (UV-2700, Shimadzu) at wavelengths of 520, 485, 600, and 528 nm for SO, ORII, MB, and DR80, respectively. Figure 3-5 illustrates the process flow diagram of the cross-flow membrane unit used during this study.

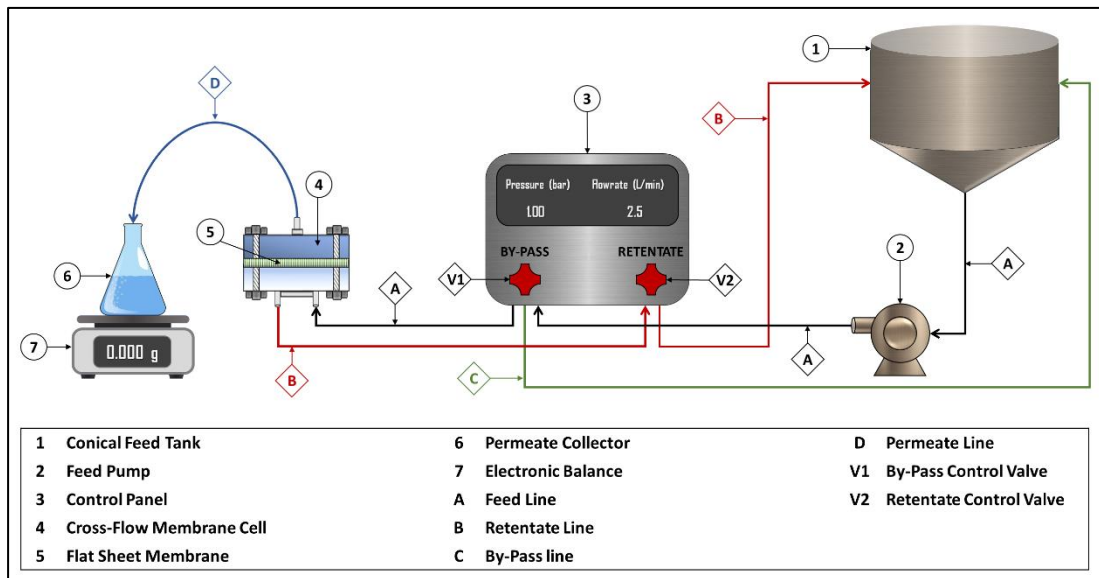
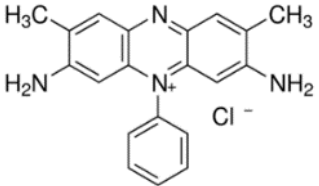
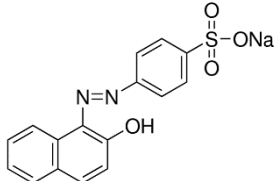
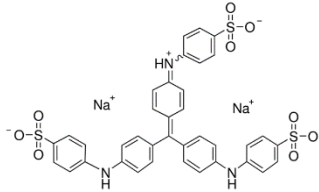
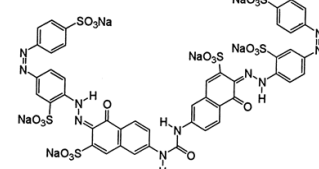


Figure 3-5: Process flow diagram of the cross-flow membrane unit.

Table 3-2: Chemical formulas, structures and molecular weights of chemicals used for separation and fouling measurements.

Material	Chemical formula	Structure	M _w (DA)
Bovine serum albumin (BSA)	C ₁₂₃ H ₁₉₃ N ₃₅ O ₃₇	-	~ 66,000
Humic acid (HA)	C ₁₈₇ H ₁₈₆ O ₈₉ N ₉ S ₁	-	2,000 - 500,000
Safranin O (SO)	C ₂₀ H ₁₉ N ₄ Cl		350.88
Orange II sodium salt (ORII)	C ₁₆ H ₁₁ N ₂ NaO ₄ S		350.32
Methyl Blue (MB)	C ₃₇ H ₂₇ N ₃ Na ₂ O ₉ S ₃		799.81
Direct Red 80 (DR80)	C ₄₅ H ₂₆ N ₁₀ Na ₆ O ₂₁ S ₆		1373.07

3.7 Dynamic Fouling Experiments

Antifouling properties of the prepared UF membranes were investigated using 500 mg/L BSA and 25 mg/L HA as the model foulants representing protein and natural organic matters (NOMs) fouling (each foulant was studied separately). Three dynamic fouling cycles were conducted for each membrane. In brief, the membrane was compacted with DIW at 4 bar for 30 min. The pressure was then reduced to 1 ± 0.1 bar with cross-flow velocity of 46.1 ± 0.3 cm.s⁻¹ and the steady pure water flux was recorded (J_{w0}). The feed is then shifted to freshly prepared foulant solution at the same pressure and cross-flow velocity for 1 h and the foulant flux (J_{wf}) was then

recorded. After foulant filtration, the membrane was washed two times with DIW at the same cross-flow velocity without applied pressure for 30 min. Finally, the feed is shifted to pure DIW at 1 bar and the steady flux was recorded (J_{w1}). The total fouling ratio (R_t), flux recovery ratio (FRR), the reversible fouling ratio (R_r) and the irreversible fouling ratio (R_{ir}) were estimated using the equations 8 to 11, respectively [115]:

$$R_t(\%) = \frac{J_{w0} - J_{wf}}{J_{w0}} \times 100 \quad (8)$$

$$FRR(\%) = \frac{J_{w1}}{J_{w0}} \times 100 \quad (9)$$

$$R_r(\%) = \frac{J_{w1} - J_{wf}}{J_{w0}} \times 100 \quad (10)$$

$$R_{ir}(\%) = \frac{J_{w0} - J_{w1}}{J_{w0}} \times 100 \quad (11)$$

The second and third cycles were conducted by repeating the same steps of cycle 1, and the corresponding FRR_x was recorded for each cycle, where x is the cycle number. The concentrations of BSA and HA in the feed and permeate, C_f and C_p , were measured using UV-VIS spectrophotometer (UV-2700, Shimadzu). BSA concentration was measured at 278 nm [301], while HA concentration was measured at 254 and 280 nm [238]. All separation and antifouling experiments were performed at room temperature (23 ± 0.5 °C). Minimum of three samples of each membrane were tested and the average value was taken for all performance and fouling parameters. Table 3-3 summarizes the measurements and analyses performed for GO nanoparticles from the improved Hummers' method, pristine GO and rGO-PDA nanoparticles, and the prepared membranes.

Table 3-3: Summary of the measurements and characterization performed on GO, rGO-PDA nanoparticles and the prepared membranes.

Measurement/characterization	GO samples	rGO-PDA	Membranes
FTIR-UATR	✓	✓	✓
Raman spectroscopy	✓	✓	
XRD		✓	
XPS	✓	✓	
CHNSO	✓	✓	
TGA	✓	✓	
SEM	✓	✓	✓
TEM	✓	✓	
AFM			✓
Dispersibility		✓	
Contact angle		✓	✓
Porosity and mean pore size			✓
Permeability and separation			✓
Antifouling properties			✓

CHAPTER 4: RESULTS & DISCUSSION

This chapter presents and discusses the outcomes and results of each phase of the research. Section 4.1 discusses the characterization results of the GO samples prepared in the first phase. A comprehensive analysis on the pristine GO and rGO-PDA characterization is presented in Section 4.2. Section 4.3 discusses the characterizations of the prepared membranes. The separation performance and the antifouling properties of the prepared membranes are then discussed in Sections 4.4 and 4.5, respectively. Finally, Section 4.6 compares the membranes prepared in this work with other GO-based UF-MMMs reported in the literature.

4.1 Characterization of GO Nanoparticles

4.1.1 Morphology and chemical compositions

SEM images of the prepared GO particles at different magnifications are presented in Figure 4-1. The images show different GO sample morphologies resulted from varying the reaction conditions. All GO samples have wrinkled surfaces with folded regions which is attributed to the formation oxygen-containing functional groups and Sp^3 carbons in the basal planes [70]. The GO samples were found to have separated graphitic layers with different separation levels, which is also attributed to the difference in oxidation level. Separated graphitic layers in GO result from a high oxygen content and the intercalation of oxygen atoms between graphene sheets [66].

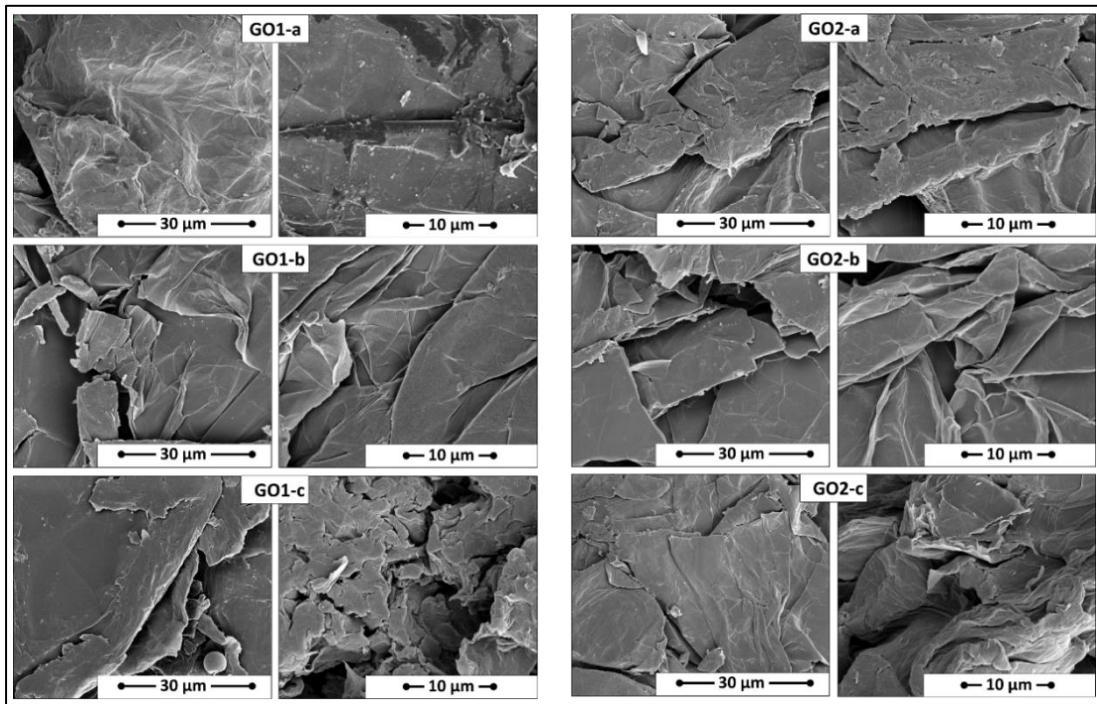


Figure 4-1: SEM images of the prepared GO samples.

The TEM images in Figure 4-2 show different stacking levels of GO sheets, which affect the transparency of the GO flakes. The comparatively high amount of sheet stacking in GO1-a and GO1-c results in opaque and dense flakes. GO1-b exhibits two morphologies, corresponding to dense and transparent regions. By contrast, GO2-a, GO2-b, and GO2-c exhibit comparatively lower levels of stacking, resulting in highly transparent sheets. The more wrinkled sheets of GO1-c and GO2-a indicate the presence of oxygen functional groups and a higher oxidation level than for the other samples [41, 70].

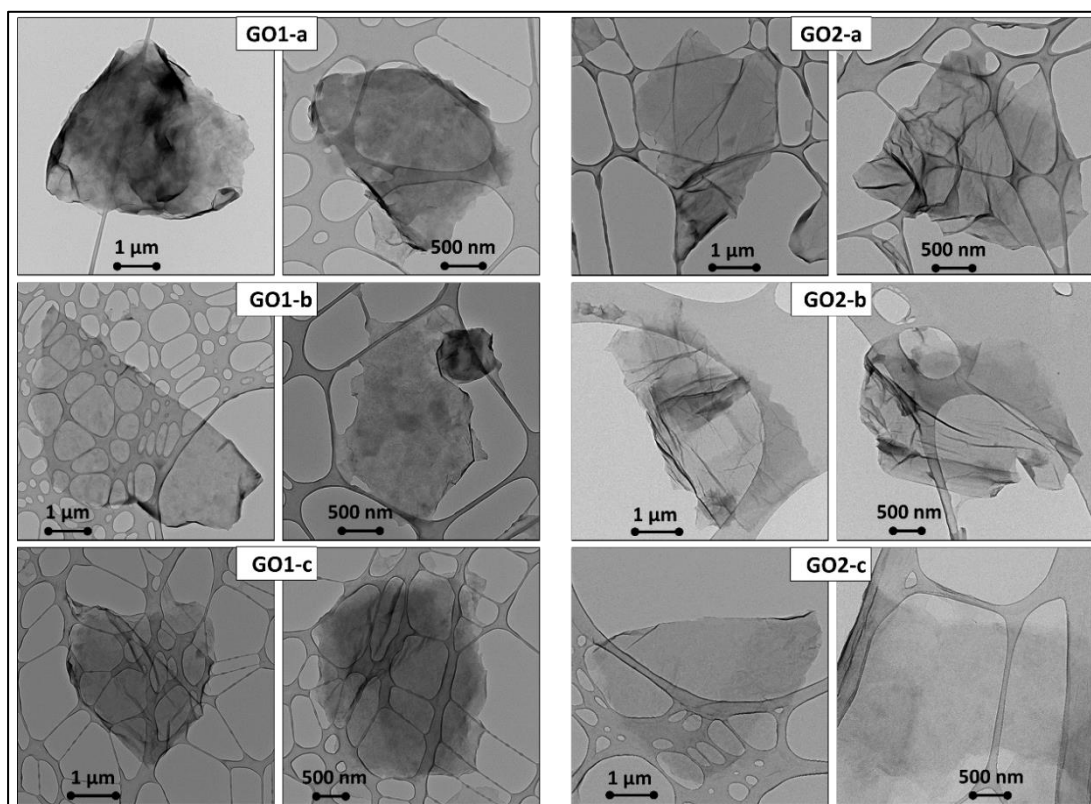


Figure 4-2: TEM images of the prepared GO samples

The elemental compositions of the prepared GOs, as determined by the CHNSO elemental analysis, are listed in Table 4-1. The oxygen content of the prepared GO ranged between 34.7 and 50 wt%. For group 1, the highest oxygen content was recorded for GO1-c (45.2 wt%). This result suggests that for the ratio of graphite to the other reactants (0.5 wt%) and temperature (85 °C) used to prepare GO1-c, the oxidation degree increased with the reaction time. However, for group 2, which had a high ratio of graphite to the other reactants (1.7 wt%), the highest oxygen content and O/C ratio were obtained for the shortest reaction time (GO2-a). Muzyka et al. [66] reported similar result, that is, the highest oxygen content (41.4 wt%) was obtained for 2 hr of oxidation and decreased to 21.1 wt% for a reaction time of 72 hr.

The samples with the highest oxygen contents of the prepared GOs, GO1-c and GO2-a, also exhibited the highest O/C atomic ratios (0.65 and 0.8, respectively).

This result suggests that a high graphite composition in the reactants at high temperature produces a good degree of oxidation in a short time, as in the case of GO2-a. The results of the elemental analysis are also in good agreement with observations of TEM analysis where GO1-c and GO2-a samples were found to have more wrinkled sheets indicating higher level of oxidation than other samples.

Table 4-1: Elemental compositions of GO samples from CHNSO analysis

Sample	Weight composition (wt%)					Atomic composition (at.%)					
	N%	C%	H%	S%	O%	N%	C%	H%	S%	O%	O/C
GO1-a	0.3	54.6	2.4	0.2	42.6	0.2	47.4	24.6	0.1	27.7	0.59
GO1-b	1.9	60.5	2.7	0.2	34.7	1.3	50.1	26.9	0.1	21.6	0.43
GO1-c	0.2	51.9	2.5	0.0	45.2	0.2	44.7	25.9	0.0	29.2	0.65
GO2-a	0.3	46.8	2.6	0.3	50.0	0.2	40.3	27.1	0.1	32.3	0.80
GO2-b	0.4	58.1	1.8	0.2	39.5	0.3	53.2	19.4	0.1	27.1	0.51
GO2-c	0.0	56.1	1.9	0.0	41.9	0.0	50.6	20.9	0.0	28.4	0.56

XPS spectra were recorded to investigate the chemical states, the nature of the functional groups and the surface elemental compositions of the synthesized GOs. The complete XPS surveys of all the GO samples in Figure 4-3 show the presence of C 1s and O 1s core-levels in all the samples. The functional groups were further analysed by deconvoluting the C 1s and O 1s core-levels of the XPS spectra, as illustrated in Figure 4-4. The deconvolution of the C 1s region of all the GO samples resulted in four peaks at binding energies of ~284, 286, 289, and 290 eV, corresponding to C=C/C—C, C—O, C=O, and COOH, respectively. These functional groups have been reported in several studies in the literature [60, 61, 66, 302]. Following study [70], the O 1s region of the XPS spectra was similarly deconvoluted into four main peaks at ~530, 532, 533, and 536 eV, corresponding to O—C=O, C=O, C—O, and C—O—C, respectively.

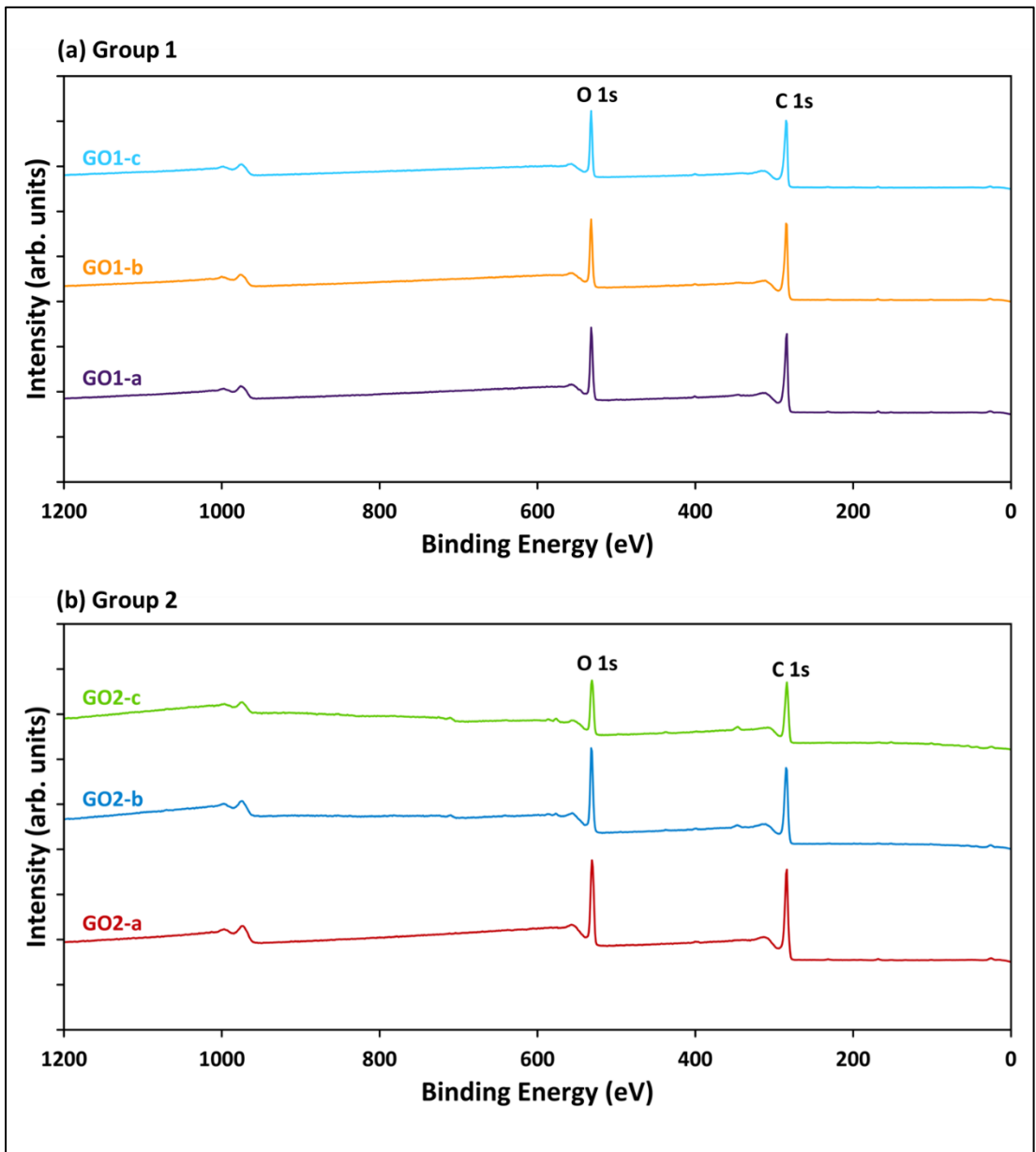


Figure 4-3: XPS survey spectra of the prepared GO samples.

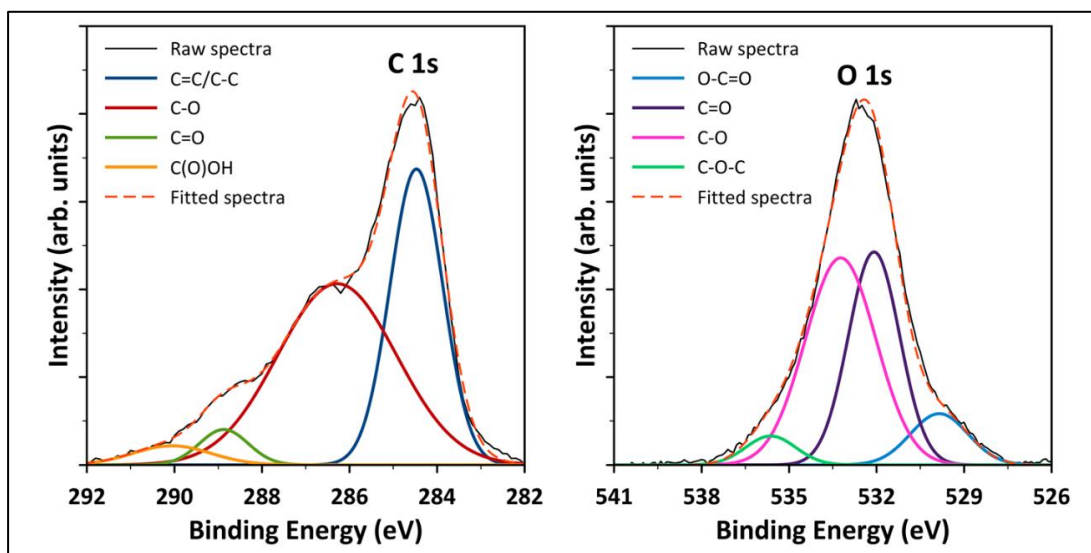


Figure 4-4: Deconvolution of C 1s and O 1s core-level XPS spectra of GO1-a.

Table 4-2 shows the surface elemental compositions obtained from the XPS analysis. In comparison to the elemental compositions obtained from CHNSO, carbon is clearly overestimated in all the tested samples. This observation has been previously reported in some studies [60, 66, 70, 303]. The elemental compositions obtained from XPS and CHNSO differ because XPS only provides information on the elemental distribution on the surface and represents only the area surveyed [304], whereas the CHNSO analysis provides information about the bulk sample [305, 306].

Table 4-2: Elemental compositions of GO samples from XPS analysis

Sample	Elemental analysis (at.%)				
	C 1s	O 1s	N 1s	S 2p	O/C
GO1-a	63.16	34.27	0.56	1.17	0.54
GO1-b	80.1	19.1	0	0.8	0.24
GO1-c	66.2	31.65	0.73	1.43	0.48
GO2-a	65.27	33.89	0.57	0.27	0.52
GO2-b	70.98	27.11	0	1.9	0.38
GO2-c	66.53	33.04	0.32	0.1	0.50

Table 4-3 is a comparison of the oxidation conditions, reactants and O/C atomic ratios of the GO prepared in this study with results from the literature. A higher oxidation degree of GO (i.e., for GO2-a) was obtained in this study than in the literature. Thus, the experimental conditions clearly affect the GO properties. The graphite characteristics also affect the GO properties. Hou et al. [69] investigated the effect of oxidant, intercalator, and graphite flakes size on GO properties. It was found that the oxidation level increases with the increase of both oxidant and intercalator. Further, the authors reported that the use of excessive amount of NaNO_3 reduces the oxidation level. In a similar study, Chen et al. [56] investigated the effect of the properties of the starting graphite material on the GO characteristics. It was found that GO prepared from small graphite flakes had a higher O/C ratio than that prepared from large graphite flakes. Similar oxygen contents and O/C ratios were obtained in this study as by Al-Gaashani et al. [70], although different oxidation conditions were used. This result is related to the type and characteristics of graphite, because Al-Gaashani et al. used a similar type of graphite as that used in this study (-10 mesh, 99.9%, Alfa Aesar, Germany). Hence, GO characteristics are determined by the graphite properties and the experimental conditions.

In terms of cost, compared to high-oxidation-degree GO in literature, GO2-a was produced with lower cost with respect to the amount of acids used or the reaction time. For example, Al-Gaashani et al. [70] used 100 ml acid per 1 g of graphite for 3 h reaction to produce GO with O/C of 0.7. However, GO2-a (O/C = 0.8) was produced with 30 ml acids per 1 g of graphite in 1 h reaction. Muzyka et al. [66] produced high-oxidation-degree GO (O/C = 0.74) with low amount of acids (30 ml per 1 g of graphite) with the use of NaNO_3 which results in NO_x formation and release during the reaction. Therefore, the method used in this work can be considered cost effective

and NO_x-free for production of large quantities of high-oxidation-degree GO particles.

Table 4-3: Comparison of experimental conditions and O/C atomic ratio of GO prepared in this study with literature values

Reactants	T (°C)	t (h)	O/C	Ref.
Gr (100 g); KMnO ₄ (100 g); NaNO ₃ (50 g); H ₂ SO ₄ (2.3 L)	98	0.75	0.44	[57]
Gr (1 g); KMnO ₄ (3 g); H ₂ SO ₄ (23 mL)	95	0.75	0.50	[56]
Gr (1 g); KMnO ₄ (3 g); H ₂ SO ₄ (20 mL); HNO ₃ (15 mL)	25	24	0.69	[66]
Gr (1 g); KMnO ₄ (3 g); NaNO ₃ (3 g); H ₂ SO ₄ (30 mL)	25	2	0.74	
Gr (7.5 g); KMnO ₄ (45 g); NaNO ₃ (7.5 g); H ₂ SO ₄ (360 mL)	35	3	0.56	[68]
Gr (1 g); KMnO ₄ (3 g); NaNO ₃ (0.75 g); H ₂ SO ₄ (23 mL)	98	3	0.20	[41]
Gr (1 g); KMnO ₄ (6 g); H ₂ SO ₄ (46 mL)	98	1	0.59	[67]
Gr (1 g); KMnO ₄ (6 g); H ₂ SO ₄ (46 mL)	95	6.5	0.37	[69]
Gr (1 g); KMnO ₄ (6 g); NaNO ₃ (2 g); H ₂ SO ₄ (46 mL)	95	6.5	0.33	
Gr (1 g); KMnO ₄ (6 g); H ₂ SO ₄ (70 mL); H ₃ PO ₄ (20 mL); HNO ₃ (10 mL)	85	3	0.7	[70]
GO2-a: Gr (1 g); KMnO ₄ (3 g); H ₂ SO ₄ (24 mL); H ₃ PO ₄ (6 mL)	95	1	0.8	Present study

4.1.2 FTIR-UATR spectral analysis

The FTIR spectra of the prepared GO samples and graphite are presented in Figure 4-5. There are several bands associated with oxygen functionalization in the spectra of all the samples, clearly showing the oxidation of graphite. The presence and nature of the functional groups in the FTIR spectra are in good agreement with the XPS analysis results. The following functional group signals were identified in the spectra of the prepared GO samples: the epoxy C—O—C stretching vibration (~1030–1050 cm⁻¹), C—OH bending vibrations of hydroxyl groups (~1235 cm⁻¹), the C=O stretching vibration of carbonyl functional groups at the edge of the GO sheets (~1705 cm⁻¹), the C=C skeletal vibration from unoxidized graphene (~1600–1620

cm^{-1}) [41, 66], and O—H stretching vibrations corresponding to the residual water intercalated between the GO sheets ($\sim 3200 \text{ cm}^{-1}$) [56].

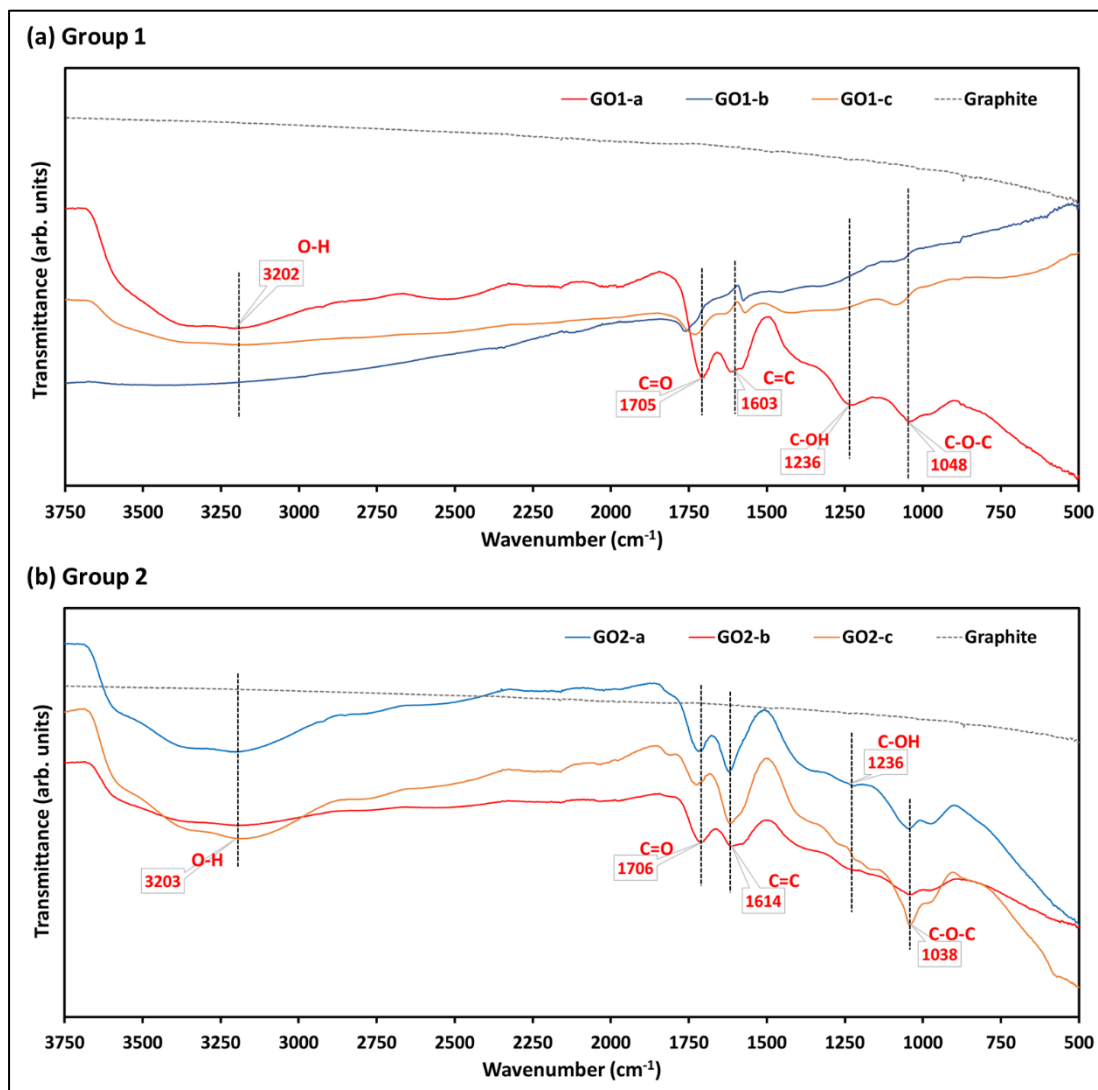


Figure 4-5: FTIR spectra of prepared GO samples: (a) group 1 and (b) group 2.

The comparatively large area of oxygen related bands (ORB) in these samples indicated a relatively high oxygen content. Figure 4-6 is a graphical treatment of the FTIR spectra of GO1-a as an example. The graphical treatment and FTIR quantification of the other GO samples are presented in Figure A1 in Appendix A.

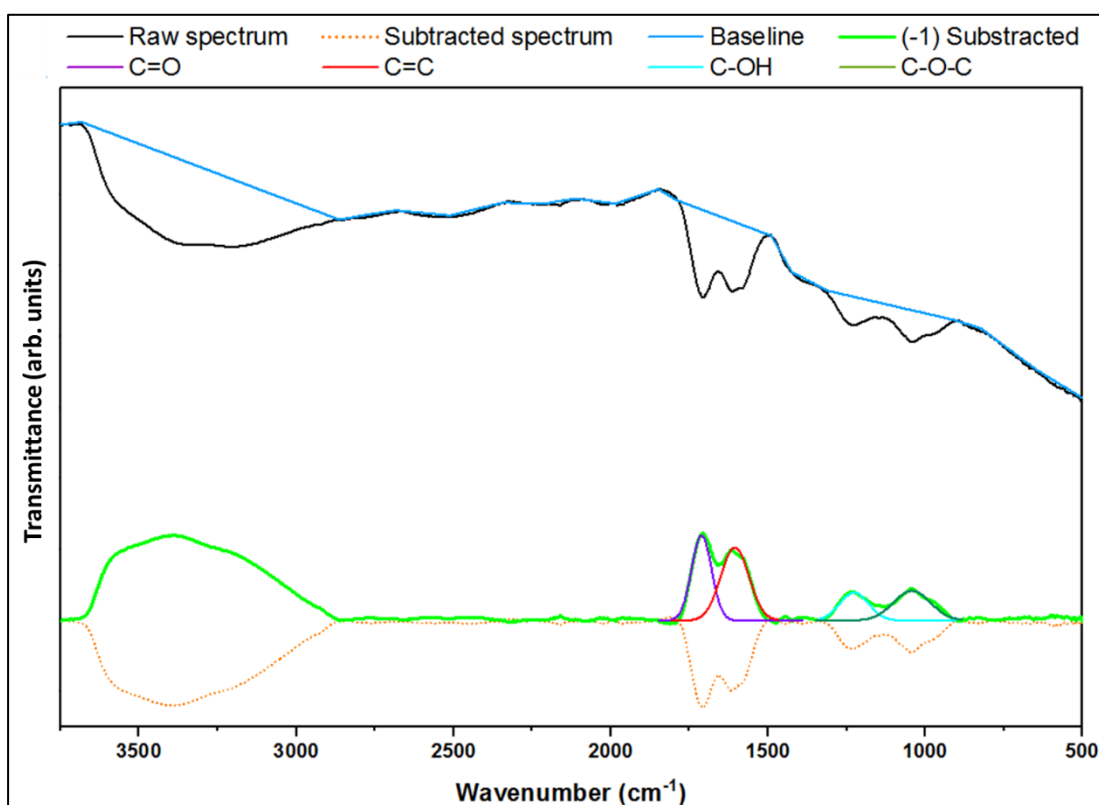


Figure 4-6: FTIR spectra treatment and deconvolution for the quantitative analysis of GO1-a.

Different oxidation conditions have produced GO samples with different properties related to the oxygen content. This conclusion was borne out by the FTIR spectra as well as the other characterization results. The calculated areas of the ORBs differed from one sample to the next, resulting in comparable results to those obtained by the elemental analysis. Figure 4-7 is a comparison of the calculated ORB% from the FTIR spectra with the O% obtained from the elemental analysis. The calculated ORB% differs slightly from the elemental analysis results for GO1-b and GO2-b by 3 and 8 wt%, respectively. For GO1-a and GO1-c, the corresponding differences between the two analyses were higher by 15% and 20%, respectively. By contrast, the results of the two analyses were identical for GO2-a and GO2-c.

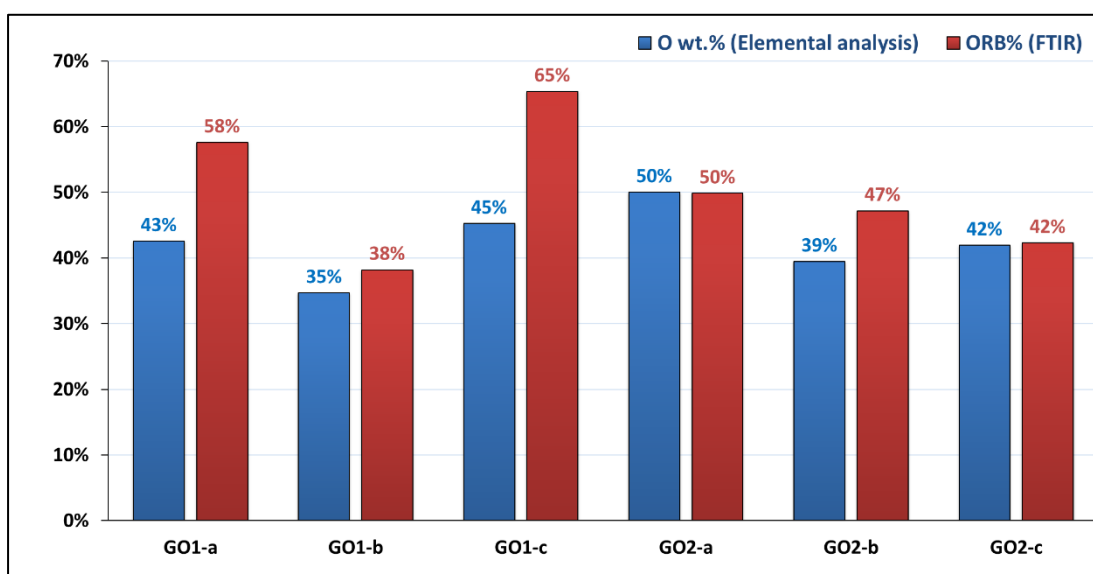


Figure 4-7: ORB% obtained from FTIR quantification compared to O wt% obtained from CHNSO elemental analysis

4.1.3 Raman spectral analysis

Raman spectroscopy is an essential tool for the characterization of GO and other graphene-based materials [307]. A good analysis of the Raman spectra provide quantitative and qualitative information about the properties of GO like defects, the number of layers, and crystallite size [307, 308]. The Raman spectra of the prepared GO samples are shown in Figure 4-8. All the spectra exhibit two characteristic bands for D and G at ~ 1350 and 1590 cm^{-1} , respectively, in addition to second-order bands ($\sim 2500\text{--}3200\text{ cm}^{-1}$) [307]. To enable a more accurate interpretation of the spectra, the first-order spectra were deconvoluted and fitted to four peaks, D, D', G, and D'. Shadetzky et al. [309-311] reported another peak at approximately 1110 cm^{-1} related to disordered graphitic lattices. However, this peak was not subsequently reported for GOs synthesized from natural graphite [312] and was not observed in this study either.

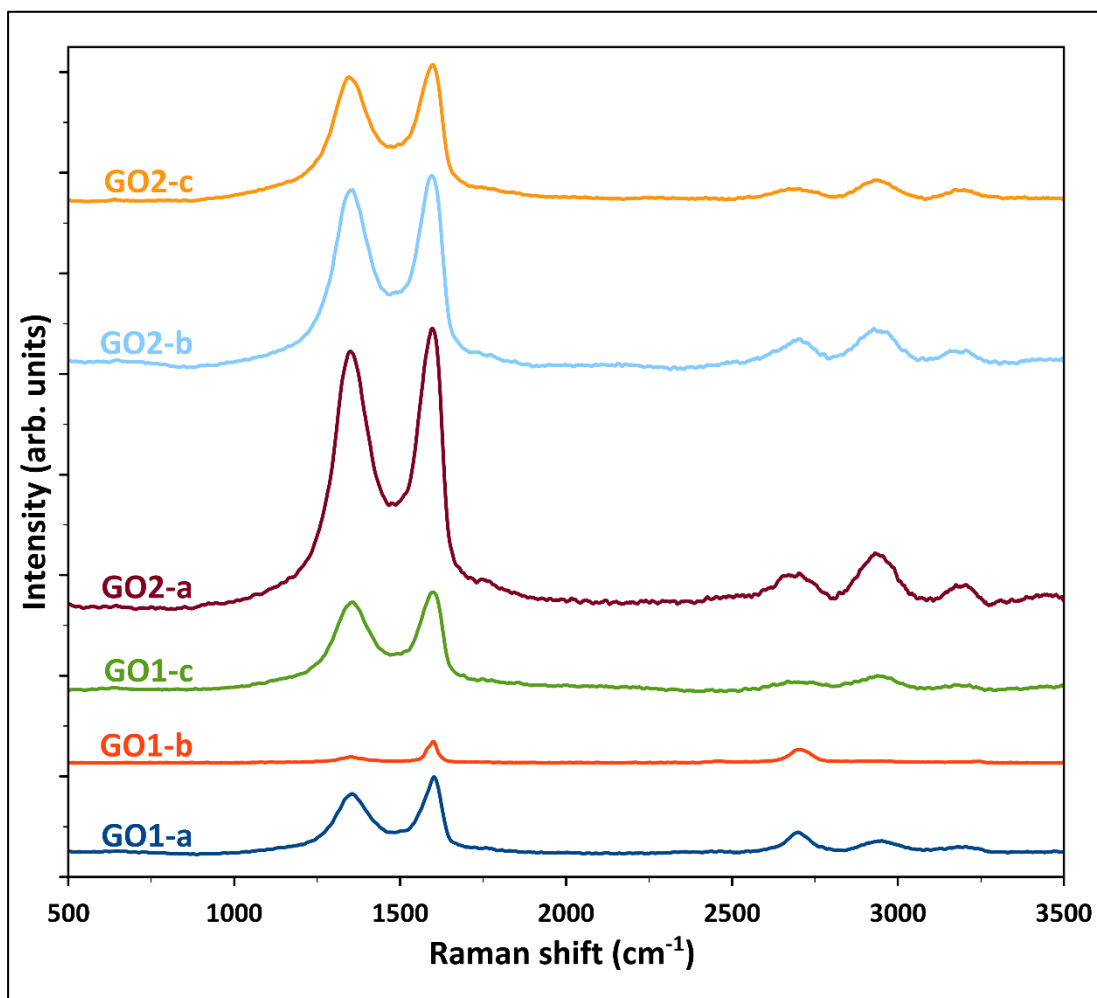


Figure 4-8: Raman spectra of prepared GO samples: spectra have been stacked vertically for clarity.

Figure 4-9 illustrates the spectral deconvolution and peak fitting using GO1-a as an example. The deconvolution and fitting details of the other GO samples are presented in Figure A2 in Appendix A. It is well established that first-order bands are related to the crystallite size of graphene-based materials. The D'' band has been correlated with reduced crystallite size that is related to amorphous phases in GO nanoparticles [313].

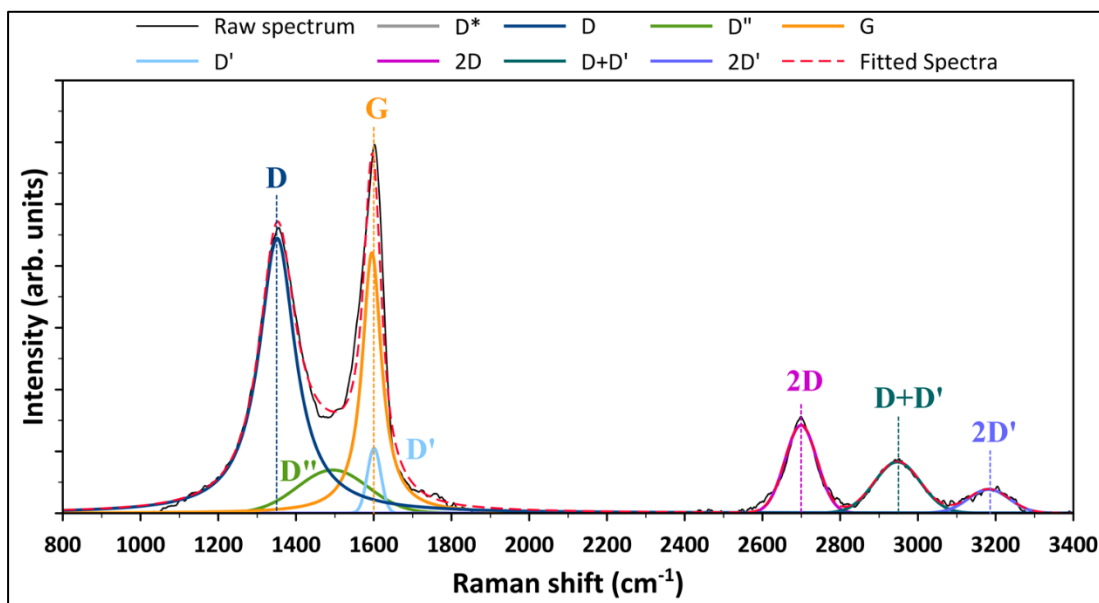


Figure 4-9: Illustration of Raman spectra deconvolution and peak fitting using GO1-a as an example.

There have been several reports that the in-plane sp^2 crystallite size (L_a) is inversely proportional to the ratio of the D and G intensities (I_D/I_G) [41, 56, 312, 314, 315]. Hence, the relative intensities of the D and G bands were calculated from the fitted spectra and used to estimate the crystallite size. GO1-b has a strong G band accompanied with a weak D band and a correspondingly low I_D/I_G ratio (0.38) compared to those of the other samples. The I_D/I_G ratio of the other samples ranges between 1.06 and 1.15, which suggests that all the prepared GOs have almost similar crystallinities and structures, except for GO1-b. The band parameters estimated from the first-order spectra fits are presented in Table A1 in [Appendix A](#). The crystallite size L_a (nm) was estimated using the Tuinstra-Koenig model [314, 316]:

$$L_a = (2.4 \times 10^{-10})\lambda^4(I_D/I_G)^{-1} \quad (12)$$

where λ is the laser wavelength (nm), and I_D and I_G are the integrated intensities under the D and G bands, respectively. The estimated crystallite sizes of GO samples are listed in Table 4-4.

Table 4-4: Crystallite sizes of GO samples estimated by Tuinstra-Koenig model

Sample	GO1-a	GO1-b	GO1-c	GO2-a	GO2-b	GO2-c
L_a (nm)	9.7	23.6	9.2	10.9	9.0	9.0

The second-order spectra of the GOs can be used to assess graphene quality [317]. Ferrari et al. [318] related the position and width of the 2D band to the number of layers in GO. The 2D band was found to shift to higher wavenumbers as the number of layers increased. López-Díaz et al. [310] found that the I_D/I_G ratio and the position of the 2D-band were good estimators of the graphitization degree in graphene oxides. To investigate these results, the second-order region of the spectra was deconvoluted and fitted to 3 peaks, 2D, D+D', and 2D', as illustrated in Figure 4-9. The band parameters estimated from the second-order spectra are presented in Table A2 in Appendix A. The I_D/I_G ratio from the first-order spectra and the positions of the 2D and D+D' bands from the second-order spectra are plotted against the C (%) values obtained from the CHNSO analysis in Figure 4-10a and b, respectively.

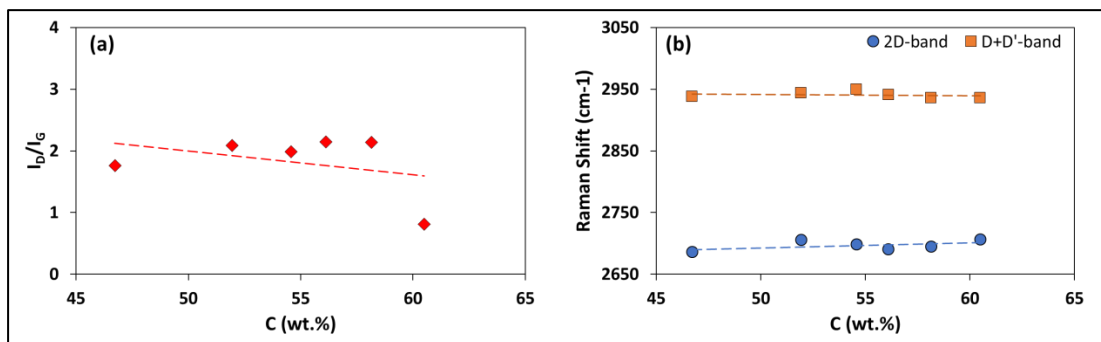


Figure 4-10: (a) I_D/I_G ratio of first-order Raman spectra and (b) positions of 2D and D+D' bands of second-order Raman spectra as functions of C (%).

It has been reported by López-Díaz et al. [310] that both the I_D/I_G ratio and the positions of the 2D and D+D' bands are correlated with C (%). However, no clear correlation can be observed in the results shown in Figure 4-10a and b.

4.1.4 Thermal stability

TGA was conducted to investigate the thermal stability of the prepared GO. Figure 4-11 shows the TGA curves of the prepared GO nanoparticles and the corresponding derivatives. The curves exhibit three stages of weight loss: the slight weight loss before 100 °C resulted from the evaporation of water trapped between GO sheets [27, 56], the major weight loss between 200 and 250 °C resulted from the thermal degradation of unstable oxygen-containing functional groups (hydroxyl, epoxy and carboxyl) [60, 319], and the final stage can be attributed to the decomposition of most of the stable groups at higher temperatures [60, 302]. The prepared GO exhibited different thermal stabilities. The major degradation of the unstable oxygen-containing groups occurred at approximately 222–239 °C and 243 °C for group 1 and group 2, respectively, as depicted in the derivative curves. The major percentage weight loss was found to increase for the samples in the following order: GO1-b < GO1-a < GO2-b < GO1-c < GO2-a < GO2-c. The difference in the weight loss of the GO samples mainly resulted from differences in the elemental compositions [319], because the thermal decomposition of GO depends on bond dissociation energies, whose magnitudes increase in the following order: H-bonding < C-O-C < COOH, HO-C-C-OH < C-C < C=C [320]. The relation between thermal stability and elemental composition can be more clearly seen by plotting the weight loss % (in decomposition stages 2 and 3) versus the GO oxygen content as illustrated in Figure 4-12. Figure 4-12 shows the clear dependence of the weight loss on the GO elemental composition, and the thermal stability decreases with the increase of oxygen content and vice versa. For example, GO with a high oxygen content tends to have a low thermal stability (e.g., GO2-a), whereas a low-oxygen-content GO (e.g., GO1-b) exhibits a high thermal stability.

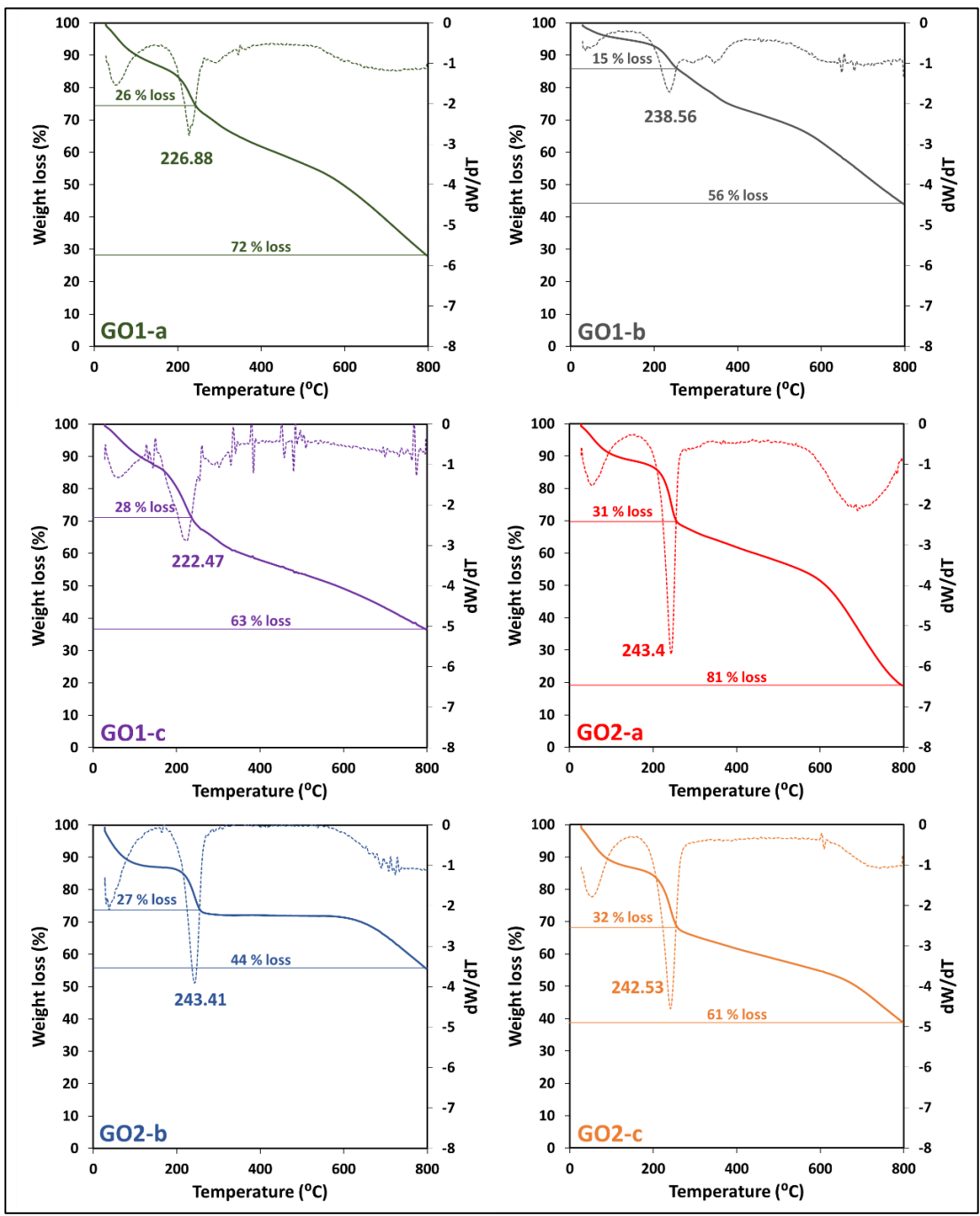


Figure 4-11: TGA curves (solid lines) of GO samples and corresponding derivative curves (dotted lines).

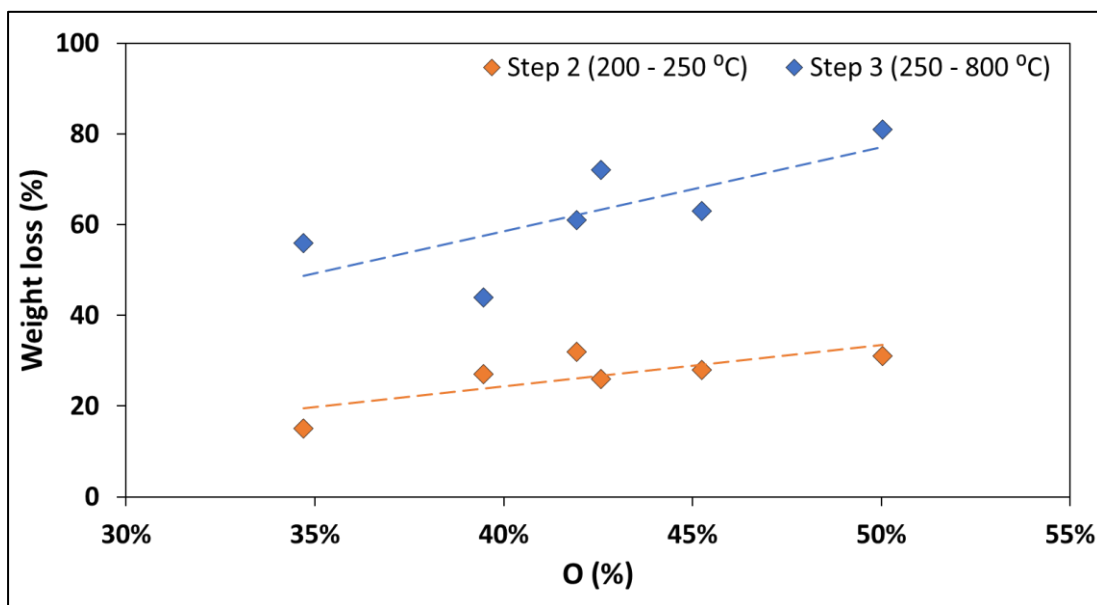


Figure 4-12: Plots of weight loss (%) in stages 2 and 3 of thermal decomposition obtained by TGA as a function of O (wt%)

4.2 Characterization of rGO-PDA Nanoparticles

Bases on the results obtained from the characterization of GO samples (Section 4.1), GO2-a was found to have the highest oxidation degree among the samples. Therefore, GO2-a (hereinafter referred as GO) was selected to be functionalized with PDA and for the embedding into membranes as well. The following subsections elaborates on the differences between GO and rGO-PDA nanoparticles with respect to their morphology, structure, chemical compositions, thermal stability, dispersibility and hydrophilicity.

4.2.1 Structural and morphological properties

The structural change represented by the XRD patterns of the pristine GO and rGO-PDA nanoparticles is shown in Figure 4-13. The diffraction peak of the GO sample at 11.2° corresponds to the 001 plane of the hexagonal crystal structure of GO [70]; while the peak at 25.9° corresponds to the 002 plane which can be attributed to

unoxidized graphite in the synthesized GO [60, 321, 322]. The incomplete oxidation of graphite results in the formation of graphite-GO mixture which is considered one of the main drawbacks of Hummers-based methods [56]. For rGO-PDA, the 001 plane was shifted to 10.9° with the presence of several peaks confirming the structural change resulted from the functionalization reaction. A sharp diffraction peak has emerged in the rGO-PDA patterns at 21.7° which is close to the graphite diffraction peak at 25.9° indicating a partial reduction of GO [99]. The diffraction peaks at 31° , 32.2° and 32.9° have been previously reported with PDA-functionalized carbon nanotubes (CNT-PDA) and they were related to the PDA [323]. Furthermore, the diffraction peaks around 41.4° and 42.9° were previously reported with rGO/PDA nanoparticles [324].

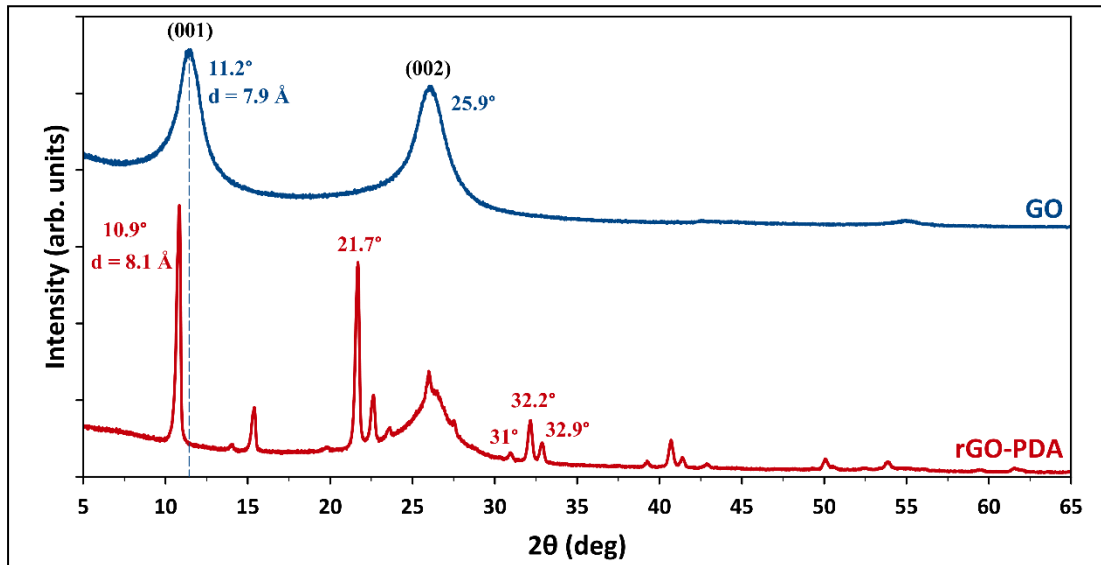


Figure 4-13: XRD patterns of GO and rGO-PDA nanoparticles.

The interlayer spacing of the samples (d-spacing) can be correlated to the oxygenated functional groups of GO. The interlayer spacing of the 001 plane ($d_{(001)}$ -spacing) was calculated by Bragg's equation to be 7.9 \AA for GO which is close to the

values reported for GO synthesized by modified Hummers methods [60, 70, 302]. The $d_{(001)}$ -spacing of rGO-PDA was found to be 8.1 Å indicating a slight expansion in the interlayer spacing. The expansion in the interlayer spacing confirms the formation of new oxygenic functional groups from the PDA between the GO layers. This can be also demonstrated in the SEM images of GO and rGO-PDA presented in Figure 4-14. SEM images at different magnifications show a clear difference in the morphological characteristics resulted from the amination of GO. Images of the unfunctionalized GO nanoparticles exhibit sharp, clear, and smoother flakes while the rGO-PDA nanoparticles exhibited rougher surface and irregular structure. SEM images at high magnifications show well distribution and attachment of PDA particles on the surface and between the GO sheets which lower the stacking level of GO layers and expands the interlayer spacing as demonstrated by XRD results.

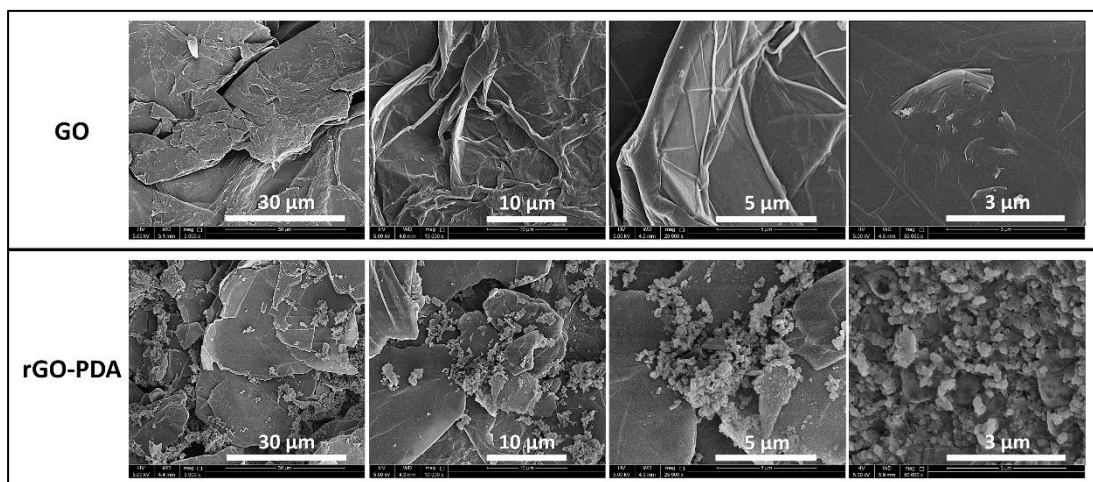


Figure 4-14: SEM images of GO and rGO-PDA nanoparticles.

The TEM images in Figure 4-15 depict two distinct morphologies of GO and rGO-PDA nanoparticles. The pristine GO exhibited wrinkled surface and highly transparent sheets which can be related to the lower stacking level of GO sheets. The

high transparency and wrinkled surface indicate a high oxidation level of GO sheets [41, 59]. In contrast, the TEM images show dense and opaque surface of the rGO-PDA indicating a successful grafting of PDA on the GO surface, which agrees with the results obtained by the SEM images.

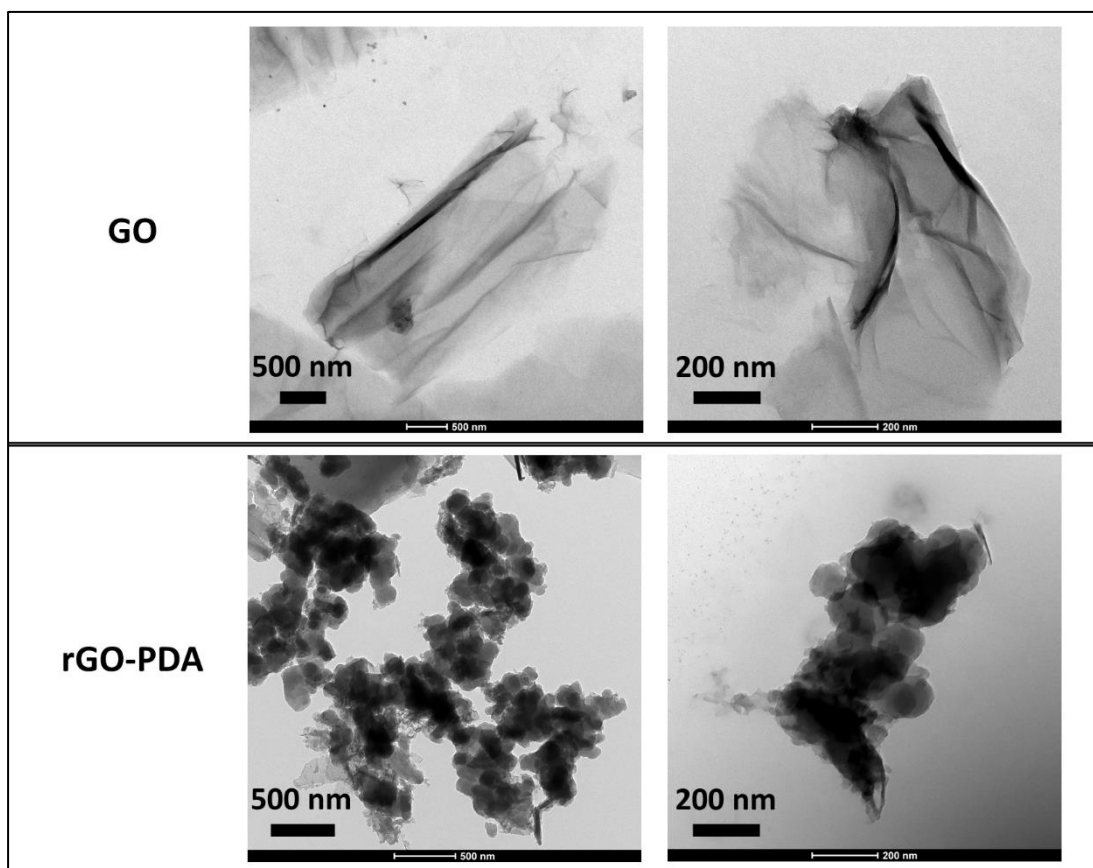


Figure 4-15: TEM images of GO and rGO-PDA nanoparticles.

4.2.2 Compositional properties

XPS survey spectra were recorded to explore the effect of PDA functionalization on the surface elemental compositions, nature, and the chemical states of the functional groups of GO nanoparticles. The complete XPS survey spectra of GO and rGO-PDA in Figure 4-16 shows the existence of O 1s and C 1s core-levels around binding energies of 531 and 284 eV, respectively. The small peaks at 166 eV

correspond to S 2p indicating the presence of trace amounts of sulphur in both samples. The N 1s peak emerged in GO-PDA spectra at binding energy of ~398 eV indicates that GO was successfully aminated with PDA. Additional two peaks emerged in the spectra of rGO-PDA around 196 and 266 eV corresponding to Cl 2p and Cl 2s due to the chlorine content of dopamine.

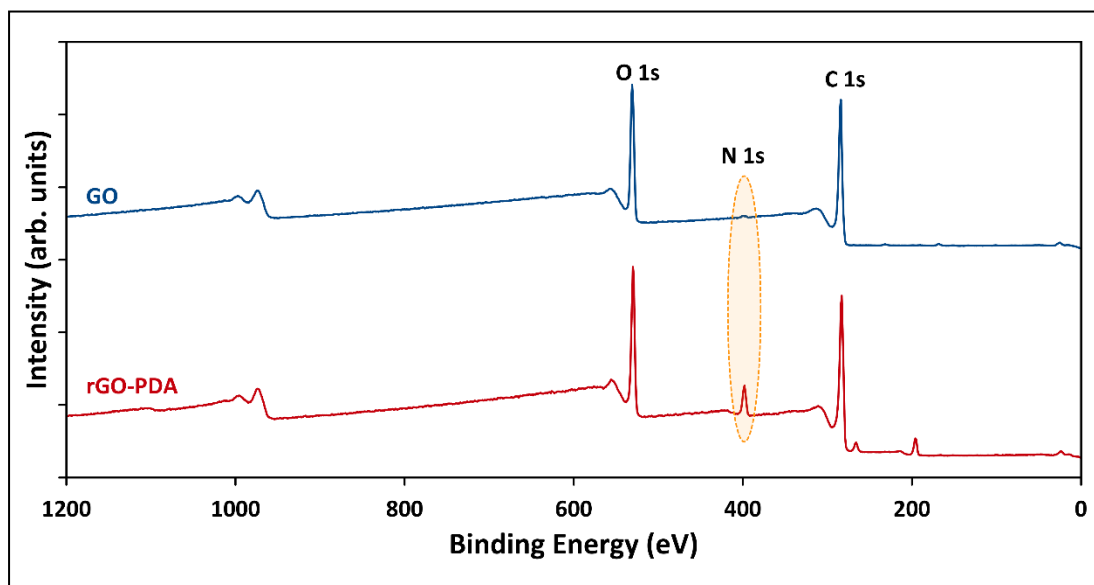


Figure 4-16: XPS survey spectra of GO and rGO-PDA nanoparticles.

For a better interpretation of the XPS spectra, C 1s and O 1s core-levels were deconvoluted and the abundance percentage of functional groups are presented in Figure 4-17a and b. Four peaks were obtained by deconvoluting the C 1s region of GO: C=C/C—C (40%) at a binding energy of 284 eV attributed to sp^2 bound graphitic carbon, C—O (41%) at 286 eV related to the epoxide groups, C=O (14%) of the carbonyl functional groups at 287 eV, and the carboxylic group on the GO edges (COOH) at 289 eV (5%). These peaks were reported in the literature for GO nanoparticles [60, 61, 66]. Similar peaks were obtained from the deconvolution of C 1s core-level of GO-PDA in addition to a fifth peak corresponding to C—NH₂ at a

binding energy of 281 eV emerged from the PDA amine groups [325], which resulted in a slight reduction in the compositions of oxygen-containing groups. The deconvolution of the O 1s spectra illustrated in Figure 4-17c and d resulted into four main peaks, O—C=O, C=O, C—O, and C—O—C, at binding energies of ~530, 531, 533, and 535 eV, respectively [70].

The N 1s peak emerged in the rGO-PDA spectra was deconvoluted and fitted into three main peaks at binding energies of 402, 399, and 396 eV corresponding to primary amine (N—H₂), secondary amine (N—H), and aromatic/tertiary amine (N—C) functional groups, respectively, as illustrated in Figure 4-17e [326-328]. Peak parameters and the corresponding compositions estimated from the XPS fit are listed in Table A3 in Appendix A.

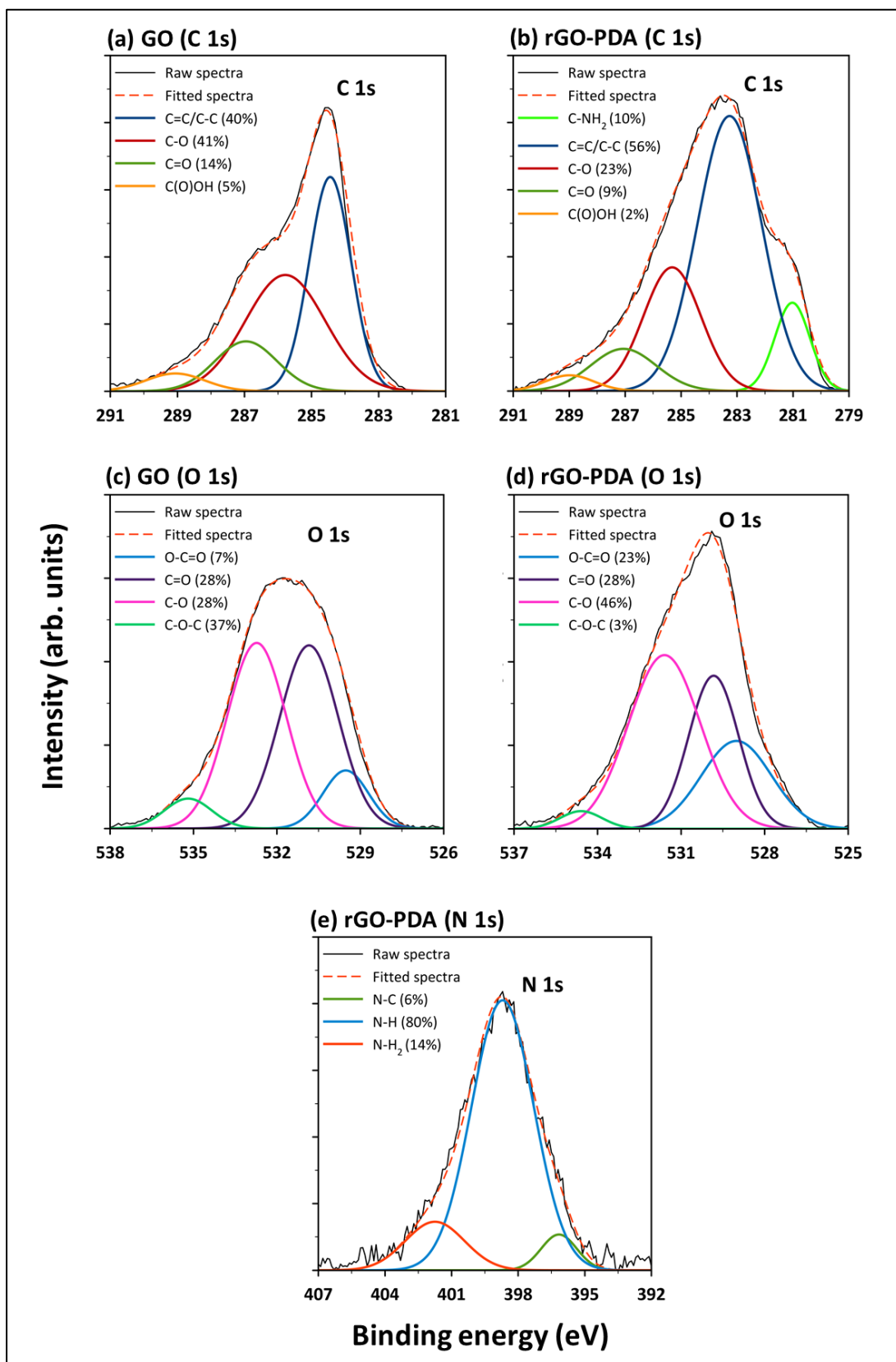


Figure 4-17: High-resolution and deconvolution of XPS spectra of (a) GO C 1s, (b) GO-PDA C 1s, (c) GO O 1s, (d) GO-PDA O 1s, and (e) GO-PDA N 1s core-levels.

Table 4-5 and Table 4-6 compare the elemental compositions of GO and rGO-PDA as determined by the XPS and CHNSO elemental analyzer, respectively. The results obtained from CHNSO analysis show a good oxidation degree of graphite to GO with an oxygen content of 50 wt% and an atomic O/C ratio of 0.8. However, the functionalization with PDA resulted in partial reduction of GO lowering its oxygen content to 37.7 wt% and the O/C ratio to 0.6 which agrees with the FTIR results. The reduction is not as significant as this reported with other amines like n-butylamine [67], dodecylamine [329] or melamine [30], which can be attributed to the oxygenated functional groups of PDA that compensated some of the reduced oxygen in GO.

Table 4-5: XPS elemental compositions of the GO and rGO-PDA.

Sample	Atomic composition (at.%)					
	C 1s	O 1s	N 1s	S 2p	Cl 2p	Cl 2s
GO	74.58	24.52	0.5	0.4	-	-
rGO-PDA	69.94	20.61	6.61	0.11	1.82	0.91

Table 4-6: CHNSO elemental compositions of the GO and rGO-PDA.

Sample	Weight composition (wt%)					Atomic composition (at.%)					
	N	C	H	S	O	N	C	H	S	O	O/C
GO	0.3	46.8	2.6	0.3	50.0	0.2	40.3	27.1	0.1	32.3	0.80
rGO-PDA	7.8	49.8	4.8	0.0	37.7	4.7	35.2	40.1	0.0	20.0	0.6

4.2.3 FTIR-UATR and Raman spectral analysis

The FTIR spectra of the pristine GO and rGO-PDA nanoparticles are shown in Figure 4-18. As discussed in Section 4.1.2, the spectra of the GO confirm the oxidation of graphite owing to the presence of several bands attributed to oxygen functionalization. The successful functionalization of GO particles can be also

confirmed by the emerging bands in the spectra of rGO-PDA that are attributed to the amide functionality at ~ 1285 , 1500 , 1619 , 3038 , and 3184 cm^{-1} . These bands have been previously reported in literature and were related to PDA [330-332]. Further, it was found that the C=O band at 1707 cm^{-1} was almost disappeared with rGO-PDA spectra demonstrating a partial reduction of GO nanoparticles [39].

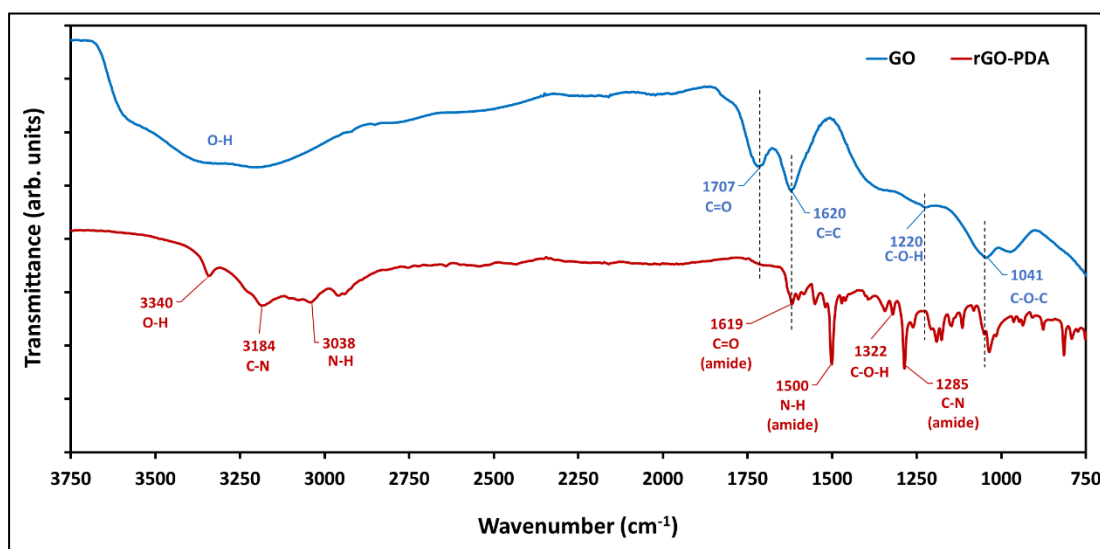


Figure 4-18: FTIR spectra of the pristine GO and rGO-PDA nanoparticles.

Raman spectra of the pristine GO and rGO-PDA are shown in Figure 4-19a. The two distinctive bands for graphene-based materials, G and D, are existing in both spectra at ~ 1590 and ~ 1350 cm^{-1} , respectively. As demonstrated in Section 4.1.3, the I_D/I_G in the first-order spectra is related to the crystallite size of GO nanoparticles [312]. Consequently, the first-order spectra of both samples were deconvoluted and fitted into four peaks, D, D'', G, and D' at ~ 1352 , 1495 , 1585 , and 1610 cm^{-1} , respectively. A fifth peak (D*) emerged in the spectra of rGO-PDA at ~ 1188 cm^{-1} which was earlier reported and attributed to disordered graphitic lattices [309, 310]. The I_D/I_G ratio was then estimated from the fitted spectra. Figure 4-19b and c depicts

the spectra deconvolution and peak fitting of GO and rGO-PDA, respectively. From the estimated intensities (I_D and I_G), the crystallite size (L_a , nm) for both samples was then calculated using the Tuinstra–Koenig model (Eq. 12) [316]. The parameters of G and D bands and the evaluated crystallite sizes L_a of the pristine GO and rGO-PDA nanoparticles are presented in Table A4 in Appendix A. The crystallite sizes estimated from the I_D/I_G ratios were found to be 10.9 and 15.2 nm for the pristine GO and rGO-PDA, respectively. Further, the I_D/I_G ratio of rGO-PDA (1.3) was found to be lower than this of the pristine GO (1.8) indicating lower oxygen content of rGO-PDA [41, 318]. This is in a good agreement with the results obtained from XRD, FTIR analyses and the elemental analysis. The complete bands parameters estimated from the first order spectra fitting are listed in Table A5 in Appendix A. Second-order bands around ($\sim 2500\text{-}3200\text{ cm}^{-1}$) are also presented in the spectra of both samples. The second-order spectra were deconvoluted into three peaks, 2D, D+D', and 2D', as depicted in Figure 4-19b and c. Bands parameters estimated from the deconvolution and fitting of the second-order spectra are listed in Table A6 in Appendix A. The second-order bands are associated with the quality of GO [317]. The positions of the 2D and D+D' peaks were reported to be good estimators of graphitization degree, represented by C_{sp^2} content, in GO nanoparticles [310]. It was demonstrated in Section 4.1.3 that the correlations reported by López-Díaz et al. [310] don't always provide accurate values of the C_{sp^2} content especially when other elements like nitrogen are presented in the sample. However, it can be said that the positions of 2D and D+D' shifts to higher wavenumbers with samples having lower oxygen contents. Therefore, the slight shift of 2D and D+D' positions in the rGO-PDA spectra could be attributed to the lower oxygen content of rGO-PDA due to the partial reduction resulted from the functionalization reaction.

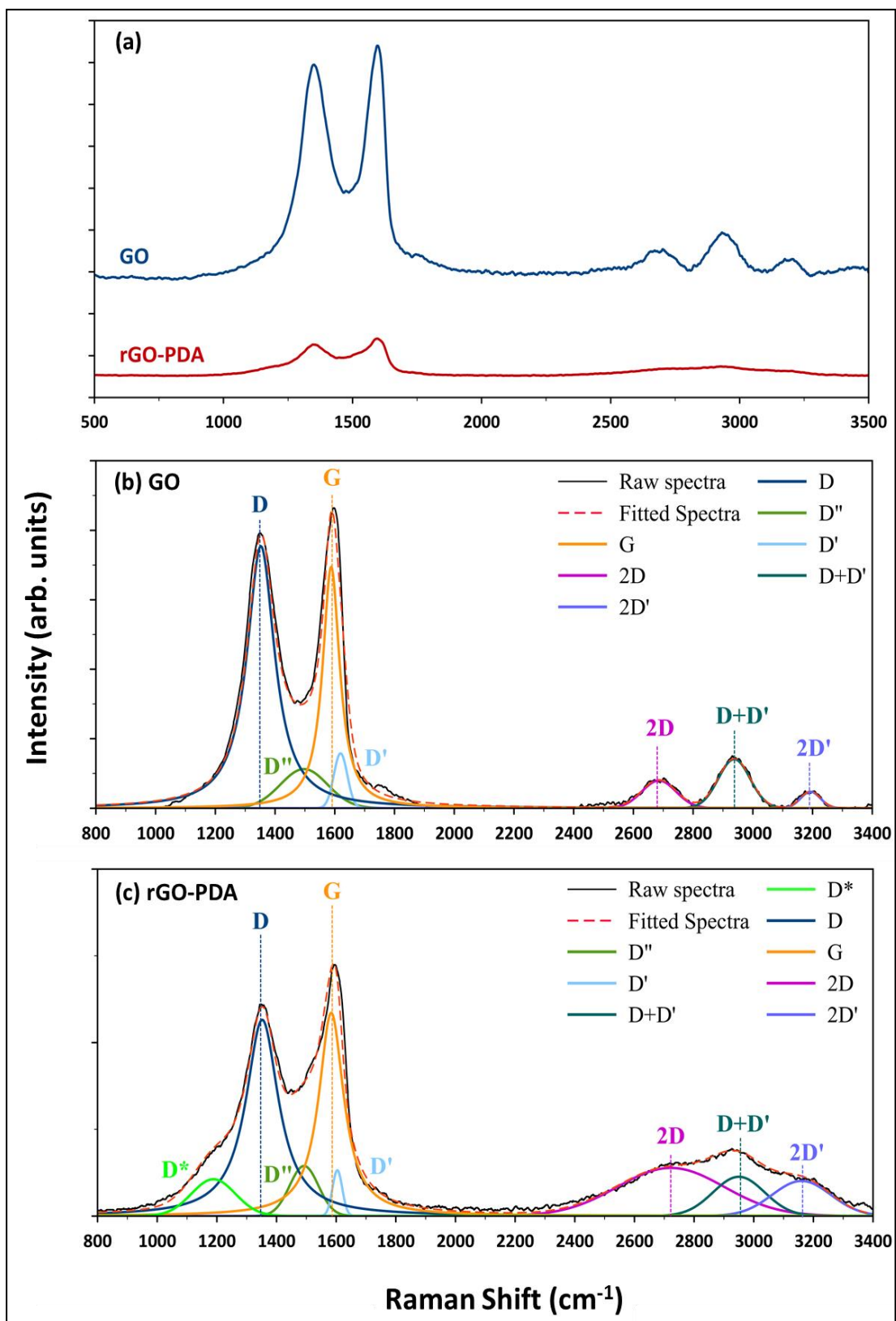


Figure 4-19: (a) Raman spectra of GO and rGO-PDA nanoparticles and illustration of Raman spectra deconvolution and peaks fitting for (b) GO and (c) rGO-PDA.

4.2.4 Dispersibility & hydrophilicity properties

Figure 4-20 shows photographs of GO and rGO-PDA suspensions after sonication. The pristine GO nanoparticles exhibited good dispersibility in DIW, NMP, DMF, and DMA; while with other solvents (i.e. hexane, toluene, and dodecane), the dispersibility was very poor. These observations were previously reported in some studies in literature and are mainly attributed to the polarity of GO [67, 333]. In contrast, rGO-PDA nanoparticles showed high dispersion in all solvents except in hexane with average dispersibility. The high dispersibility of rGO-PDA in polar and nonpolar solvents expands its potential uses for various applications over the pristine GO including surface functionalization of RO and NF membranes [32, 111], anticorrosive coatings [334], conductive inks [335], and oil recovery [336].

Figure 4-21 presents the optical micrographs of GO and rGO-PDA dispersion in DIW with a low concentration (0.02 mg/mL). It is obvious that the pristine GO particles agglomerate even at this low concentration. In contrast, rGO-PDA showed less agglomeration and have better dispersibility in water than the pristine GO. This observation indicates that GO-PDA nanoparticles have higher dispersion stability in water with less agglomeration. This could be attributed to the hydrophilic functional groups of PDA that provide better dispersibility and stability of GO nanoparticles.

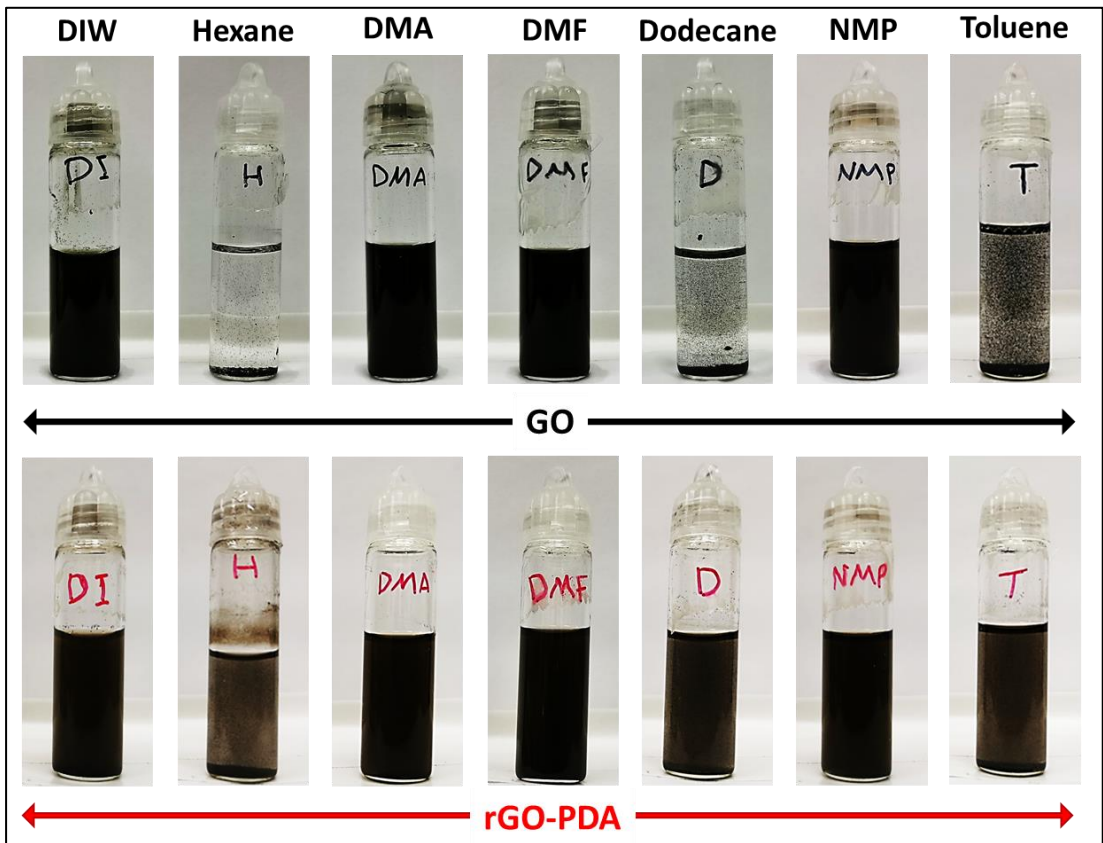


Figure 4-20: Photographs of GO and rGO-PDA dispersions in various solvents.

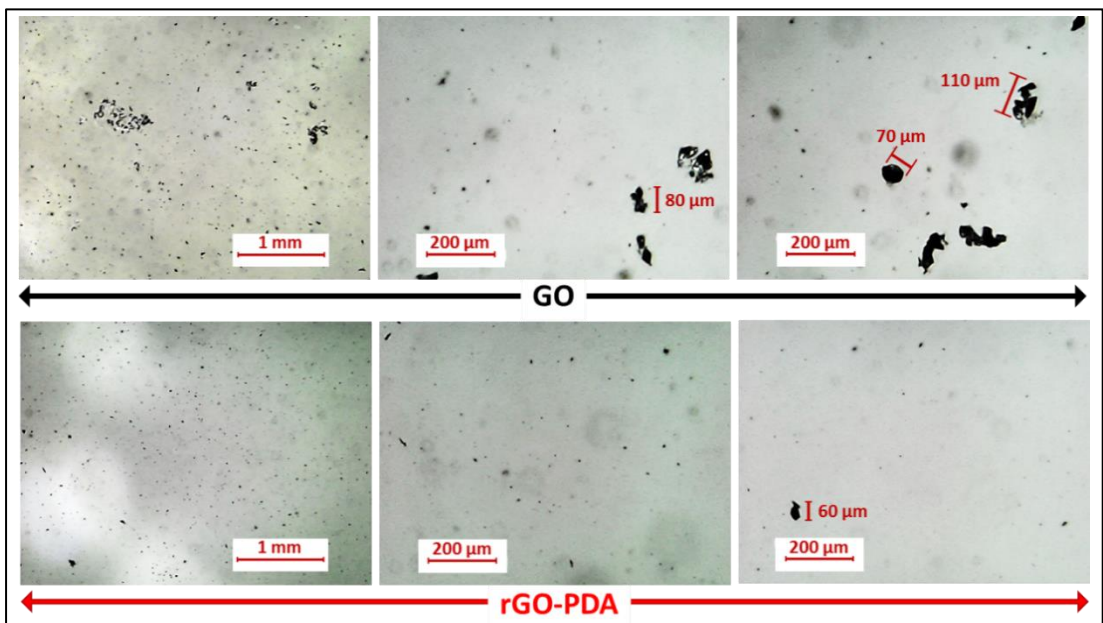


Figure 4-21: Optical micrographs of GO and rGO-PDA dispersions in DIW (0.02 mg/mL).

Figure 4-22 depicts photographs of the pristine PS-30 and the nanoparticles-coated membranes with their hydrophilicity in terms of contact angle. Obviously, the surface hydrophilicity of PS-30 was slightly enhanced with the pristine GO deposition. The average contact angle of the pristine PS-30 substrate was measured to be 76.7° while it was reduced to 53.3° after the coating with the GO layer. This observation has been reported in several studies with different membrane materials and was attributed to the hydrophilic nature of GO particles [75, 90]. Interestingly, the contact angle was much lower (27.8°) with the assembly of the rGO-PDA layer suggesting higher hydrophilicity of rGO-PDA than the pristine GO nanoparticles. The high hydrophilicity of rGO-PDA can be explained by the presence of abundant hydroxyl groups of PDA that is consistent with the predicted chemical structure of rGO-PDA nanoparticles in Figure 3-2. The high hydrophilicity accompanied by the high dispersibility makes the rGO-PDA an efficient nanofiller in membrane technology. The high dispersibility allows the utilization of rGO-PDA with different types of membranes that use NMP, DMF, and DMA to prepare mixed matrix membranes (MMMs), dodecane or hexane, to prepare thin-film nanocomposite (TFN) membranes, or water to prepare coated membranes based on assembly approaches.



Figure 4-22: Contact angle measurements of the pristine PS-30, PS/GO, and PS/rGO-PDA membranes.

4.2.5 Thermal stability

The thermal stability of the pristine GO and rGO-PDA nanoparticles was studied using the TGA analysis. Figure 4-23 illustrates the TGA curves of GO and rGO-PDA and their corresponding derivatives. Three stages of weight loss can be observed from the TGA curves of both samples. A minor weight loss around 100 °C attributed to the release of water intercalated between GO sheets [27, 56]. The second stage represents the thermal decomposition of unstable oxygenic functional groups (carboxyl, epoxy, and hydroxyl) [60, 319] resulting in a major weight loss of the sample. The major weight loss of GO and rGO-PDA occurred around 243 and 263 °C, respectively, as depicted by the derivative curves. This indicates better thermal stability, at this stage, of rGO-PDA than the pristine GO which can be explained by the partial GO reduction and the replacement of some oxygen-containing functional groups with amine groups that slow down the thermal decomposition. The final stage of thermal decomposition occurs then at high temperatures at which the most stable functional groups decompose [60, 302]. The weight of rGO-PDA at the final stage decreased sharply to 50% around 440 °C; while the 50% loss occurred around 612 °C for pristine GO. The TGA curves also suggest a lower char yield of rGO-PDA (about 35% at 600 °C and 13% at 800 °C) compared to the pristine GO (about 52% at 600 °C and 19% at 800 °C). The difference in thermal stability of GO and rGO-PDA can be related to the different functional groups presented in each sample, as the thermal decomposition is highly dependent on the bond dissociation energies as demonstrated earlier in Section 4.1.4.

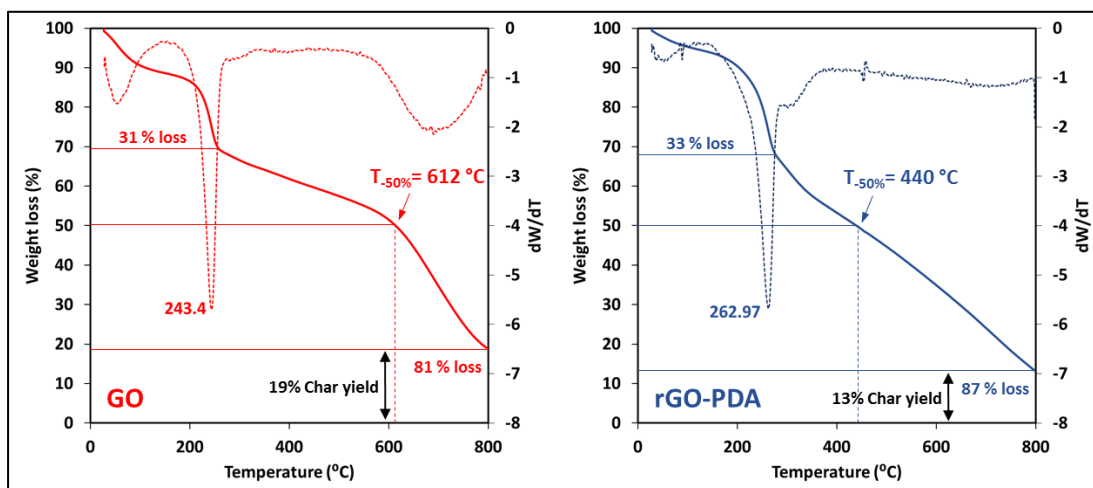


Figure 4-23: TGA curves (solid lines) of GO and rGO-PDA nanoparticles and the corresponding derivative curves (dotted lines).

4.3 Characterization of the membranes

After the preparation and functionalization of GO nanoparticles, the pristine GO and rGO-PDA nanoparticles were embedded into PSF ultrafiltration membranes using the NIPS approach to produce two sets of PSF mixed matrix membranes (MMMs): PSF/GO and PSF/rGO MMMs. The pristine PSF and the MMMs were analyzed using several analytical techniques to investigate the effects of each type of nanoparticles on the PSF properties with respect to the structure, morphology, hydrophilicity, pore size and porosity.

4.3.1 Structural and morphological properties

The FTIR-UATR spectra of the prepared membranes were obtained to investigate the effects of GO and rGO-PDA embedding on the chemical structure of PSF. The FTIR-UATR spectra of the control PSF (M_0), M_{GO4} , and M_{PDA4} as an example are shown in Figure 4-24. The spectra of the other membranes are presented in Figure B2 in Appendix B. Spectra for all membranes show the characteristic bands of

polysulfone that have been reported in literature [230, 293, 294]. The following functional groups were identified in the spectra of the prepared membranes: S=O stretching ($\sim 1106\text{ cm}^{-1}$), O—S—O symmetric stretching ($\sim 1150\text{ cm}^{-1}$), C—O—C stretching ($\sim 1242\text{ cm}^{-1}$), S=O stretching ($\sim 1294\text{ cm}^{-1}$), O—S—O asymmetric stretching ($\sim 1320\text{ cm}^{-1}$), aromatic ring stretching ($\sim 1488, 1588\text{ cm}^{-1}$), and aromatic ring breathing ($\sim 1660\text{ cm}^{-1}$). No obvious difference was found in the spectra of PSF and PSF composites due to the low concentration of GO and rGO-PDA and the dominance of PSF in the membrane matrix. Similar observations were reported with PSF MMMs incorporating low loadings of GO nanoparticles [90].

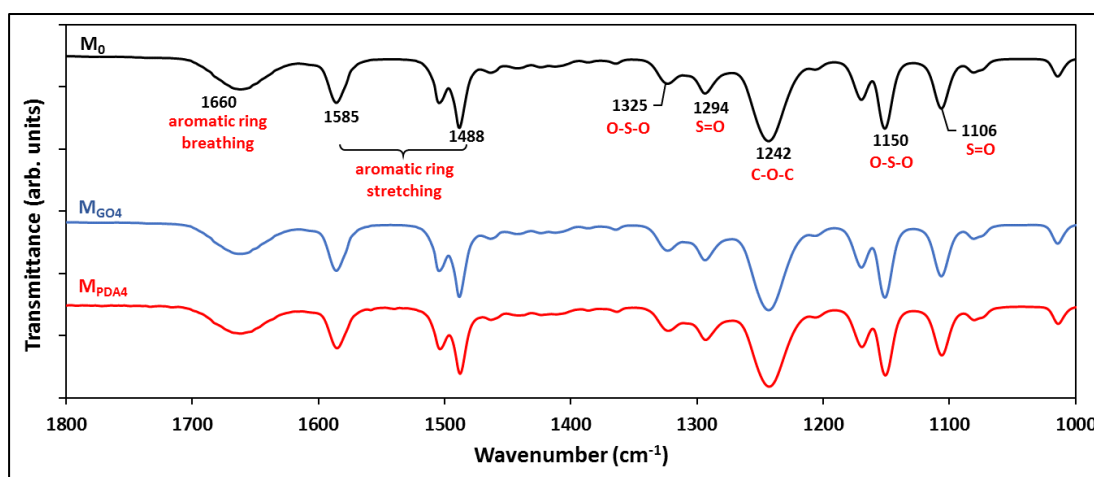


Figure 4-24: FTIR-UATR spectra of M_0 , M_{GO4} , and M_{PDA4} membranes.

The surface and cross-section SEM images of the prepared membranes were obtained at different magnifications to study the effect of GO and rGO-PDA embedding on the PSF structure. The surface and cross-section SEM images of the pristine PSF, PSF/rGO-PDA-0.02, and PSF/GO-0.02 are presented in Figure 4-25. The SEM images of the other PSF/GO and PSF/rGO-PDA composite membranes are presented in Figure B3 and Figure B4 in Appendix B, respectively. The surface SEM

images do not show significant difference between the pristine PSF and PSF composites. However, the cross-section SEM images exhibited clear influence of GO and rGO-PDA embedding onto the PSF structure. Two distinct layers can be observed in all membranes: a thin dense layer on the top and a typical sponge structure sub-layer. The sub-layer consists of several finger-like macro-voids and small pores surrounded by the polymer wall. With the addition of GO and rGO-PDA particles, the finger-like macro-voids became wider and longer because of the hydrophilicity of GO and rGO-PDA that increase the mass transfer rate between the solvent (NMP) and non-solvent (water) during phase inversion process [189]. Similar observations were reported in several studies in literature [201, 235]. At high magnifications, it can be clearly seen that both GO and rGO-PDA nanoparticles are distributed on the polymer wall of the sub-layer with spherical shape. Similar observations were previously reported with PEI/GO MMMs [44]. The high magnification SEM images show also that the pristine GO nanoparticles are agglomerated in some areas of the sub-layer causing a partial clogging of the membrane pores even at low concentrations (e.g. 0.02 wt% GO). This clogging usually reduces the water flux through the membrane as discussed in the coming sections. On the other hand, the rGO-PDA nanoparticles exhibited better distribution without obvious agglomeration which can be related to the higher dispersity of rGO-PDA in NMP than the pristine GO nanoparticles. It is worth mentioning that rGO nanoparticles were reported to have higher dispersibility than the pristine GO nanoparticles in several organic solvents making them good nanofillers for different membrane materials [37]. This was also demonstrated by the dispersibility measurements in Section 4.2.4.

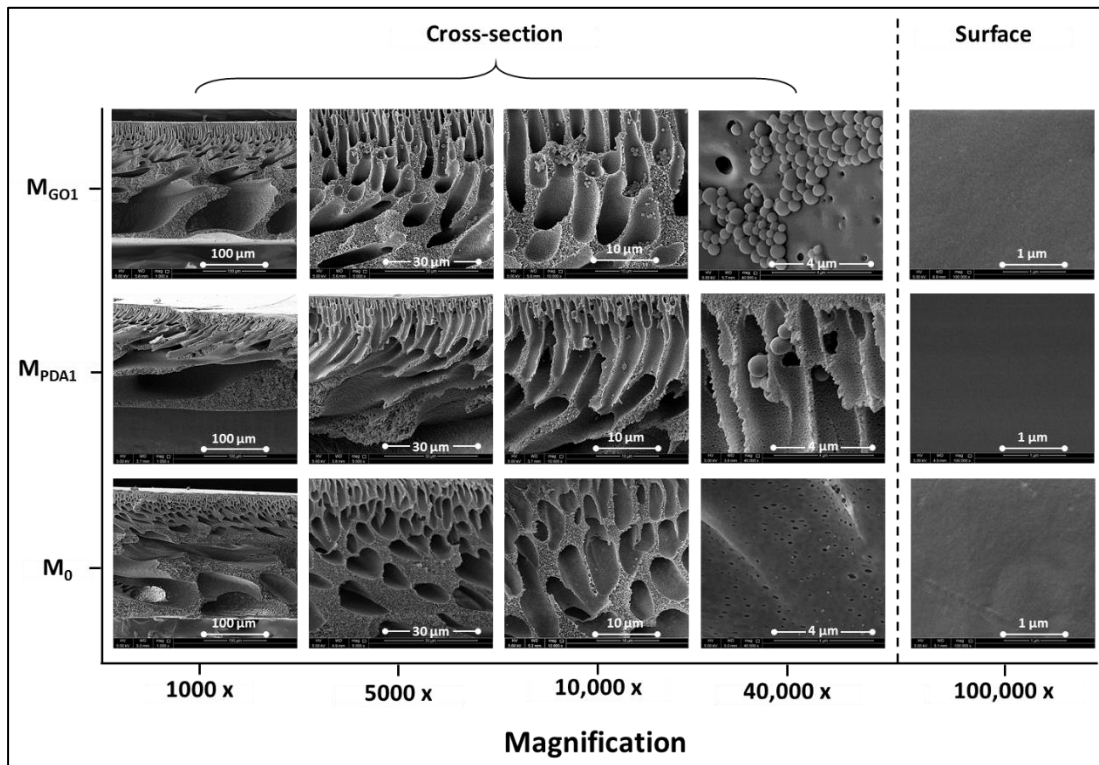


Figure 4-25: Surface and cross-section SEM images of M_0 , M_{PDA1} , and M_{GO1} membranes.

Surface roughness is an essential factor that affects the separation and fouling resistance of a membrane. Hence, AFM analysis was conducted to study the effect of GO and rGO-PDA incorporation on membrane roughness. The three-dimensional surface AFM images of PSF, PSF/GO and PSF/rGO-PDA composites over $10 \times 10 \mu\text{m}$ scan area are shown in Figure 4-26. The roughness parameters represented by the root-mean-square roughness (RMS) and the average roughness (Ra) are listed in Table 4-7. Two pieces of each membrane were tested, and the average RMS and Ra values were calculated. The surface roughness was found to increase with the addition of GO and rGO-PDA nanoparticles except for M_{GO1} (PSF/GO-0.02). The RMS and Ra values of pristine PSF were found to be 9.4 and 7.8 nm, respectively, that lie in the range of roughness parameters for other PSF membranes in literature [125, 337]. The highest roughness values among the PSF/GO composites were obtained with M_{GO4}

(PSF/GO-0.15) with RMS and Ra of 21.6 and 16.9 nm, respectively. On the other hand, the roughness increase was much higher with the addition of rGO-PDA nanoparticles even at low concentrations which can be attributed to the presence of the amine and hydroxyl groups of PDA [338]. The highest roughness among the PSF/rGO-PDA composites was obtained with M_{PDA3} (PSF/rGO-PDA-0.1) with RMS and Ra values of 34.0 and 28.2 nm, respectively. It can be also observed that the roughness decreased with higher loadings of rGO-PDA (M_{PDA4}). This is can be explained by the high viscosity of the casting solution which delays the phase inversion process and result in highly dense surface [230, 339]. It is well established that membranes with rough surface have higher surface area which enhance the water flux through the membrane [230]. However, the high roughness could increase the fouling due to the contaminants accumulation in the valleys [340].

Table 4-7: The average values of the root-mean-square roughness (RMS) and the average roughness (Ra) of the prepared membranes.

Membrane	RMS (nm)	Ra (nm)
M_0	9.4 ± 2.3	7.8 ± 2.1
M_{GO1}	6.2 ± 0.8	5.1 ± 0.6
M_{GO2}	14.1 ± 0.9	11.3 ± 0.8
M_{GO3}	16.2 ± 3.0	13.0 ± 2.5
M_{GO4}	21.6 ± 5.6	16.9 ± 5.4
M_{PDA1}	25.7 ± 3.4	20.6 ± 2.8
M_{PDA2}	31.0 ± 0.8	24.7 ± 1.2
M_{PDA3}	34.0 ± 0.2	28.2 ± 0.7
M_{PDA4}	27.7 ± 1.3	22.7 ± 1.1

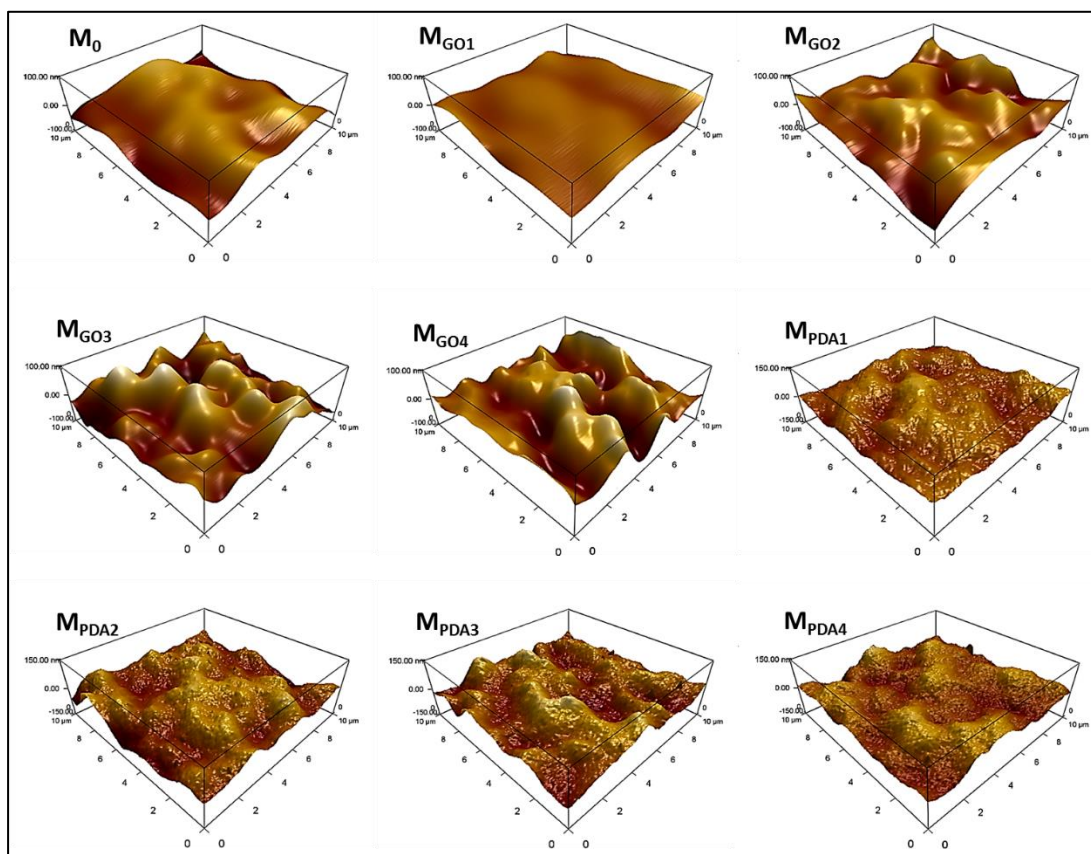


Figure 4-26: AFM images of the pristine PSF, PSF/GO and PSF/rGO-PDA composite membranes.

4.3.2 Hydrophilicity, porosity and mean pore size

Other parameter that affect the flux and fouling resistance are the membrane porosity, pore size and hydrophilicity. The surface hydrophilicity of the pristine and composite membranes in terms of static contact angle (CA) is illustrated in Figure 4-27. Obviously, CA decreased slightly with the addition of GO providing more hydrophilicity to membrane surface. The average CA of pristine PSF was found to be 84.4° while it decreased up to 75.5° with the addition of 0.15 wt% GO. This observation was previously reported in different studies with PSF and other polymers and was related to the hydrophilic nature of GO [75, 90, 233]. The decrease in CA was more obvious with the addition of rGO-PDA particles. This observation can be

linked to the abundant hydroxyl groups of PDA grafted on the surface and between GO sheets [115]. The average CA of PSF/rGO-PDA composite membranes ranged between 73.2° and 74.6°. The observed CA values for both PSF/GO and PSF/rGO-PDA composites are lying in the same range (70° – 80°) of other PSF/GO-based MMMs reported in literature [90, 235, 341]. Although the measured CA values of the membranes do not show significant improvement, the GO and rGO-PDA particles are expected to have more effect on pores hydrophilicity than the surface hydrophilicity. This can be confirmed from the SEM images that show higher distribution of nanoparticles within the membrane pores and polymer wall than this on the surface. Additionally, rGO-PDA particles have much higher hydrophilicity than the pristine GO particles as confirmed by the CA measurements in Section 4.2.4 accompanied with better distribution within the membrane matrix as confirmed by SEM images in Figure 4-25. This suggests higher pore hydrophilicity of PSF/rGO-PDA MMMs than this of PSF/GO MMMs.

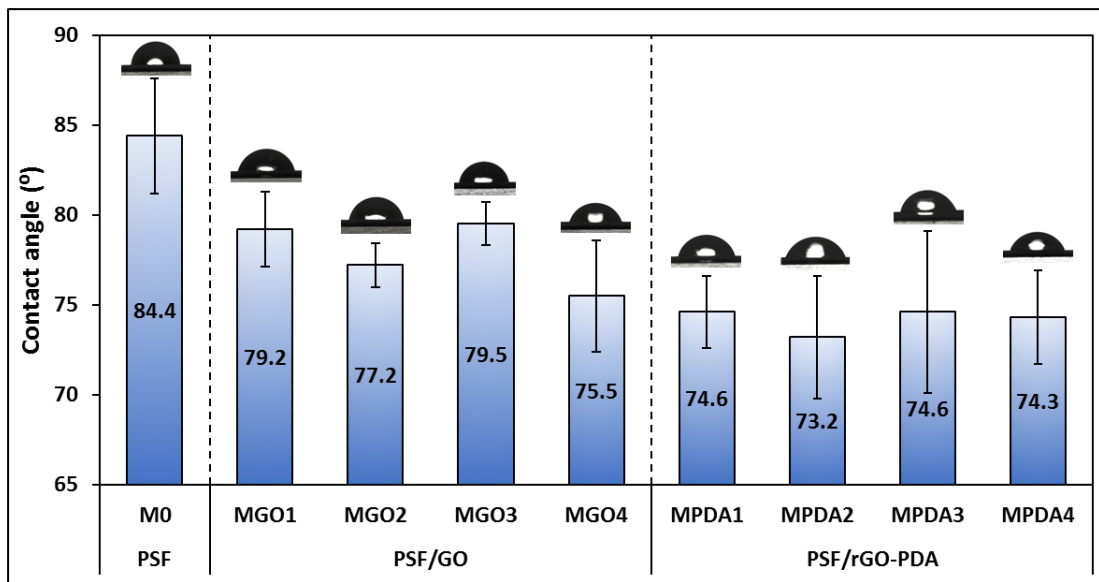


Figure 4-27: Contact angle values of the pristine PSF, PSF/GO, and PSF/rGO-PDA composite membranes.

The overall porosity (ϵ) and the mean pore size (R_m) of the prepared membranes are listed in Table 4-8. With the addition of 0.02 wt% of GO and rGO-PDA, the porosity of PSF increased from 81.2% to 86.6% and 87.7%, respectively. This can be explained by the increase of mass-transfer rate between the solvent (NMP) and non-solvent (DIW) during the phase inversion process caused by the addition of hydrophilic nanofiller, namely GO and rGO-PDA [239]. However, with further increase of the both nanofillers concentration, the porosity decreases. Excessive loadings of the nanofiller increase the viscosity of the casting solution which delays the de-mixing during the phase inversion process and leads to lower porosity and the formation of smaller pores [230]. The estimated mean pore size (r_m) of PSF/GO composite membranes was lower than this of the pristine PSF. The mean pore size of the pristine PSF membrane was found to be around 37.5 nm while it ranged between 33 – 36.9 nm for PSF/GO composites. This can be linked to the agglomeration of GO particles inside the pores resulting in a partial blockage as evidenced by the cross-section SEM images. Similar observations have been reported with GO-based MMMs in earlier studies [44, 189, 239]. Conversely, the PSF/rGO-PDA composite membranes exhibited bigger pore sizes than the pristine PSF. This could be attributed to the high dispersibility of rGO-PDA particles in the solvent which prevents the aggregation of rGO-PDA particles inside the pores as confirmed by the SEM images.

Table 4-8: The average values of the membrane thickness (l), porosity (ϵ), and mean pore size (r_m) of the prepared membranes.

Membrane	l (μm)	ϵ (%)	r_m (nm)
M_0	205.3 ± 0.5	81.2 ± 0.1	37.5 ± 0.1
M_{GO1}	188.3 ± 4.2	86.6 ± 5.1	33.7 ± 2.1
M_{GO2}	174.3 ± 2.6	85.5 ± 0.2	34.4 ± 0.1
M_{GO3}	255 ± 2.9	82.9 ± 0.1	36.9 ± 0.0
M_{GO4}	208.9 ± 3.4	79.9 ± 2.8	33.0 ± 1.1
M_{PDA1}	161.2 ± 3.5	87.7 ± 2.9	37.5 ± 1.6
M_{PDA2}	206.3 ± 5.1	79 ± 2.1	48.2 ± 2.2
M_{PDA3}	200.7 ± 0.9	80.5 ± 1.1	50.6 ± 0.9
M_{PDA4}	210.4 ± 0.5	78.7 ± 0.2	42.7 ± 1.3

4.4 Permeability & Separation Performance

The pure water permeability (PWP) of the prepared membranes are depicted in Figure 4-28. The PWP of the pristine PSF was recorded to be 182.9 ± 4.5 LMH/bar. With low concentration of the pristine GO (0.02 wt%), the PWP was not significantly affected (181.1 ± 9.4 LMH/bar). However, with further loadings of the GO particles, membranes exhibited clear decreases in the PWP to 166.5 ± 10.5 , 164.5 ± 2.7 , and 132.8 ± 3.7 LMH/bar for M_{GO2} , M_{GO3} , and M_{GO4} , respectively. On the other hand, the PWP was significantly enhanced with the embedding of rGO-PDA nanoparticles. The PWP values of PSF/rGO-PDA composite membranes were found to be 241.5 ± 13.7 , 291.9 ± 8.1 , and 326.5 ± 10.3 LMH/bar for M_{PDA1} , M_{PDA2} , and M_{PDA3} , respectively. The PWP was then decreased to 212.9 ± 10 LMH/bar with excessive loadings of rGO-PDA particles (0.15 wt%). The flux reduction upon high loadings of nanomaterial have been previously reported in several studies [90, 233, 234] and can be attributed to the presence of a tipping mass percentage of nanofiller [240, 242]. The embedding of a hydrophilic nanofiller changes the overall hydrophilicity of the casting solution which accelerates the solvent and non-solvent

exchange during phase inversion process. However, excessive loadings of the nanomaterial increase the viscosity of the casting solution resulting in porosity and pore size reduction as shown in the results obtained from porosity and pore size measurements in Section 4.3.2. The tipping mass percentage is a critical point after which the permeability decreases because of the increase in casting solution viscosity [239, 242]. It varies depending on the type of nanofiller and polymer [90]. Therefore, the results herein suggest a tipping mass percentage < 0.02 wt% for the pristine GO and < 0.1 wt% for rGO-PDA particles. These findings can be confirmed by the viscosity measurements of the casting solutions of M_0 , M_{GO3} and M_{PDA3} presented in Figure B5 in Appendix B. The addition of 0.1 wt% GO-PDA increased the viscosity of the casting solution by approximately 11%. However, the viscosity was increased by approximately 76% with the addition of 0.1 wt% pristine GO. Similar observations were recently reported by Alammari et al. [236] where the viscosity increase was higher with pristine GO particles than this with rGO particles. The significant increase in the dope solution viscosity resulted in the formation of a semi-dense top layer leading to the reduction in water flux [64].

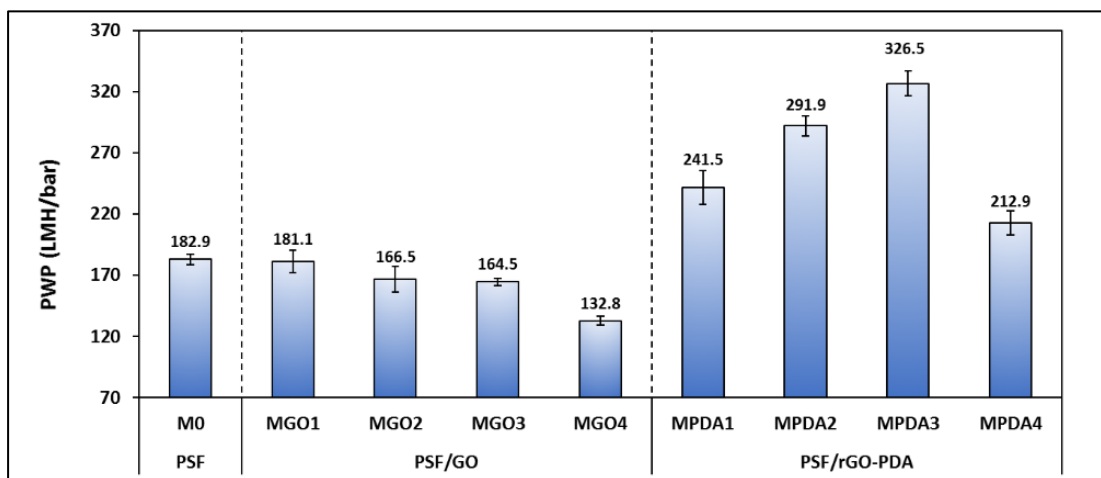


Figure 4-28: The PWP (LMH/bar) of the pristine PSF, PSF/GO, and PSF/rGO-PDA composite membrane (1 bar, 23 °C, 1 h).

Further analysis of the results obtained from PWP, mean pore size, roughness and hydrophilicity measurements helps to elaborate more on the factors affecting the change in PWP. Therefore, a simple data analysis was conducted (Microsoft Excel) to find the correlation coefficient between the PWP and the average roughness (Ra), and contact angle (CA). The correlation coefficient is a statistical measure that indicates the strength of the linear relationship between two variables by measuring and relating the variance and standard deviation of each variable as shown in Eq.13.

$$Correl(A, B) = \frac{Covariance(A,B)}{Std.Dev A \times Std.Dev B} \quad (13)$$

The output of the correlation test is presented in Table B1 in Appendix B. Figure 4-29 depicts the plots of the PWP against other parameters. The findings suggest that the PWP, of membranes studied herein, is more affected by the average roughness with a correlation factor of 0.7614 (Figure 4-29b) followed by CA with slight correlation of -0.5236 (Figure 4-29a). Figure 4-29c shows that CA is affected by the surface roughness with a correlation factor of -0.8205. It has been reported that for hydrophilic surfaces ($CA < 90^\circ$), the increase in surface roughness leads to a decrease in contact angle and vice versa for hydrophobic surfaces ($CA > 90^\circ$) [342, 343]. This can explain the slight increase in MMMs hydrophilicity at low concentrations of nanoparticles. This also suggests a dominance of the surface roughness (Ra) on the water permeability compared to other factors like contact angle and membrane porosity. This agrees with some findings in the literature [344, 345], while other studies showed the porosity to have higher impact on the membrane permeability [90, 346].

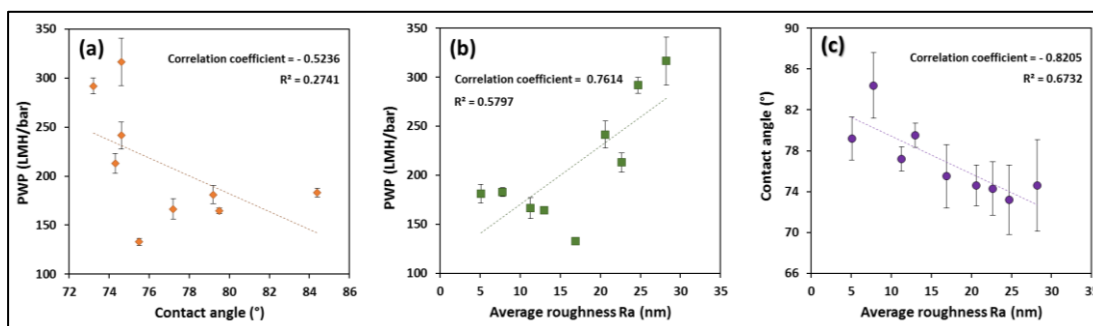


Figure 4-29: The correlations of the PWP with (a) water contact angle (CA), (b) average roughness (Ra), and (d) the correlation of CA with Ra.

The separation performance was studied by the filtration of 500 ppm BSA and 25 ppm HA solutions. All tested membranes, including the pristine PSF, exhibited a complete rejection of both BSA and HA (virtually 100%). Similar findings have been reported by different studies [76, 230, 238, 251]. The rejection performance of M_0 , M_{GO3} , and M_{PDA3} with four other aqueous solutions containing different dyes with small molecules were also tested and presented in Figure 4-31. The SO (350.88 Da) and ORII (350.32 Da) dyes were tested to find the rejection properties of the two dyes as they have almost similar molecular weight. The rejection of SO dye ranged between 18.5 and 22.9% while the ORII dye rejection ranged between 31.1 and 35.2%. This could be to the higher affinity of the prepared membranes to reject the negatively charged molecules (e.g. ORII) than the positively charged molecules (e.g. SO). PSF membranes were reported in several studies to exhibit negative surface charge at $pH > 6$ [347]. The rejection of the MB (799.81 Da) was found to be 88.2 ± 1.2 , 90.6 ± 0.4 , and 87 ± 1.2 % with M_0 , M_{GO3} , and M_{PDA3} , respectively; while all these membranes exhibited excellent rejection ($> 98.5\%$) of DR80 (1373.07 Da). Figure 4-31a and b show photographs of the feed and permeate samples during the filtration of DR80 and MB dyes, respectively.

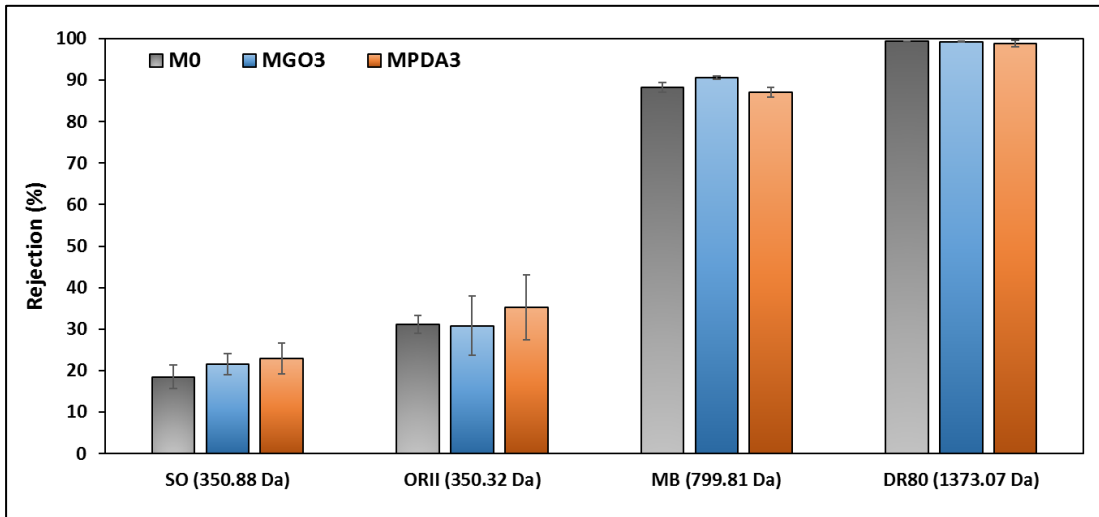


Figure 4-30: Dyes rejection performance of M₀, M_{GO3}, and M_{PDA3} (25 ppm dye concentration, 1 bar, 23 °C, 1 h)

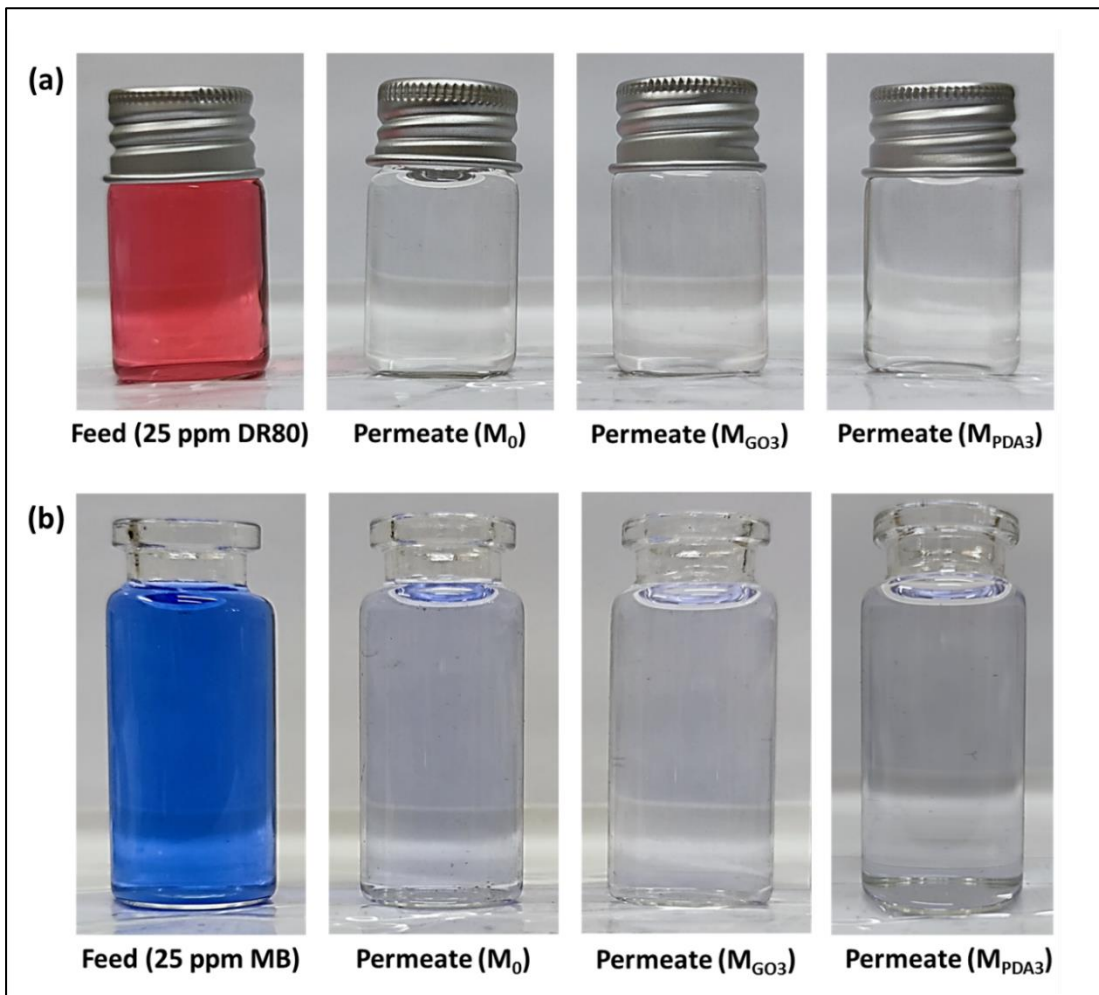


Figure 4-31: Photographs of the feed and permeate sample from the filtration experiments of (a) DR80 and (b) MB dyes.

Generally, the rejection mechanisms in membranes include sieving (size-based), charge, and adsorption-based mechanisms; and for UF membranes, sieving is considered the key mechanism of rejection [90]. However, it can be clearly seen from the dyes rejection results that the pristine PSF and the composite membranes exhibit almost similar rejection performance regardless of the differences in their mean pore size. Also, the rejection values of DR80 and MB are considered high for ultrafiltration membranes. This performance was reported with some GO-based UF membranes against low molecular weight dyes such as PES/GO (~90% rejection of Sunset Yellow dye, 452.4 Da) [82], PVDF/rGO-SiO₂ and CA/rGO-PDA-g-C₃N₄ (99.8% rejection of Methylene Blue, 319.85 Da) [130, 237]. These findings suggest that the separation performance of these membranes is not only dependent on the physical sieving and might be affected by the surface charge and additional interactions (e.g. adsorption mechanisms), indicating that the prepared membranes can be utilized in the treatment of different types of wastewater.

4.5 Antifouling Properties

The fouling resistance is one of the key properties of a good-performance membrane. The filtration process typically leads to the blockage of membrane pores, formation of cake layers on the membrane surface and concentration polarization [348]. In the current study, it was observed that all membranes exhibited a flux decline after switching the feed from pure water to BSA or HA solutions. This can be attributed to the formation of foulant layers as a result of the deposition of BSA or HA molecules onto the membranes surface. After 30 min of membrane washing with DIW, the pure water flux was partially recovered for all membranes and the flux recovery ratio of the first fouling cycle (FRR₁) was then calculated. The second and

third fouling cycles were performed under the same conditions (1 h filtration followed by 30 min washing) and the corresponding recovery values were calculated (FRR₂ and FRR₃). The antifouling performance of the tested membranes represented by their FRR against BSA and HA are depicted in Figure 4-32a and b, respectively.

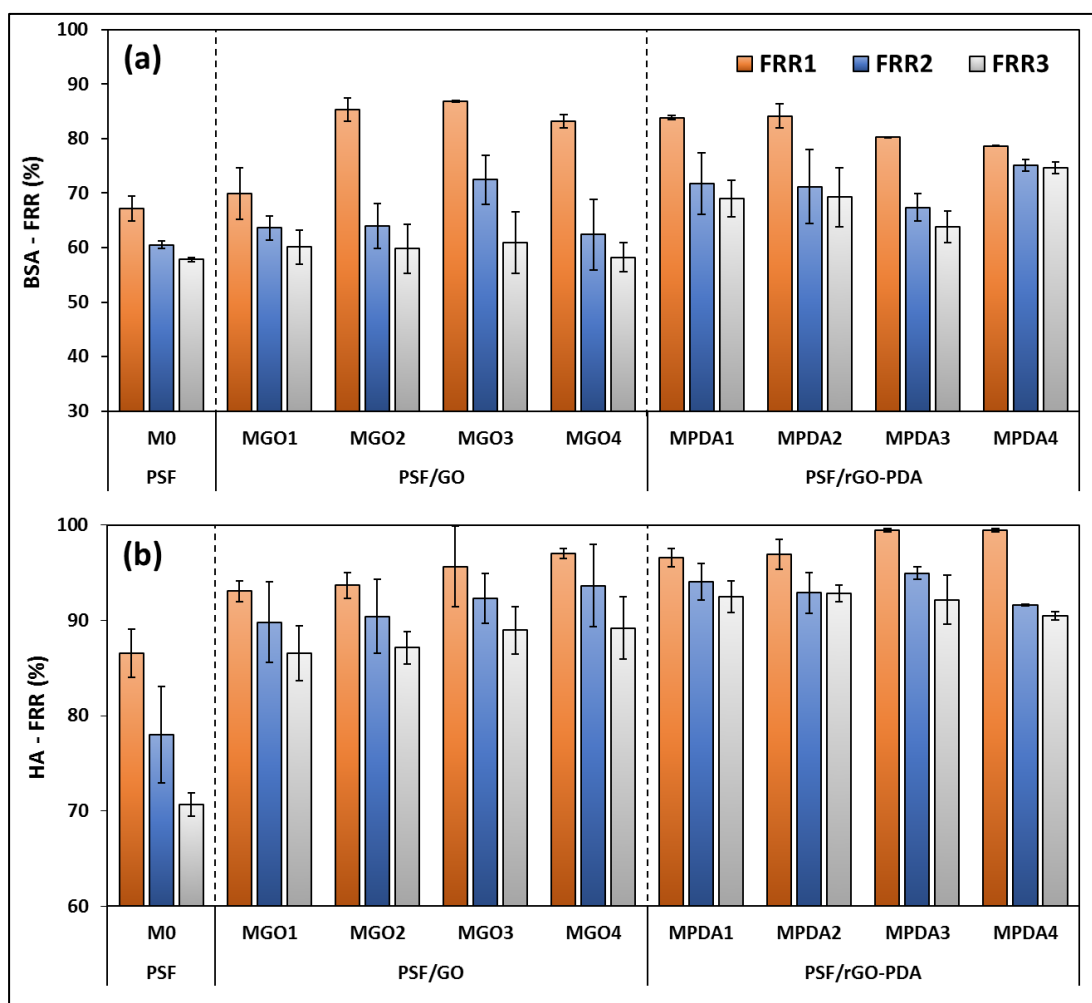


Figure 4-32: The flux recovery ratio (FRR%) of the tested membranes against (a) BSA and (b) HA.

Obviously, all PSF/GO and PSF/rGO-PDA composite membranes exhibited higher FRR compared to the pristine PSF. FRR₁, FRR₂, and FRR₃ of the pristine PSF against BSA were found to be 67.2 ± 2.2 %, 60.5 ± 0.7 %, and 57.8 ± 0.4 %, respectively.

respectively. M_{GO3} (PSF/GO-0.1) exhibited the highest recovery ratio in the first cycle ($86.9 \pm 0.1\%$) and then decreased to $72.5 \pm 4.5\%$ and $60.9 \pm 5.6\%$ in the second and third cycles, respectively. The highest BSA-FRR among the PSF/rGO-PDA composite membranes were obtained with M_{PDA2} (PSF/rGO-PDA-0.05) with FRR₁, FRR₂, and FRR₃ of $84.2 \pm 2.2\%$, $71.2 \pm 6.8\%$, and $69.2 \pm 3.3\%$, respectively. Interestingly, after 3 cycles of protein fouling, the flux recovery (FRR₃) of PSF/rGO-PDA composites were found to be higher than those of PSF/GO composites indicating higher antifouling stability of rGO-PDA based composites in long runs. When using HA as the model foulant, the flux recovery ratios of the pristine PSF were found to be $86.5 \pm 2.5\%$, $78.0 \pm 5.1\%$ and $70.7 \pm 1.2\%$ for FRR₁, FRR₂, and FRR₃, respectively. The highest HA antifouling properties were obtained with M_{PDA3} (PSF/rGO-PDA-0.1) that achieved $99.4 \pm 0.2\%$, $94.9 \pm 0.7\%$, and $92.1 \pm 2.6\%$ for FRR₁, FRR₂, and FRR₃, respectively. The highest FRRs among the PSF/GO composites was obtained with M_{GO4} (PSF/GO-0.15) with $97.0 \pm 0.5\%$, $93.6 \pm 4.3\%$, and $89.2 \pm 3.3\%$ for FRR₁, FRR₂, and FRR₃, respectively.

For further analysis of the fouling resistance of the tested membranes, R_t , R_r and R_{ir} of cycle 1 were estimated and presented in Figure 4-33a and b for BSA and HA, respectively. As depicted by Figure 4-33a, all composite membranes exhibited lower total fouling ratio (R_t) and irreversible fouling ratio (R_{ir}) with higher reversible ratio (R_r) compared to those of the pristine PSF against BSA. The reversible fouling (R_r) of the pristine PSF was 6.2% which was elevated to 10.8% and 15% with 0.1wt% addition of GO and rGO-PDA, respectively. With HA fouling, the reversible fouling ratio was not enhanced with GO addition, while it was elevated up to 14.6% and 28.5% with M_{PDA3} and M_{PDA4} , respectively, compared to 7.5% of the pristine PSF membrane. These results indicate higher fouling resistance against protein and

organic fouling of the PSF/rGO-PDA composite membranes compared to the pristine PSF and PSF/GO composite membranes.

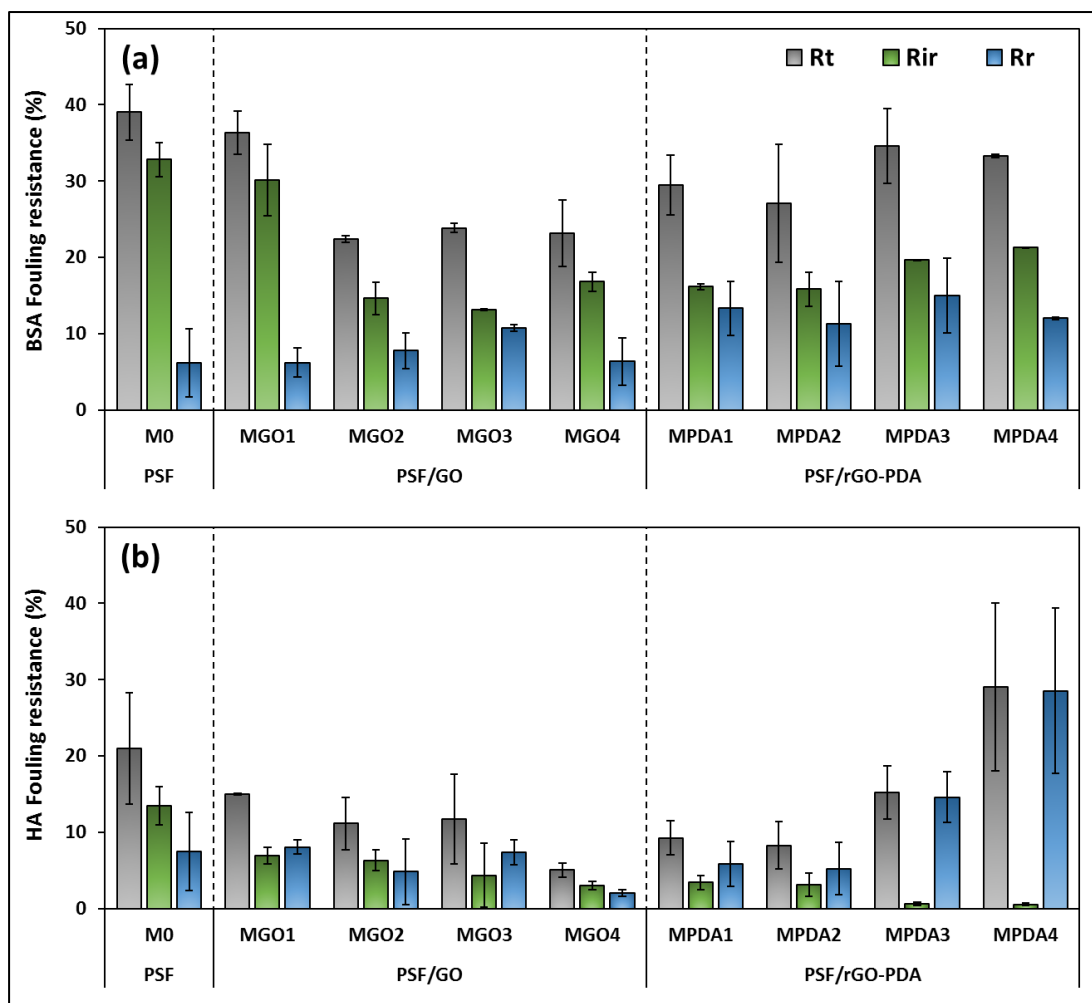


Figure 4-33: The fouling resistance parameters (cycle 1) of the tested membranes against (a) BSA and (b) HA.

It is well established that both surface hydrophilicity, pore size, and roughness affect the membranes antifouling properties [104]. As elaborated in the morphological study above, both PSF/GO and PSF/rGO-PDA composites showed higher surface roughness and hydrophilicity than the pristine PSF. Therefore, in the first stage of foulant filtration, foulant molecules accumulate in the valleys and the pores because of the high surface roughness leading to clear reduction in the flux. During the

washing step with water, GO and rGO-PDA particles attached to the pores and on the surface enhance the removal of foulants by water due to their hydrophilicity [104, 231, 251]. Therefore, the FRRs of all composite membranes were higher than this of the pristine PSF. Similar observations were reported by Yang et al. where the FRR increased disregards the increase in surface roughness [194]. To further investigate the effect of hydrophilicity on the membranes fouling resistance, the correlation coefficient between FRR₃ and CA was calculated and depicted in Figure 4-34.

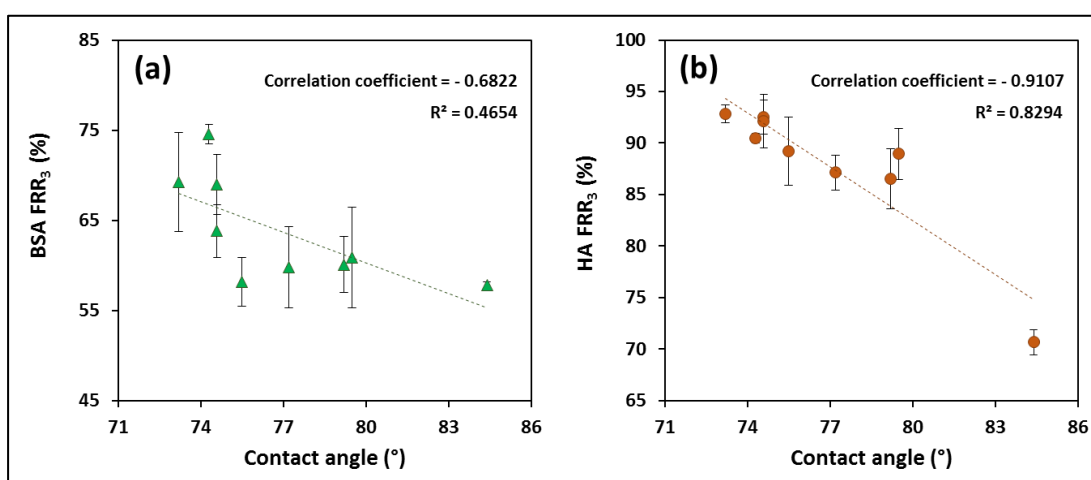


Figure 4-34: The correlations of the (a) BSA FRR₃ and (b) HA FRR₃ with the contact angle.

Clearly, the resistance against both foulants are affected by the membrane's hydrophilicity. The HA fouling resistance is highly dependent on the hydrophilicity as shown in Figure 4-34b, while the BSA FRR₃ have lower correlation. This can be explained by the penetration and accumulation of BSA molecules into the pores, which impedes their removal during the membrane washing. In contrast, HA molecules have lower possibility to penetrate into the pores due to their higher molecular sizes and hence can be easily washed out from the surface [349]. Consequently, it can be concluded from these results that the antifouling properties, of

these membranes, were mainly enhanced by the hydrophilic nature of GO and rGO-PDA nanoparticles. Figure 4-35 shows photographs of the washed pristine PSF, M_{GO4} , and M_{PDA4} after the third fouling cycle with HA. The photographs of BSA-fouled membranes were not shown as BSA is almost colorless on membrane surface.

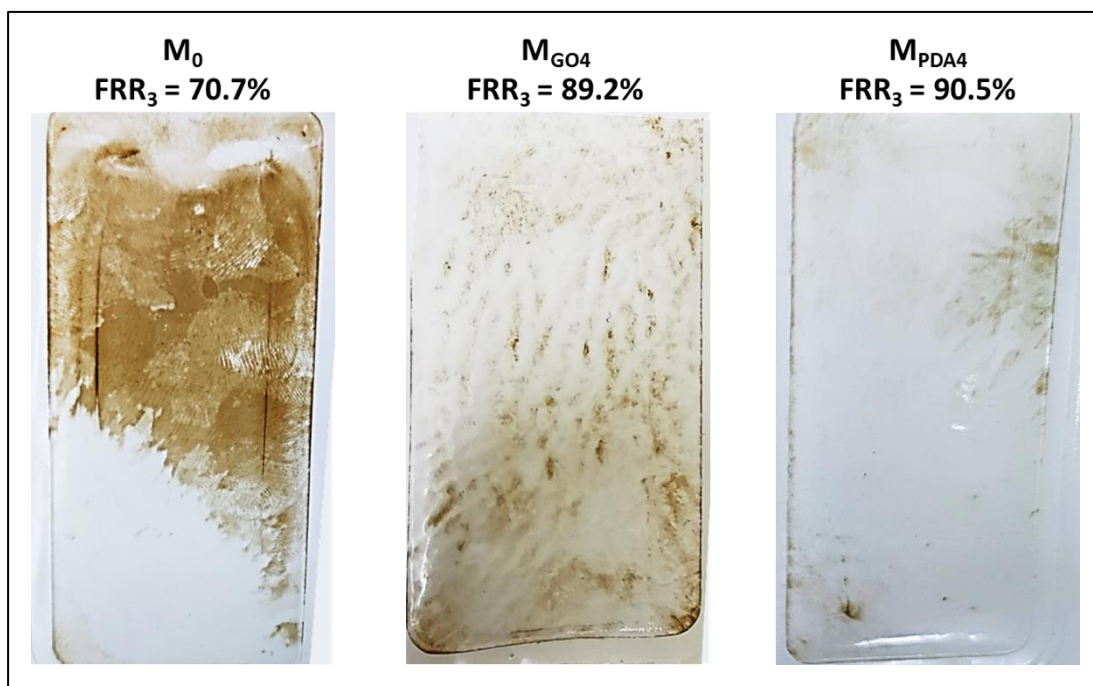


Figure 4-35: Photographs of M_0 , M_{GO4} , and M_{PDA4} after the third cycle of HA fouling.

4.6 Comparison with the Literature

Based on the permeability, rejection, and antifouling measurements, it can be concluded that the optimum nanoparticles concentration for both PSF/GO and PSF/rGO-PDA MMMs is 0.1 wt%. Therefore, the optimum membranes were considered to be M_{GO3} and M_{PDA3} . Table 4-9 compares the performance of M_{GO3} and M_{PDA3} with other GO-based UF composite membranes reported in literature that are fabricated using the same technique (NIPS approach). The comparison was performed in terms of the PWP, rejection, and FRR_1 . Obviously, M_{PDA3} performs better than most of PSF MMMs incorporating different GO-based materials reported in literature

either with respect to the flux, rejection, fouling resistance, or with respect to the overall performance. Zambare et al. [64] investigated the effect of GO oxidation degree on the PSF microstructure and the overall performance. It was found that the highest performance was obtained with membranes embedding GO nanoparticles of high oxidation degree. The authors related this performance to the higher dispersibility of these nanoparticles in the solvent and the uniform distribution within the polymer matrix. With 1% of GO nanoparticles, the flux was 249.5 LMH/bar and the BSA rejection and FRR% were 97.2% and 99%, respectively. When increasing the concentration to 2% of GO, the flux enhanced up to 352.2 while the rejection and FRR declined to 88.6% and 71.9%, respectively, indicating a trade-off between the flux and rejection. Jiang et al. [90] embedded pristine GO (p-GO) and crumpled GO (CGO) nanoparticles into PSF MMMs and reported that the embedding of p-GO nanoparticles enhanced the flux of PSF while the CGO nanoparticles lowered the flux. The authors linked this to the lower dispersibility of CGO particles caused by the shape effect. However, the MO dyes rejection was approximately 27% higher with CGO than p-GO nanoparticles accompanied with slight enhancement in the BSA fouling resistance (76.3% FRR). PSF MMMs embedding GOQD (PSF/GOQD) were found to have also complete rejection of BSA with good antifouling properties (~85% FRR) [249]. However, these membranes were found to have lower flux than other UF membranes reported in literature.

When compared to GO-MMMs made of other polymers, M_{PDA3} was also found to perform as well as or better than most of these membranes. Most of these membranes have a trade-off between the flux, rejection and the antifouling properties. Liu et al. [244] fabricated high-flux PVDF membranes embedding perfluorosulfonic acid-grafted GO nanoparticles (PFSA-g-GO). The optimum membrane (PVDF/PFSA-

g-GO-0.5%) exhibited a PWP of 587.4 LMH/bar with an FRR of 90.8% against BSA. However, the rejection of BSA and HA were 93.9 and 79.6%, respectively which is lower than this of other UF membranes. PVDF MMMs embedding GO-ZnO nanocomposite were also found to have high antifouling properties against BSA [198]. However, the PWP and BSA rejection of these membranes were 170.7 LMH/bar and 92%, respectively. Similar findings were also obtained with PVDF MMMs embedding TiO₂-GO nanocomposite [199]. Several PES MMMs embedding different types of GO-based nanomaterials were also reported with varying performance. Some of these membranes suffer from the low flux such as PES/CSGO [45] and PES/ZIF-8-GO [110] while other membranes suffer from the low fouling resistance such as PES/GO-Ag [140] and PES/GO [82]. On the other hand, some literature reported high performing GO-based MMMs with respect to flux, rejection and antifouling properties like PES/SPSF/GO [76], PES/GO [238], and PES/Co₃O₄-GO [233].

Additionally, it can be clearly noticed from the table that composite membranes incorporating pristine GO nanoparticles [64, 82, 83, 194] suffer from the low FRR (<75%) against BSA fouling. In contrast, composite membranes embedding functional GO structures generally exhibit high fouling resistance (~90%) [104, 199]. This emphasizes on the importance of GO functionalization on GO properties as well as on the overall membrane's performance. However, proper selection of the functional material should be considered to avoid the trade-off between the performance parameters and to produce high-performance membrane with high antifouling properties.

Table 4-9: Performance comparison of the MMMs prepared in this work with other GO-based UF MMMs prepared by phase inversion in literature.

Membrane	Feed composition (ppm)	Conditions	PWP (LMH/bar)	Rejection %	FRR ₁ %	Year & Ref.
PES/CSGO	1000 ppm BSA	Dead-end, 2 bar, 1 h	41.3	99.8	92.1	2020 [45]
PSF/GO	1000 ppm BSA	Cross-flow, 1 bar, 100 min	352.2	88.6	71.9	2020 [64]
PVDF/PFSA-g-GO	500 ppm BSA and HA	Dead-end, 1 bar, 30 min	587.4	R _{BSA} = 93.9 R _{HA} = 79.6	90.8	2020 [244]
SPES/GO-SiO ₂ -NH ₂	100 ppm BSA, HA and SA	Dead-end, 2 bar, 2 h	268.5	R _{BSA} =92.8±0.7 R _{HA} =97±0.4 R _{SA} =89.7±0.6	FRR _{BSA} = 82 FRR _{HA} = 91 FRR _{SA} = 95	2020 [36]
PVDF/GO-ZnO	500 ppm BSA	Cross-flow, 1 bar, 1 h	170.73	92	92.79	2020 [198]
PES/ZIF-8-GO	1000 ppm BSA	Cross-flow, 1 bar, 90 min	95.49	> 95	84.4	2020 [110]
PSF/GO-TiO ₂	500 ppm BSA	Dead-end, 3 bar	165.4	96.6	75.8	2020 [247]
PSF/GOQD	500 ppm BSA	Dead-end, 1 bar, 2 h	130.54	100	~ 85	2019 [249]
PSF/GFG	200 ppm BSA	Cross-flow, 1 bar, 1 h	217	95.2	82.4	2019 [100]
PES/SPSF/GO	1000 ppm BSA	Cross-flow, 1 bar, 1 h	816.9	99.5	94.2	2019 [76]
PSF/CGO	1000 ppm BSA, 10 ppm Methyl Orange (MO) dye	Dead-end, 1 bar, 2 h	48.8 ± 3.7	R _{BSA} = 100 R _{MO} =52.7	76.3 ± 17	2019 [90]
PES/GO	50 ppm HA	Dead-end, 1 bar, 2 h	340	94.5	95	2019 [238]
PVDF/TiO ₂ -GO	1000 ppm BSA	Cross-flow, 1 bar	199.97	91.38	89.22	2019 [199]
PES/GO	1000 ppm BSA	Dead-end, 1 bar, 30 min	245	97	75	2018 [82]
PSF/SGO	1000 ppm BSA	Dead-end, 2 bar, 700 min	175.2	> 98		2018 [230]
PSF/Fe ₃ O ₄ -GO	20 ppm HA	Dead-end, 1 bar	156.99	84	-	2017 [350]
PVC/GO	1000 ppm BSA	Dead-end, 1 bar, 20 min	430	91.2	70.4	2016 [83]
PES/GO-Ag	500 ppm BSA	Dead-end, 3 bar, 90 min	143.3	98	67.2	2015 [140]
PES/Co ₃ O ₄ -GO	1000 ppm BSA	Dead-end, 1 bar, 2 h	347.9	95	81.1	2015 [233]
PVDF/GO-APTS	1000 ppm BSA	Dead-end, 1 bar, 1 h	401.39	57	> 95	2014 [104]
BPPO/PEI-GO	500 ppm BSA	Cross-flow, 2 bar, 1 h	532.5	91	63	2014 [194]

Membrane	Feed composition (ppm)	Conditions	PWP (LMH/bar)	Rejection %	FRR ₁ %	Year & Ref.
PVDF/GO	1000 ppm BSA	Dead-end, 1 bar	~ 90	~ 85	90	2014 [75]
PSF/Isocyanate-GO	1000 ppm BSA	Cross-flow, 1 bar, 2 h	135	95	40.27	2013 [235]
PSF/rGO-PDA-0.1 (M _{PDA3})	500 ppm BSA 25 ppm HA 25 ppm SO, ORII, MB and DR80 dyes	Cross-flow, 1 bar, 1 h	326.5 ± 10.3	R _{BSA} =R _{HA} = 100 R _{SO} = 22.9 ± 3.8 R _{ORII} = 35.2 ± 7.8 R _{MB} = 87 ± 1.2 R _{DR80} = 98.8 ± 0.7	FRR _{BSA} = 80.4 FRR _{HA} = 99.4	Present study
PSF/GO-0.1 (M _{GO3})	500 ppm BSA 25 ppm HA 25 ppm SO, ORII, MB and DR80 dyes	Cross-flow, 1 bar, 1 h	164.5 ± 2.7	R _{BSA} =R _{HA} = 100 R _{SO} = 21.5 ± 2.5 R _{ORII} = 30.8 ± 7.1 R _{MB} = 90.6 ± 0.4 R _{DR80} = 99.2 ± 0.1	FRR _{BSA} = 86.9 FRR _{HA} = 95.4	Present study

CHAPTER 5: CONCLUSIONS & FUTURE WORK

Amongst the various nanofillers utilized in membrane technology, GO and its derivatives gained a remarkable interest in the recent years in academia and practical applications. Owing to their unique and tunable properties, several GO-based materials have been developed and customized for this aspect. As per the review provided in Chapter 2, much work has been done in utilizing pristine GO (p-GO) and functionalized GO (f-GO) particles as membranes nanofillers to produce different membranes and for different purposes. Based on the GO embedding method, these membranes were classified into MMMs, PRL, TFN, s-TFC, i-TFC, m-TFC and free-standing GO membranes. The performance of these membranes in terms of flux, rejection, and antifouling properties with pressure, thermal, and concentration-driven membrane processes was also reviewed and discussed.

The incorporation of p-GO nanoparticles was reported to enhance the membranes performance in few studies; though, more studies reported a deterioration in the performance of p-GO-based membranes. This variation in the performance of p-GO-based membranes could be attributed to several factors including the flake size, shape, and oxygen content of p-GO particles. One of the major challenges being faced when using p-GO as nanofiller is the tendency to aggregate caused by their poor dispersibility in some solvents. Therefore, many functionalization methods have been proposed in literature aiming to enhance GO properties and consequently allowing them to achieve their highest potential for improving the performance of GO-based membranes.

Recently, bio-inspired functionalization of nanoparticles with polydopamine (PDA) gained a remarkable attention due to its versatility and unique properties.

Owing to the abundant functional groups on its surface, PDA can significantly enhance the hydrophilic, dispersion, antibacterial and adhesion properties of nanomaterials which increase their potential use for several purposes.

In this dissertation, the use of polydopamine-functionalized graphene oxide (rGO-PDA) nanoparticles as membrane nanofiller has been successfully demonstrated. Starting from natural graphite flakes, a high-oxidation and NO_x-free synthesis of GO nanoparticles was carried out using several variations on the conventional Hummers' method in the absence of NaNO₃, and by varying the reaction temperature, time, and reactant ratios. Benefiting from the self-polymerization, versatility and high adhesive properties of PDA, the prepared GO nanoparticles were functionalized with PDA using a simple temperature-assisted reflux technique. The structural change was evaluated using XRD, FTIR-UATR, Raman spectroscopy, SEM and TEM. Several bands have emerged in the FTIR spectra of the rGO-PDA attributed to the amine groups of PDA confirming the high functionalization degree of GO nanoparticles. Raman spectra and XRD patterns showed different crystalline structures and defects and higher interlayer spacing of rGO-PDA. The change in elemental compositions was confirmed by XPS and CHNSO elemental analysis and showed an emerging N 1s core-level in the rGO-PDA survey spectra corresponding to the amine groups of PDA. Furthermore, the rGO-PDA nanoparticles showed better dispersibility in polar and nonpolar solvents than the pristine GO, accompanied with excellent hydrophilicity expanding their potential use as nanofiller for modifying different membrane materials and types.

To investigate their potential use as membrane nanofillers, the pristine GO and rGO-PDA nanoparticles were embedded into PSF MMMs via the well-known NIPS technique. The influence of both nanofillers on the PSF structural morphological

properties, hydrophilicity, pore size and porosity has been investigated using various analytical techniques. The effect of both nanofillers on the ultrafiltration performance of PSF was investigated with respect to permeability and separation efficiency of different dyes. Furthermore, the dynamic antifouling properties of the prepared membranes against protein and organic fouling were evaluated. Overall, the main outcomes of this dissertation can be summarized by the following points:

1. A NO_x-free and high-oxidation of graphite was carried out using an improved Hummers' method. The highest oxygen content and O/C ratio were found to be 50 wt% and 0.8, respectively, which are considered higher than most of those reported in literature. Additionally, the improved method conducted in this work consumed less oxidants and acids and could achieve high O/C ratio which would have positive impact on cost issues associated with GO production.
2. Highly aminated GO nanoparticles were obtained by the amine-functionalization of GO with PDA.
3. All characterization techniques confirmed the successful functionalization of GO. FTIR-UATR and XPS spectra showed the presence of several nitrogen-containing functional groups corresponding to amine groups of PDA. A partial reduction in oxygen content was also confirmed by the XRD, FTIR-UATR, XPS, and CHNSO elemental analysis caused by the reduction of C=O in functionalized GO. Raman spectra showed the two typical bands of GO (D and G) with a lower I_D/I_G ratio for rGO-PDA suggesting different crystallite properties and defects and lower oxygen content.
4. Two sets of PSF MMMs embedding the pristine GO and rGO-PDA nanoparticles were fabricated via the NIPS approach.

5. Obvious differences in the pore structure were observed by the cross-section SEM images. The pristine GO particles were found to agglomerate in the pores and some regions of the polymer matrix. In contrast, better distribution of rGO-PDA particles in the PSF matrix was confirmed by the SEM images owing to the high dispersity of rGO-PDA in NMP.
6. The increase in membrane surface roughness was much higher when embedding rGO-PDA nanoparticles than this with the pristine GO nanoparticles.
7. The performance of the prepared membranes with respect to their permeability, separation, and antifouling properties were evaluated using a cross-flow membrane filtration system.
8. The pure water flux was enhanced with the embedding of rGO-PDA while a flux decline was observed with the embedding of pristine GO nanoparticles. This can be attributed to the better distribution of rGO-PDA in the polymer matrix than the pristine GO nanoparticles that were found to aggregate and block the pores as confirmed by the SEM images.
9. The optimum concentration of both GO and rGO-PDA in PSF was found to be 0.1 wt% after which the flux decreases as a result of the increase in the dope solution viscosity. Therefore, the optimum membranes among the two membrane sets are $M_{\text{PDA}3}$ (PSF/rGO-PDA-0.1) and $M_{\text{GO}3}$ (PSF/GO-0.1).
10. The pure water permeability (PWP) of $M_{\text{PDA}3}$ was approximately 1.8 and 2 times higher than this of the pristine PSF (M_0) and $M_{\text{GO}3}$.
11. All the prepared membranes exhibited almost similar rejection performance including M_0 .
12. rGO-PDA-based MMMs showed higher fouling resistance against protein and

organic fouling. After 3 cycles of protein fouling (BSA), M_{PDA3} exhibited a flux recovery ratio (FRR_3) of 74.6% that was approximately 29% and 22% higher than this of M_0 and M_{GO3} . Similarly, against organic fouling represented by humic acid (HA), the FRR_3 of M_{PDA3} was approximately 30% and 3% higher than this of M_0 and M_{GO3} .

Taken together, results reported in this work showed that the incorporation of rGO-PDA nanoparticles could greatly enhance the flux and antifouling properties of PSF ultrafiltration membranes without affecting the rejection performance. The results reported herein are expected to be of a great benefit in protein-rich and NOMs-rich wastewater treatment and provide insights on developing other rGO-PDA-based membranes with different materials and for different purposes.

Numerous lines of research have raised from this dissertation which should be pursued and addressed in the future:

1. Separation and fouling mechanisms of the prepared membranes

The rejection of the prepared membranes will be tested using different conditions (pH, ionic strength of the feed solution, temperatures, etc.) to investigate the mechanisms governing the separation and fouling properties of these membranes.

2. Antibacterial activity of the prepared membranes:

Both GO and PDA were reported to have antibacterial activity against different bacteria. The prepared rGO-PDA could pose higher antibacterial activity as it combines both GO and PDA. Therefore, further analysis will be conducted to evaluate the antibacterial activity of the prepared membranes.

3. Developing other rGO-PDA-based membranes:

The use of rGO-PDA nanoparticles is not limited to the membranes prepared in this work as the high dispersibility would enhance their utilization with different membrane processes and with different materials. For example, it can be used to fabricate other MMMs with other polymers like PVDF and PES due to its high dispersibility in NMP, DMF, and DMA. The high dispersibility in dodecane and hexane allows its usage in the preparation of thin-film nanocomposite (TFN) membranes for NF, RO, and FO applications. Additionally, it can be used in membrane coating by the assembly approaches because of the high dispersibility in water.

4. Effect on the mechanical strength:

Some studies reported a deterioration in the membrane performance, low stability, or a deformation in the membrane structure resulted from the embedding of nanoparticles into the membrane. Therefore, the effect of GO nanoparticles embedding on the membrane's mechanical strength should be investigated.

5. The effect of GO surface chemistry and characteristics on the membrane performance with various membrane processes need to be adequately investigated. This would give insights on new ways to synthesize functional GO materials (f-GO) and tailoring them for the desired applications at which they can achieve their highest potential.

LIST OF PUBLICATIONS

Four articles in peer-reviewed journals and two conference proceedings have been published from this dissertation. Following is the list of the publications:

1. Alkhouzaam, A. and H. Qiblawey, Functional GO-based membranes for water treatment and desalination: fabrication methods, performance and advantages. A review. *Chemosphere*, 2021. 274: p. 129853.
2. Alkhouzaam, A. and H. Qiblawey, Novel polysulfone ultrafiltration membranes incorporating polydopamine functionalized graphene oxide with enhanced flux and fouling resistance. *Journal of Membrane Science*, 2021. 620: p. 118900.
3. Alkhouzaam, A., H. Qiblawey, and M. Khraisheh, Polydopamine Functionalized Graphene Oxide as Membrane Nanofiller: Spectral and Structural Studies. *Membranes*, 2021. 11(2): p. 86.
4. A. Alkhouzaam, H. Qiblawey, M. Khraisheh, M. Atieh, M. Al-Ghouti, Synthesis of graphene oxides particle of high oxidation degree using a modified Hummers method, *Ceramics International*, 46 (2020) 23997-24007.
5. A.I. Alkhouzaam, H. Qiblawey, M. Khraisheh, Synthesis of High-Antifouling and Antibacterial Ultrafiltration Membranes Incorporating Low Concentrations of Graphene Oxide, in: *Qatar University Annual Research Forum and Exhibition (QUARFE 2020)*, Qatar University Press, Doha, Qatar, 2020.
6. A. Alkhouzaam, H. Qiblawey, M. Khraisheh, Synthesis of High-Antifouling Ultrafiltration Polysulfone Membranes Incorporating Low Concentrations of Graphene Oxide, in: *International Conference on Wastewater Treatment, Water Cycle and Water Pollution (ICWTWCWP 2019)*, Istanbul, Turkey, December 2019.

REFERENCES

1. Yang, Z., X.-H. Ma, and C.Y. Tang, *Recent development of novel membranes for desalination*. Desalination, 2018. **434**: p. 37-59.
2. Shannon, M.A., et al., *Science and technology for water purification in the coming decades*. Nature, 2008. **452**(7185): p. 301-310.
3. Ashfaq, M.Y., et al., *Use of DPSIR Framework to Analyze Water Resources in Qatar and Overview of Reverse Osmosis as an Environment Friendly Technology*. Environmental Progress & Sustainable Energy, 2019. **38**(4): p. 13081.
4. Aghigh, A., et al., *Recent advances in utilization of graphene for filtration and desalination of water: A review*. Desalination, 2015. **365**: p. 389-397.
5. Albatrni, H., H. Qiblawey, and M.H. El-Naas, *Comparative study between adsorption and membrane technologies for the removal of mercury*. Separation and Purification Technology, 2021. **257**: p. 117833.
6. Wang, Z., et al., *Effective desalination by capacitive deionization with functional graphene nanocomposite as novel electrode material*. Desalination, 2012. **299**: p. 96-102.
7. Yao, M., et al., *A review of membrane wettability for the treatment of saline water deploying membrane distillation*. Desalination, 2020. **479**: p. 114312.
8. Zsirai, T., et al., *The impact of mechanical shear on membrane flux and energy demand*. Journal of Membrane Science, 2016. **516**: p. 56-63.
9. Mahmoud, K.A., et al., *Functional graphene nanosheets: The next generation membranes for water desalination*. Desalination, 2015. **356**: p. 208-225.
10. Hafiz, M.A., A.H. Hawari, and A. Altaee, *A hybrid forward osmosis/reverse*

- osmosis process for the supply of fertilizing solution from treated wastewater. Journal of Water Process Engineering, 2019. 32: p. 100975.*
11. Lee, K.P., T.C. Arnot, and D. Mattia, *A review of reverse osmosis membrane materials for desalination—Development to date and future potential. Journal of Membrane Science, 2011. 370(1): p. 1-22.*
 12. Lavanya, C. and R. Geetha Balakrishna, *Naturally derived polysaccharides-modified PSF membranes: A potency in enriching the antifouling nature of membranes. Separation and Purification Technology, 2020. 230: p. 115887.*
 13. Ma, S., et al., *A new strategy to simultaneously improve the permeability and antifouling properties of EVAL membranes via surface segregation of macrocyclic supra-amphiphiles. Journal of Membrane Science, 2019: p. 117562.*
 14. Naik, N.S., et al., *The efficient mixed matrix antifouling membrane for surfactant stabilized oil-in-water nanoemulsion separation. Journal of Water Process Engineering, 2019. 32: p. 100959.*
 15. Hou, S., et al., *Renewable antibacterial and antifouling polysulfone membranes incorporating a PEO-grafted amphiphilic polymer and N-chloramine functional groups. Journal of Colloid and Interface Science, 2019. 554: p. 658-667.*
 16. Chiao, Y.-H., et al., *Zwitterionic forward osmosis membrane modified by fast second interfacial polymerization with enhanced antifouling and antimicrobial properties for produced water pretreatment. Desalination, 2019. 469: p. 114090.*
 17. Zou, D., et al., *Facile co-sintering process to fabricate sustainable antifouling silver nanoparticles (AgNPs)-enhanced tight ceramic ultrafiltration*

- membranes for protein separation*. Journal of Membrane Science, 2020. **593**: p. 117402.
18. Goh, P.S., A.F. Ismail, and N. Hilal, *Nano-enabled membranes technology: Sustainable and revolutionary solutions for membrane desalination?* Desalination, 2016. **380**: p. 100-104.
 19. Song, N., et al., *A review of graphene-based separation membrane: Materials, characteristics, preparation and applications*. Desalination, 2018. **437**: p. 59-72.
 20. Pendergast, M.M. and E.M.V. Hoek, *A review of water treatment membrane nanotechnologies*. Energy & Environmental Science, 2011. **4**(6): p. 1946-1971.
 21. Zhang, N., et al., *Review on structural control and modification of graphene oxide-based membranes in water treatment: From separation performance to robust operation*. Chinese Journal of Chemical Engineering, 2019. **27**(6): p. 1348-1360.
 22. Zhang, Y. and T.-S. Chung, *Graphene oxide membranes for nanofiltration*. Current Opinion in Chemical Engineering, 2017. **16**: p. 9-15.
 23. Khanzada, N.K., et al., *Evaluation of anti-bacterial adhesion performance of polydopamine cross-linked graphene oxide RO membrane via in situ optical coherence tomography*. Desalination, 2020. **479**: p. 114339.
 24. Luque-Allied, J.M., et al., *Polyethersulfone membranes: From ultrafiltration to nanofiltration via the incorporation of APTS functionalized-graphene oxide*. Separation and Purification Technology, 2020. **230**: p. 115836.
 25. Yi, Z., et al., *Adsorption of aniline on aminated chitosan/graphene oxide composite material*. Journal of Molecular Structure, 2020. **1209**: p. 127973.

26. Bai, C., L. Wang, and Z. Zhu, *Adsorption of Cr(III) and Pb(II) by graphene oxide/alginate hydrogel membrane: Characterization, adsorption kinetics, isotherm and thermodynamics studies*. International Journal of Biological Macromolecules, 2020. **147**: p. 898-910.
27. Naeem, H., et al., *Facile synthesis of graphene oxide–silver nanocomposite for decontamination of water from multiple pollutants by adsorption, catalysis and antibacterial activity*. Journal of Environmental Management, 2019. **230**: p. 199-211.
28. Qureshi, K., et al., *Graphene oxide decorated ZnWO₄ architecture synthesis, characterization and photocatalytic activity evaluation*. Journal of Molecular Liquids, 2019. **285**: p. 778-789.
29. Ramesh, P. and B. Jebasingh, *A facile synthesis of bis-(phtthalimidoethyl)-amine functionalized graphene oxide and its dual performance as a supercapacitor electrode and fluorescence sensor*. Materials Chemistry and Physics, 2019. **222**: p. 45-54.
30. Ajdari, F.B., et al., *Melamine-functionalized graphene oxide: Synthesis, characterization and considering as pseudocapacitor electrode material with intermixed POAP polymer*. Applied Surface Science, 2018. **459**: p. 874-883.
31. Ashfaq, M.Y., et al., *Investigating the effect of temperature on calcium sulfate scaling of reverse osmosis membranes using FTIR, SEM-EDX and multivariate analysis*. Science of The Total Environment, 2020. **703**: p. 134726.
32. Zhang, Y., et al., *Thin-film nanocomposite reverse osmosis membranes with enhanced antibacterial resistance by incorporating p-aminophenol-modified graphene oxide*. Separation and Purification Technology, 2020. **234**: p.

116017.

33. Jin, L., et al., *Polyamide-crosslinked graphene oxide membrane for forward osmosis*. Journal of Membrane Science, 2018. **545**: p. 11-18.
34. Xue, S.-M., et al., *Chlorine resistant TFN nanofiltration membrane incorporated with octadecylamine-grafted GO and fluorine-containing monomer*. Journal of Membrane Science, 2018. **545**: p. 185-195.
35. Nakagawa, K., et al., *Fabrication of Stacked Graphene Oxide Nanosheet Membranes Using Triethanolamine as a Crosslinker and Mild Reducing Agent for Water Treatment*. Membranes (Basel), 2018. **8**(4).
36. Kumar, M., et al., *High-Flux, Antifouling Hydrophilized Ultrafiltration Membranes with Tunable Charge Density Combining Sulfonated Poly(ether sulfone) and Aminated Graphene Oxide Nanohybrid*. ACS Applied Materials & Interfaces, 2020. **12**(1): p. 1617-1627.
37. Lu, K.-J., J. Zuo, and T.-S. Chung, *Novel PVDF membranes comprising n-butylamine functionalized graphene oxide for direct contact membrane distillation*. Journal of Membrane Science, 2017. **539**: p. 34-42.
38. Zhao, Z., et al., *Polydopamine functionalized graphene oxide nanocomposites reinforced the corrosion protection and adhesion properties of waterborne polyurethane coatings*. European Polymer Journal, 2019. **120**: p. 109249.
39. Faraji, M., H. Gharibi, and M. Javaheri, *High Pt Loading on Polydopamine Functionalized Graphene as a High Performance Cathode Electrocatalyst for Proton Exchange Membrane Fuel Cells*. Journal of Nanostructures, 2016. **6**(2): p. 156-166.
40. Palanisamy, S., et al., *A Facile Electrochemical Preparation of Reduced Graphene Oxide@Polydopamine Composite: A Novel Electrochemical*

- Sensing Platform for Amperometric Detection of Chlorpromazine*. Scientific Reports, 2016. **6**(1): p. 33599.
41. Guerrero-Contreras, J. and F. Caballero-Briones, *Graphene oxide powders with different oxidation degree, prepared by synthesis variations of the Hummers method*. Materials Chemistry and Physics, 2015. **153**: p. 209-220.
 42. Lim, J.Y., et al., *Recent trends in the synthesis of graphene and graphene oxide based nanomaterials for removal of heavy metals — A review*. Journal of Industrial and Engineering Chemistry, 2018. **66**: p. 29-44.
 43. Yi, Z., et al., *Chemical grafting N-GOQD of polyamide reverse osmosis membrane with improved chlorine resistance, water flux and NaCl rejection*. Desalination, 2020. **479**: p. 114341.
 44. Bandehali, S., et al., *New mixed matrix PEI nanofiltration membrane decorated by glycidyl-POSS functionalized graphene oxide nanoplates with enhanced separation and antifouling behaviour: Heavy metal ions removal*. Separation and Purification Technology, 2020. **242**: p. 116745.
 45. Kong, S., et al., *High-flux and antifouling polyethersulfone nanocomposite membranes incorporated with zwitterion-functionalized graphene oxide for ultrafiltration applications*. Journal of Industrial and Engineering Chemistry, 2020. **84**: p. 131-140.
 46. Reynosa-Martínez, A.C., et al., *Effect of the degree of oxidation of graphene oxide on As(III) adsorption*. Journal of Hazardous Materials, 2020. **384**: p. 121440.
 47. Tu, T.H., et al., *Synthesis and application of graphene oxide aerogel as an adsorbent for removal of dyes from water*. Materials Letters, 2019. **238**: p. 134-137.

48. Luo, J., et al., *Investigation on the optimization, design and microwave absorption properties of BaTb_{0.2}Eu_{0.2}Fe_{11.6}O₁₉/PANI decorated on reduced graphene oxide nanocomposites*. Journal of Materials Science, 2019. **54**(8): p. 6332-6346.
49. Chen, J.-P., et al., *Construction of C-Si heterojunction interface in SiC whisker/reduced graphene oxide aerogels for improving microwave absorption*. Carbon, 2020. **164**: p. 59-68.
50. Ahmad, M.Z., et al., *Graphene oxide supported Fe₂(MoO₄)₃ nano rods assembled round-ball fabrication via hydrothermal route and photocatalytic degradation of nonsteroidal anti-inflammatory drug*. Journal of Molecular Liquids, 2020. **301**: p. 112343.
51. Xiong, Y., et al., *A flexible pressure sensor based on melamine foam capped by copper nanowires and reduced graphene oxide*. Materials Today Communications, 2020. **24**: p. 100970.
52. Alrammouz, R., et al., *Highly porous and flexible capacitive humidity sensor based on self-assembled graphene oxide sheets on a paper substrate*. Sensors and Actuators B: Chemical, 2019. **298**: p. 126892.
53. Lerf, A., et al., *Structure of Graphite Oxide Revisited*. The Journal of Physical Chemistry B, 1998. **102**(23): p. 4477-4482.
54. Stankovich, S., et al., *Graphene-based composite materials*. Nature, 2006. **442**: p. 282.
55. Brodie, B.C., *XIII. On the atomic weight of graphite*. Philosophical Transactions of the Royal Society of London, 1859. **149**: p. 249-259.
56. Chen, J., et al., *High-yield preparation of graphene oxide from small graphite flakes via an improved Hummers method with a simple purification process*.

- Carbon, 2015. **81**: p. 826-834.
57. Hummers, W.S. and R.E. Offeman, *Preparation of graphitic oxide*. Journal of the American Chemical Society, 1958. **80**(6).
 58. Chen, J., et al., *An improved Hummers method for eco-friendly synthesis of graphene oxide*. Carbon, 2013. **64**: p. 225-229.
 59. Alkhouzaam, A., et al., *Synthesis of graphene oxides particle of high oxidation degree using a modified Hummers method*. Ceramics International, 2020. **46**(15): p. 23997-24007.
 60. Yadav, N. and B. Lochab, *A comparative study of graphene oxide: Hummers, intermediate and improved method*. FlatChem, 2019. **13**: p. 40-49.
 61. Krishnamoorthy, K., et al., *The chemical and structural analysis of graphene oxide with different degrees of oxidation*. Carbon, 2013. **53**: p. 38-49.
 62. Joshi, R.K., et al., *Precise and Ultrafast Molecular Sieving Through Graphene Oxide Membranes*. Science, 2014. **343**(6172): p. 752.
 63. Sun, M. and J. Li, *Graphene oxide membranes: Functional structures, preparation and environmental applications*. Nano Today, 2018. **20**: p. 121-137.
 64. Zambare, R.S., et al., *Effect of oxidation degree of GO nanosheets on microstructure and performance of polysulfone-GO mixed matrix membranes*. Separation and Purification Technology, 2020. **244**: p. 116865.
 65. Zhang, L., et al., *Effect of physical and chemical structures of graphene oxide on water permeation in graphene oxide membranes*. Applied Surface Science, 2020. **520**: p. 146308.
 66. Muzyka, R., et al., *Oxidation of graphite by different modified Hummers methods*. New Carbon Materials, 2017. **32**(1): p. 15-20.

67. Chakraborty, S., et al., *High yield synthesis of amine functionalized graphene oxide and its surface properties*. RSC Advances, 2016. **6**(72): p. 67916-67924.
68. Botas, C., et al., *Graphene materials with different structures prepared from the same graphite by the Hummers and Brodie methods*. Carbon, 2013. **65**: p. 156-164.
69. Hou, Y., et al., *High-quality preparation of graphene oxide via the Hummers' method: Understanding the roles of the intercalator, oxidant, and graphite particle size*. Ceramics International, 2020. **46**(2): p. 2392-2402.
70. Al-Gaashani, R., et al., *XPS and structural studies of high quality graphene oxide and reduced graphene oxide prepared by different chemical oxidation methods*. Ceramics International, 2019. **45**(11): p. 14439-14448.
71. Hamdy, G. and A. Taher, *Enhanced chlorine-resistant and low biofouling reverse osmosis polyimide-graphene oxide thin film nanocomposite membranes for water desalination*. Polymer Engineering & Science, 2020. **60**(10): p. 2567-2580.
72. Cao, B., et al., *Gypsum scale formation on graphene oxide modified reverse osmosis membrane*. Journal of Membrane Science, 2018. **552**: p. 132-143.
73. Kang, X., et al., *Spin-assisted interfacial polymerization strategy for graphene oxide-polyamide composite nanofiltration membrane with high performance*. Applied Surface Science, 2020. **508**: p. 145198.
74. Wang, J., et al., *Graphene oxide polypiperazine-amide nanofiltration membrane for improving flux and anti-fouling in water purification*. RSC Advances, 2016. **6**(85): p. 82174-82185.
75. Chang, X., et al., *Exploring the synergetic effects of graphene oxide (GO) and polyvinylpyrrolidone (PVP) on poly(vinylidene fluoride) (PVDF)*

- ultrafiltration membrane performance*. Applied Surface Science, 2014. **316**: p. 537-548.
76. Hu, M., et al., *Ultra-low graphene oxide loading for water permeability, antifouling and antibacterial improvement of polyethersulfone/sulfonated polysulfone ultrafiltration membranes*. Journal of Colloid and Interface Science, 2019. **552**: p. 319-331.
 77. Hu, X., et al., *The improved oil/water separation performance of graphene oxide modified Al₂O₃ microfiltration membrane*. Journal of Membrane Science, 2015. **476**: p. 200-204.
 78. Zhao, C., et al., *Optimization of preparation conditions of poly(vinylidene fluoride)/graphene oxide microfiltration membranes by the Taguchi experimental design*. Desalination, 2014. **334**(1): p. 17-22.
 79. Camacho, L.M., T.A. Pinion, and S.O. Olatunji, *Behavior of mixed-matrix graphene oxide – Polysulfone membranes in the process of direct contact membrane distillation*. Separation and Purification Technology, 2020. **240**: p. 116645.
 80. Halakoo, E. and X. Feng, *Layer-by-layer assembly of polyethyleneimine/graphene oxide membranes for desalination of high-salinity water via pervaporation*. Separation and Purification Technology, 2020. **234**: p. 116077.
 81. Ugur Nigiz, F., *Graphene oxide -sodium alginate membrane for seawater desalination through pervaporation*. Desalination, 2020. **485**: p. 114465.
 82. Abdel-Karim, A., et al., *High flux and fouling resistant flat sheet polyethersulfone membranes incorporated with graphene oxide for ultrafiltration applications*. Chemical Engineering Journal, 2018. **334**: p. 789-

799.

83. Zhao, Y., et al., *Performance enhancement of polyvinyl chloride ultrafiltration membrane modified with graphene oxide*. *Journal of Colloid and Interface Science*, 2016. **480**: p. 1-8.
84. Chen, H., et al., *Separation Performance of Hg²⁺ in Desulfurization Wastewater by the Graphene Oxide Polyethersulfone Membrane*. *Energy & Fuels*, 2019. **33**(9): p. 9241-9248.
85. Lai, G.S., et al., *Graphene oxide incorporated thin film nanocomposite nanofiltration membrane for enhanced salt removal performance*. *Desalination*, 2016. **387**: p. 14-24.
86. Ravishankar, H., J. Christy, and V. Jegatheesan, *Graphene Oxide (GO)-Blended Polysulfone (PSf) Ultrafiltration Membranes for Lead Ion Rejection*. *Membranes*, 2018. **8**(3): p. 77.
87. Alkhouzaam, A.I., H. Qiblawey, and M. Khraisheh. *Synthesis of High-Antifouling and Antibacterial Ultrafiltration Membranes Incorporating Low Concentrations of Graphene Oxide*. in *Qatar University Annual Research Forum and Exhibition (QUARFE 2020)*. 2020. Doha, Qatar: Qatar University Press.
88. Wang, J., et al., *Graphene Oxide as an Effective Barrier on a Porous Nanofibrous Membrane for Water Treatment*. *ACS Applied Materials & Interfaces*, 2016. **8**(9): p. 6211-6218.
89. Chen, K., et al., *Fabrication and properties of graphene oxide-embedded cellulose triacetate RO composite membrane via melting method*. *Desalination*, 2018. **425**: p. 175-184.
90. Jiang, Y., et al., *Graphene oxides as nanofillers in polysulfone ultrafiltration*

- membranes: Shape matters*. Journal of Membrane Science, 2019. **581**: p. 453-461.
91. Fan, X., et al., *Hydrothermal reduced graphene oxide membranes for dyes removing*. Separation and Purification Technology, 2020. **241**: p. 116730.
 92. Chatterjee, S., et al., *Size and synergy effects of nanofiller hybrids including graphene nanoplatelets and carbon nanotubes in mechanical properties of epoxy composites*. Carbon, 2012. **50**(15): p. 5380-5386.
 93. Zhou, Y., et al., *Hydrothermal Dehydration for the “Green” Reduction of Exfoliated Graphene Oxide to Graphene and Demonstration of Tunable Optical Limiting Properties*. Chemistry of Materials, 2009. **21**(13): p. 2950-2956.
 94. Alotaibi, F., et al., *Scanning atmospheric plasma for ultrafast reduction of graphene oxide and fabrication of highly conductive graphene films and patterns*. Carbon, 2018. **127**: p. 113-121.
 95. Chen, L.I.N., C.A. Perfetti, and Y. Leng, *Reading Pinyin activates character orthography for highly experienced learners of Chinese*. Bilingualism: Language and Cognition, 2017. **22**(1): p. 103-111.
 96. Toh, S.Y., et al., *Graphene production via electrochemical reduction of graphene oxide: Synthesis and characterisation*. Chemical Engineering Journal, 2014. **251**: p. 422-434.
 97. Stankovich, S., et al., *Synthesis of graphene-based nanosheets via chemical reduction of exfoliated graphite oxide*. Carbon, 2007. **45**(7): p. 1558-1565.
 98. Zhu, C., et al., *Reducing Sugar: New Functional Molecules for the Green Synthesis of Graphene Nanosheets*. ACS Nano, 2010. **4**(4): p. 2429-2437.
 99. Xu, L.Q., et al., *Dopamine-Induced Reduction and Functionalization of*

- Graphene Oxide Nanosheets*. *Macromolecules*, 2010. **43**(20): p. 8336-8339.
100. Zhang, G., et al., *Guanidyl-functionalized graphene/polysulfone mixed matrix ultrafiltration membrane with superior permselective, antifouling and antibacterial properties for water treatment*. *Journal of Colloid and Interface Science*, 2019. **540**: p. 295-305.
 101. Kim, H.J., et al., *Reverse osmosis nanocomposite membranes containing graphene oxides coated by tannic acid with chlorine-tolerant and antimicrobial properties*. *Journal of Membrane Science*, 2016. **514**: p. 25-34.
 102. Yang, Y., et al., *Rapid co-deposition of graphene oxide incorporated metal-phenolic network/piperazine followed by crosslinking for high flux nanofiltration membranes*. *Journal of Membrane Science*, 2019. **588**: p. 117203.
 103. Ambre, J.P., et al., *High flux hyperbranched starch-graphene oxide piperazinamide composite nanofiltration membrane*. *Journal of Environmental Chemical Engineering*, 2019. **7**(6): p. 103300.
 104. Xu, Z., et al., *Organosilane-functionalized graphene oxide for enhanced antifouling and mechanical properties of polyvinylidene fluoride ultrafiltration membranes*. *Journal of Membrane Science*, 2014. **458**: p. 1-13.
 105. Jiang, Y., et al., *Engineered Crumpled Graphene Oxide Nanocomposite Membrane Assemblies for Advanced Water Treatment Processes*. *Environmental Science & Technology*, 2015. **49**(11): p. 6846-6854.
 106. Thakur, A.K., et al., *Graphene oxide on laser-induced graphene filters for antifouling, electrically conductive ultrafiltration membranes*. *Journal of Membrane Science*, 2019. **591**: p. 117322.
 107. Izadmehr, N., et al., *TETA-anchored graphene oxide enhanced polyamide thin*

- film nanofiltration membrane for water purification; performance and antifouling properties*. Journal of Environmental Management, 2020. **276**: p. 111299.
108. Zhu, J., et al., *Surface zwitterionic functionalized graphene oxide for a novel loose nanofiltration membrane*. Journal of Materials Chemistry A, 2016. **4**(5): p. 1980-1990.
109. Leaper, S., et al., *Flux-enhanced PVDF mixed matrix membranes incorporating APTS-functionalized graphene oxide for membrane distillation*. Journal of Membrane Science, 2018. **554**: p. 309-323.
110. Ahmad, N., et al., *Enhanced performance and antibacterial properties of amine-functionalized ZIF-8-decorated GO for ultrafiltration membrane*. Separation and Purification Technology, 2020. **239**: p. 116554.
111. Shao, W., et al., *Fabrication of pH-sensitive thin-film nanocomposite nanofiltration membranes with enhanced performance by incorporating amine-functionalized graphene oxide*. Applied Surface Science, 2019. **487**: p. 1209-1221.
112. Lee, H., et al., *Mussel-Inspired Surface Chemistry for Multifunctional Coatings*. Science, 2007. **318**(5849): p. 426-430.
113. Qiu, W.-Z., H.-C. Yang, and Z.-K. Xu, *Dopamine-assisted co-deposition: An emerging and promising strategy for surface modification*. Advances in Colloid and Interface Science, 2018. **256**: p. 111-125.
114. Wang, T., et al., *Novel methodology for facile fabrication of nanofiltration membranes based on nucleophilic nature of polydopamine*. Journal of Membrane Science, 2016. **511**: p. 65-75.
115. Wang, T., et al., *Fabrication of high flux nanofiltration membrane via*

- hydrogen bonding based co-deposition of polydopamine with poly(vinyl alcohol)*. Journal of Membrane Science, 2018. **552**: p. 222-233.
116. Zhang, L., et al., *Engineering of ultrafine polydopamine nanoparticles in-situ assembling on polyketone substrate for highly-efficient oil-water emulsions separation*. Journal of Membrane Science, 2020. **613**: p. 118501.
117. Zhou, Z., et al., *New approach for improving anticorrosion and biocompatibility of magnesium alloys via polydopamine intermediate layer-induced hydroxyapatite coating*. Surfaces and Interfaces, 2020. **19**: p. 100501.
118. Yang, S., et al., *A novel fluorescent DNA sensor system based on polydopamine modified MgAl-layered double hydroxides*. Colloid and Interface Science Communications, 2020. **37**: p. 100294.
119. Cheng, D., et al., *Immobilizing reduced graphene oxide on polydopamine-templated PET fabrics for UV protection, electrical conduction and application as wearable sensors*. Materials Chemistry and Physics, 2020. **241**: p. 122371.
120. Zia, Q., et al., *Polydopamine-assisted grafting of chitosan on porous poly (L-lactic acid) electrospun membranes for adsorption of heavy metal ions*. International Journal of Biological Macromolecules, 2020.
121. Wai, K.P., et al., *In situ immobilization of silver on polydopamine-coated composite membrane for enhanced antibacterial properties*. Journal of Water Process Engineering, 2020. **33**: p. 100989.
122. Teng, X., et al., *A polydopamine-coated polyamide thin film composite membrane with enhanced selectivity and stability for vanadium redox flow battery*. Journal of Membrane Science, 2020. **601**: p. 117906.
123. Sun, R., et al., *Polydopamine functionalized multi-walled carbon nanotubes*

- supported PdAu nanoparticles as advanced catalysts for ethylene glycol oxidation. Colloids and Surfaces A: Physicochemical and Engineering Aspects*, 2019. **578**: p. 123566.
124. Kumar, A., B. Mishra, and B.P. Tripathi, *Polydopamine assisted synthesis of ultrafine silver nanoparticles for heterogeneous catalysis and water remediation. Nano-Structures & Nano-Objects*, 2020. **23**: p. 100489.
125. Mu, Y., et al., *Development of highly permeable and antifouling ultrafiltration membranes based on the synergistic effect of carboxylated polysulfone and bio-inspired co-deposition modified hydroxyapatite nanotubes. Journal of Colloid and Interface Science*, 2020. **572**: p. 48-61.
126. Zhao, B., et al., *Polyamide thin film nanocomposite membrane containing polydopamine modified ZIF-8 for nanofiltration. Colloids and Surfaces A: Physicochemical and Engineering Aspects*, 2020: p. 125971.
127. Cui, J., et al., *Bio-inspired fabrication of superhydrophilic nanocomposite membrane based on surface modification of SiO₂ anchored by polydopamine towards effective oil-water emulsions separation. Separation and Purification Technology*, 2019. **209**: p. 434-442.
128. Sun, X., et al., *Surface modification of TiO₂ with polydopamine and its effect on photocatalytic degradation mechanism. Colloids and Surfaces A: Physicochemical and Engineering Aspects*, 2019. **570**: p. 199-209.
129. Jin, A., et al., *Nanoparticles modified by polydopamine: Working as “drug” carriers. Bioactive Materials*, 2020. **5**(3): p. 522-541.
130. Peng, Y., et al., *A novel reduced graphene oxide-based composite membrane prepared via a facile deposition method for multifunctional applications: oil/water separation and cationic dyes removal. Separation and Purification*

- Technology, 2018. **200**: p. 130-140.
131. Liu, Z., et al., *A mussel inspired highly stable graphene oxide membrane for efficient oil-in-water emulsions separation*. Separation and Purification Technology, 2018. **199**: p. 37-46.
 132. Choi, H.-g., et al., *Thin-film composite membranes comprising ultrathin hydrophilic polydopamine interlayer with graphene oxide for forward osmosis*. Desalination, 2019. **449**: p. 41-49.
 133. Liu, Y., et al., *Bioinspired dopamine modulating graphene oxide nanocomposite membrane interposed by super-hydrophilic UiO-66 with enhanced water permeability*. Separation and Purification Technology, 2020. **253**: p. 117552.
 134. Yang, E., et al., *Enhanced desalination performance of forward osmosis membranes based on reduced graphene oxide laminates coated with hydrophilic polydopamine*. Carbon, 2017. **117**: p. 293-300.
 135. Mazinani, S., et al., *Phase separation analysis of Extem/solvent/non-solvent systems and relation with membrane morphology*. Journal of Membrane Science, 2017. **526**: p. 301-314.
 136. Kahrs, C. and J. Schwellenbach, *Membrane formation via non-solvent induced phase separation using sustainable solvents: A comparative study*. Polymer, 2020. **186**: p. 122071.
 137. Ma, N., et al., *Nanocomposite substrates for controlling internal concentration polarization in forward osmosis membranes*. Journal of Membrane Science, 2013. **441**: p. 54-62.
 138. Jung, J.T., et al., *Understanding the non-solvent induced phase separation (NIPS) effect during the fabrication of microporous PVDF membranes via*

- thermally induced phase separation (TIPS)*. Journal of Membrane Science, 2016. **514**: p. 250-263.
139. Park, M.J., et al., *Graphene oxide incorporated polysulfone substrate for the fabrication of flat-sheet thin-film composite forward osmosis membranes*. Journal of Membrane Science, 2015. **493**: p. 496-507.
140. Vatanpour, V., et al., *Fabrication and characterization of anti-fouling and anti-bacterial Ag-loaded graphene oxide/polyethersulfone mixed matrix membrane*. Journal of Industrial and Engineering Chemistry, 2015. **30**: p. 342-352.
141. Alkhouzaam, A., et al., *Membranes for CO₂ Separation*, in *Nanostructured Polymer Membranes*. 2016, John Wiley & Sons, Inc. p. 237-292.
142. Sadrzadeh, M. and S. Bhattacharjee, *Rational design of phase inversion membranes by tailoring thermodynamics and kinetics of casting solution using polymer additives*. Journal of Membrane Science, 2013. **441**: p. 31-44.
143. Qian, X., et al., *Chitosan/graphene oxide mixed matrix membrane with enhanced water permeability for high-salinity water desalination by pervaporation*. Desalination, 2018. **438**: p. 83-96.
144. Chen, J., et al., *Controllable fabrication of ultrathin free-standing graphene films*. Philosophical Transactions of the Royal Society A: Mathematical, Physical and Engineering Sciences, 2014. **372**(2013): p. 20130017.
145. Tsou, C.-H., et al., *Effect of microstructure of graphene oxide fabricated through different self-assembly techniques on 1-butanol dehydration*. Journal of Membrane Science, 2015. **477**: p. 93-100.
146. Liu, H., H. Wang, and X. Zhang, *Facile Fabrication of Freestanding Ultrathin Reduced Graphene Oxide Membranes for Water Purification*. Advanced

- Materials, 2015. **27**(2): p. 249-254.
147. Zhao, X., et al., *Free-Standing Graphene Oxide-Palygorskite Nanohybrid Membrane for Oil/Water Separation*. ACS Applied Materials & Interfaces, 2016. **8**(12): p. 8247-8256.
 148. Wei, Y., et al., *Multilayered graphene oxide membranes for water treatment: A review*. Carbon, 2018. **139**: p. 964-981.
 149. Halakoo, E. and X. Feng, *Layer-by-layer assembled membranes from graphene oxide and polyethyleneimine for ethanol and isopropanol dehydration*. Chemical Engineering Science, 2020. **216**: p. 115488.
 150. Jia, T., et al., *Constructing multilayered membranes with layer-by-layer self-assembly technique based on graphene oxide for anhydrous proton exchange membranes*. European Polymer Journal, 2020. **122**: p. 109362.
 151. Nan, Q., P. Li, and B. Cao, *Fabrication of positively charged nanofiltration membrane via the layer-by-layer assembly of graphene oxide and polyethylenimine for desalination*. Applied Surface Science, 2016. **387**: p. 521-528.
 152. Choi, W., et al., *Layer-by-Layer Assembly of Graphene Oxide Nanosheets on Polyamide Membranes for Durable Reverse-Osmosis Applications*. ACS Applied Materials & Interfaces, 2013. **5**(23): p. 12510-12519.
 153. Kang, H., et al., *Interlamination restrictive effect of carbon nanotubes for graphene oxide forward osmosis membrane via layer by layer assembly*. Applied Surface Science, 2019. **465**: p. 1103-1106.
 154. Raaijmakers, M.J.T. and N.E. Benes, *Current trends in interfacial polymerization chemistry*. Progress in Polymer Science, 2016. **63**: p. 86-142.
 155. Perera, D.H.N., et al., *Regulating the aqueous phase monomer balance for flux*

- improvement in polyamide thin film composite membranes*. Journal of Membrane Science, 2015. **487**: p. 74-82.
156. Gohil, J.M. and R.R. Choudhury, *Chapter 2 - Introduction to Nanostructured and Nano-enhanced Polymeric Membranes: Preparation, Function, and Application for Water Purification*, in *Nanoscale Materials in Water Purification*, S. Thomas, et al., Editors. 2019, Elsevier. p. 25-57.
157. Safarpour, M., et al., *Development of a novel high flux and fouling-resistant thin film composite nanofiltration membrane by embedding reduced graphene oxide/TiO₂*. Separation and Purification Technology, 2015. **154**: p. 96-107.
158. Yin, J., G. Zhu, and B. Deng, *Graphene oxide (GO) enhanced polyamide (PA) thin-film nanocomposite (TFN) membrane for water purification*. Desalination, 2016. **379**: p. 93-101.
159. Fathizadeh, M., et al., *Polyamide/nitrogen-doped graphene oxide quantum dots (N-GOQD) thin film nanocomposite reverse osmosis membranes for high flux desalination*. Desalination, 2019. **451**: p. 125-132.
160. Saeedi-Jurkuyeh, A., et al., *A novel synthetic thin-film nanocomposite forward osmosis membrane modified by graphene oxide and polyethylene glycol for heavy metals removal from aqueous solutions*. Reactive and Functional Polymers, 2020. **146**: p. 104397.
161. Safarpour, M., A. Khataee, and V. Vatanpour, *Thin film nanocomposite reverse osmosis membrane modified by reduced graphene oxide/TiO₂ with improved desalination performance*. Journal of Membrane Science, 2015. **489**: p. 43-54.
162. Li, S., et al., *Antibacterial thin film nanocomposite reverse osmosis membrane by doping silver phosphate loaded graphene oxide quantum dots in polyamide*

- layer. *Desalination*, 2019. **464**: p. 94-104.
163. Rajakumaran, R., et al., *Effect of ZnO morphology on GO-ZnO modified polyamide reverse osmosis membranes for desalination*. *Desalination*, 2019. **467**: p. 245-256.
164. Shakeri, A., et al., *Blue lemon@quaternary graphene oxide open frameworks: As a novel nanostructure for performance enhancement of thin film nanocomposite forward osmosis membrane*. *Chemical Engineering Research and Design*, 2019. **148**: p. 451-459.
165. Hegab, H.M., et al., *Fine-Tuning the Surface of Forward Osmosis Membranes via Grafting Graphene Oxide: Performance Patterns and Biofouling Propensity*. *ACS Applied Materials & Interfaces*, 2015. **7**(32): p. 18004-18016.
166. Abbaszadeh, M., D. Krizak, and S. Kundu, *Layer-by-layer assembly of graphene oxide nanoplatelets embedded desalination membranes with improved chlorine resistance*. *Desalination*, 2019. **470**: p. 114116.
167. Ng, Z.C., W.J. Lau, and A.F. Ismail, *GO/PVA-integrated TFN RO membrane: Exploring the effect of orientation switching between PA and GO/PVA and evaluating the GO loading impact*. *Desalination*, 2020: p. 114538.
168. Perreault, F., M.E. Tousley, and M. Elimelech, *Thin-Film Composite Polyamide Membranes Functionalized with Biocidal Graphene Oxide Nanosheets*. *Environmental Science & Technology Letters*, 2014. **1**(1): p. 71-76.
169. Zhao, W., et al., *Thin-Film Nanocomposite Forward-Osmosis Membranes on Hydrophilic Microfiltration Support with an Intermediate Layer of Graphene Oxide and Multiwall Carbon Nanotube*. *ACS Applied Materials & Interfaces*,

2018. **10**(40): p. 34464-34474.
170. Yadav, S., et al., *Recent developments in forward osmosis membranes using carbon-based nanomaterials*. Desalination, 2020. **482**: p. 114375.
171. Wang, Y., et al., *Graphene oxide modified graphitic carbon nitride as a modifier for thin film composite forward osmosis membrane*. Journal of Membrane Science, 2015. **475**: p. 281-289.
172. Choudhury, R.R., et al., *Antifouling, fouling release and antimicrobial materials for surface modification of reverse osmosis and nanofiltration membranes*. Journal of Materials Chemistry A, 2018. **6**(2): p. 313-333.
173. Thabit, M.S., et al., *Evaluation of forward osmosis as a pretreatment process for multi stage flash seawater desalination*. Desalination, 2019. **461**: p. 22-29.
174. Lohaus, J., Y.M. Perez, and M. Wessling, *What are the microscopic events of colloidal membrane fouling?* Journal of Membrane Science, 2018. **553**: p. 90-98.
175. Kim, J., et al., *Influence of colloidal fouling on pressure retarded osmosis*. Desalination, 2016. **389**: p. 207-214.
176. Kim, H.-S., et al., *Effect of biofilm inhibitor on biofouling resistance in RO processes*. Fuel, 2019. **253**: p. 823-832.
177. Yang, Z., et al., *Improved anti-biofouling performance of polyamide reverse osmosis membranes modified with a polyampholyte with effective carboxyl anion and quaternary ammonium cation ratio*. Journal of Membrane Science, 2019: p. 117529.
178. Tong, T., et al., *Mineral scaling in membrane desalination: Mechanisms, mitigation strategies, and feasibility of scaling-resistant membranes*. Journal of Membrane Science, 2019. **579**: p. 52-69.

179. Ashfaq, M.Y., et al., *Isolation, identification and biodiversity of antiscalant degrading seawater bacteria using MALDI-TOF-MS and multivariate analysis*. Science of The Total Environment, 2019. **656**: p. 910-920.
180. Ashfaq, M.Y., et al., *Effect of concentration of calcium and sulfate ions on gypsum scaling of reverse osmosis membrane, mechanistic study*. Journal of Materials Research and Technology, 2020. **9**(6): p. 13459-13473.
181. Pramanik, B.K., et al., *Effect of the coagulation/persulfate pre-treatment to mitigate organic fouling in the forward osmosis of municipal wastewater treatment*. Journal of Environmental Management, 2019. **249**: p. 109394.
182. Ly, Q.V., et al., *Characteristics and influencing factors of organic fouling in forward osmosis operation for wastewater applications: A comprehensive review*. Environment International, 2019. **129**: p. 164-184.
183. Alkhouzaam, A. and H. Qiblawey, *Functional GO-based membranes for water treatment and desalination: fabrication methods, performance and advantages. A review*. Chemosphere, 2021. **274**: p. 129853.
184. *Why Is Bovine Serum the Preferred Standard for Protein Assays?* 2019 [cited 2021 1/1]; Available from: <https://info.gbiosciences.com/blog/why-is-bovine-serum-the-preferred-standard-for-protein-assays>.
185. Singh, R., *Chapter 2 - Water and Membrane Treatment*, in *Membrane Technology and Engineering for Water Purification (Second Edition)*, R. Singh, Editor. 2015, Butterworth-Heinemann: Oxford. p. 81-178.
186. Olk, D.C., et al., *Environmental and Agricultural Relevance of Humic Fractions Extracted by Alkali from Soils and Natural Waters*. Journal of Environmental Quality, 2019. **48**(2): p. 217-232.
187. Valamohammadi, E., et al., *Preparation of positively charged thin-film*

- nanocomposite membranes based on the reaction between hydrolyzed polyacrylonitrile containing carbon nanomaterials and HPEI for water treatment application.* Separation and Purification Technology, 2020. **242**: p. 116826.
188. Chen, X., et al., *A reduced graphene oxide nanofiltration membrane intercalated by well-dispersed carbon nanotubes for drinking water purification.* Nanoscale, 2016. **8**(10): p. 5696-5705.
189. Zinadini, S., et al., *Preparation of a novel antifouling mixed matrix PES membrane by embedding graphene oxide nanoplates.* Journal of Membrane Science, 2014. **453**: p. 292-301.
190. Chu, K.H., et al., *Evaluation of graphene oxide-coated ultrafiltration membranes for humic acid removal at different pH and conductivity conditions.* Separation and Purification Technology, 2017. **181**: p. 139-147.
191. Zhao, C., et al., *Effect of graphene oxide concentration on the morphologies and antifouling properties of PVDF ultrafiltration membranes.* Journal of Environmental Chemical Engineering, 2013. **1**(3): p. 349-354.
192. Homem, N.C., et al., *Surface modification of a polyethersulfone microfiltration membrane with graphene oxide for reactive dyes removal.* Applied Surface Science, 2019. **486**: p. 499-507.
193. Igbiginun, E., et al., *Graphene oxide functionalized polyethersulfone membrane to reduce organic fouling.* Journal of Membrane Science, 2016. **514**: p. 518-526.
194. Yang, L., B. Tang, and P. Wu, *UF membrane with highly improved flux by hydrophilic network between graphene oxide and brominated poly(2,6-dimethyl-1,4-phenylene oxide).* Journal of Materials Chemistry A, 2014. **2**(43):

- p. 18562-18573.
195. Gu, Q., et al., *Chemical-grafting of graphene oxide quantum dots (GOQDs) onto ceramic microfiltration membranes for enhanced water permeability and anti-organic fouling potential*. Applied Surface Science, 2020. **502**: p. 144128.
 196. Kang, Y., et al., *Sulfonated graphene oxide incorporated thin film nanocomposite nanofiltration membrane to enhance permeation and antifouling properties*. Desalination, 2019. **470**: p. 114125.
 197. Rastgar, M., et al., *Highly-efficient forward osmosis membrane tailored by magnetically responsive graphene oxide/Fe₃O₄ nanohybrid*. Applied Surface Science, 2018. **441**: p. 923-935.
 198. Ayyaru, S., T.T.L. Dinh, and Y.-H. Ahn, *Enhanced antifouling performance of PVDF ultrafiltration membrane by blending zinc oxide with support of graphene oxide nanoparticle*. Chemosphere, 2020. **241**: p. 125068.
 199. Wu, L.-g., et al., *Enhanced performance of polyvinylidene fluoride ultrafiltration membranes by incorporating TiO₂/graphene oxide*. Chemical Engineering Research and Design, 2019. **141**: p. 492-501.
 200. Safarpour, M., A. Khataee, and V. Vatanpour, *Preparation of a Novel Polyvinylidene Fluoride (PVDF) Ultrafiltration Membrane Modified with Reduced Graphene Oxide/Titanium Dioxide (TiO₂) Nanocomposite with Enhanced Hydrophilicity and Antifouling Properties*. Industrial & Engineering Chemistry Research, 2014. **53**(34): p. 13370-13382.
 201. Zhang, J., et al., *Synergetic effects of oxidized carbon nanotubes and graphene oxide on fouling control and anti-fouling mechanism of polyvinylidene fluoride ultrafiltration membranes*. Journal of Membrane Science, 2013. **448**: p. 81-92.

202. Yu, L., et al., *Antibacterial Thin-Film Nanocomposite Membranes Incorporated with Graphene Oxide Quantum Dot-Mediated Silver Nanoparticles for Reverse Osmosis Application*. ACS Sustainable Chemistry & Engineering, 2019. **7**(9): p. 8724-8734.
203. Saleem, H. and S.J. Zaidi, *Nanoparticles in reverse osmosis membranes for desalination: A state of the art review*. Desalination, 2020. **475**: p. 114171.
204. Majali, F., et al., *Design and operating characteristics of pilot scale reverse osmosis plants*. Desalination, 2008. **222**(1): p. 441-450.
205. Perera, D.H.N., et al., *Room-temperature development of thin film composite reverse osmosis membranes from cellulose acetate with antibacterial properties*. Journal of Membrane Science, 2014. **453**: p. 212-220.
206. Seman, M.N.A., M. Khayet, and N. Hilal, *Nanofiltration thin-film composite polyester polyethersulfone-based membranes prepared by interfacial polymerization*. Journal of Membrane Science, 2010. **348**(1): p. 109-116.
207. Chae, H.-R., et al., *Graphene oxide-embedded thin-film composite reverse osmosis membrane with high flux, anti-biofouling, and chlorine resistance*. Journal of Membrane Science, 2015. **483**: p. 128-135.
208. Kim, S., et al., *Non-swelling graphene oxide-polymer nanocomposite membrane for reverse osmosis desalination*. Journal of Membrane Science, 2018. **562**: p. 47-55.
209. Ghaseminezhad, S.M., M. Barikani, and M. Salehirad, *Development of graphene oxide-cellulose acetate nanocomposite reverse osmosis membrane for seawater desalination*. Composites Part B: Engineering, 2019. **161**: p. 320-327.
210. Shao, F., et al., *Layer-by-layer self-assembly TiO₂ and graphene oxide on*

- polyamide reverse osmosis membranes with improved membrane durability.* Desalination, 2017. **423**: p. 21-29.
211. Chae, H.-R., et al., *Synergetic effect of graphene oxide nanosheets embedded in the active and support layers on the performance of thin-film composite membranes.* Journal of Membrane Science, 2017. **525**: p. 99-106.
212. Oatley-Radcliffe, D.L., et al., *Nanofiltration membranes and processes: A review of research trends over the past decade.* Journal of Water Process Engineering, 2017. **19**: p. 164-171.
213. Ji, Y., et al., *Recent developments in nanofiltration membranes based on nanomaterials.* Chinese Journal of Chemical Engineering, 2017. **25**(11): p. 1639-1652.
214. Zhao, W., et al., *Graphene oxide incorporated thin film nanocomposite membrane at low concentration monomers.* Journal of Membrane Science, 2018. **565**: p. 380-389.
215. Yuan, Y., et al., *Enhanced desalination performance of carboxyl functionalized graphene oxide nanofiltration membranes.* Desalination, 2017. **405**: p. 29-39.
216. Wang, J., et al., *O-(Carboxymethyl)-chitosan Nanofiltration Membrane Surface Functionalized with Graphene Oxide Nanosheets for Enhanced Desalting Properties.* ACS Applied Materials & Interfaces, 2015. **7**(7): p. 4381-4389.
217. Zhang, Z., et al., *Interfacial Force-Assisted In-Situ Fabrication of Graphene Oxide Membrane for Desalination.* ACS Applied Materials & Interfaces, 2018. **10**(32): p. 27205-27214.
218. Abdi, G., et al., *Removal of dye and heavy metal ion using a novel synthetic*

- polyethersulfone nanofiltration membrane modified by magnetic graphene oxide/metformin hybrid*. Journal of Membrane Science, 2018. **552**: p. 326-335.
219. Liang, Y., et al., *Graphene quantum dots (GQDs)-polyethyleneimine as interlayer for the fabrication of high performance organic solvent nanofiltration (OSN) membranes*. Chemical Engineering Journal, 2020. **380**: p. 122462.
220. Abadikhah, H., et al., *High flux thin film nanocomposite membrane incorporated with functionalized TiO₂@reduced graphene oxide nanohybrids for organic solvent nanofiltration*. Chemical Engineering Science, 2019. **204**: p. 99-109.
221. Liu, M.-L., et al., *Graphene oxide/cross-linked polyimide (GO/CLPI) composite membranes for organic solvent nanofiltration*. Chemical Engineering Research and Design, 2019. **146**: p. 182-189.
222. Kang, X., et al., *Bio-inspired co-deposited preparation of GO composite loose nanofiltration membrane for dye contaminated wastewater sustainable treatment*. Journal of Hazardous Materials, 2020. **400**: p. 123121.
223. Li, P., et al., *A novel loose-NF membrane based on the phosphorylation and cross-linking of polyethyleneimine layer on porous PAN UF membranes*. Journal of Membrane Science, 2018. **555**: p. 56-68.
224. Amiri, S., et al., *Fabrication and characterization of a novel polyvinyl alcohol-graphene oxide-sodium alginate nanocomposite hydrogel blended PES nanofiltration membrane for improved water purification*. Separation and Purification Technology, 2020. **250**: p. 117216.
225. Xu, P., et al., *“Bridge” graphene oxide modified positive charged nanofiltration thin membrane with high efficiency for Mg²⁺/Li⁺ separation*.

- Desalination, 2020. **488**: p. 114522.
226. Yang, M., et al., *Preparation of graphene oxide modified poly(m-phenylene isophthalamide) nanofiltration membrane with improved water flux and antifouling property*. Applied Surface Science, 2017. **394**: p. 149-159.
227. Wang, N., et al., *Self-assembly of graphene oxide and polyelectrolyte complex nanohybrid membranes for nanofiltration and pervaporation*. Chemical Engineering Journal, 2012. **213**: p. 318-329.
228. Hilal, N., et al., *The use of ultrafiltration and nanofiltration membranes in the treatment of metal-working fluids*. Desalination, 2004. **167**: p. 227-238.
229. Khakpour, S., Y. Jafarzadeh, and R. Yegani, *Incorporation of graphene oxide/nanodiamond nanocomposite into PVC ultrafiltration membranes*. Chemical Engineering Research and Design, 2019. **152**: p. 60-70.
230. Kang, Y., et al., *Novel sulfonated graphene oxide incorporated polysulfone nanocomposite membranes for enhanced-performance in ultrafiltration process*. Chemosphere, 2018. **207**: p. 581-589.
231. Hwang, T., et al., *Ultrafiltration using graphene oxide surface-embedded polysulfone membranes*. Separation and Purification Technology, 2016. **166**: p. 41-47.
232. Prince, J.A., et al., *Ultra-wetting graphene-based membrane*. Journal of Membrane Science, 2016. **500**: p. 76-85.
233. Ouyang, G., et al., *Remarkable permeability enhancement of polyethersulfone (PES) ultrafiltration membrane by blending cobalt oxide/graphene oxide nanocomposites*. RSC Advances, 2015. **5**(86): p. 70448-70460.
234. Yu, L., et al., *Preparation and characterization of HPEI-GO/PES ultrafiltration membrane with antifouling and antibacterial properties*. Journal

- of Membrane Science, 2013. **447**: p. 452-462.
235. Zhao, H., et al., *Improving the antifouling property of polysulfone ultrafiltration membrane by incorporation of isocyanate-treated graphene oxide*. Physical Chemistry Chemical Physics, 2013. **15**(23): p. 9084-9092.
236. Alammar, A., et al., *Oil-in-water separation with graphene-based nanocomposite membranes for produced water treatment*. Journal of Membrane Science, 2020. **603**: p. 118007.
237. Li, F., et al., *A Mussel-inspired method to fabricate reduced graphene oxide/g-C₃N₄ composites membranes for catalytic decomposition and oil-in-water emulsion separation*. Chemical Engineering Journal, 2017. **322**: p. 33-45.
238. Algamdi, M.S., et al., *Fabrication of graphene oxide incorporated polyethersulfone hybrid ultrafiltration membranes for humic acid removal*. Separation and Purification Technology, 2019. **223**: p. 17-23.
239. Xia, S. and M. Ni, *Preparation of poly(vinylidene fluoride) membranes with graphene oxide addition for natural organic matter removal*. Journal of Membrane Science, 2015. **473**: p. 54-62.
240. Ayyaru, S. and Y.-H. Ahn, *Application of sulfonic acid group functionalized graphene oxide to improve hydrophilicity, permeability, and antifouling of PVDF nanocomposite ultrafiltration membranes*. Journal of Membrane Science, 2017. **525**: p. 210-219.
241. Meng, N., et al., *The effect of reduction degree of GO nanosheets on microstructure and performance of PVDF/GO hybrid membranes*. Journal of Membrane Science, 2016. **501**: p. 169-178.
242. Sun, H., B. Tang, and P. Wu, *Development of Hybrid Ultrafiltration Membranes with Improved Water Separation Properties Using Modified*

- Superhydrophilic Metal–Organic Framework Nanoparticles*. ACS Applied Materials & Interfaces, 2017. **9**(25): p. 21473-21484.
243. Karkooti, A., et al., *Development of advanced nanocomposite membranes using graphene nanoribbons and nanosheets for water treatment*. Journal of Membrane Science, 2018. **560**: p. 97-107.
244. Liu, X., et al., *A novel PVDF/PFSA-g-GO ultrafiltration membrane with enhanced permeation and antifouling performances*. Separation and Purification Technology, 2020. **233**: p. 116038.
245. Tofighy, M.A., T. Mohammadi, and M.H. Sadeghi, *High-flux PVDF/PVP nanocomposite ultrafiltration membrane incorporated with graphene oxide nanoribbons with improved antifouling properties*. Journal of Applied Polymer Science, 2020. **138**(4): p. 49718.
246. Liu, H., et al., *Preparation of a hydrophilic and antibacterial dual function ultrafiltration membrane with quaternized graphene oxide as a modifier*. Journal of Colloid and Interface Science, 2020. **562**: p. 182-192.
247. Jaleh, B., et al., *Preparation and Characterization of Polyvinylpyrrolidone/Polysulfone Ultrafiltration Membrane Modified by Graphene Oxide and Titanium Dioxide for Enhancing Hydrophilicity and Antifouling Properties*. Journal of Inorganic and Organometallic Polymers and Materials, 2020. **30**(6): p. 2213-2223.
248. Ma, C., et al., *Graphene oxide-polyethylene glycol incorporated PVDF nanocomposite ultrafiltration membrane with enhanced hydrophilicity, permeability, and antifouling performance*. Chemosphere, 2020. **253**: p. 126649.
249. Zhao, G., et al., *Graphene oxide quantum dots embedded polysulfone*

- membranes with enhanced hydrophilicity, permeability and antifouling performance.* Science China Materials, 2019. **62**(8): p. 1177-1187.
250. Zhang, W., et al., *Functionalization of ultrafiltration membrane with polyampholyte hydrogel and graphene oxide to achieve dual antifouling and antibacterial properties.* Journal of Membrane Science, 2018. **565**: p. 293-302.
251. Lee, J., et al., *Graphene oxide nanoplatelets composite membrane with hydrophilic and antifouling properties for wastewater treatment.* Journal of Membrane Science, 2013. **448**: p. 223-230.
252. Wang, Z., et al., *Novel GO-blended PVDF ultrafiltration membranes.* Desalination, 2012. **299**: p. 50-54.
253. Eykamp, W., *Chapter 1 Microfiltration and ultrafiltration,* in *Membrane Science and Technology*, R.D. Noble and S.A. Stern, Editors. 1995, Elsevier. p. 1-43.
254. Anis, S.F., R. Hashaikh, and N. Hilal, *Microfiltration membrane processes: A review of research trends over the past decade.* Journal of Water Process Engineering, 2019. **32**: p. 100941.
255. Shao, L., et al., *One-step preparation of sepiolite/graphene oxide membrane for multifunctional oil-in-water emulsions separation.* Applied Clay Science, 2019. **181**: p. 105208.
256. Sun, J., et al., *One-step preparation of GO/SiO₂ membrane for highly efficient separation of oil-in-water emulsion.* Journal of Membrane Science, 2018. **553**: p. 131-138.
257. Zhao, H., et al., *Integration of microfiltration and visible-light-driven photocatalysis on g-C₃N₄ nanosheet/reduced graphene oxide membrane for enhanced water treatment.* Applied Catalysis B: Environmental, 2016. **194**: p.

134-140.

258. Kim, Y., et al., *Effective removal of cesium from wastewater via adsorptive filtration with potassium copper hexacyanoferrate-immobilized and polyethyleneimine-grafted graphene oxide*. Chemosphere, 2020. **250**: p. 126262.
259. Samantaray, P.K., G. Madras, and S. Bose, *PVDF/PBSA membranes with strongly coupled phosphonium derivatives and graphene oxide on the surface towards antibacterial and antifouling activities*. Journal of Membrane Science, 2018. **548**: p. 203-214.
260. Suwaileh, W., et al., *Forward osmosis membranes and processes: A comprehensive review of research trends and future outlook*. Desalination, 2020. **485**: p. 114455.
261. Alfahel, R., et al., *Fabrication of fouling resistant Ti₃C₂T_x (MXene)/cellulose acetate nanocomposite membrane for forward osmosis application*. Journal of Water Process Engineering, 2020. **38**: p. 101551.
262. Ang, W.L., et al., *Forward osmosis research trends in desalination and wastewater treatment: A review of research trends over the past decade*. Journal of Water Process Engineering, 2019. **31**: p. 100886.
263. Altaee, A., et al., *Energy efficiency of hollow fibre membrane module in the forward osmosis seawater desalination process*. Journal of Membrane Science, 2019. **587**: p. 117165.
264. Mondal, S., R.W. Field, and J.J. Wu, *Novel approach for sizing forward osmosis membrane systems*. Journal of Membrane Science, 2017. **541**: p. 321-328.
265. Wang, Y.-N., et al., *Membranes and processes for forward osmosis-based*

- desalination: Recent advances and future prospects*. Desalination, 2018. **434**: p. 81-99.
266. Lee, W.J., et al., *Fouling mitigation in forward osmosis and membrane distillation for desalination*. Desalination, 2020. **480**: p. 114338.
267. Akther, N., et al., *Influence of graphene oxide lateral size on the properties and performances of forward osmosis membrane*. Desalination, 2020. **484**: p. 114421.
268. Shakeri, A., H. Salehi, and M. Rastgar, *Antifouling electrically conductive membrane for forward osmosis prepared by polyaniline/graphene nanocomposite*. Journal of Water Process Engineering, 2019. **32**: p. 100932.
269. Rastgar, M., et al., *Substantially improved antifouling properties in electro-oxidative graphene laminate forward osmosis membrane*. Chemical Engineering Research and Design, 2019. **141**: p. 413-424.
270. Stankovich, S., et al., *Systematic Post-assembly Modification of Graphene Oxide Paper with Primary Alkylamines*. Chemistry of Materials, 2010. **22**(14): p. 4153-4157.
271. Jang, J., et al., *Graphene oxide nanocomposite membrane cooperatively cross-linked by monomer and polymer overcoming the trade-off between flux and rejection in forward osmosis*. Journal of Membrane Science, 2020. **598**: p. 117684.
272. Pang, J., et al., *Exploring the sandwich antibacterial membranes based on UiO-66/graphene oxide for forward osmosis performance*. Carbon, 2019. **144**: p. 321-332.
273. Chen, L., et al., *Ion sieving in graphene oxide membranes via cationic control of interlayer spacing*. Nature, 2017. **550**(7676): p. 380-383.

274. Salehi, H., M. Rastgar, and A. Shakeri, *Anti-fouling and high water permeable forward osmosis membrane fabricated via layer by layer assembly of chitosan/graphene oxide*. Applied Surface Science, 2017. **413**: p. 99-108.
275. Wu, X., et al., *Polyvinylpyrrolidone modified graphene oxide as a modifier for thin film composite forward osmosis membranes*. Journal of Membrane Science, 2017. **540**: p. 251-260.
276. Shen, L., S. Xiong, and Y. Wang, *Graphene oxide incorporated thin-film composite membranes for forward osmosis applications*. Chemical Engineering Science, 2016. **143**: p. 194-205.
277. Wang, Q., et al., *Desalination by pervaporation: A review*. Desalination, 2016. **387**: p. 46-60.
278. Wang, P. and T.-S. Chung, *Recent advances in membrane distillation processes: Membrane development, configuration design and application exploring*. Journal of Membrane Science, 2015. **474**: p. 39-56.
279. Abdel-Karim, A., et al., *PVDF membranes containing reduced graphene oxide: Effect of degree of reduction on membrane distillation performance*. Desalination, 2019. **452**: p. 196-207.
280. Zahirifar, J., et al., *Fabrication of a novel octadecylamine functionalized graphene oxide/PVDF dual-layer flat sheet membrane for desalination via air gap membrane distillation*. Desalination, 2018. **428**: p. 227-239.
281. Bhadra, M., S. Roy, and S. Mitra, *Desalination across a graphene oxide membrane via direct contact membrane distillation*. Desalination, 2016. **378**: p. 37-43.
282. Lecaros, R.L.G., et al., *Alcohol dehydration performance of pervaporation composite membranes with reduced graphene oxide and graphene quantum*

- dots homostructured filler*. Carbon, 2020. **162**: p. 318-327.
283. Zhao, D., et al., *Facilitated water-selective permeation via PEGylation of graphene oxide membrane*. Journal of Membrane Science, 2018. **567**: p. 311-320.
284. Ang, M.B.M.Y., et al., *Graphene oxide functionalized with zwitterionic copolymers as selective layers in hybrid membranes with high pervaporation performance*. Journal of Membrane Science, 2019. **587**: p. 117188.
285. Cheng, C., et al., *Integrated polyamide thin-film nanofibrous composite membrane regulated by functionalized interlayer for efficient water/isopropanol separation*. Journal of Membrane Science, 2018. **553**: p. 70-81.
286. Li, W., et al., *Recovery of bio-butanol from aqueous solution with ZIF-8 modified graphene oxide composite membrane*. Journal of Membrane Science, 2020. **598**: p. 117671.
287. Salehian, P. and T.-S. Chung, *Thermally treated ammonia functionalized graphene oxide/polyimide membranes for pervaporation dehydration of isopropanol*. Journal of Membrane Science, 2017. **528**: p. 231-242.
288. Castro-Muñoz, R., et al., *Towards the dehydration of ethanol using pervaporation cross-linked poly(vinyl alcohol)/graphene oxide membranes*. Journal of Membrane Science, 2019. **582**: p. 423-434.
289. Zhu, T., et al., *ZIF-8@GO composites incorporated polydimethylsiloxane membrane with prominent separation performance for ethanol recovery*. Journal of Membrane Science, 2020. **598**: p. 117681.
290. Khazaei, A., et al., *Energy consumption in pervaporation, conventional and hybrid processes to separate toluene and i-octane*. Chemical Engineering and

- Processing - Process Intensification, 2018. **128**: p. 46-52.
291. Majooni, Y., H.R. Mortaheb, and A. Khodadadi Dizaji, *Enhancement in pervaporative performance of PDMS membrane for separation of styrene from wastewater by hybridizing with reduced graphene oxide*. Journal of Environmental Management, 2020. **261**: p. 110189.
292. Semenova, S.I., H. Ohya, and K. Soontarapa, *Hydrophilic membranes for pervaporation: An analytical review*. Desalination, 1997. **110**(3): p. 251-286.
293. Khraisheh, M., et al., *Characterization of polysulfone/diisopropylamine 1-alkyl-3-methylimidazolium ionic liquid membranes: high pressure gas separation applications*. Greenhouse Gases: Science and Technology, 2020. **10**(4): p. 795-808.
294. Alkhouzaam, A., et al., *High-pressure CO₂/N₂ and CO₂/CH₄ separation using dense polysulfone-supported ionic liquid membranes*. Journal of Natural Gas Science and Engineering, 2016. **36**: p. 472-485.
295. Chapman, P.D., et al., *Membranes for the dehydration of solvents by pervaporation*. Journal of Membrane Science, 2008. **318**(1): p. 5-37.
296. Sun, J., et al., *Tailoring the microstructure of poly(vinyl alcohol)-intercalated graphene oxide membranes for enhanced desalination performance of high-salinity water by pervaporation*. Journal of Membrane Science, 2020. **599**: p. 117838.
297. Xu, K., et al., *Synthesis of highly stable graphene oxide membranes on polydopamine functionalized supports for seawater desalination*. Chemical Engineering Science, 2016. **146**: p. 159-165.
298. Alkhouzaam, A., H. Qiblawey, and M. Khraisheh, *Polydopamine Functionalized Graphene Oxide as Membrane Nanofiller: Spectral and*

- Structural Studies. Membranes*, 2021. **11**(2): p. 86.
299. Alkhouzaam, A., et al., *High-pressure CO₂/N₂ and CO₂/CH₄ separation using dense polysulfone-supported ionic liquid membranes*. *Journal of Natural Gas Science and Engineering*, 2016. **36**: p. 472-485.
300. Alkhouzaam, A. and H. Qiblawey, *Novel polysulfone ultrafiltration membranes incorporating polydopamine functionalized graphene oxide with enhanced flux and fouling resistance*. *Journal of Membrane Science*, 2021. **620**: p. 118900.
301. Tian, J., et al., *Effect of membrane fouling on chiral separation*. *Journal of Membrane Science*, 2020. **593**: p. 117352.
302. Marcano, D.C., et al., *Improved Synthesis of Graphene Oxide*. *ACS Nano*, 2010. **4**(8): p. 4806-4814.
303. Tobi, A.R., et al., *Comparative analysis of physiochemical properties of physically activated carbon from palm bio-waste*. *Journal of Materials Research and Technology*.
304. Pumera, M., *Carbon Nanotubes Contain Residual Metal Catalyst Nanoparticles even after Washing with Nitric Acid at Elevated Temperature Because These Metal Nanoparticles Are Sheathed by Several Graphene Sheets*. *Langmuir*, 2007. **23**(11): p. 6453-6458.
305. Plata, D., P. Gschwend, and C. Reddy, *Industrially synthesized single-walled carbon nanotubes: Compositional data for users, environmental risk assessments, and source apportionment*. *Nanotechnology*, 2008. **19**: p. 185706.
306. Braun, E.I. and P. Pantano, *The importance of an extensive elemental analysis of single-walled carbon nanotube soot*. *Carbon*, 2014. **77**: p. 912-919.

307. Malard, L.M., et al., *Raman spectroscopy in graphene*. Physics Reports, 2009. **473**(5): p. 51-87.
308. Graf, D., et al., *Spatially Resolved Raman Spectroscopy of Single- and Few-Layer Graphene*. Nano Letters, 2007. **7**(2): p. 238-242.
309. Sadezky, A., et al., *Raman microspectroscopy of soot and related carbonaceous materials: Spectral analysis and structural information*. Carbon, 2005. **43**(8): p. 1731-1742.
310. López-Díaz, D., et al., *Evolution of the Raman Spectrum with the Chemical Composition of Graphene Oxide*. The Journal of Physical Chemistry C, 2017. **121**(37): p. 20489-20497.
311. Ferrari, A.C. and J. Robertson, *Resonant Raman spectroscopy of disordered, amorphous, and diamondlike carbon*. Physical Review B, 2001. **64**(7): p. 075414.
312. Lowe, S.E., et al., *The role of electrolyte acid concentration in the electrochemical exfoliation of graphite: Mechanism and synthesis of electrochemical graphene oxide*. Nano Materials Science, 2019.
313. Vollebregt, S., et al., *Influence of the growth temperature on the first and second-order Raman band ratios and widths of carbon nanotubes and fibers*. Carbon, 2012. **50**(10): p. 3542-3554.
314. Claramunt, S., et al., *The Importance of Interbands on the Interpretation of the Raman Spectrum of Graphene Oxide*. The Journal of Physical Chemistry C, 2015. **119**(18): p. 10123-10129.
315. Lin, T.N., et al., *Laser-ablation production of graphene oxide nanostructures: from ribbons to quantum dots*. Nanoscale, 2015. **7**(6): p. 2708-2715.
316. Tuinstra, F. and J.L. Koenig, *Raman Spectrum of Graphite*. The Journal of

- Chemical Physics, 1970. **53**(3): p. 1126-1130.
317. Zhu, Y., et al., *Graphene and Graphene Oxide: Synthesis, Properties, and Applications*. Advanced Materials, 2010. **22**(35): p. 3906-3924.
 318. Ferrari, A.C., et al., *Raman Spectrum of Graphene and Graphene Layers*. Physical Review Letters, 2006. **97**(18): p. 187401.
 319. Talyzin, A.V., et al., *Brodie vs Hummers graphite oxides for preparation of multi-layered materials*. Carbon, 2017. **115**: p. 430-440.
 320. Pan, S. and I.A. Aksay, *Factors Controlling the Size of Graphene Oxide Sheets Produced via the Graphite Oxide Route*. ACS Nano, 2011. **5**(5): p. 4073-4083.
 321. Panicker, N.J., J. Das, and P.P. Sahu, *Synthesis of highly oxidized graphene (HOG) by using HNO₃ and KMnO₄ as oxidizing agents*. Materials Today: Proceedings, 2020.
 322. Manwatkar, H.P., et al., *Synthesis and properties of amino and thiol functionalized graphene oxide*. Materials Today: Proceedings, 2020.
 323. Lee, M., et al., *Mussel-inspired functionalization of carbon nanotubes for hydroxyapatite mineralization*. Journal of Materials Chemistry, 2010. **20**(40): p. 8848-8853.
 324. Liu, Y., et al., *A mussel-induced method to fabricate reduced graphene oxide/halloysite nanotubes membranes for multifunctional applications in water purification and oil/water separation*. Chemical Engineering Journal, 2018. **336**: p. 263-277.
 325. Patel, K., et al., *Polydopamine films change their physicochemical and antimicrobial properties with a change in reaction conditions*. Physical Chemistry Chemical Physics, 2018. **20**(8): p. 5744-5755.

326. Liu, S., et al., *Polydopamine as a bridge to decorate monodisperse gold nanoparticles on Fe₃O₄ nanoclusters for the catalytic reduction of 4-nitrophenol*. RSC Advances, 2017. **7**(72): p. 45545-45551.
327. Liu, T., et al., *Self-polymerized dopamine as an organic cathode for Li- and Na-ion batteries*. Energy & Environmental Science, 2017. **10**(1): p. 205-215.
328. Li, X., et al., *Mussel-inspired modification of PTFE membranes in a miscible THF-Tris buffer mixture for oil-in-water emulsions separation*. Journal of Membrane Science, 2018. **555**: p. 237-249.
329. Ren, P.G., et al., *Characterization and performance of dodecyl amine functionalized graphene oxide and dodecyl amine functionalized graphene/high-density polyethylene nanocomposites: A comparative study*. Journal of Applied Polymer Science, 2014. **131**(2).
330. Ma, Y.-r., et al., *Polydopamine-Coated Magnetic Nanoparticles for Enrichment and Direct Detection of Small Molecule Pollutants Coupled with MALDI-TOF-MS*. ACS Applied Materials & Interfaces, 2013. **5**(3): p. 1024-1030.
331. Coskun, H., et al., *Chemical vapor deposition - based synthesis of conductive polydopamine thin-films*. Thin Solid Films, 2018. **645**: p. 320-325.
332. Wang, J., et al., *Interfacial modification of basalt fiber filling composites with graphene oxide and polydopamine for enhanced mechanical and tribological properties*. RSC Advances, 2018. **8**(22): p. 12222-12231.
333. Du, W., et al., *Graphene oxide in aqueous and nonaqueous media: Dispersion behaviour and solution chemistry*. Carbon, 2020. **158**: p. 568-579.
334. Jing, L.-C., et al., *Water-based polyurethane composite anticorrosive barrier coating via enhanced dispersion of functionalized graphene oxide in the*

- presence of acidified multi-walled carbon nanotubes*. Progress in Organic Coatings, 2020. **146**: p. 105734.
335. Konios, D., et al., *Dispersion behaviour of graphene oxide and reduced graphene oxide*. Journal of Colloid and Interface Science, 2014. **430**: p. 108-112.
336. Aliabadian, E., et al., *Application of graphene oxide nanosheets and HPAM aqueous dispersion for improving heavy oil recovery: Effect of localized functionalization*. Fuel, 2020. **265**: p. 116918.
337. Jamalludin, M.R., et al., *Antifouling polysulfone membranes blended with green SiO₂ from rice husk ash (RHA) for humic acid separation*. Chemical Engineering Research and Design, 2016. **114**: p. 268-279.
338. Ang, M.B.M.Y., et al., *Mitigating the fouling of mixed-matrix cellulose acetate membranes for oil–water separation through modification with polydopamine particles*. Chemical Engineering Research and Design, 2020. **159**: p. 195-204.
339. Rahimpour, A., et al., *Novel functionalized carbon nanotubes for improving the surface properties and performance of polyethersulfone (PES) membrane*. Desalination, 2012. **286**: p. 99-107.
340. Zhang, J., et al., *Improved hydrophilicity, permeability, antifouling and mechanical performance of PVDF composite ultrafiltration membranes tailored by oxidized low-dimensional carbon nanomaterials*. Journal of Materials Chemistry A, 2013. **1**(9): p. 3101-3111.
341. Akbari, M., et al., *Janus graphene oxide nanosheet: A promising additive for enhancement of polymeric membranes performance prepared via phase inversion*. Journal of Colloid and Interface Science, 2018. **527**: p. 10-24.

342. Sikarwar, B.S., et al., *Dropwise Condensation Studies on Multiple Scales*. Heat Transfer Engineering, 2012. **33**(4-5): p. 301-341.
343. Onda, T., et al., *Super-Water-Repellent Fractal Surfaces*. Langmuir, 1996. **12**(9): p. 2125-2127.
344. Fontananova, E., et al., *Effect of functional groups on the properties of multiwalled carbon nanotubes/polyvinylidene fluoride composite membranes*. Journal of Membrane Science, 2017. **541**: p. 198-204.
345. Luo, M.-l., et al., *Hydrophilic modification of poly(ether sulfone) used TiO₂ nanoparticles by a sol-gel process*. Journal of Materials Processing Technology, 2006. **172**(3): p. 431-436.
346. Razmjou, A., J. Mansouri, and V. Chen, *The effects of mechanical and chemical modification of TiO₂ nanoparticles on the surface chemistry, structure and fouling performance of PES ultrafiltration membranes*. Journal of Membrane Science, 2011. **378**(1): p. 73-84.
347. Khan, A., et al., *Fabrication and characterization of polysulfone/modified nanocarbon black composite antifouling ultrafiltration membranes*. Journal of Membrane Science, 2018. **554**: p. 71-82.
348. Gao, W., et al., *Membrane fouling control in ultrafiltration technology for drinking water production: A review*. Desalination, 2011. **272**(1): p. 1-8.
349. Saini, B., M.K. Sinha, and S.K. Dash, *Mitigation of HA, BSA and oil/water emulsion fouling of PVDF Ultrafiltration Membranes by SiO₂-g-PEGMA nanoparticles*. Journal of Water Process Engineering, 2019. **30**: p. 100603.
350. Chai, P.V., et al., *Preparation of novel polysulfone-Fe₃O₄/GO mixed-matrix membrane for humic acid rejection*. Journal of Water Process Engineering, 2017. **15**: p. 83-88.

APPENDIX A: CHARACTERIZATION OF NANOPARTICLES

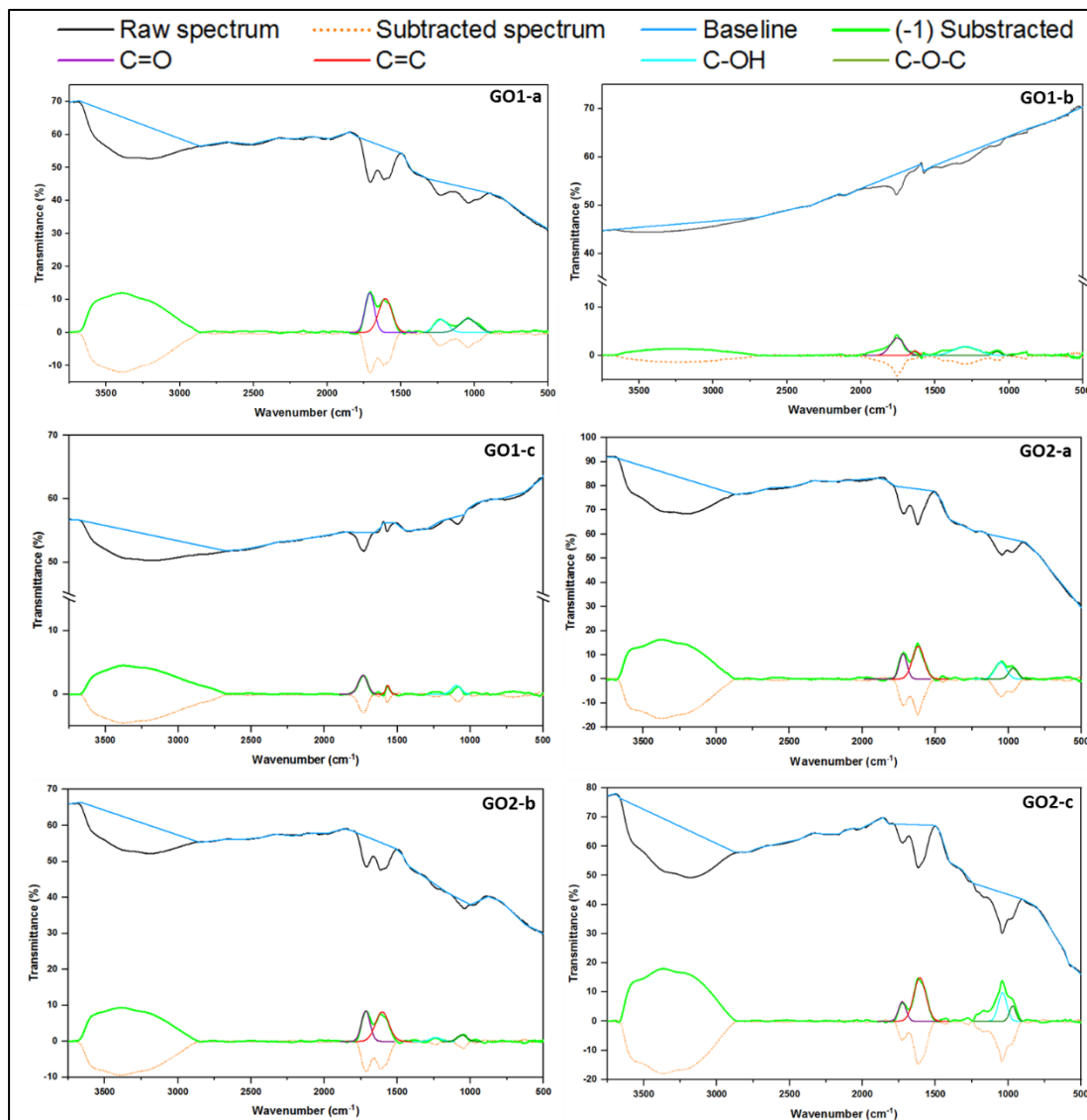


Figure A1: Illustration of FTIR spectra treatment and deconvolution for the quantitative analysis

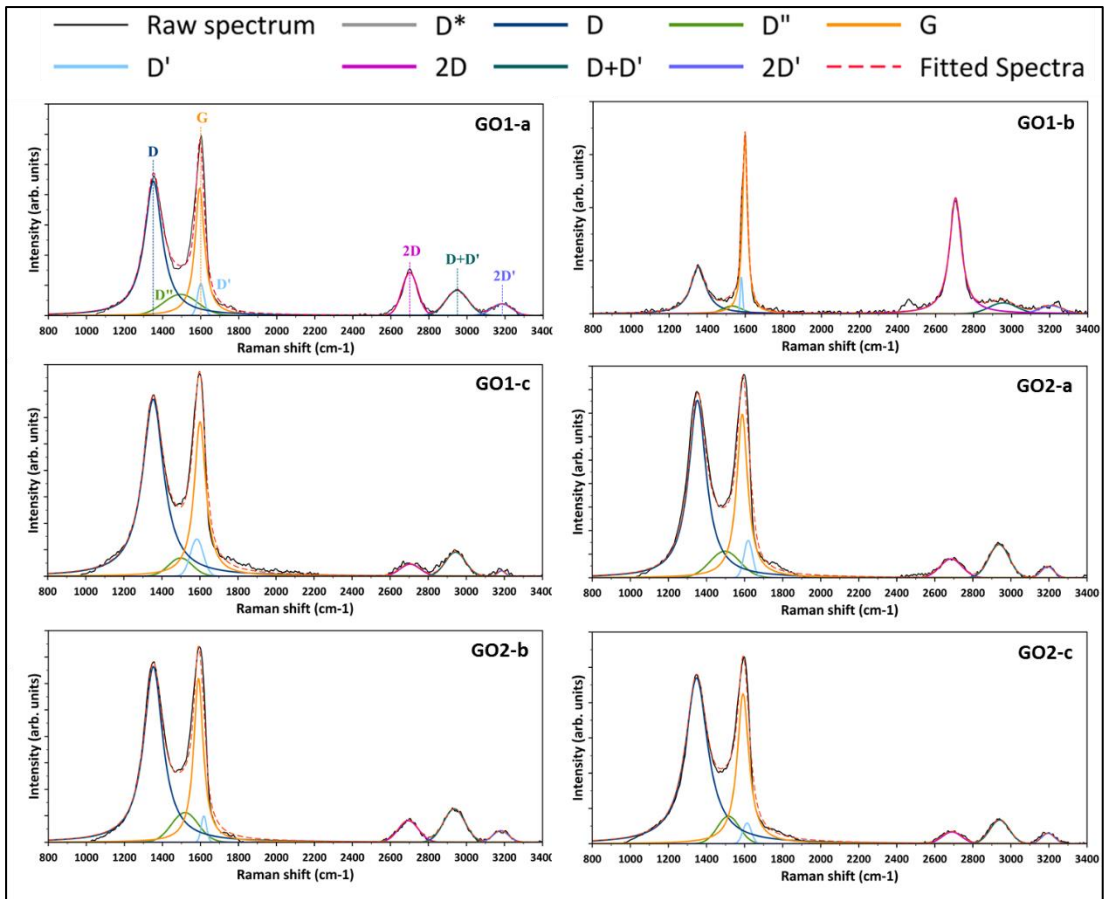


Figure A2: Illustration of Raman spectra deconvolution and peak fittings

Table A1: Bands parameters estimated from the Raman first-order spectra fits.

Sample	Band	Peak center (cm^{-1})	Peak intensity (arb. units)	Peak Area (arb. units)	I_D/I_G	L_a (nm)
GO1-a	D	1352	445	78998	2.0	9.7
	D''	1495	70	15938		
	G	1595	421	39748		
	D'	1601	105	4575		
GO1-b	D	1353	44	6684	0.8	23.6
	D''	1530	7	934		
	G	1599	166	8216		
	D'	1579	34	543		
GO1-c	D	1354	669	141196	2.1	9.2
	D''	1498	69	10705		
	G	1601	583	67732		
	D'	1584	140	11922		
GO2-a	D	1352	1884	334053	1.8	10.9
	D''	1497	282	55642		
	G	1588	1737	189857		
	D'	1619	394	22390		
GO2-b	D	1352	1328	253379	2.1	9.0
	D''	1519	224	39607		
	G	1590	1238	118540		
	D'	1618	197	7012		
GO2-c	D	1348	940	211287	2.1	9.0
	D''	1515	156	22466		
	G	1592	849	98624		
	D'	1613	117	6620		

Table A2: Bands parameters estimated from the Raman second-order spectra fits.

Sample	Band	Peak center (cm^{-1})	Peak intensity (arb. units)	Area (arb. units)
GO1-a	2D	2698.2	136	13798
	D+D'	2949.1	77	9952
	2D'	3182.3	32	3876
GO1-b	2D	2705.1	104	11361
	D+D'	2955.6	10	1846
	2D'	3208.2	7	1151
GO1-c	2D	2705.2	45	5991
	D+D'	2943.3	91	12049
	2D'	3209.6	7	766
GO2-a	2D	2685.5	199	28497
	D+D'	2937.7	353	46929
	2D'	3193	118	9796
GO2-b	2D	2694.5	163	21601
	D+D'	2936	252	35558
	2D'	3180.6	87	8939
GO2-c	2D	2690	66	8464
	D+D'	2940.7	134	17109
	2D'	3195	59	5126

Table A3: Peaks parameters and the atomic compositions estimated from the XPS spectra fits for the pristine GO and rGO-PDA nanoparticles.

Sample	Peak	functional group	Binding energy (eV)	Peak area (arb. units)	at. %
GO	C 1s	C-C	284.4	10026	11.48
	C 1s	C-O	285.8	10334	11.84
	C 1s	C=O	287.0	3444	3.94
	C 1s	C(O)OH	289.0	1170	1.34
	O 1s	O-C=O	529.5	4284	4.91
	O 1s	C=O	530.8	17439	19.97
	O 1s	C-O	532.7	17757	20.34
	O 1s	C-O-C	535.2	22856	26.18
rGO-PDA	C 1s	C-NH ₂	281.0	4129	4.36
	C 1s	C-C	283.3	23635	24.98
	C 1s	C-O	285.3	9495	10.04
	C 1s	C=O	287.0	3684	3.89
	C 1s	C(O)OH	289.0	1020	1.08
	O 1s	O-C=O	529.0	9978	10.55
	O 1s	C=O	529.8	12369	13.07
	O 1s	C-O	531.6	20223	21.37
	O 1s	C-O-C	534.6	1202	1.27
	N 1s	N-C	396.2	538	0.57
	N 1s	N-H	398.7	7125	7.53
	N 1s	N-H ⁺	401.8	1216	1.29

Table A4: D and G bands' parameters of the Raman spectra and the estimated crystallite size of the GO and rGO-PDA nanoparticles.

GO sample	Curve	Peak center (cm ⁻¹)	Peak area (arb. unit)	I _D /I _G	La (nm)
GO	D	1352	334053	1.8	10.9
	G	1588	189857		
GO-PDA	D	1352	59039	1.3	15.2
	G	1583	46638		

Table A5: Bands parameters estimated from the Raman first-order spectra fits for the pristine GO and rGO-PDA nanoparticles.

Sample	Band	Raman shift (cm^{-1})	Peak intensity (arb. units)	Peak area (arb. units)
GO	D	1352	1737	334053
	D''	1496	282	55642
	G	1588	1736	189858
	D'	1619	394	22390
rGO-PDA	D	1352	282	59039
	D''	1492	72	8735
	G	1583	292	46638
	D'	1603	66	2724
	D*	1188	53	9783

Table A6: Bands parameters estimated from the Raman second-order spectra fits for the pristine GO and rGO-PDA nanoparticles.

Sample	Band	Raman shift (cm^{-1})	Peak intensity (arb. units)	Peak area (arb. units)
GO	2D	2685	199	28497
	D+D'	2938	353	46929
	2D'	3193	118	9796
rGO-PDA	2D	2722	69	31083
	D+D'	2950	56	12224
	2D'	3160	51	12439

APPENDIX B: CHARACTERIZATION OF THE MEMBRANES

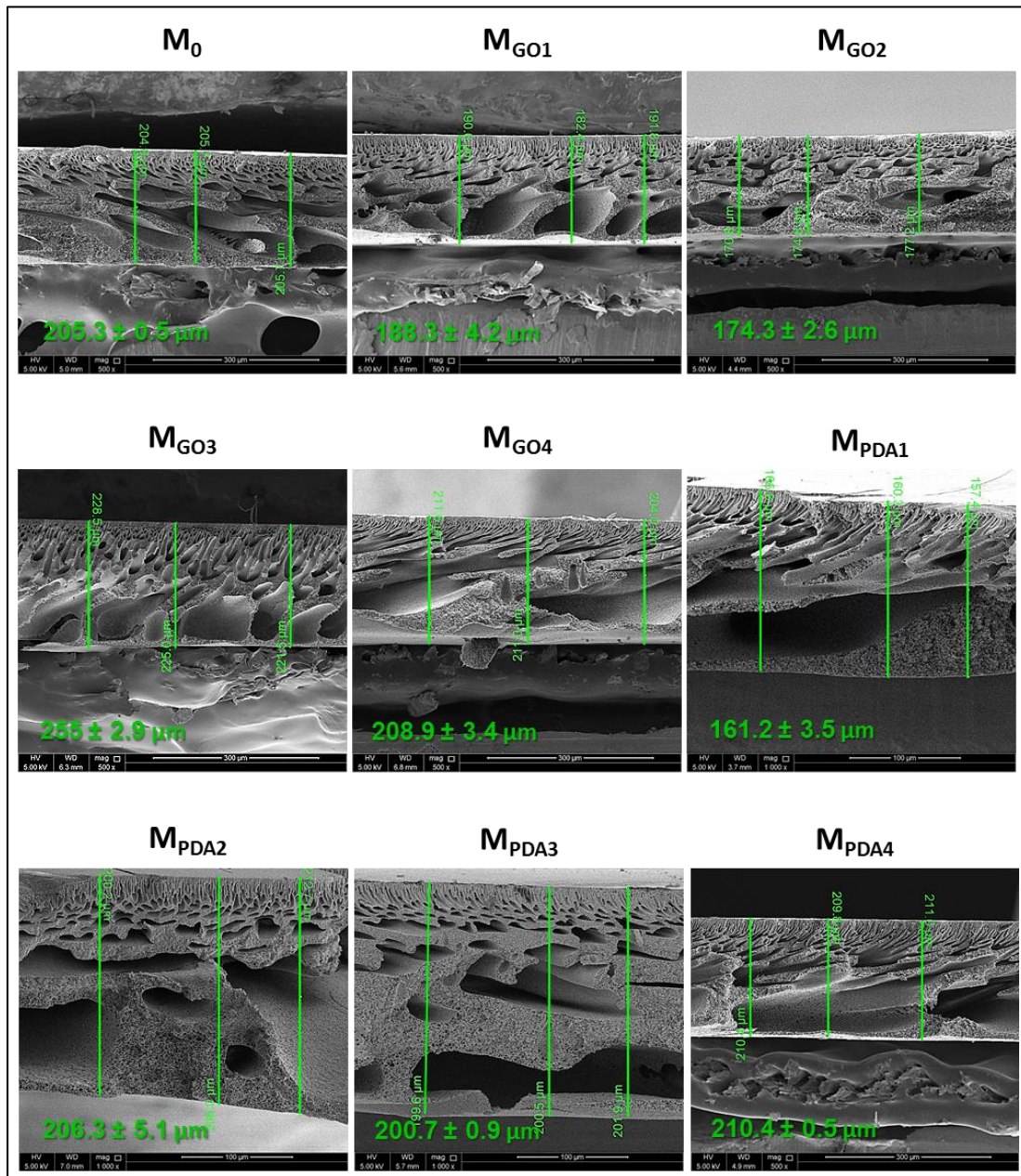


Figure B1: determination of the average membranes thickness by the cross-section SEM images.

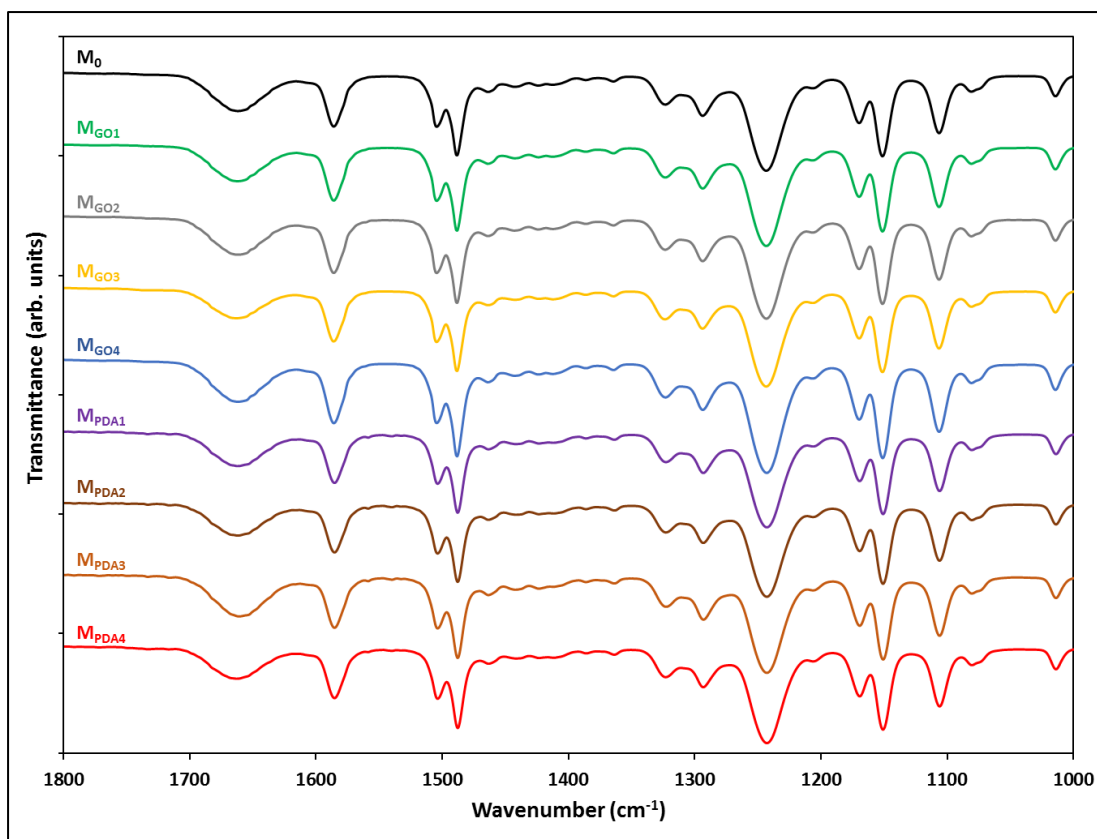


Figure B2: FTIR-UATR spectra of the prepared membranes.

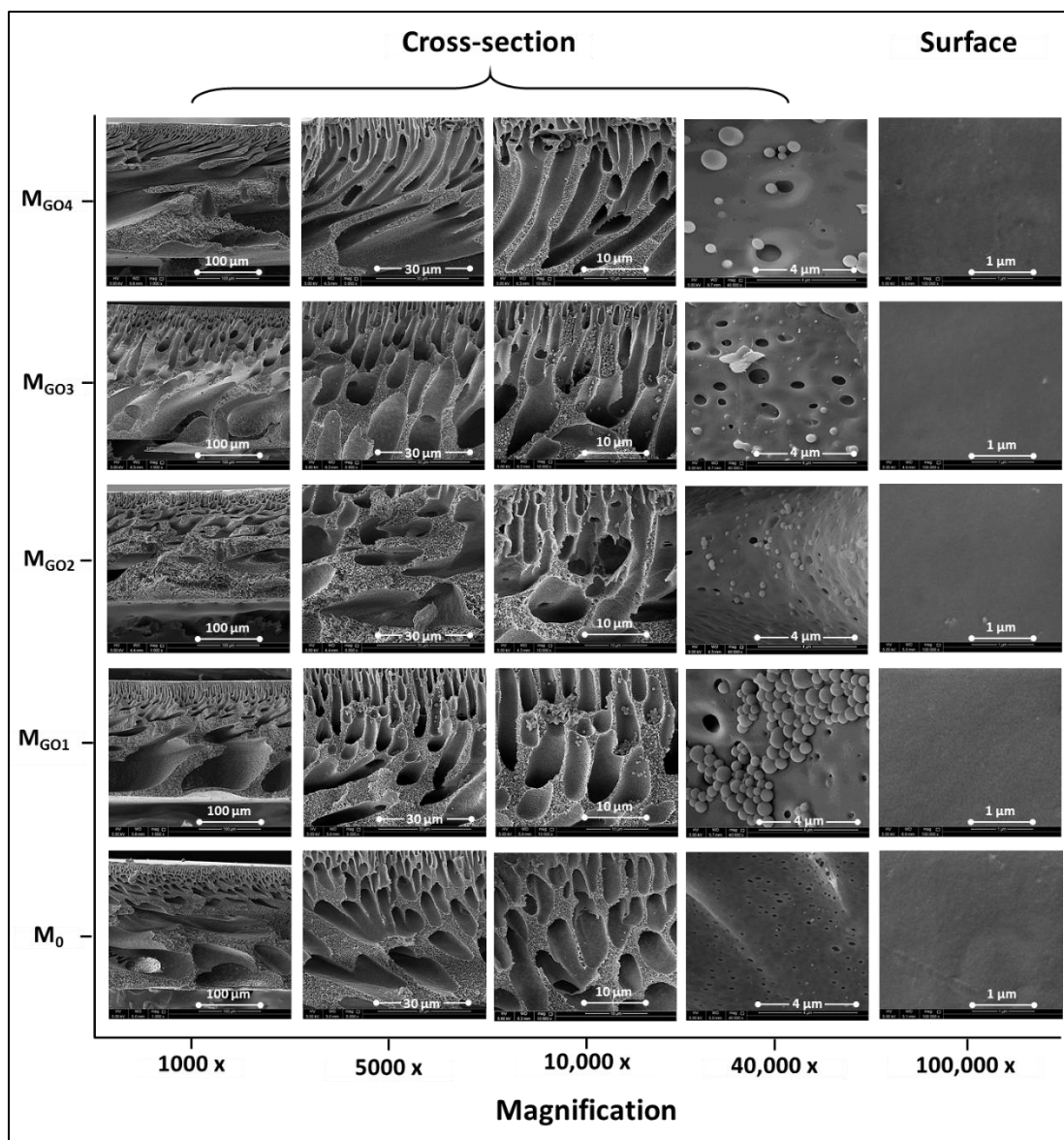


Figure B3: SEM images of pristine PSF and PSF/GO MMMs.

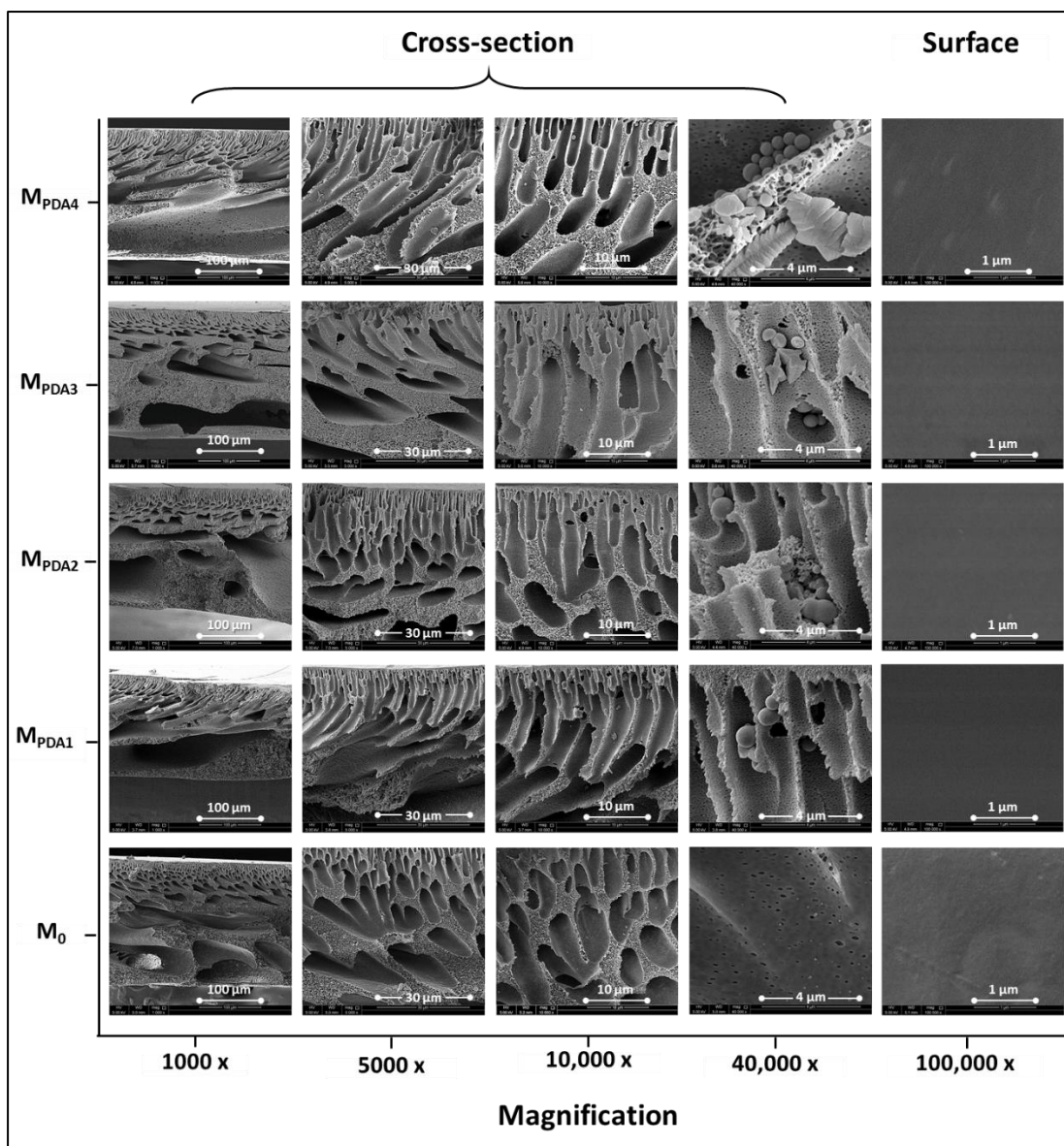


Figure B4: SEM images of pristine PSF and PSF/rGO-PDA MMMs

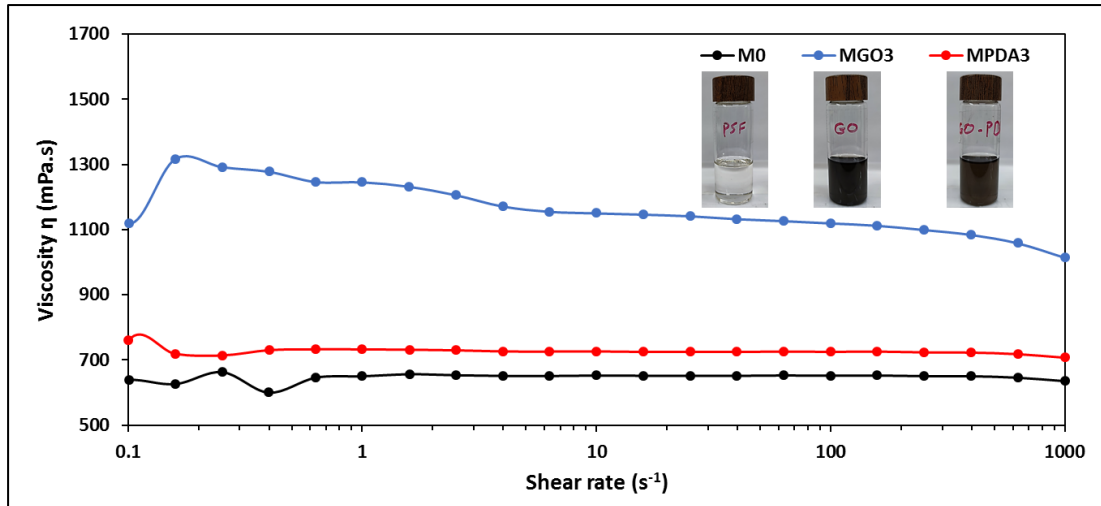


Figure B5: Viscosity measurements of the casting solutions of M₀, M_{GO3} and M_{PD_{A3}}.

Table B1: The output of the correlation test of PWP, contact angle, mean pore size (R_m), average roughness (Ra) and flux recovery ratios (FRR).

	PWP	Ra	CA	BSA-FRR ₃	HA-FRR ₃
PWP	1				
Ra	0.7614	1			
CA	-0.5235	-0.8205	1		
BSA-FRR ₃	0.5664	0.6830	-0.6822	1	
HA-FRR ₃	0.4148	0.6719	-0.9107	0.5585	1